The University of Sheffield

Faculty of Engineering

Department of Electrical and Electronic Engineering

Communications Group

Periodic Frequency Selective Surfaces for Reduction of Specular Scatter in Indoor Applications

by

Christopher James Davenport

A thesis submitted as partial fulfilment of the requirements for the degree of Doctor of Philosophy

August 2015

for Mum, Dad, Andrew, Emily, and Kelly

Summary

This thesis investigates the use of a variety of passive frequency selective surfaces for specular scatter reduction. Motivation from this work stems from the increased interest in controlling propagation in indoor environments. Influencing the propagation environment using both passive and active structures is of current research interest due to the increased use of wireless devices inside building structures. This thesis aims to develop surfaces suitable for installation on corridor walls to work alongside existing solutions.

An initial literature review of frequency selective surfaces; particularly for use inside buildings to create smart environments, suggests reducing the propagation down corridors could be beneficial in decreasing co-channel interference although no solutions have been offered.

Development of the initial comb frequency selective surface (CR-FSS) enabled measurement systems and simulation models to be constructed and compared. Due to the various limitations of the CR-FSS, design modifications and evolutions are investigated to overcome issues with poor angular performance, polarisation dependant performance, and experimental manufacture. The initial challenge was to create a rotationally symmetrical surface which could reduce specular scatter from additional angles of incidence in the elevation plane. A pin reflection FSS (PR-FSS) was created, however investigation of the structure showed that it was ineffectual for TE polarisation. In a multipath environment this could be an issue which effects performance. Investigation of additional variations of the CR-FSS such as the slanted comb FSS (SC-FSS) and crenelated CR-FSS complete the analysis.

A validation of a frequency selective comb structures is conducted with in-building multipath simulations. Statistical plots show that a comb structure can be used to significantly improve the signal-to-interference ratio (SIR) of co-channel transmitters at 2.4 GHz by reducing propagation down a corridor.

Publications

Excerpts of this work has been disseminated in both journals and conference proceedings, and are listed below:

Journal

1. **C.J. Davenport** and J. M. Rigelsford, "Design of comb reflection frequency selective surface for interference reduction in building corridors," *Electronics Lett.*, vol. 49, no. 23, pp. 1478–1479, 2013.

2. **C.J. Davenport** and J. M. Rigelsford, "Passive pin reflection frequency selective surface for interference reduction in the built environment," *Microwave and Optical Tech. Lett.*, vol. 56, no. 6, pp. 1424–1427 , 2014.

3. **C.J. Davenport** and J. M. Rigelsford, "Novel indoor bi-static measurement facility for full scattering characterisation of surfaces at oblique incidence," *Journal of Electromagnetic Waves and Applications*, vol. 28, no. 14, pp. 1798–1806 , 2014.

4. **C.J. Davenport** and J. M. Rigelsford, "Specular Reflection Reduction using Periodic Frequency Selective Surfaces," *IEEE Trans. Antennas Propag.*, vol. 62, no. 9, pp. 4518–4527 , 2014.

5. P. Valtr, **C.J. Davenport**, P. Pechac and J. M. Rigelsford, "A Mode Matching Technique for Analysis of Scattering by Periodic Comb Surfaces," *IEEE Trans. Antennas Propag.*, In Press.

Conference

6. H. Altan, K. Mohammadian, B. Voisin, **C. Davenport**, J. Rigelsford and J. Zhang, "Energy and wireless efficiency: Demonstrated through a typical UK home," in *Proceedings of Zero Energy Mass Custom Home*, Florida, USA, 2013.

7. **C.J. Davenport**, J. M. Rigelsford, J. Zhang, and H. Altan, "Periodic comb reflection frequency selective surface for interference reduction," in *Proceedings of Loughborough Antennas and Propagation Conference*, Loughborough, 2013, pp. 615–618.

8. **C.J. Davenport** and J. M. Rigelsford, "Design of a Pin Reflection Frequency Selective Surface From a Comb-Based Structure," in *Proceedings of European Conference on Antennas and Propagation*, Den Haag, 2014, pp. 1610–1613.

9. **C.J. Davenport** and J. M. Rigelsford, "Slanted-comb frequency selective surfaces for passive reduction in specular scatter," in *Proceedings of Progress in Electromagnetic Research*, Guangzhou, 2014.

10. **C.J. Davenport** and J. M. Rigelsford, "Slanted-comb Frequency Selective Surface for Use in Reducing Specular Scatter for TM Polarization," in *Proceedings of Loughborough Antennas and Propagation Conference*, Loughborough, 2014, pp. 628–630.

11. **C.J. Davenport** and J. M. Rigelsford, "In-building propagation control using passive elements installed in a corridor," in *Proceedings of Progress in Electromagnetic Research*, Prague, 2015, Presented.

Accepted conference abstracts

12. **C.J. Davenport** and J. M. Rigelsford, "Corrugated Comb Frequency Selective Surfaces for Control of Wireless Propagation in Buildings," in *Loughborough Antennas and Propagation Conference*, Loughborough, 2015, Accepted.

Acknowledgements

I would firstly like thank my supervisor, Dr Jonathan Rigelsford who was instrumental in directing my PhD. I would recommend him as a supervisor to any student in the future and the daily meetings will be missed.

I would like to thank Dr Hasim Altan and Professor Jie Zhang whom initially supervised me and provided me with great feedback as I was starting out. I would like to thank the EPSRC E-Futures DTC and British Gas for funding this project.

The whole Communications Group at the University of Sheffield are to be thanked for making the office a more friendly and lively place to study. Dr Lee Ford and Professor Richard Langley have both been able to offer me great advice and help on my project whenever I asked, and I would like to also thank them. I would like to also thank Jon Davidson, a fellow Sheffield student whom I have known since the first week of our undergraduate course, as well as all the other students and staff that helped me throughout my PhD.

A special mention to my best friends that I have known since secondary school. Tom Cairns, Rick Grammatica, Chris Lincoln, and Brad Rice have always been great mates.

I would like to thank my parents Kevin and Michelle, and younger siblings Andrew and Emily, for their support. I would never have achieved so much in life without any of them.

Finally, my fiancée Kelly has for the past 9 years supported me throughout University and this Thesis would not have got finished without her encouragement and help!

Contents

List of Figures

List of Tables

Abbreviations and Symbols

Abbreviations and acronyms

BPSK	binary phase shift keying
CDF	cumulative distribution function
CR-FSS	comb reflection frequency selective surface
CST MWS	Computer Simulation Technology - Microwave Studio
DTV	digital television
FIT	finite integral technique
FSS	frequency selective surface
GPIB	general purpose interface bus
GSM	Global System for Mobile Communications
GUI	graphical user interface
HIS	high impedance surface
ILS	industrial landing system
ISM	industrial, scientific and medical
ITU-R	International Telecommunication Union Radiocommunication
LOS	line-of-sight
MVDS	multipoint video distribution system
NaN	not a number
N-LOS	non-line-of-sight
NRL	Naval Research Laboratories
OFDM	orthogonal frequency-division multiplexing
RAM	radar absorbing material
RF	radio frequency
Rx	receiver
PEC	perfect electrical conductor
PR-FSS	pin reflection frequency selective surface
QAM	quadrature amplitude modulation
QPSK	quadrature phase shift keying
RCS	radar cross section
SC-FSS	slanted comb frequency selective surface

SINR	signal-to-interference-plus-noise ratio
SIR	signal-to-interference ratio
SUT	surface under test
TE	transverse electric
TETRA	terrestrial trunked radio
TM	transverse magnetic
Tx	transmitter
USB	universal serial bus
VOD	video on demand
VNA	vector network analyser
WiFEEB	Wireless Friendly Energy Efficient Buildings
Wi-Fi	wireless fidelity
WLAN	wireless local area network

Symbols and units

Symbols

α = period of FSS in mm

θ_c = crenelation angle

θ_i = angle of incidence in azimuth plane

θ_r = reflection angle

θ_s = scattering angle

θ_{slant} = slant angle of the SC-FSS

$\theta_{slant(2)}$ = secondary slant angle of the SC-FSS

λ = wavelength

ϕ_i = angle of incidence in the elevation plane

ω_o = resonant frequency

f_B = frequency of direct backscatter

h = Fin or pin height in mm

h_A = height of flat absorber in mm

h_c = height of fin in mm h_s = length of slanted comb in mm

R_1 = transmitter to SUT distance

R_2 = SUT to receiver distance

t = thickness of fin or pin in mm

w_1 = top crenelation thickness

w_2 = bottom crenelation thickness

Units

° = degree

dB = decibel

dBm = decibel-milliwatts

GHz = gigahertz

MHz = megahertz

ns = nanosecond

Chapter 1

Introduction

The control of wireless propagation in buildings has recently been of interest, however various issues still exist. This thesis presents an alternate solution to controlling wireless propagation in an indoor environment. The surfaces proposed in this work are ideally used simultaneously with other solutions within the field of indoor electromagnetic propagation. They aim to provide a low-cost method of preventing interference between co-channel transmitters by electromagnetically separating rooms by reducing propagation down building corridors.

This problem has been described as an issue by researchers, and could reduce the performance of other solutions in many scenarios. Previous research has described the use of frequency selective surfaces installed as either a wallpaper [1], or as a small window installed on an otherwise metallic (and thus reflective to all electromagnetic signals) wall. In some cases, the installation of such surfaces is expensive and requires redesign of buildings or installation of new walls to function suitably well. It is thus the overall purpose of this study to investigate inexpensive solutions that can be easily incorporated into the building structure.

Consideration is also given to the influence of energy efficient design and construction methods used. The use of thick and metallic building materials and insulation can significantly alter the propagation environment, and these are considered in the review of literature, and the design of surfaces and propagation scenarios.

1.1 Wireless friendly buildings

In most cases, a brute force method of ensuring good wireless connectivity within buildings is to use many transmitting nodes to provide sufficiently high strength connections. However, there are many issues associated with deployment of many nodes, such as high levels of interference [2], the added cost of multiple transmitters, and issues with installation of nodes. Interference is often caused by co-channel transmissions – signals broadcasting at the same frequency which interfere with each other, reducing the signal-to-interference-plus-noise ratio (SINR). At 2.4 GHz, this interference can be difficult to counteract as there is only 3 non-overlapping channels [3].

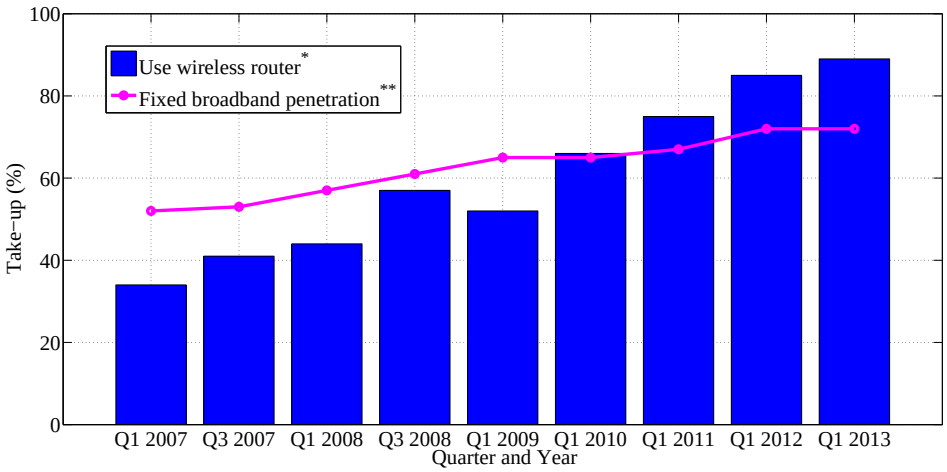

Figure 1.1: Ofcom research on wireless router take-up for those with a broadband connection at home [8]. (*from 2009 based on fixed broadband connections only. **prior to 2009 this is total broadband penetration.)

Several alternatives are currently available, each with their own advantages. By switching to 5 GHz, the user is presented with 23 non-overlapping channels [4], meaning that co-channel interference is unlikely to be an issue, particularly as Wi-Fi nodes are increasingly dual band and intelligent enough to switch to a less noisy channel [5]. Currently, two dual band router types exist for public use. The first is a simultaneous dual band router, offering twice the bandwidth of a single band router by operating at both 2.4 and 5 GHz. Secondly, a selectable dual band router allows the user to switch between either frequency and offers the same bandwidth

as a single band router. There are however disadvantages to using 5 GHz routers. Currently, very few devices actually have 5 GHz receivers and transmission through building walls decreases as the frequency of signal increases retrospectively shortening range [6]. However, the scattering of signals around corners and through doorways from edge diffractions is better at these higher frequencies.

High capacity wireless connectivity is increasingly an issue in the modern world, particularly as the large majority of IP traffic is due to video content. Cisco report that by 2018, IP video traffic will constitute 79% of all traffic, up from 66% in 2013 [7]. This means the requirement for high throughput and low interference wireless connections is essential due to the large quantity of data that must be transmitted. There has also been a distinguishable increase in consumer electronics within the last decade. Consequently, the number of devices requiring access to a high data rate wireless internet connection is increasing. Since 2007, the percentage of homes using a wireless router for connection to broadband has risen from 34% to 89% at the start of 2013 [8]. This year-on-year growth is illustrated in Fig. 1.1. Explanations for this uptake of wireless routers include an increase in the number of devices requiring wireless connectivity, and the low cost and ease of obtaining wireless routers when signing up to broadband contracts. Similarly for larger buildings, the reliability and coverage of a high throughput connection can be extremely useful.

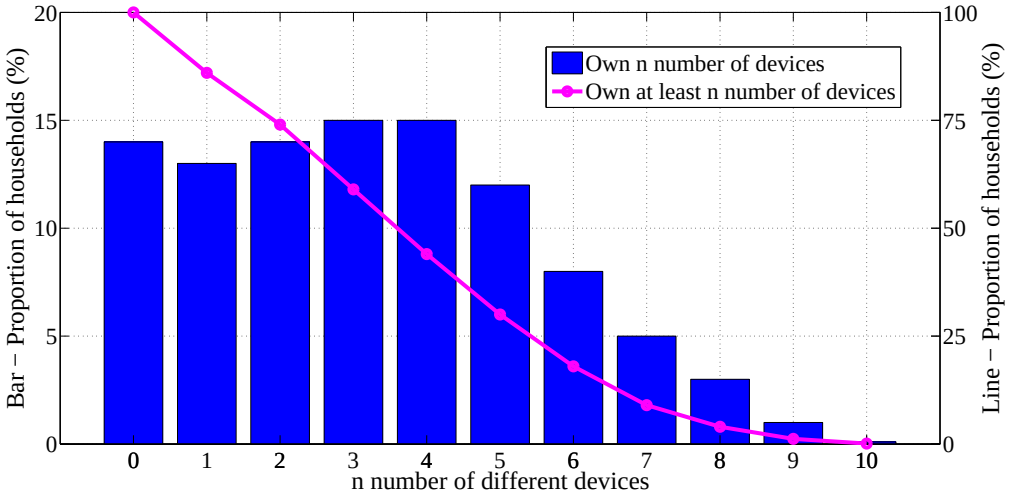

Figure 1.2: Ofcom research on the number of electrical devices in the home environment

There has also been a 20% increase in the use of fixed broadband in homes since 2007, with the figure at 72% for 2013. Furthermore, there has been a large increase in the number of electronic devices in the home requiring internet connectivity. 59% of households in the UK have at least 3 devices at home and these are most likely to be a laptop, smart phone, and a games console [8]. Other devices requiring broadband connection include desktop PCs, VOD boxes (such as BT, Virgin Media and Sky+), tablets, and smart televisions.

Due to the fact that these often share the same router and require high data rates for streaming videos and games, a high capacity wireless connection is required. This can be said of any scenario where there are a lot of end devices requiring high data rates. We can also consider that 44.1% of homes also have 4 or more electronic devices. This means that many routers are in close proximity to each other, particularly in semi-detached or terraced houses, where the transmitting ranges overlap. This problem also exists in buildings with much larger permanent and migrating populations, such as lecture theatres, restaurants, and places of work. Many of the devices requiring wireless internet connectivity are portable: electronic tablets, laptops, and mobile phones are all often used outside of the home environment. Such devices are also increasingly being used for both teaching and recreational purposes, requiring many high throughput wireless connections.

1.2 Energy efficient buildings

The building structure itself is integral to the design and application of any frequency selective surface (FSS) to be installed to control the propagation in buildings. Various building design regulations and favourable building techniques are described later in this thesis. Measurement of both thermal and electrical properties of various building material compositions will further the current knowledge in the subject area.

Government policies are the main driver for energy efficient developments [9] and according to a consultation on policy options report by Communities and Local Government [10], 17% of all UK emissions are from non-domestic buildings and 27% are from domestic dwellings. This has led to a large increase in interest into energy efficiency improvements to new buildings, and retrofitting older ones. Further interest

in new building materials and methods will increase considering new build dwellings and schools must be zero carbon by 2016 [11], and new build non-domestic buildings by 2019 [10].

Often, the techniques and methods used cause issue with the propagation of wireless signals, effecting connectivity and throughput of many services. For example, the use of metallic insulation in both small and large buildings has the potential to disrupt expected signal paths, including outdoor-to-indoor and in-building propagation. An example of such a structure is shown in Fig. 1.3, where all of the walls are coated with metallic insulation. However, there are still potential routes of propagation through window and door structures. These are traditionally seen as ideal transmission medium for signals as glass is reasonably good at allowing the transmission of high frequency signals. However, some additional building standards are leading to more potential issues.

Figure 1.3: A building coated in metallic insulation such as Celotex could have a negative impact on expected propagation routes for wireless signals.

The Passivhaus standard demands some of the highest energy efficiency and installation methods currently in use in the building sector. Once a structure is built to such a high level of performance, it is assessed against various criteria based on heating and cooling demand, air tightness and primary energy demand. These figures are much lower than other high efficiency standards, requiring the most advanced technologies in order to fulfil them. The Passivhaus standard in the UK

utilises thick insulation and triple pane double low-e glazed windows. As well as being triple glazed, the low emissivity glass is coated with a thin metallic layer to increase performance. Inevitably, this can effect outdoor-to-indoor signal level. The Passivhaus standard is not restricted to residential housing as non-domestic buildings can also be awarded such accolades for energy efficiency.

Metallized insulations are often used in the deployment of frequency selective surfaces to ensure adequate performance. Additionally, advances in some sectors drive the research and development in others and the wireless propagation sector has profited already with various research and cross-departmental collaboration projects such as the Wireless Friendly and Energy Efficient Buildings (WiFEEB) project at the University of Sheffield. There has been recent discussion related to the wireless friendliness of a building [12], however the WiFEEB project has several objectives related to an energy efficient building as well as its potential to be wireless friendly [13].

1.3 Proposed method of application

As described previously, the CR-FSS surface is ideal for use in long corridors, where any propagating signal is likely to reflect multiple times. An example of the necessary arrangement is shown in Fig. 1.4. The scenario shown displays two co-channel Wi-Fi transmitters, which are interfering with each other due to the propagation down the corridor.

The effect of building materials on cross-polarisation will be considered in the literature review, and will drive the investigation for a structure that works well for both TE and TM polarisations. In this case, the transmission frequency is arbitrary, however in the validation chapter later in the Thesis, they are Wi-Fi transmitters operating at 2.4 GHz. In the case of only two transmitters, the problem of interference would be reduced by switching channels. However, in large buildings where there are many transmitters, finding a clear channel is difficult, especially at 2.4 GHz where there are limited non-overlapping channels. The introduction of the CR-FSS into the corridor wall structure in Fig. 1.5 would have the effect of reducing specular scatters, redirecting this either back towards the transmitter or another pre-defined direction.

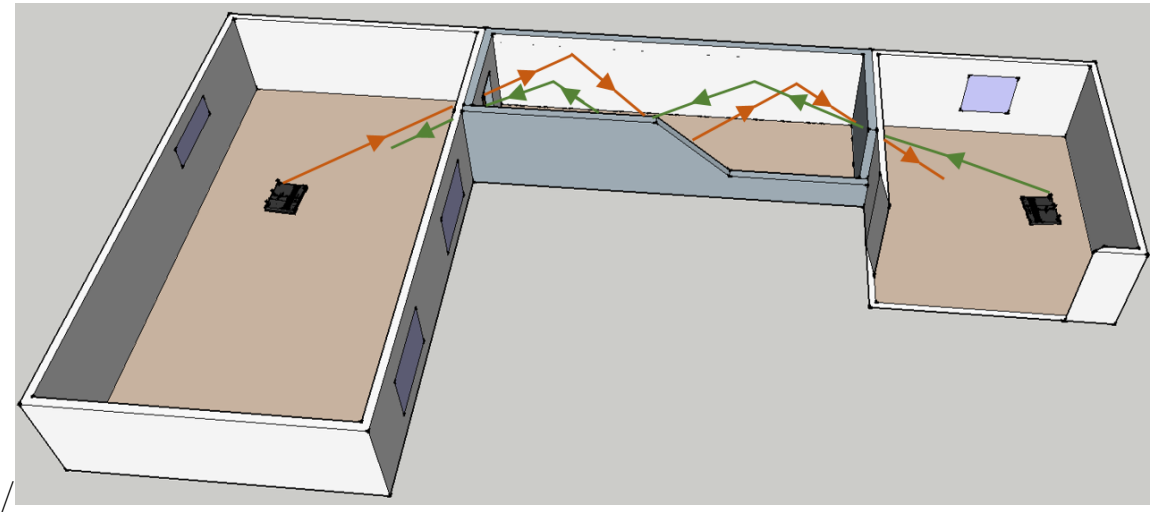

Figure 1.4: The propagating signal from two co-channel transmitters can cause interference between each, reducing router performance.

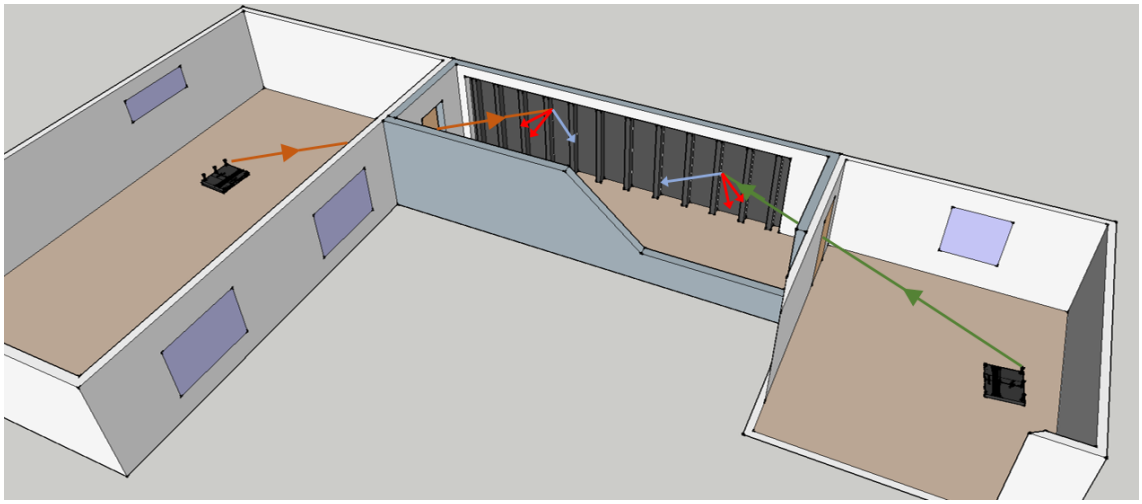

Figure 1.5: A visualisation of the installation of such surfaces in an interior environment to reduce effective interference.

For mass production of the surface, the CR-FSS would be integrated into metallic insulation, providing the same energy efficiency performance whilst acting as an FSS. Surfaces made from foam and metal foils are investigated in chapter 6. A potential design of the surface is shown in Fig. 1.6, whereby the CR-FSS structure is supported by a foam substrate either side. An additional foil layer is applied to the underside for additional energy efficiency and for stability of the structure.

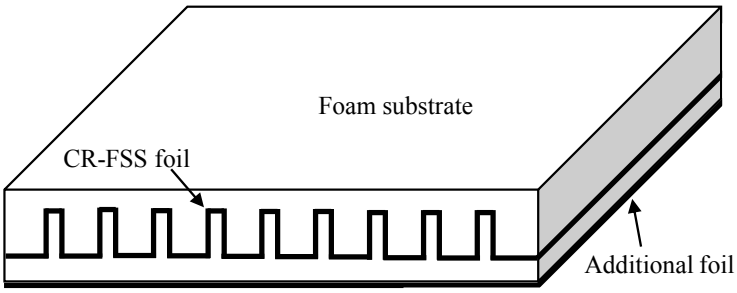

Figure 1.6: A metallised insulation incorporating the CR-FSS structure.

1.4 Thesis structure

The thesis is structured as shown in Fig. 1.7, with chapter headings providing a brief overview of the content.

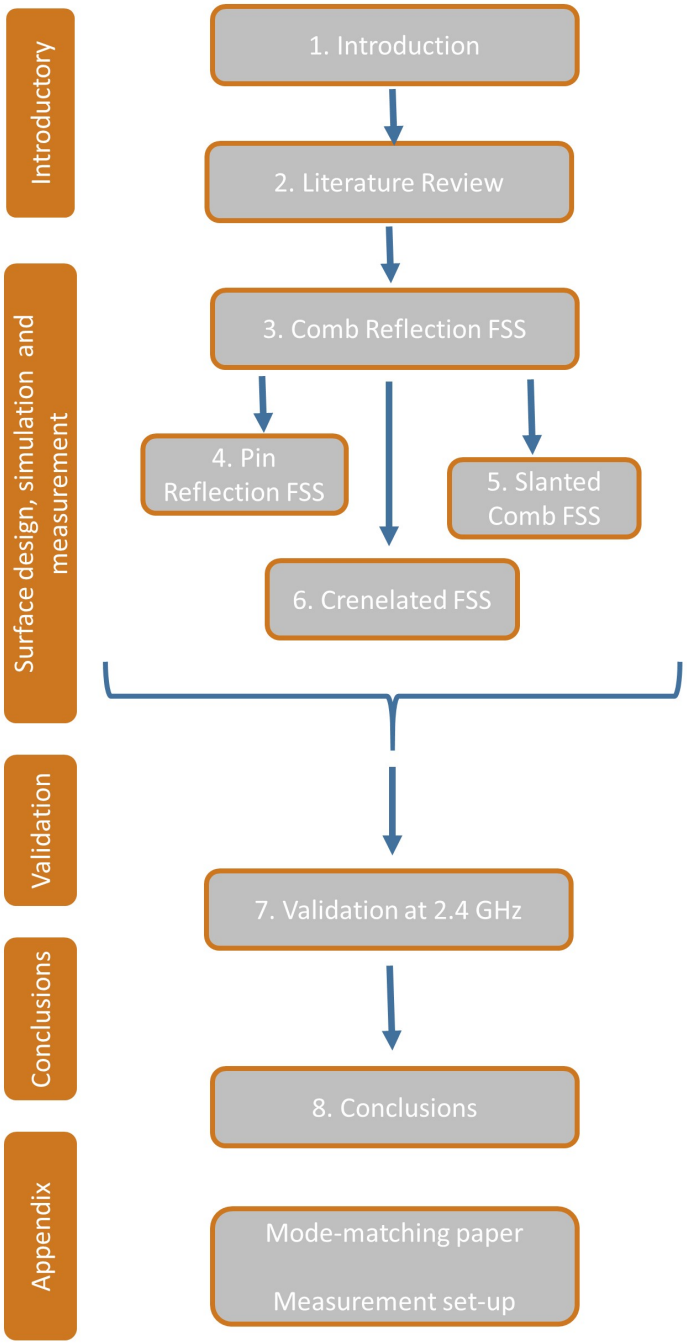

Figure 1.7: A flow-chart of the work in this thesis.

The thesis begins with Chapter 1, where a general introduction to this research area is given with specific points about the cross-over between energy efficiency and wireless propagation in buildings.

Following this, a detailed literature review of many of the state of the art in frequency selective surfaces (FSS) - both passive and active - is conducted in Chapter 2. The limitations of many of these surfaces is discussed and standards of comparison for the development of our surfaces are set.

Chapter 3 offers a detailed explanation of the comb reflection FSS (CR-FSS), with thorough analysis of a variety of structure parameters, such as fin height, period, and thickness. Performance at oblique incidence is investigated for comparison with similar structures already in literature. Various limitations of this surface lead onto the design of a different passive structure described in the next chapter.

Chapter 4 offers an in-depth analysis of a pin reflection FSS (PR-FSS), developed to try and overcome the limitations of the CR-FSS. Problems with polarisation of the incident wave are discussed, and the advantages of this surface are also considered compared to the CR-FSS.

Slanted comb FSS (SC-FSS) offer an alternate method of developing the basic comb structure discussed in Chapter 3. The use of such a structure can reduce its effective height, negating the need for large wall cavities for installation in buildings particularly at lower frequencies such as 2.4 GHz. Simulations and measurements once again show the characteristics of the surface for both TM and TE polarisation. Furthermore, alternately slanted structures and their performance are investigated for completion.

Chapter 6 concludes the development of the surface structures, investigating crenelated CR-FSS structures. These have been designed to add possible additional mechanical strength to the foam structures which were initially investigated for use with the CR-FSS structures for final implementation. Upon initial fabrication of the foam structures, it was found that the comb structure was fragile and could easily bend or break off. Also coating of foil onto the surface was found to be more difficult around the CR-FSS foam substrate. By forming a crenelated shape, the stability of

the surface structure is increased and foiling accuracy is increased.

Validation at 2.4 GHz of the CR-FSS was completed in chapter 7. This involved designing a surface that offered adequate reduction in specular scatter at 2.4 GHz for both TE and TM polarisation, requiring optimisation of thickness, height, and period parameters. Following this, a variety of in-building simulation models are conducted on CST. Analysis of the electric field plots show that the CR-FSS can offer a frequency selective response, reducing the potential for co-channel interference.

Finally, the thesis is concluded in chapter 8 with the novelties summarised, contributions to existing literature, limitations, and potential for further work discussed.

A relevent paper on mode-matching techniques is attached in appendix A.1 as it was co-authored by the Thesis author and is of relevence to work studied in this PhD.

Addiotnally, the measurement techniques and experimental systems are then discussed in appendix A.2, with summaries of both the NRL reflectivity arch and the bi-static scattering measurement system which was developed as part of this project. Software and hardware specifications are given for ease of repeatability and replication of our results. These methods of measurement are used in the analysis of the surfaces designed in chapters 3 to 6.

Chapter 2

Literature Review

This Chapter provides a detailed review of the important literature in the field of indoor wireless propagation, frequency selective surfaces, periodic structures and other related research within the area of electromagnetic propagation.

2.1 Introduction

Existing literature published as journal articles and conference proceedings offers a variety of different viewpoints regarding electromagnetic propagation and surface designed to control and change any transmission or reflection response. Moreover, the literature can be used as a benchmark for measurement systems, design, and simulation modelling in this work.

The review of literature in this section will cover a range of topics surrounding the use of structures and surfaces for in-building propagation control. The work currently published in this field offers several solutions of controlling and isolating wireless signals in a building, and they are discussed in this chapter. Relevant previously published material can be categorised into:

- **Periodic structures -** The work contained in this thesis is based significantly on the work and ideas covered in this set of literature, particularly that surrounding the design of the surfaces.
- **Smart indoor environments -** Considered to be a building which has integrated control over the propagation of RF signals, whether transmitted from inside or outside the building .

- **Frequency selective surfaces -** Explanation of the common surfaces and structures used to enable the filtering of electromagnetic signals, depending on the frequency of transmission.
- **High impedance surfaces -** Consideration of surfaces which have a different set of properties compared to the periodic structures used in this thesis.
- **Absorbers -** An alternative solution to the reflection of signals in a different direction. A traditional topic in the area of wireless communications and RF propagation, this section covers a multitude of different surfaces and common research.
- **Materials characterisation -** A review of the electrical parameters of various building materials and how their composition could effect the deployment of the structures developed in this thesis.

These characterisations are important as they compare alternate surfaces and structures of similar performance such as frequency selective surfaces, whilst also considering the overall system performance when applied to a building in smart indoor environments. By comparing both the system and unit level research, the gaps within current literature can be pin-pointed and applied as objectives for the work in this thesis.

2.2 Periodic corrugated structures

Passive periodic corrugations such as in Fig. 2.1 have been have been extensively used in electromagnetic propagation, waveguide surface wave control [14] and specular scatter analysis and as such, this thesis does not give an exhaustive review of each paper in this topic. Of particular interest is where corrugated surfaces have been experimentally verified for use in reducing specular scatter [15] or backscatter [16]. Analytical solutions are acknowledged, however are not considered in this thesis.
Initial experimental work carried out on periodic comb structures was conducted by Ebbeson [17] for the purpose of installation of airport hangars and terminal buildings in order to reduce the interference from the instrument landing system (ILS), which can be an issue, especially due to large taxiing aircraft [18]. The ILS is a radio transmission at carrier frequencies between 108.1 MHz and 111.95 MHz used for precision guidance of landing and approaching aircraft on a runway. Their research

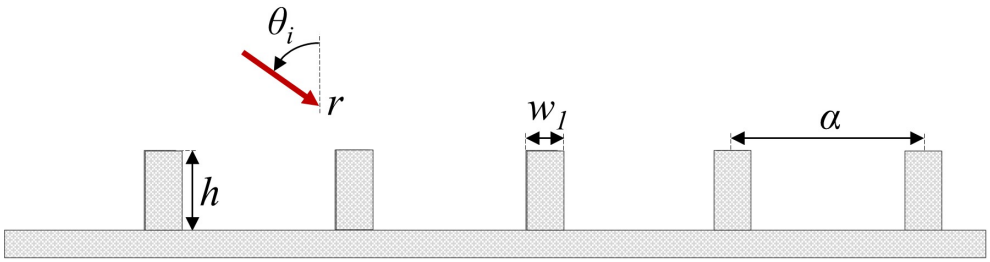

Figure 2.1: A basic periodic corrugated structure, with period α, height, h, and thickness, w_1.

focuses on the reduction of signals at 35 GHz, requiring a surface period of 8.6 mm effective for reducing the specular scatter [19].

Ebbeson provides an experimental analysis and review of numerical literature for a brass surface at 35 GHz, although the considered bandwidth is small making it difficult to see any expected frequency ranges [17]. For example, the relative power of the an incident wave on the surface is considered between 33 GHz and 37 GHz, making it difficult to understand any frequency selective trends or secondary peaks.

Also of interest is how the angle of incidence effects the amount of secularly scattered power. Measurements are used to suggest an optimum angle of incidence, whereby the amount of specular scatter is reduced by the greatest. Either side of this optimum, the performance of the surface is not as good, however there is a 6 dB reduction between 44° and 73°. The optimum angle can be changed by considering an alternate frequency. Example of this is given in [17] where at 37 GHz, the optimum angle of incidence is 70°.

This work is further presented in [19, 20], where links to their use in reducing scattering from ILS transmissions at airports is envisaged. Indeed, a surface has been installed at Toulouse-Blagnac Airport in France for the purpose of preventing possible ILS scattering onto a nearby runway from adjacent aircraft [21]. These surfaces have periodicities of nearly 3 meters, nearing 1λ at 108 MHz [22]. For these large wavelength signals it is acknowledged that diffractive effects can become an issue unless the surfaces are not significantly larger than a wavelength. Thus, in the sim-

ulations and experimental tests carried out in this thesis, surface dimensions must be considered to avoid or minimise such edge effects.

As the interfering signals are transmitted from stationary transmitters in this case, the angle of incidence is well defined and the surface periodicity can be based on Eq. 2.1. Bragg's Law defines the angle of incidence, frequency and period of a crystal lattice whereby constructive interference occurs [23]. The basic equation used to calculate when constructive interference in the direction of transmission will be greatest is thus:

$$n\lambda = 2\alpha \sin\theta_i \tag{2.1}$$

where n = 1,2,...,∞, λ is the wavelength of interest, α is the period of the surface and θ_i is the angle of incidence of the propagating wave.

Alternative solutions to the three dimensional structures include the use of reflector backed blazed gratings, such as those in [24]. They reduce the complexity of some of three dimensional structures by removing the vertical portion of the comb, leaving just two thin layers - one solid on the bottom of the structure, and one periodic, on the top. There are many more complex structures such as the tunable metallo-dieletric structure in [25], where the thickness of the substrate can be used to change resonant frequency, whilst tunable elements can alter them in-application. Scattering of incoming waves in predefined directions has also be researched by Doumanis et al. with use of their engineered reflectors [51]. The basis of operation is similar to the three dimensional structures reported in this Thesis, as they reduce specular reflection, re-directing the incident power in the direction required. Measurements of the surface show that it is stable for a range of angles of incidence. However, the surface designed is complex and in order to coat a whole corridor wall would be expensive. Thus, more suitable designs are preferred for this scenario. Other research in this area considers sinusoidal corrugations [26], strip gratings [27], and T-shaped 1D analytical solutions [28].

An alternate use of corrugated surfaces was investigated by Kapasi et al. [29]. Large corrugations of height 30 mm and period 5 mm were used to improve the signal strength in the shadow region of buildings. In this case, the period and height of

the surface are much less than the wavelength of the transmitted signal. Both CST simulation and experimental results were used to obtain information of the signal strength. Their simulations suggest that surface wave propagation on the corrugated surface increases the signal level in the shadow region, marked by A in Fig. 2.2.

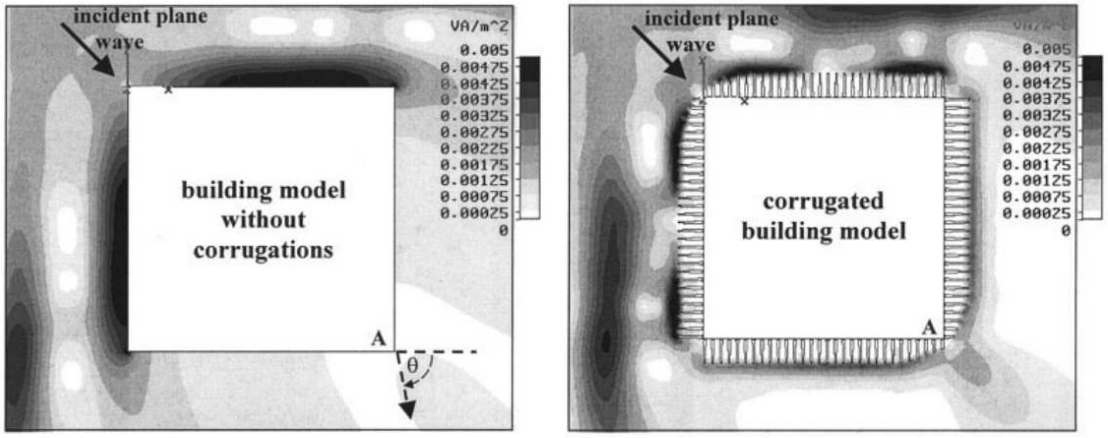

Figure 2.2: Improvements of the shadow region of buildings using corrugated surfaces.

Further to their simulations, experimental measurement of multipath and non-multipath scenarios were conducted. These reveal that in non-multipath environments, corrugations can be beneficial as suggested by previous simulations. However, the introduction of multipath signals means there is little difference in signal level whether corrugations are used or not. As interior scenarios such as corridors are likely to be multipath environments, these type of corrugations are likely to have limited use.

2.3 Smart indoor environments

As previously suggested in the introduction, the control of propagation in buildings can be implemented using various frequency selective surfaces and structures, integrating various passive and active structures. This reduces the need for an excessive number of wireless transmitters to cope with high data rate connections, reducing cost and wireless interference. The common use of the 802.11g Wi-Fi nodes also causes issues with co-channel interference. This should not be an issue for non-

overlapping channels, however the 2.4 GHz frequency band is limited to only three of these respective channels. In a high density network, there will be multiple users on the same channels or overlapping ones, reducing the network capacity due to increased levels of co-channel interference. This means that relatively high power transmissions such as Wi-Fi transmitters at 20 dBm can cause interference to others [2]. Separating and isolating these transmissions can increase the throughput of the wireless nodes, improving both performance and efficiency of the whole wireless network. These should offer an increased SIR not matter what the receiver sensitivity of the affected receiver. Similarly, if the SIR is increased in a specific scenario the receiver sensitivity need not be so high in magnitude.

Considering a wireless system may have a variation of different polarised transmitting and receiving antennas, it is important to consider both TE and TM modes of propagation. Literature has also reported that cross-polarisation is important to consider particularly in complex indoor scattering environments [30], especially where there are multiple dielectric materials present. It has also been acknowledged that scatters and reflectors can cause polarisation changes in propagating signals. It is concluded that there is no degradation of the signal quality even with random positioning of receiving antennas, because of the cross-polarisation of the propagating signals. [31].

Also of interest, is how the basic building environment can affect the propagation of signals in multiple cases such as indoor-to-outdoor propagation (and the reciprocal), and indoor propagation. Yan et al. [32] simulate the effect of metallic insulation (such as Celotex or Kingspan) on the reception of digital TV (DTV) signals broadcast from 50 meters away and 20 meters high. The metallic insulation was positioned exclusively in exterior walls – in more complex indoor environments, there may well be metallic insulation located in interior walls too [33, 34]. Under non line-of-sight (NLOS) conditions, the insulation significantly effects the path loss for all three measurements at 70, 200, and 600 MHz. Unsurprisingly, LOS routes are unaffected by the insulation, as the signal can simply travel through a window. With further consideration of an energy efficient environment, this may not represent a more complex building environment.

Window construction and design is important, particularly in energy efficient build-

ing design. Traditionally, a significant amount of heat energy is lost through windows, hence the improvement to double glazed windows, increasing the U-value[1] and reducing the emissivity of the window. The more energy efficient a window becomes, the more difficult it is for a signals such as GSM and DTV to propagate through. Conversely, it can be argued that such high reflectivity and low emissivity windows improve security and connectivity of indoor wireless systems.

The development of various frequency selective windows have been investigated to solve the issue of poor electromagnetic transmission through windows. It is suggested in [35] that low-emissivity windows can unintentionally reduce transmission at frequencies between 1 and 2 GHz by 20 to 35 dB. By removing periodic hexagonal shapes in the metallic coating, improvements can be made to the total transmitted power, and measurements and simulations shows this is effective for frequencies between 0.8 and 3 GHz. Future investigation into the effect of triple glazed windows will be of interest, particularly as they are the PassivHaus standard [36].

The main bulk of the research in this area has been based on indoor propagation scenarios, where exterior and interior walls, and transmitter deployment positions can all effect signal level. This research has been of interest over the last ten years, particularly with the increase in wireless connectivity in homes and non-domestic buildings. The future of in-building wireless transmission and propagation is likely to change furthermore, with more and more devices requiring wireless connectivity, higher throughput and high levels of security.

The use of frequency selective surfaces (FSS) in interior walls requires the installation of a passive or active structures, capable of providing a transmission path through the wall. The FSS must either coat the whole wall [37], which is potentially expensive depending on the surface type used, or the FSS is installed onto a wall that is otherwise coated in metallic or reflective insulation . Several publications are available in literature on this subject and are subsequently discussed.

Sung et al. investigate various aspects of passive FSS deployment in a building structure, with the aim of acting as an electromagnetic filter; allowing signals of

[1]The U-value is a metric for measuring the thermal performance of a building. A higher level of insulation will result in a lower U-value.

chosen frequency to penetrate, whilst others are reflected [1]. This is generally important in development and deployment of these surfaces in indoor environments. The work carried out in [1] focusses on many aspects of FSS deployment including position and size on wall, the angle of incidence of propagating signal, and angular stability. These three factors have shown to be important in much of the research in this subject area.

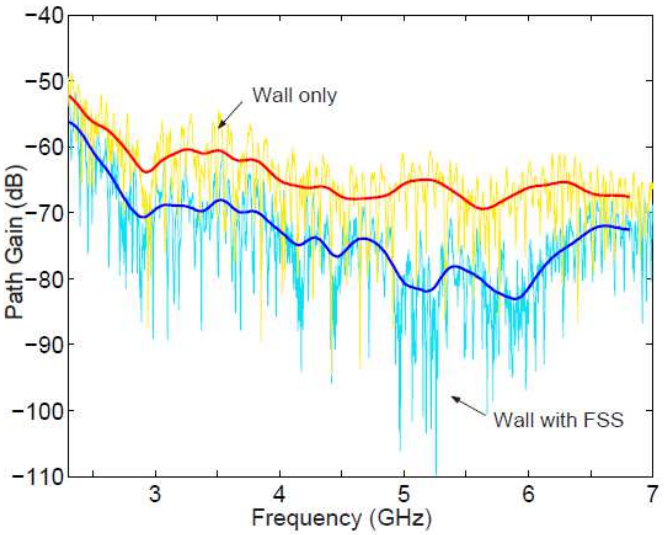

Figure 2.3: In-situ measurements conducted in [1] considering the use of FSS in a wall to reduce propagation into an adjacent wall.

Alignment of separate sheets of FSS 'wallpaper' are investigated, with results showing that when they are misaligned, there is no reduction in performance or shift in harmonic frequency of a simple square loop FSS. The square loop FSS has relatively good frequency stability for varying angles of incidence however, there is an obvious shift in peak frequency from 5.7 to 5.4 GHz, for angles of incidence ranging from 0° to 60°. Measurement results of the signal strength for a propagating transmission through a wall show that over a wide range of frequencies (2 to 7 GHz) the installation of the FSS provides 10 to 20 dB less signal than for the wall only, as shown in Fig. 2.3. This is interesting to note, as even though the FSS wallpaper is designed for a narrow frequency range, the reduction in signal level is for a much larger frequency range.

Measurements and simulations by Sung et al. on the same FSS structure in [38] reveal that spacing between the wall structure and FSS are also important considerations when installing the surface. Considering the FSS in air, the resonant frequency occurs at approximately 9.9 GHz. This resonant frequency does not change when the FSS is positioned 10 and 20 mm in front of the wall. However, when placed directly (0 mm) on the wall, the FSS resonant frequency shifts to 8.5 GHz. This means that positioning of such FSS should be considered. It is also noted that the FSS and wall distance could be further reduced using dielectrics such as polystyrene foams, although this is flammable and may be problematic to use for building installation.

One final conclusion drawn in [1] is that alternative propagation paths such as through windows and down corridors can affect the performance the FSS – the signal simply propagates around the FSS and metallic wall, rather than through it.
Following this work on FSS in building design, solutions for issues such as spectral overcrowding, interference, and security are examined. Work published by Batchelor et al. [39] introduces the issue of prevent outdoor-to-indoor propagation in prison cells, to prevent prisoners using their mobile phones. The method to prevent the use of phones must be frequency selective as TETRA bands must be available for emergency service communications, whilst GSM is to be blocked. The results of their double layer FSS show that a 100 MHz pass band can be created at 400 MHz and can give 10 to 15 dB reduction at all other frequencies. Here, two manufacturing techniques were used to create the FSS, with a 1 GHz shift in resonant frequency from 13.8 to 14.8 GHz. They suggest that the inaccuracy of using inject printing rather than etching on a copper clad sheet could be the reason for the shift in frequency. Thus, it has been seen that manufacturing accuracies can alter frequency responses quite considerably.

The installation of FSS surfaces in the building structure is further investigated by Raspopoulos and Stavrou in [40]. They provide a detailed experimental and simulation prediction for the signal power of a transmitter throughout a large building. This paper provides several interesting results, including a comparison of various FSS element shapes, such as cross dipole, square loop, and jerusalem cross. Their analysis suggests that this shape is best for various parameters such as cross polarisation, bandwidth size, small band separation, and angular stability. This suggests

why many in the literature prefer to use such a shape when developing an FSS. An example of the angular stability of the structures designed in [40] is given for both TE and TM polarisation. Off-normal incidence shows that the structures vary by nearly 500 MHz between 0° and 54°, whilst only having a narrow bandwidth, resulting in poor stability over a range of angles of incidence at their chosen frequency of 2.4 GHz. This angular stability can be improved by miniaturising the unit cell design [41], but this will inevitably increase complexity of any full FSS as well as adding cost to any active components.

More interestingly is the use of ray tracing models using MATLAB to predict the signal level in a building structure, using only four material parameters. These were brick, concrete, plaster, and wood, each with their own electrical parameters assigned. Simulations using Wireless Insite [42], the ray tracing model using MATLAB, and in-situ measurements are well correlated despite so few materials used in the building structure. Results comparing the original building walls, and walls coated in FSS show that signal level only various at a few locations when added to both external and internal walls at 2.4 GHz. At 5.2 GHz for an interior environment coated in FSS on external walls and floors and ceilings, there is no reduction in signal level, since this is out of the operational bandwidth, reinforcing the frequency selective nature of the surface.

Scaling of surfaces for measurement in chambers is common, with Sanz-Izquierdo increasing the parameters of their FSS by tenfold to perform measurements at 4 GHz [43]. They note that at 400 MHz, issues such as multipath can cause measurement issue, particularly in small measurement systems. Other issues such as edge effects can influence measurement accuracy at low frequency. Scaling parameters will prove useful for our work for several reasons. Firstly, size of simulation models can be reduced, as increased frequency requires a smaller period and height of elements. Secondly, production of prototype surfaces becomes cheaper, and their measurement becomes easier.

Significant work on autonomous and intelligent walls was conducted by Subrt et al. [44, 45], with the main focus of their studies revolving around the use of an active FSS installed on a metallised wall, which pro-actively learns about the propagation environment using sensors to improve the wireless system performance. In [46], a

basic simulation model of a building is constructed. Basic materials with arbitrary electrical parameters are used, such as concrete and plasterboard. Their FSS is simply modelled as being a high or low transmission material, rather than placed as a whole surface or structure in the wall.

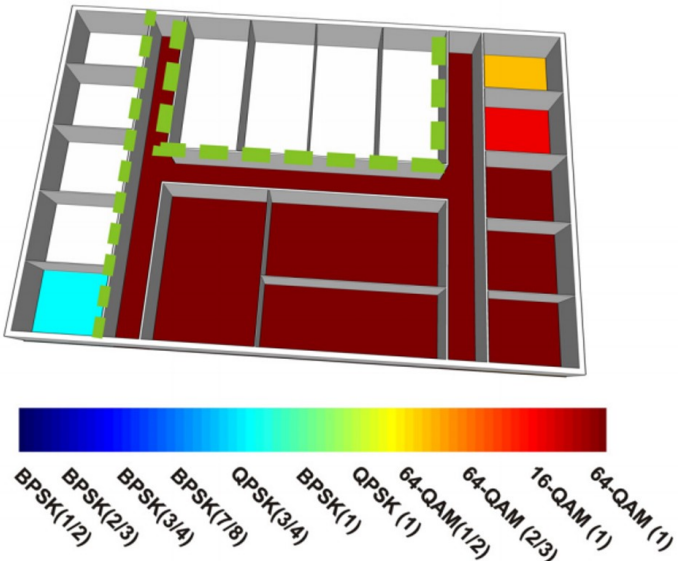

Figure 2.4: An ideal example of propagation control in [46].

2.4 Frequency selective surfaces

Frequency selective surfaces are periodic structures capable of reducing the transmitted electromagnetic energy at select frequencies [47]. They are predominantly used as bandpass or band stop radio frequency (RF) filtering applications, and typical examples include allowing mobile cellular network signals into buildings while rejecting other frequencies [39, 43]. Such designs are usually constrained to operational angular performance at near normal (perpendicular) incidence. Alternatively, FSS have been applied to offer specular scatter reduction [48–50], and flexibility in angle of backscatter [51].

FSSs have also been used for stealth in both military [52] and wind turbine construction [53], WLAN in buildings [54], and for general control of propagation of wireless signals inside buildings [46]. Installation of these surfaces is often an issue

in the indoor environment, with walls designed to include the FSS [1, 55]. These structures are positioned in-between walls which separate internal rooms.

Initial FSS in the built environment focus on the propagation of signals from the outside to the inside, especially via windows [56, 57]. The use of an hexagonal FSS in an energy efficient window can improve signal by at least 10 dB over a frequency range 1 to 2.5 GHz [35]. As well as increasing signal level of indoor-to-outdoor signals, FSS can also be used to prevent indoor interference. The basic theory is that the FSS filters out any signals of a desired frequency, whilst letting others pass. For this to be functional, the wall must be fully covered with FSS, or part-FSS part-metallic. This is to ensure the propagating signal can pass only through the FSS structure. Depending on the complexity and cost of the FSS design, either deployment method may be viable. In [38], a square loop FSS is used to reduce the signal level of at a frequency of 10 GHz. Parameters such as necessary air gap between the FSS and the original wall are examined, and it is concluded that a 10 mm gap is needed for their case. When scaling to 2.4 GHz, this means an air gap of at least 40 mm will be needed, and thus unsuitable in some cases where space is an issue. Inevitably the installation of these structures could have an effect on sound and thermal insulation. Where a large air gap is required, the use of thermal and sound insulation materials alongside the FSS structures should be considered. Current building regulations suggest that an air gap of at least 50 to 100 mm can be used in a cavity wall, so such a structure may well have to be used in conjunction with insulation materials.

The active configuration of FSS in application has been considered by many. The tunability and switching of surfaces is often performed by changing the impedance of the surface. Controlled using a bias voltage [58, 59], various diodes offer the ability to frequency tune any surface even after installation. Inevitably, this adds cost and complexity to a system, however in many applications it can be worthwhile. The area coverage of such structures should be considered, particularly where active components are required. Both the total cost and availability of components will have an effect on whether these solutions can become realisable. One such configurable FSS is described by Sanz-Izquierdo et al. [60]. Proposed is a double layered FSS, with the bottom layer using pin diodes and the top layer using varactor diodes. The pin diode is used as a switch, enabling the structure to be electromagnetically

reflective or transmissive. The top layer uses varactor diodes which can be used to tune the pass band frequency of any signal. These effects are shown at normal incidence in Fig. 2.5.

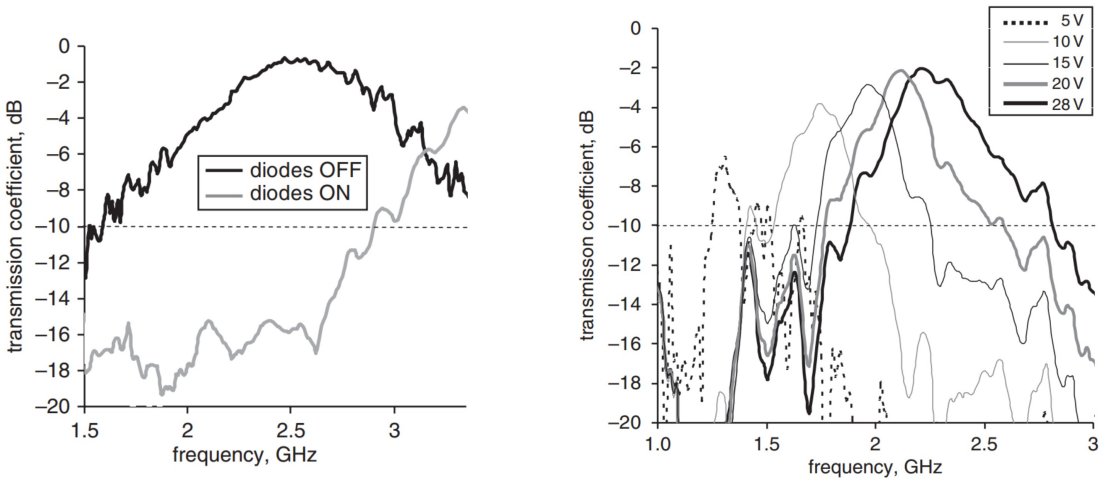

(a) (b)

Figure 2.5: The transmission response of (a) the pin diode switching and (b) the varactor diode tuning at normal incidence.

In this case, BB857 varactor diodes are used to tune a capacitance range of 0.5 pF (28 V) to 7.2 pF (1 V) and operate at the 2.4 GHz region. BAR64-2 pin diodes were used for the switching layer. One issue with the dipole design used in [60], is that the FSS works only for one polarisation. This is because the E-field must be in the direction of the lumped element. Mias mitigates this by using varactor pairs per unit cell, one of which is rotated 90° with respect to the other [61]. The effective tuning range of the FSS is also investigated, with Mias concluding that the reduction in normalised transmitted power must be sufficiently large to act as either a transmitter, or reflector. When acting as a transmitter, the reduction in transmitted power must not exceed 1–2 dB. This is considered to be the insertion loss of the system. Conversely, when operating as a reflector, the surface must have a reduction in transmission of at least 10 dB to work effectively.

Kiani et al. demonstrate the use of pin diodes with a similar 90° symmetry [62], with the final prototype shown in Fig. 2.6. In this case, BAP51-03 pin diodes are

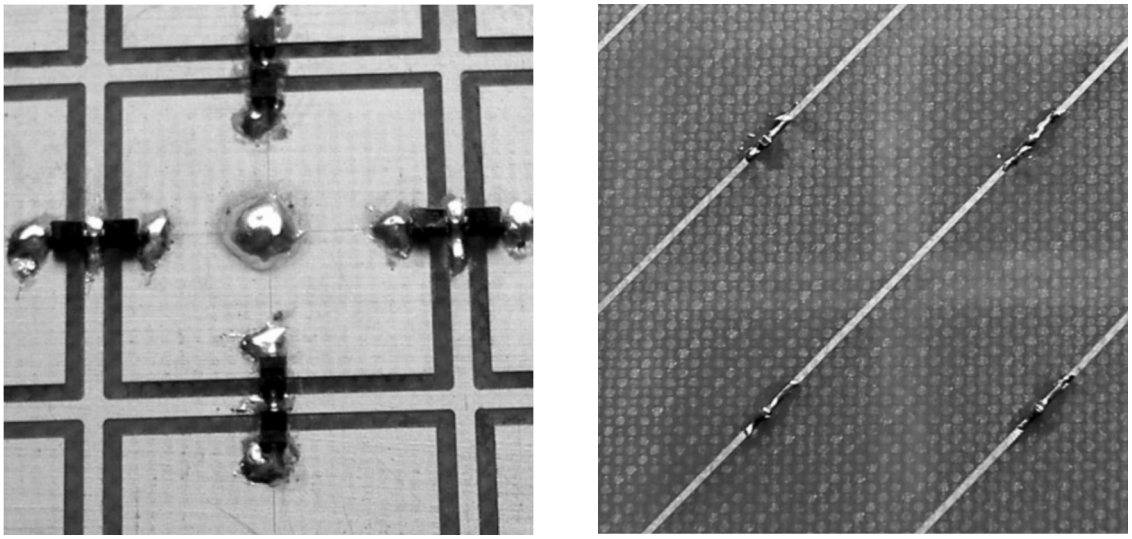

(a) (b)

Figure 2.6: Prototype of the switchable FSS for dual polarised signals [62]. Pin diodes are located on the (a) front of the FSS, and connected on the (b) rear.

used, with an operating (or resonant) frequency of 3.2 GHz. In theoretical results given in [63], it was expected that the resonant frequency be much lower, at 2.4 GHz. Multiple reasons were given for this shift, and will be considered in work in this Thesis. These differences are likely to be caused by the following design issues:

- Differences in dielectric constant of the substrate.
- Diode model inaccuracies - the use of a diode model in CST will be discussed later.
- Inductances due to by the dc bias lines seen in Fig. 2.6b.
- The use of soldering material, seen in Fig. 2.6a.

The results in both simulation and experimental results show a stable surface for angles of incidence up to 45° for both TE and TM polarisation, with insertion loss of between 2.3 to 2.6 dB when the pin diodes are off. When the diodes are turned on, difference in transmission loss can be between 9 and 12 dB, depending on polarisation.

2.5 High impedance surfaces

Similar periodic structures exist which act as so-called high impedance surfaces. Corrugated metal slabs have been utilised as HIS, however have multiple corrugations per wavelength as shown in Fig. 2.7 [64]. The height of the fin is particularly important in the design of these surfaces, with a short circuit where the fin terminates with the ground plate. As the height of the fins is a quarter wavelength, this in turn creates an open circuit on the top of the surface.

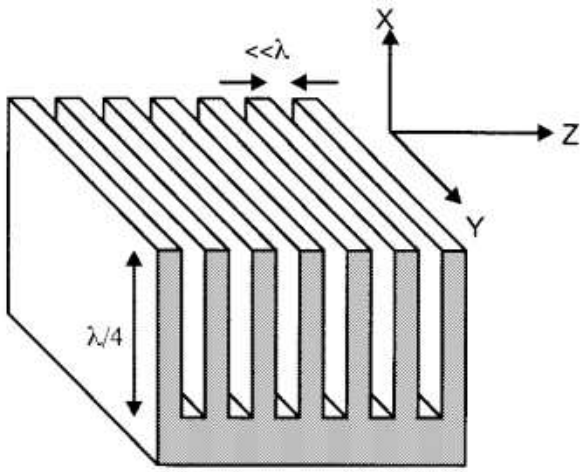

Figure 2.7: High impedance surface structure.

Structures developed from the corrugated metal slab include Sievenpiper's HIS which supresses surface waves at certain frequencies. These are described as forbidden frequencies and lie in this region at the resonant frequency, where the impedance is very high. The resonant frequency, ω_0 is simply described as:

$$\omega_0 = \frac{1}{\sqrt{LC}}$$

where L and C are the associated inductance and capacitance respectively. The impedance of the structure stems from the interaction of electric charges as shown in Fig. 2.8. It should also be noted, that at this resonant frequency the reflection phase is 0.

These surfaces have found use in control of antenna radiation patterns and active beam steering is also reported using electrically tunable impedance surfaces using

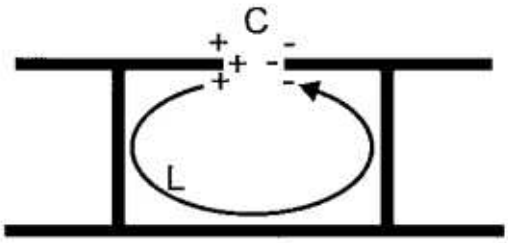

Figure 2.8: High impedance surface structure.

varactor diodes. Changing the voltage of the diodes result in a shift in resonant frequency and thus reflection phase characteristics. Similar structures include artificial magnetic conductors [65], however these surfaces are limited in use in oblique incidence specular reductions across a relatively large bandwidth.

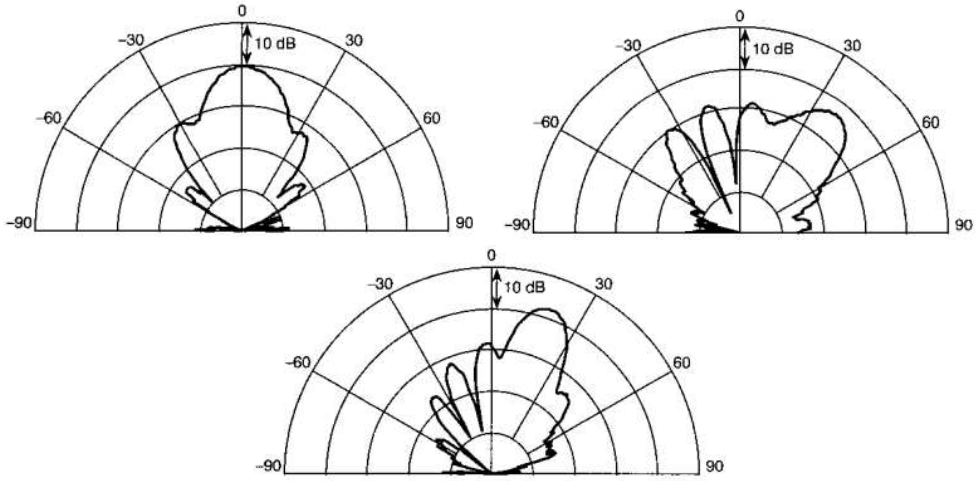

Figure 2.9: Various beam patterns for a range of varactor diode bias voltages.

2.6 Absorbers

The use of absorbers is common in applications where reduced electromagnetic reflections are required at specific frequency ranges. There is a multitude of radar absorbing materials (RAM) for a wide range of functions, and this section describes the most important. RAM work by absorbing electromagnetic energy and converting it into heat, thus reducing the amount of electromagnetic energy reflected back towards the radar source. A variety of material types and techniques are used to

achieve this, including elastomers, flat and pyramidal shaped foams and spray coatings.

Their in-building use is limited due to a range of reasons such as high cost, large thickness, and bandwidth restrictions. However, their performance and fundamental principles can still be used to quantify the surfaces designed in this Thesis.

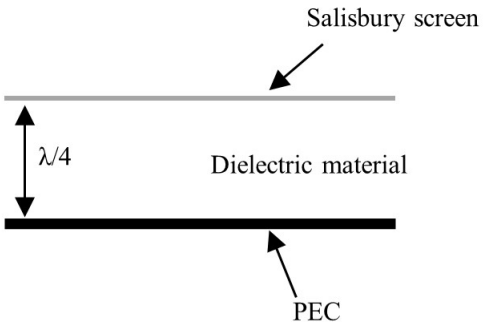

Figure 2.10: Many resonant layer absorbers are based on the Salisbury screen.

Their frequency performance can also be designed to operate as wideband or multiband structures. Resonant lossy screens such as the Salisbury screen [66] are single frequency absorbers, using phase cancellation to reduce reflected signals. A Salisbury screen with impedance equal to the free space impedance (377 Ω) is placed a quarter of a wavelength above a reflective surface [67], as shown in Fig. 2.10. Of an incident wave, some is reflected off the Salisbury screen, whilst the remainder is reflected from the PEC plate. As the total distance of a reflected wave is half a wavelength, electromagnetic signals are 180° out of phase and cancel each other. There are several disadvantages of this basic technique such as single frequency operation and the large thickness of the structure at lower frequencies.

Further complexity can be added to create a structure capable of operation at multiple frequencies. Double and multi-layer screens spaced with dielectric materials between them can increase the working bandwidth of such surfaces [68]. Jaumann absorbers work in the same way as Salisbury screens, applying additional lossy

screens at other distances to form multi frequency performance. Tuneable surfaces have also been investigated using devices with changeable characteristics such as diodes. A single layer tuneable FSS is used in [69] to change the reflectivity of a flat absorber. Depending on voltage bias of the pin diode, the surface can essentially become highly reflective, or highly absorbent, as seen in Fig. 2.11.

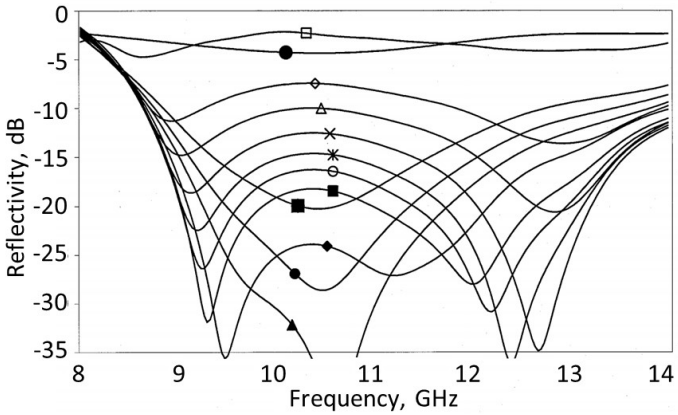

Figure 2.11: Reflectivity characteristics of the tuneable active FSS in [69].

Absorbers are also commonly used in anechoic chambers, with pyramidal shaped RAM usually lining most of the room. The purpose of these absorbers is to reduce the reflections from the wall which may affect any measurements taking place. Pyramidal absorbers are commonly produced from foam-based materials loaded with carbon. The quantity of carbon in the absorber is gradually increased from the top to base, to provide a gradual increase in impedance between air and the absorber [70]. Pyramidal absorbers provide high attenuation over a large frequency band and for a wide range of angles of incidence, making them one of the best choices for absorbers based on performance alone [71]. However their composition of foam and loaded-carbon makes them large, fragile, and costly; thus limiting their applications to anechoic chambers.

In order to improve their performance, it was proposed that a square loop FSS was loaded into the absorber, providing an additional impedance layer [72]. The initial implementation of this surface results in slight improvements to the performance at a low frequency (2 to 6 GHz) and narrow bandwidth. At oblique incidence, there is a noticeable improvement in reflectivity performance. However above an incidence

angle of 45°,the performance is similar to the unloaded absorber.

The use of frequency selective surfaces (FSS) to modify the reflectivity of various types of absorber at normal and oblique incidence acting as impedance layers has been recently investigated. When integrated with an impedance FSS, pyramidal absorber can have marginally better performance over a narrow frequency band, particularly at normal incidence [72]. However, at oblique incidence this combination is not effective, as there are issues dependant on the polarization of the plane wave [73]. The FSS described in [73] is positioned in a cavity below the pyramidal spikes, but above the ground plane and encased in absorber. By optimising a surface for either TE or TM using a square loop FSS, it was thought the performance could be improved, however this was not the case.

In [72], for a TE polarised wave there is slight improvements of 5 dB to 10 dB between 5 GHz and 6 GHz, when the FSS is TE optimised and compared to the unmodified absorber. The reflectivity of the unmodified absorber and TM optimised FSS are very similar over the whole frequency range. For a TM polarised plane wave, there is little difference between the unmodified and TM optimised FSS reflectivity. The TE optimised FSS has worse reflectivity, thus requiring an alternate approach. By using a dipole FSS, the reflectivity performance can be improved for one polarization, and in this case TE polarization was investigated. It is shown that the reflectivity can be reduced further between 4 GHz and 5.3 GHz by an additional 10 dB to 20 dB. For TM polarization, the response was exactly the same as unmodified absorber. Another disadvantage to the impedance loaded FSS like those in [74, 75] are that due to manufacturing process of the pyramidal absorber, it is difficult to know where to position the FSS. By placing the FSS on the bottom of the absorber, they negate this issue.

Chapter 3

Comb Reflection FSS

This Chapter investigates the use of a comb reflection frequency selective surface for the purpose of reducing specular scatter, re-redirecting signals at a pre-defined backscatter angle. The effect of various parameters such as height, period, and thickness of the elements are discussed, and simulation and measurement results are used to offer recommendations.

3.1 Introduction

This Chapter will introduce:

- The basic operating principles of the CR-FSS structure.
- Simulation and design of the CR-FSS in CST microwave studio at X-band.
- Measurement of the CR-FSS in both the NRL reflectivity arch and bi-static measurement chamber.
- The application of CR-FSS surfaces.
- Issues with the CR-FSS for varying azimuth incident angle, ϕ_i.

The use of comb and corrugated surfaces for manipulation of electromagnetic signals is well documented, with analytical and mathematical formulae forming the basis to published work. Few have provided an experimental validation to this work. This chapter aims to offer a detailed simulation and experimental analysis to comb surfaces - so called comb reflection frequency selective surface (CR-FSS) due to their ability to redirect an incoming signal to another direction.

3.2 Initial design

The operating principle of the CR-FSS structure is illustrated in Fig. 3.1. Firstly, compared to a flat metallic plate the CR-FSS will reduce specular scatter for a certain frequency range. Secondly, the reflection can be redirected towards the region of transmission. It can be seen in Fig. 3.1(a) that all energy of a plane wave from a flat metal plate is reflected at angle $\theta_r = \theta_i$. The introduction of periodic elements in Fig. 3.1(b) result in the specular reflection being reduced, re-directed as backscatter. The direction of θ_B will be dependant on the direction of incidence, frequency of the incoming wave, and the period of the elements.

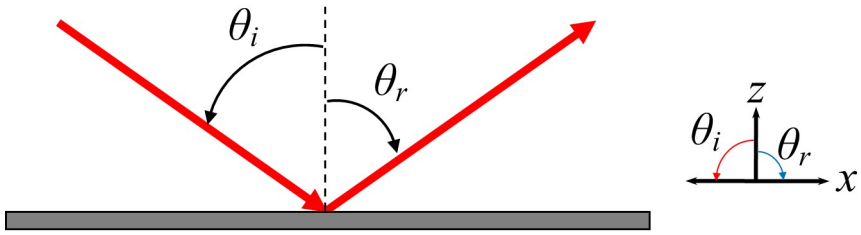

(a)

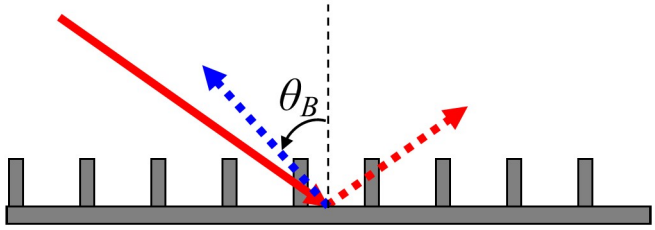

(b)

Figure 3.1: (a) An incoming electromagnetic wave is reflected completely as specular scatter from a flat PEC metal plate, where $\theta_i = \theta_r$. The introduction of periodic elements in (b) results in the specular scatter being reduced with the remaining energy redirected as backscatter with angle θ_B. θ_B can be tuned between 0° and 90° depending on preferred specification.

Generally, these periodic FSS can be characterised by Bragg's Law, which states:

$$\alpha = \frac{c}{2f_B \sin\theta_i} \tag{3.1}$$

	Angle of Incidence, θ_i		
	40°	50°	60°
$f = 2$ GHz			
α (mm)	97.23	81.59	72.17
$f = 5.8$ GHz			
α (mm)	40.23	33.76	29.86
$f = 12.2$ GHz			
α (mm)	19.13	**16.05**	14.20

Table 3.1: Example design parameters based on frequency and angle of incidence of a surface using Equation 3.1.

where α is the period of the combs, c is the speed of light in a vacuum, f_B is the frequency at which peak backscatter will occur, and θ_i is the angle of incidence of the plane wave.

The general size of both the simulation model and experimental prototypes is first considered. Firstly, the prototype surface must be the correct size for accurate testing using experimental methods. Traditionally, measurement systems used a surface size of 600 mm × 600 mm [76] , and thus this was chosen as our ground plane dimensions. The number of comb repetitions should next be considered. Too many and the surface will be costly to manufacture and difficult to make. Too few and the measurement of the surface may become inaccurate. With use of Equation 3.1, the periods at various basic frequencies and angles of incidence can be calculated.

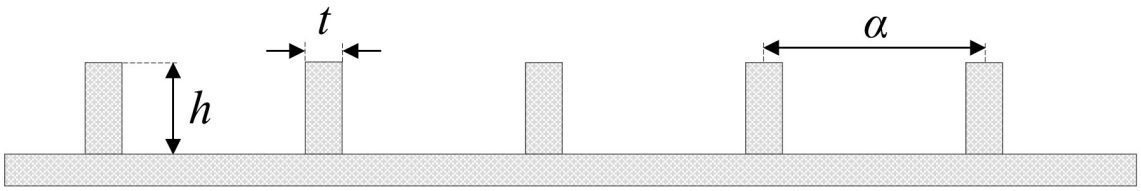

Figure 3.2: Comb with dimensions: height, h, thickness, t, and period, α.

The frequency of experimental testing should also be considered. Low frequency measurements are difficult because the necessary size of the surface under test becomes very large if edge effects are to be avoided. Measurements are concentrated in the X and K_u frequency bands (covering a frequency range from 8 GHz to 18 GHz.). For a frequency of 12.2 GHz, a period of 16.05 mm is required for an angle of incidence of 50 ° to provide maximum backscatter to the transmission source. For this period and the previously described ground plane dimensions, 37 repetitions can be used to create the periodic surface.

3.2.1 Simulation set-up

In order to optimise the simulation time of the CR-FSS, a thin slice of the structure with 37, 16 mm periodic repititions in the y-axis used with total length of 592 mm. This was because periodic or H/E-field boundaries could not be used in the same ordinal plane as the plane wave excitation in the time domain. The length should be large enough to mitigate the effects of edge diffractions. In the x-axis a width of 20 mm was used with E/H-field boundaries selected depending on polarisation of the signal of interest, vastly reducing the simulation time.

3.3 Experimental measurement

Simulated results of the CR-FSS can be validated using the experimental techniques described in Section A.2. The NRL reflectivity arch allows for accurate specular scatter measurements due to the stationary antenna horns, whilst the bi-static measurement system is capable of full scattering measurements, offering a more complete characterisation of the surfaces. An adequate surface was manufactured to fulfil the requirements of both systems.

Table 3.2: CR-FSS plate dimensions.

Parameter	**Dimension**
Fin period	16 mm
Fin height	16 mm
Fin thickness	1.7 mm
Width	600 mm
Length	600 mm

Figure 3.3: The CR-FSS manufactured for experimental measurements. The structure is manufactured from aluminium angle screwed onto a ground plane.

3.3.1 Surface manufacture

The CR-FSS structure used for experimental measurements was made from aluminium, with aluminium angle secured to the plate, forming the comb fins. The final surface is shown in Fig. 3.3, with the dimensions listed in Table 3.2. As the fins were created using pre-made aluminium angle, both the period and height had to be the same. The thickness was also limited to 1.7 mm due to the lack of aluminium angle with a thinner profile. The width and length of the surface were both 600 mm. The flat plate in both the bi-static measurement system and NRL arch use a flat metal plate of the same dimensions, making for accurate comparison of the two surfaces.

Mass manufacture would not be from such expensive and weighty materials, but incorporated into metallic insulation material using energy efficient foils and foams, however this shall be discussed in Section 1.3.

3.4 Initial simulation and measurement results

This section presents comprehensive results from simulation and experimentation of the CR-FSS. To summarise, the following aspects are reported on:

- The performance of the CR-FSS for changing oblique incidence for both TM and TE polarisation.
- The specular scatter reduction for a selection of angles of incidence.
- The effects of pin height, period and thickness on any response.
- 2D and 3D scattering plots produced by simulation and measurement on the bi-static system.

3.4.1 Comb height

The effect on increasing comb height on the reduction in specular scatter was simulated with the height ranging from 0 to 30 mm. Simulations were performed in 2 mm steps from 1 to 31 mm, where 0 mm is equivalent to the flat PEC plate. The results are extracted from the scattering plots from CST simulations [77], with TE and TM polarised plane waves excited at $\theta_i = 60°$ and $f = 12$ GHz.

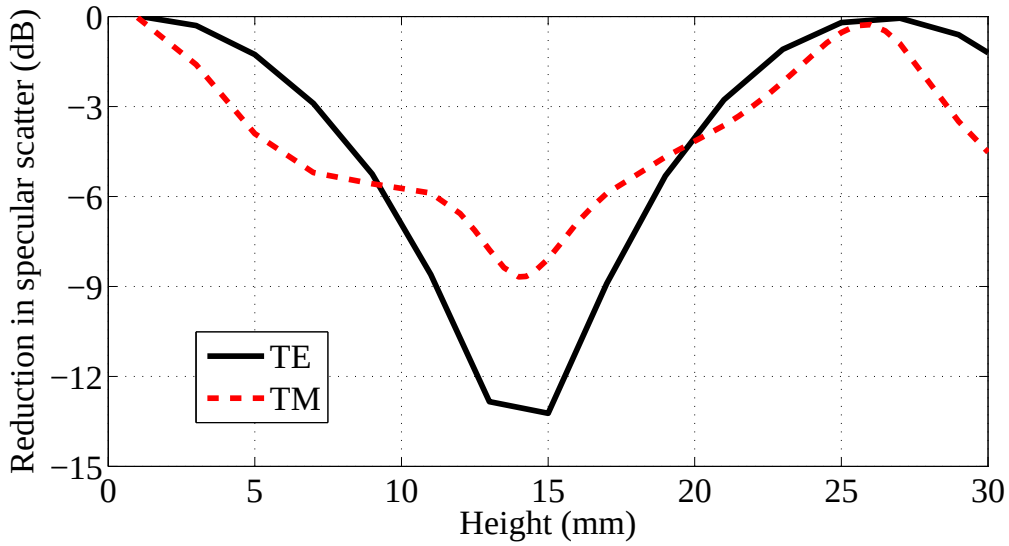

Figure 3.4: Comb height simulation results for the CR-FSS ($\alpha = 16$ mm) for TE and TM polarised signals with $\theta_i = 60°$ at $f = 12$ GHz ($\lambda = 25$ mm).

The height of the pin or fin can have a detrimental effect on performance as seen by the simulation results shown in Fig. 3.4. As expected for lower comb heights, the FSS has a poor performance. At least 6 dB reduction in the specular scatter magnitude is visible for comb heights between 11 and 17 mm, and 9 and 18 mm for TM and TE polarisations. The greatest reduction in specular scatter occurs at 0.56λ (14 mm) and 0.6λ (15 mm) for TM and TE polarisation respectively. The performance at this frequency then reduces, becoming ineffectual once more at 1λ (25mm) for both TM and TE polarisation, at this frequency. As the height of the fins of the CR-FSS increase the frequency at which the comb resonates also changes. In the case where one frequency is considered, such as in Fig. 3.4, there is a periodical peak in reduction of specular scatter which occurs at a function of λ which is also dependant on angle of incidence.

Ideally, the of the TE and TM responses would be equalised, to peak at a single important frequency. This can be done by changing all the parameters such as height, thickness, and period until this occurs. Although this is not done in this chapter, it will be done for the design of the 2.4 GHz surfaces.

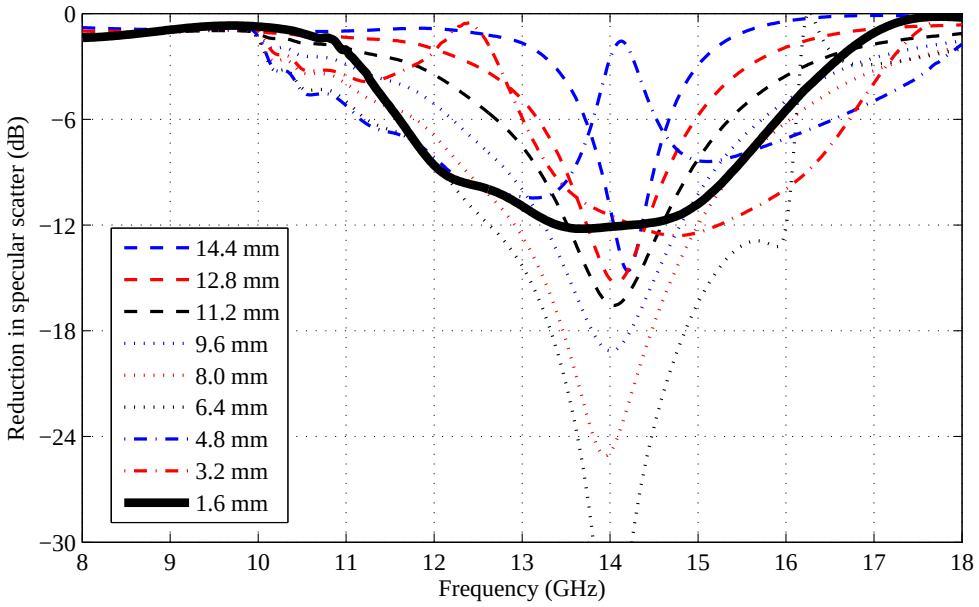

(a)

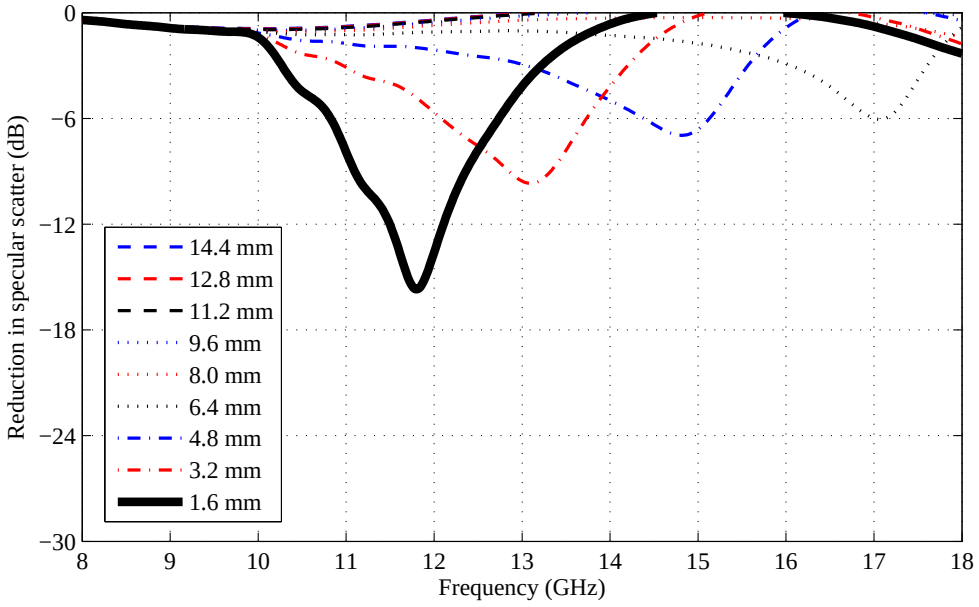

(b)

Figure 3.5: The comb thickness specular scatter graphs for (a) TM polarisation and (b) TE polarisation for $\theta_i = 60°$. A range of pin thickness from 1.6 mm to 14.4 mm are simulated.

3.4.2 Comb thickness

The effect of comb thickness, t on frequency response for TM and TE polarisations was simulated for $\theta_i = 60°$. The aim of this investigation is to understand how bandwidth and peak frequency change for different comb thickness. Fig. 3.5 shows the reduction in specular scatter magnitude for a range of comb thickness. Comb thickness is measured as in Fig. 3.2, thus a smaller t refers to a thinner element. For TM polarisation, as the comb thickness increases the frequency response becomes more narrow, with a resonant peak at 14 GHz. This peak is visible at 12.4 GHz and 16.2 GHz for thickness of 3.2 mm and 6.4 mm respectively, so can be suggested that increasing the thickness of the fins increases the frequency at which this null occurs. For TE polarisation however, the peak frequency shifts considerably to the right as the comb thickness increases.

When $t = 6.4$ mm, the resonant frequency is at 17 GHz, and offers very little reduction in specular scatter. From Fig. 3.5 it is evident that as the thickness of the comb increases the reduction decreases for TE polarisation. For the purpose of the future studies the comb thickness is chosen to optimise the potential TE and TM polarisation reduction, which occurs at a thickness of approximately 1.6 mm.

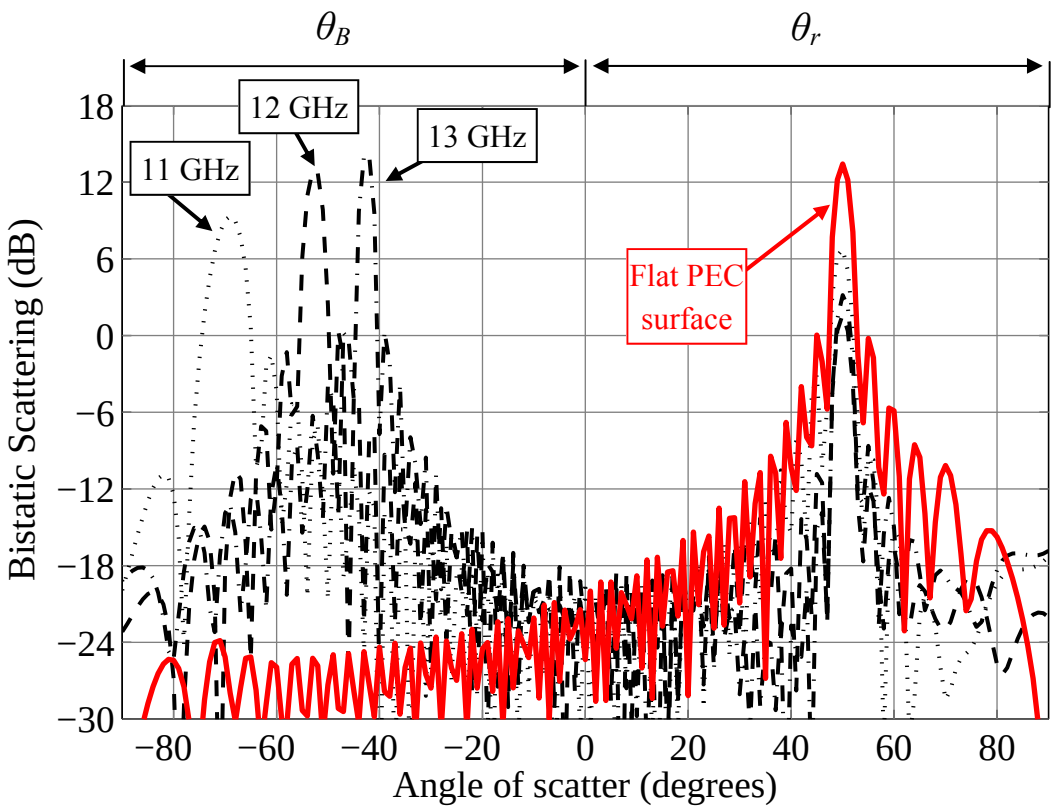

Figure 3.6: Scattering results of the PR-FSS (black dashed lines) compared to the flat PEC surface (red solid line). The PR-FSS shows a reduction in specular scatter compared to the PEC at $\theta_r = 50°$, for TM polarisation. There is also a large increase in backscatter for the PR-FSS, with the angle θ_B dependant on frequency of the plane wave.

3.4.3 Effects of changing frequency of signal and period of surface

The effect of changing parameters in equation 3.1 on the scattering for periodic structures such as the PR-FSS and CR-FSS are summarised in this section. The angle of backscatter, θ_B can be tuned by choosing the frequency of operation prior to manufacture. Fig. 3.6 shows the scattering from both a PEC (red line) and CR-FSS surface (black dashed lines) with a period, α of 16 mm at three different frequencies for a TM polarised plane wave with $\theta_i = 50°$. The TE case would show exactly the same trends, although magnitudes of scattering would be different to the TM polarised case. Considering initially the specular reflection region (denoted

by θ_r), there is a reduction in specular scatter compared to a flat PEC surface for frequencies 11, 12 and 13 GHz. The angle of specular scatter is unaffected also.

The angle of backscatter in the region θ_B also changes with frequency. Given the angle of incidence and the frequency of the incident wave, the angle of backscatter can be chosen. In Fig. 3.6, the angle varies from -70°, -53°, -42° for f = 11, 12 and 13 GHz.

If it is required to reflect all of the signal back to the transmitter ($\theta_B = -\theta_i$), then α must be carefully chosen depending on the expected frequency of the transmitted wave. Fig. 3.7 shows that by increasing the periodicity of the pins or fins, the frequency at which $\theta_B = -\theta_i$ is true decreases. For example, when $\theta_i = 50°$ and α = 12 mm, the frequency at which the condition $\theta_B = -\theta_i$ is met is f = 16.3 GHz. If the period is increased to 18 mm, this frequency shifts to 10.9 GHz.

This peak backscatter from the surface is defined by the Bragg's Law equation (3.1), previously defined in Section 3.2. Evidently, a larger period results in the peak frequency reducing. It should also be noted that only the period of the surface was increased in these simulations, and the height and thickness of the combs remained constant. To achieve realistic scaling, all parameters would be scaled equally. That is to say, if the period was doubled then the height and thickness would also need to be doubled. By decreasing the operational frequency, additional grating lobes will be introduced at lower frequencies, also as defined by Bragg's Law.

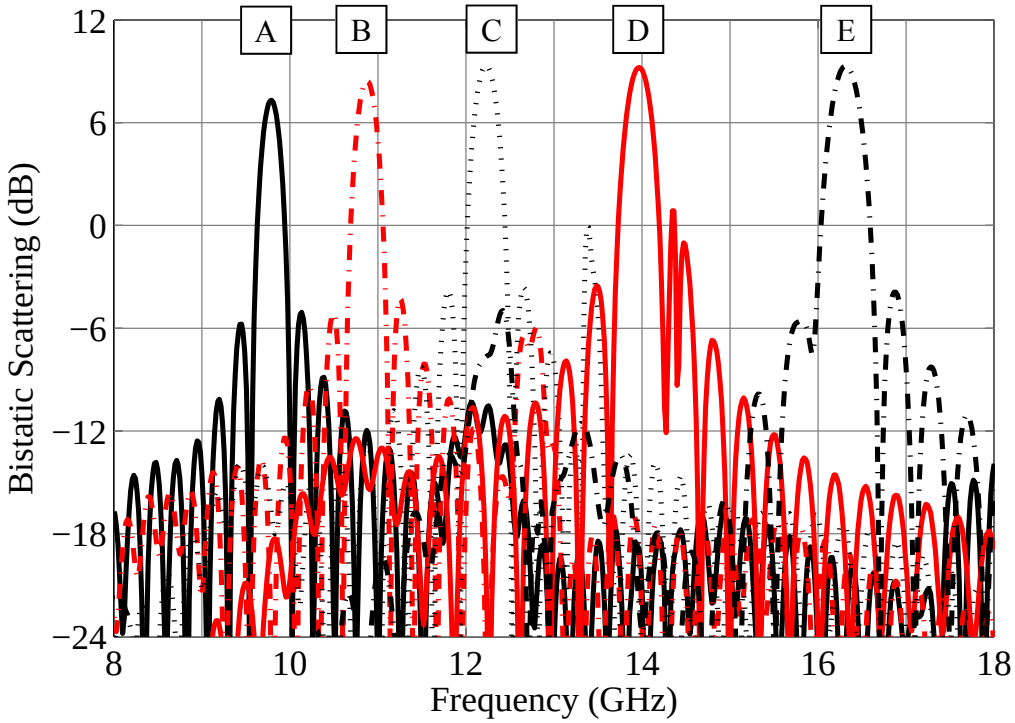

CASE	A	B	C	D	E
α (mm)	20	18	16	14	12
f_B (GHz)	9.8	10.9	12.2	14	16.3

Figure 3.7: The peak backscatter occurs at a frequency defined by the period of the surface. For case A, $\theta_i = 50°$ and $\alpha = 20$ mm, $f_B = \frac{c}{2\alpha \sin\theta_i} = 9.8$ GHz. Additional results can be seen in the accompanying table.

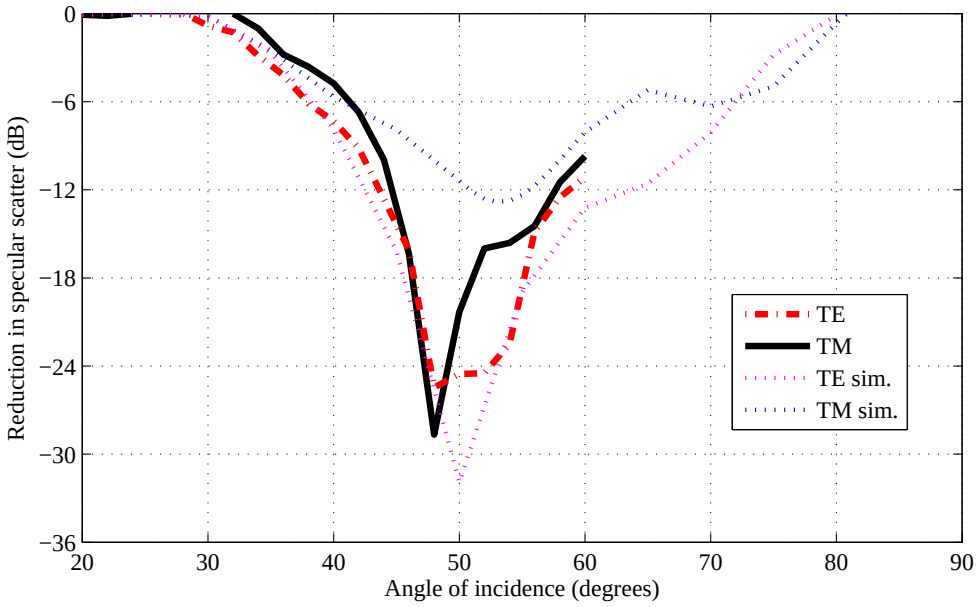

Figure 3.8: Relationship between the reduction in specular scatter and angle of incidence for TM and TE polarisation at $f = 12$ GHz. The solid lines represent the measured results, and the dashed the simulation results.

3.4.4 Oblique incidence angle performance

Interior environments are commonly full of transmitters and receivers, of different frequencies and transmission powers. The main problem is that the angle of arrival on any installed surface is often unknown, or occurs at multiple angles due to scattering and diffraction.The surface has been optimised for approximately 50°, as seen for a period of 16 mm and frequency of 12.2 GHz. Results are shown in Fig.3.8 for a frequency of 12 GHz, so a slight shift in optimum angle may be visible. The reduction in specular scatter is the difference between the magnitude of CR-FSS surface and the equivalent flat plate for a range of angles of incidence. Both TE and TM poarisations are considered, as this would be the case in a multipath environment.

Simulation results were obtained by changing the angle of incidence of the plane wave and exporting the far-field monitor data at the frequency of interest. Simulation results were completed for a θ_i range of 0° to 90°, with a resolution of 5°. A 1° resolution between 45° and 55° for the TE and 50° and 60° for the TM were used

to obtain more accurate results at the peak values. The NRL reflectivity arch was used for measurements to provide verification of simulation results. Owing to the limitations of the NRL arch, measurements of the CR-FSS were limited to between 5° and 60°. A resolution of 2° was used to obtain an accurate representation of the response. As described in Sec. A.2, time gating techniques were used to remove unwanted reflections and noise from the measurements. For each specific angle of incidence, the experiment was recalibrated and then the flat metal plate and CR-FSS were measured.

The oblique incidence performance is illustrated in Fig. 3.8. Simulations show a peak reduction at around 50° and 53° for TE and TM polarisation respectively. The performance of the TM is also lower than expected. The NRL arch measurements offer accurate comparison, particularly for TE polarisation, although the peak reduction occurs at around 48° for both polarisations.

The large difference between the measured and simulated response for TM polarisation can be explained by the slight differences in harmonic frequency, which can be seen in Fig. 3.9. As there is quite a narrowband response, a slight shift in frequency can lead to a large difference in recorded value at a singular frequency.

3.5 Specular scatter reduction

The previous section summarised the trend in reduction in specular scatter at 12 GHz for a range of angles of incidence. It is the purpose of this part of the study to understand how the broadband frequency response is effected for both TE and TM polarisation. Two examples are given for angles of incidence, $\theta_i = 50°$ and 60°. Simulation predictions are compared to NRL and scattering measurements.

3.5.1 Reduction at $\theta_i = 50°$

For incident signals greater than 45°, performance of conventional FSS is usually reduced. However, we have seen previously that at 12 GHz, the peak reduction of the CR-FSS actually occurs around this angle of incidence, due to its optimisation. Initial consideration of the results in Fig. 3.9 shows that the TM polarised response is much broader in frequency than TE. We can also see that the 6 dB bandwidths for both TE and TM polarisation are 2.3 GHz and 5.4 GHz respectively.

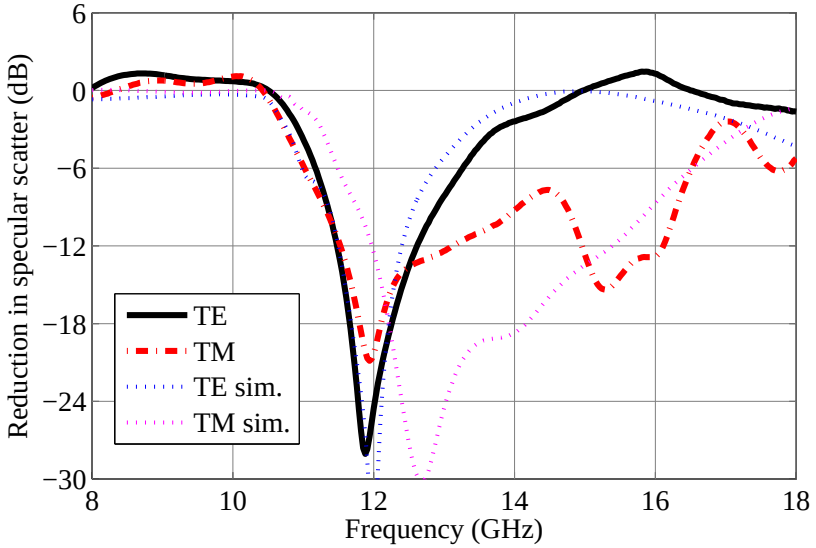

Figure 3.9: A comparison of the measured and simulation results for TE and TM polarisation.

In indoor scenarios where multipath reflections are common and polarisation is often undefined, the actual performance of this surface at this angle of incidence may be unpredictable as any incident signal could be either of the two polarisations at any given time. This is likely to be the case even if the signal is radiated from a dipole

located in a multipath environment.

The 6 dB frequency ranges for TE and TM respectively are 11 GHz to 13.3 GHz and 11.2 GHz to 16.6 GHz, although simulation results are a little more narrow band for both polarisations. That is, the simulated TE frequency band ends at 13 GHz and the TM band starts at 11.5 GHz.

Scattering graphs for TE and TM polarisation show that the backscatter angle is dependant on frequency and angle of incidence. Similar the specular performance shown previously is also reflected in these plots. Analysis at 10.8 GHz and 12 GHz show how the surface will re-direct to another direction.

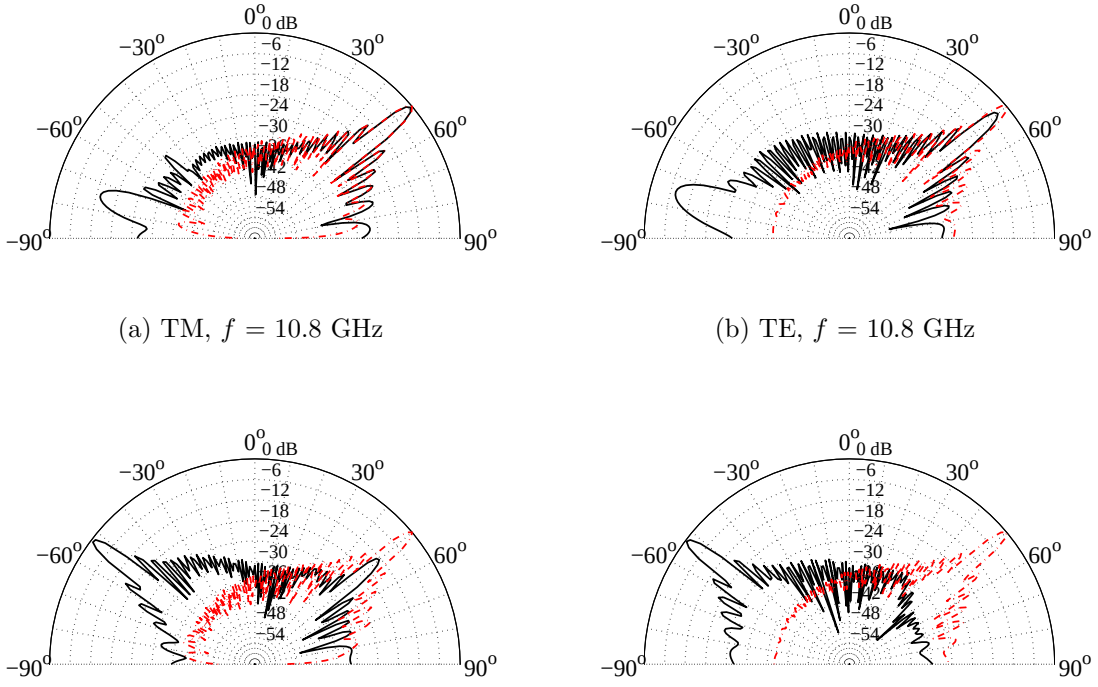

(a) TM, $f = 10.8$ GHz

(b) TE, $f = 10.8$ GHz

(c) TM, $f = 12$ GHz

(d) TE, $f = 12$ GHz

Figure 3.10: Simulated scattering plots of the CR-FSS and flat PEC plate for (a) TM and (b) TE polarisations at $f = 10.8$ GHz, (c) TM and (d) TE polarisations at $f = 12$ GHz. The specular reflection in each case can be seen at 50°, with backscatter peak at 72° and 53° for 10.8 GHz and 12 GHz respectivly.

The previous simulated scattering plots showed that in the $\phi = 0°$ plane, energy was re-directed in a range of θ angles. To ensure that energy was not redirected in any other ϕ plane, a three dimensional 600 mm^2 model was simulated. The far-field result was evaluated at 12 GHz and is shown in Fig. 3.11. The resulting field result shows that there is no scattering other than that in the $\phi = 0°$ plane.

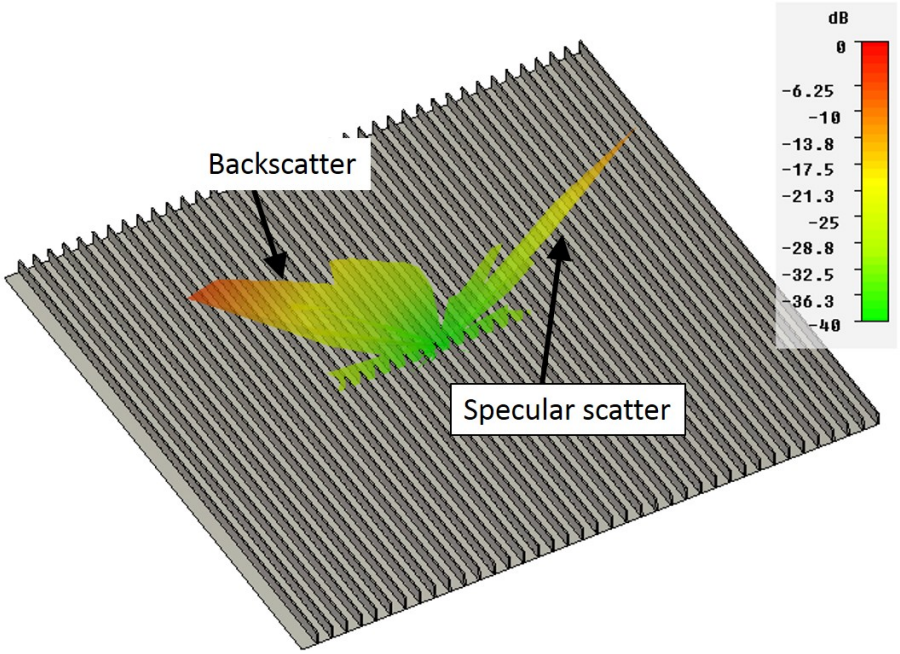

Figure 3.11: A three-dimensional scattering pattern from a 600 mm^2 comb surface, at 12 GHz, $\theta_i = 50°$. There is no scattering other than that in the $\phi = 0°$ plane.

3.5.2 Reduction at $\theta_i = 60°$

The oblique incidence measurements and simulations also show that good reduction in specular scatter can occur at angles lower or greater than 50°. At 60°, Fig. 3.8 shows that there is still at least a 10 dB reduction, depending on polarisation. Simulation and measurement results at Fig. 3.12 confirm that at 12 GHz, at least 10 to 12 dB reduction can be expected irrespective of polarisation. Furthermore, 6 dB bandwidths for TE and TM polarisation can be respectively given as 11 GHz to 13 GHz and 11 GHz to 15.9 GHz. The TM simulation result is shifted by about 0.6 GHz from the measurement however.

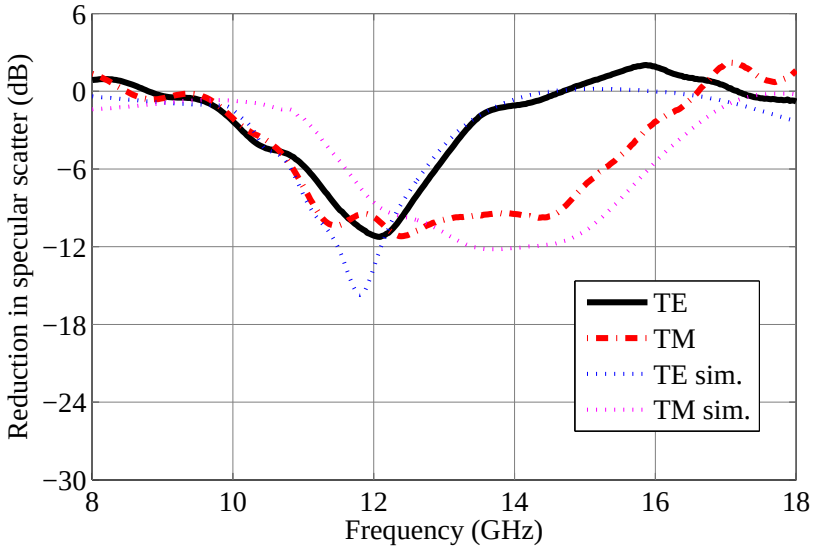

Figure 3.12: A comparison of the measured and simulation results for TE and TM polarisation.

Comparative scattering plots for $\theta_i = 60°$ are shown in Fig. 3.13 for 10.8 GHz and 12 GHz once more. At 10.8 GHz, the signal is reflected directly back to the transmission source. As expected, the performance for TM polarisation at this frequency is not as good as the TE polarised signal. For TM polarisation, the backscattered E-field level at -60° is shown to be about 10 dB less than for the TE equivalent. Similarly, there is no reduction in specular scatter in Fig. 3.13a for TM polarisation, compared to approximately 6 dB for TE polarisation in Fig. 3.13b.

Increasing the frequency to the ideal working point at 12 GHz, the performance for both polarisations is increased. However, the backscatter is no longer at -60° . In

both cases, it has shifted to -44° and the level of backscatter is greater than the specular reflections. For TM and TE polarisations, there is a respective 10 dB and 14 dB reduction in specular scatter, and can be confirmed from results in Fig. 3.12.

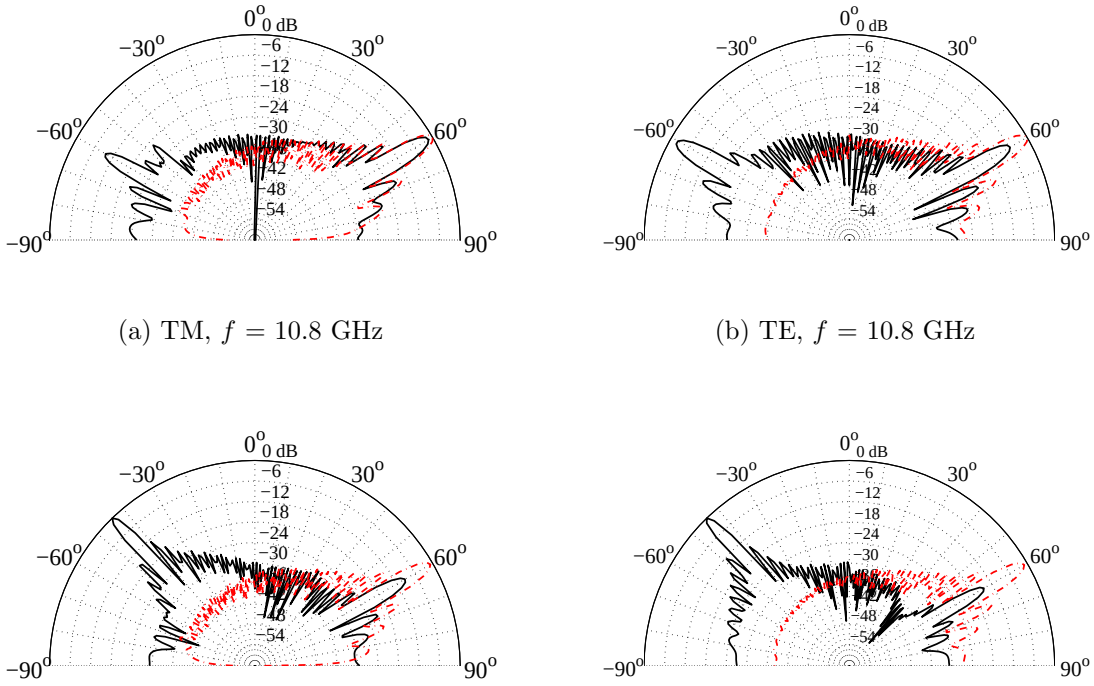

(a) TM, $f = 10.8$ GHz

(b) TE, $f = 10.8$ GHz

(c) TM, $f = 12$ GHz

(d) TE, $f = 12$ GHz

Figure 3.13: Simulated scattering plots of the CR-FSS and flat PEC plate for (a) TM and (b) TE polarisations at $f = 10.8$ GHz, (c) TM and (d) TE polarisations at $f = 12$ GHz.

3.6 Scattering plots of the CR-FSS

So far, results have investigated the performance of the CR-FSS for either a given frequency or a given angle of reflection (be that specular scatter or backscatter in most cases). By combining the two we can obtain a three-dimensional scattering plot of the CR-FSS, providing a useful demonstration of how the surface is performing over a very large frequency range. These plots are created via both simulation and measurement, and the methods are described here.

3.6.1 Simulated scattering plots

Simulated plots were created using a range of far-field monitors ranging from 8 to 18 GHz. As previously explained, at a certain frequency far-field monitors provide the scattering from the surface in question. In this case, monitors were positioned at every 0.2 GHz, providing a high resolution representation of the full frequency range.

The first 3-D scattering plot is of a flat plate and is shown in Fig. 3.14(a), where the majority of the signal is reflected in the specular direction at 60°. Due to the nature narrow beamwidth of the plane wave in CST, the sidelobes are also narrow. The level of signal elsewhere is approximately 40 dB lower than the peak of the specular reflection. The CR-FSS is then simulated, and the resulting plot shown in Fig. 3.14b.

With the introduction of the periodic CR-FSS, the scattering pattern changes considerably. Firstly, there is a large reduction in the specular scatter region between 11 and 16 GHz. There is also a considerable increase in backscatter, where the scattering angle depends on the frequency of the signal.

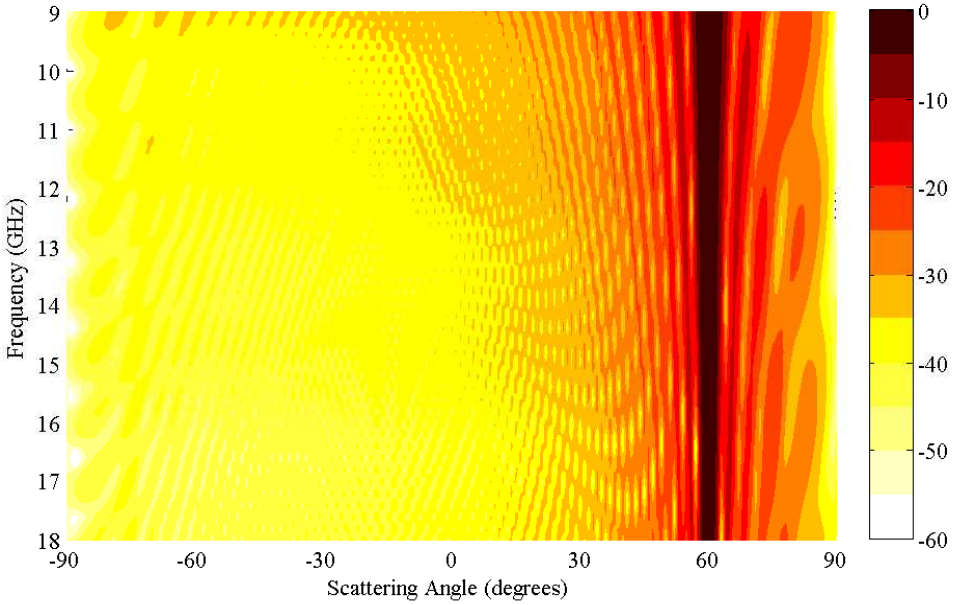

(a)

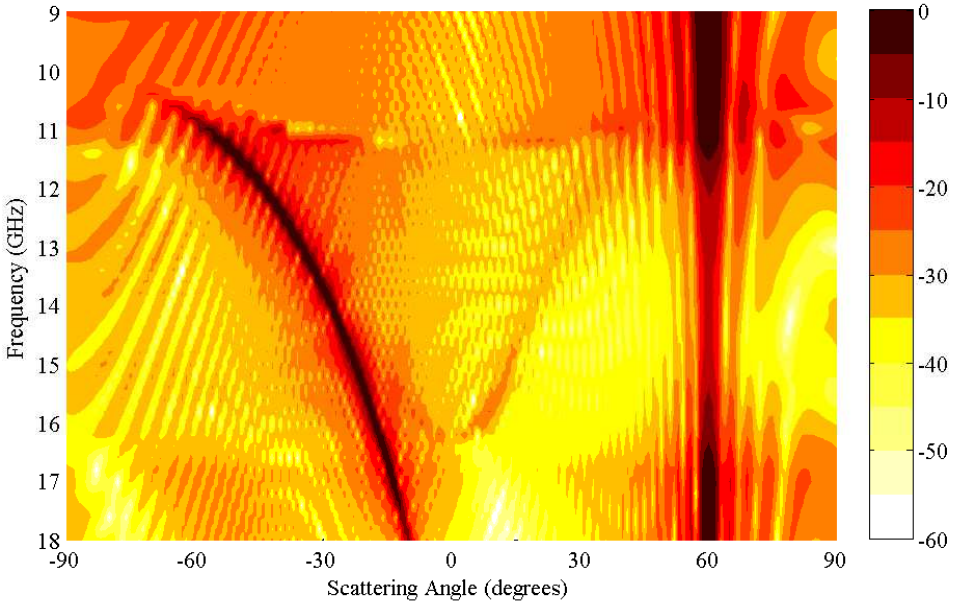

(b)

Figure 3.14: Simulated full scattering results between 9 and 18 GHz for TM polarisation. Illustrated are the (a) flat plate and (b) CR-FSS for $\theta_i = 60°$.

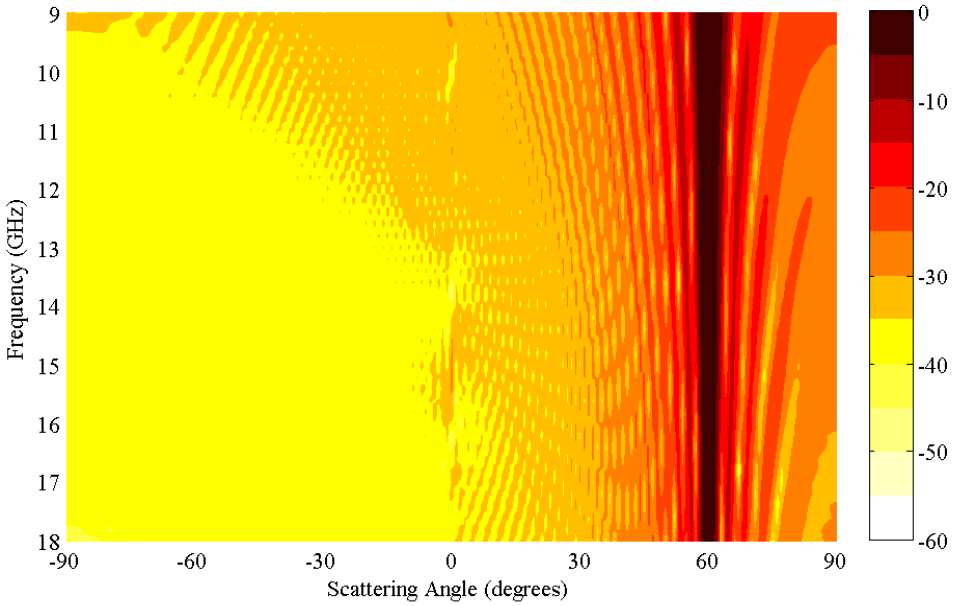

(a)

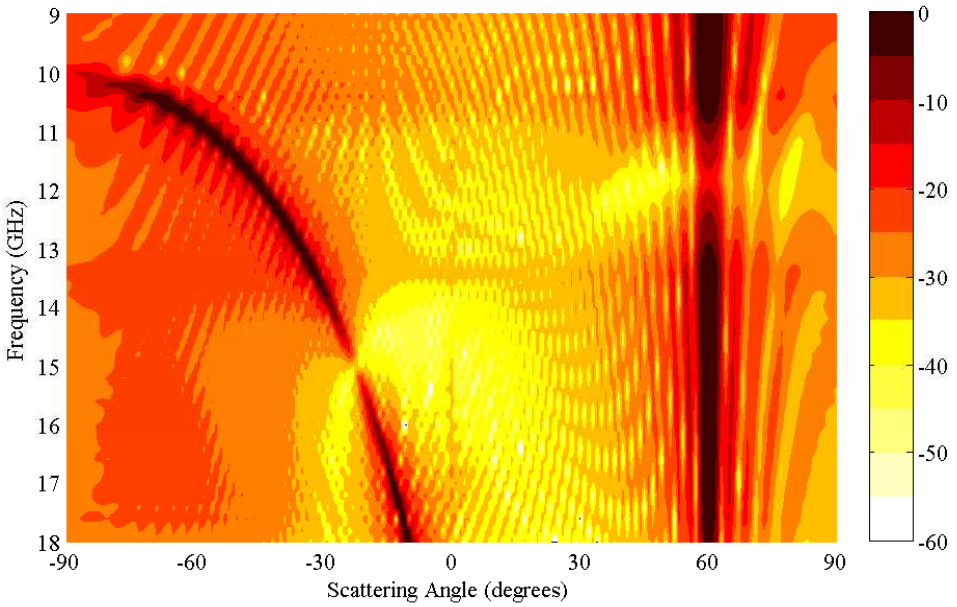

(b)

Figure 3.15: Simulated full scattering results between 9 and 18 GHz for TE polarisation. Illustrated are the (a) flat plate and (b) CR-FSS for $\theta_i = 60°$.

3.6.2 Measured scattering plots

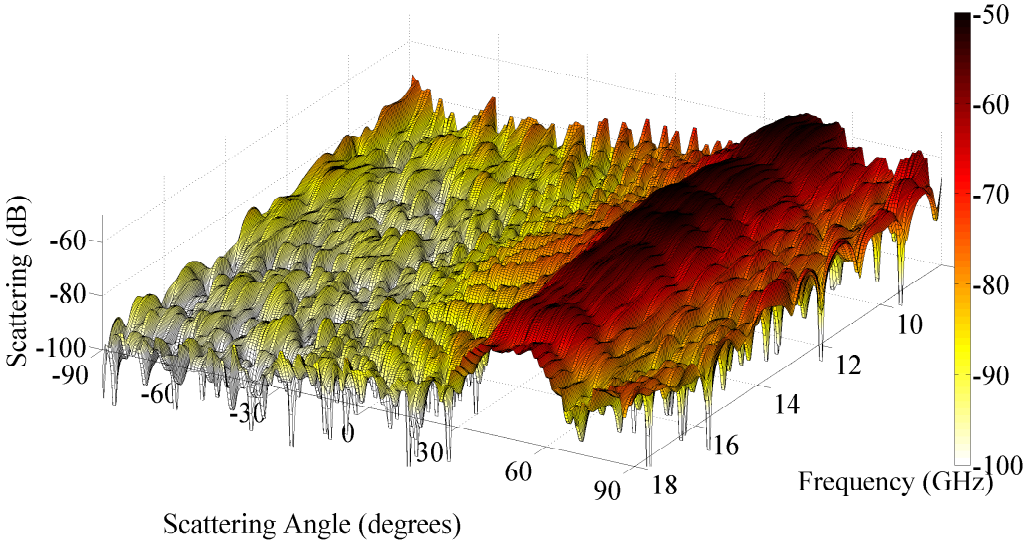

(a)

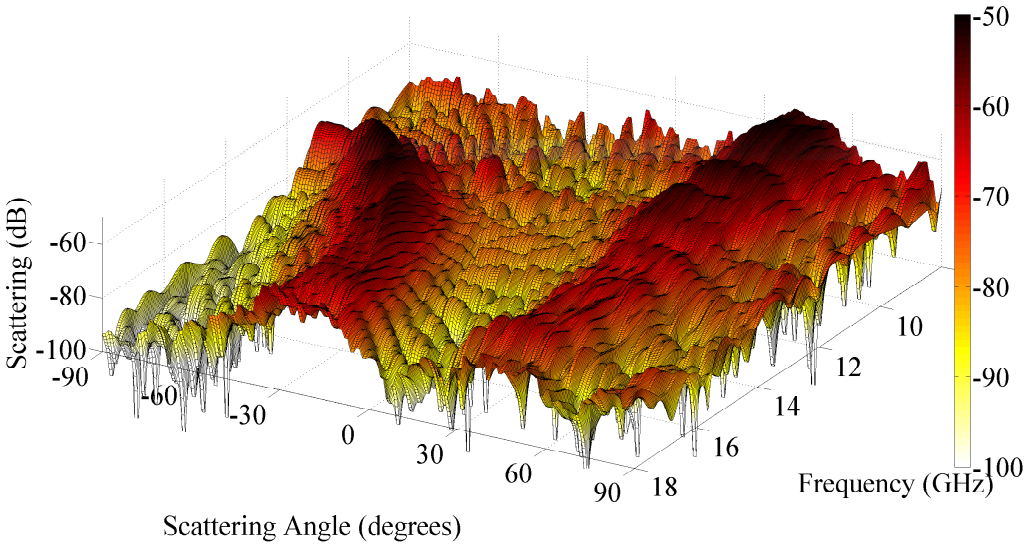

(b)

Figure 3.16: Three-dimensional scattering results between 8 and 18 GHz of (a) a flat metal plate and (b) the CR-FSS. The transmitted signal has $\theta_i = 48°$ and is TM polarised.

The bi-static rotating measurement system previously described in chapter A.2 was used to provide full three-dimensional scattering plots of the flat plate and CR-FSS for a range of frequencies and scattering angles.

The respective plots for a TM polarised plane wave with $\theta_i = 48°$ is shown in Fig. 3.16. Due to the type of horn antennas used, the specular reflection from the flat plate has a broader beam width compared to the simulated result. Use of the CR-FSS once again reduces the specular scatter, and increases the backscatter. The angles of peak backscatter are analytically predictable using the Bragg's Law equations. For example, for the peak backscatter in Fig. 3.14b the peak backscatter for $\theta_i = 60°$ is at $f = 300/(2 \times 16 \times \sin(60)) = 10.83$ GHz.

The difference in magnitude between the CR-FSS and the flat plate is shown in Fig. 3.17. In the backscatter region, there is an increase of nearly 40 dB in the backscatter region and a reduction of 10 to 20 dB in the specular region. The overall scattering measurement seems to be slightly noisy with 10 dB peaks in regions where no increase or reduction would be expected.

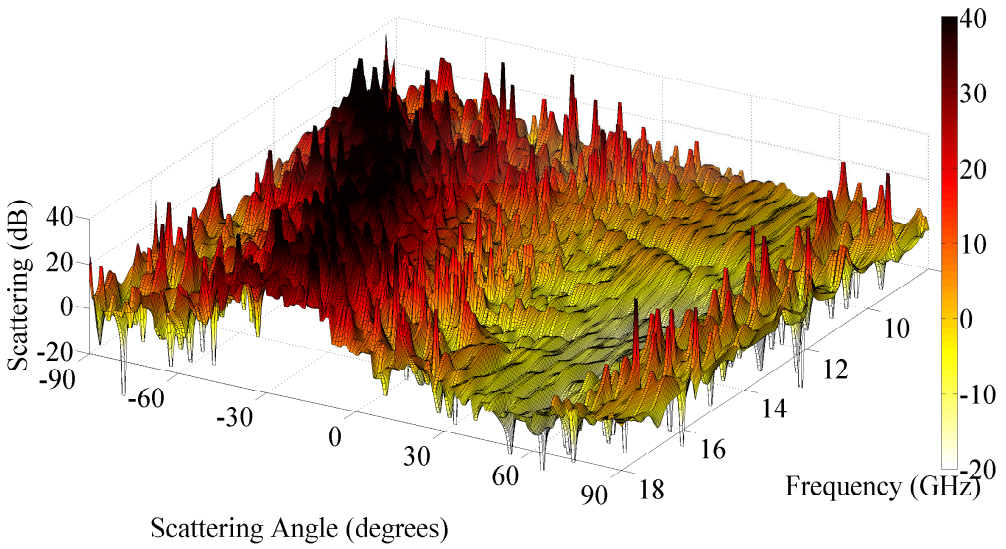

Figure 3.17: Three dimensional scattering plot showing the scattering from the flat metal plate subtracted from the CR-FSS. It reveals the decrease in specular scatter and the increase in backscatter.

3.7 CR-FSS at $\phi_i = 90°$

All measurements and simulations thus far have considered a CR-FSS when $\phi_i = 0°$. In many applications, a plane wave is unlikely to be incident only at this angle of ϕ_i. Previous investigation in this chapter has shown that the CR-FSS is effective for a chosen frequency range—offering a reduction in specular scatter, redirecting this as backscatter towards the original transmission.

Figure 3.19 illustrates how ineffectual the CR-FSS for a plane wave at $\phi_i = 90°$ compared to when $\phi_i = 0°$. The graph shows that for $\phi_i = 0°$, there is a reduction in specular scatter between 10.3 to more than 18 GHz and 11 to 14 GHz for TM and TE respectively. However, when the plane wave is rotated by 90°—so $\phi_i = 90°$—the CR-FSS offers no reduction in specular scatter over the entire frequency range.

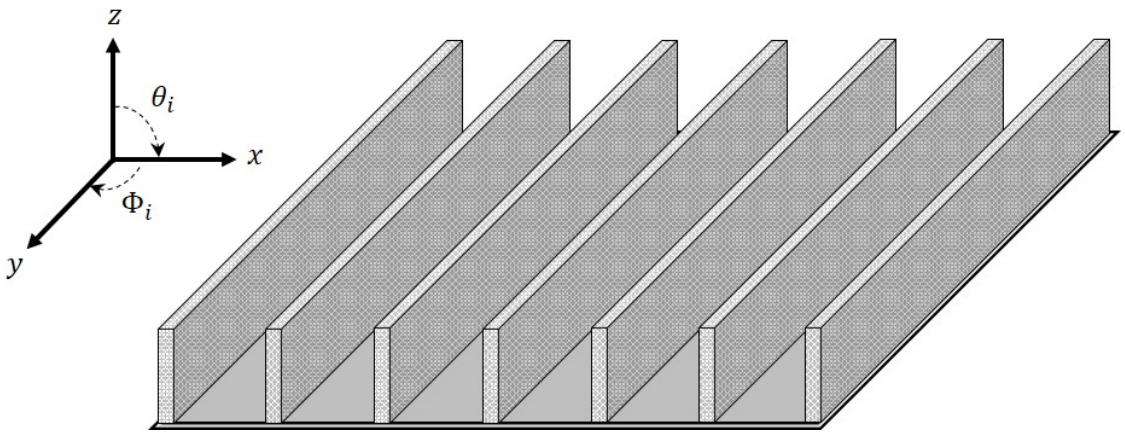

Figure 3.18: Defining the ϕ_i and θ_i angles with reference to the CR-FSS.

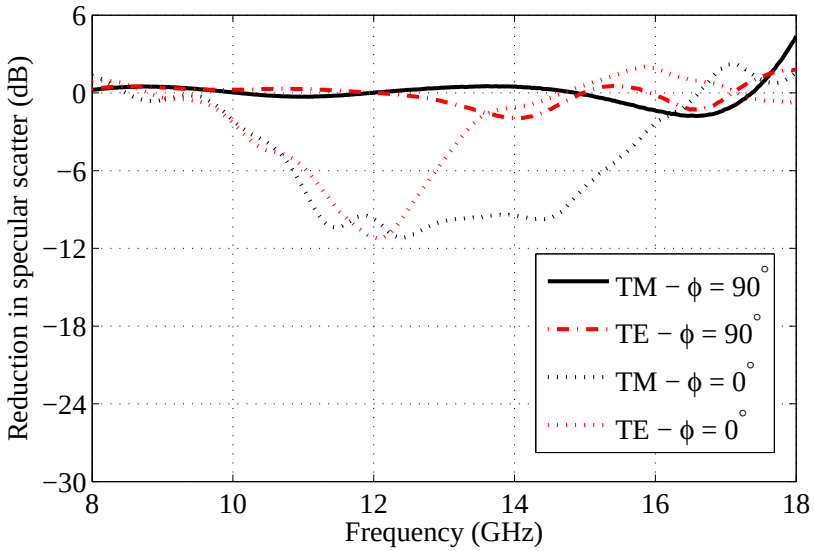

Figure 3.19: NRL measurements illustrating frequency range response for TM and TE polarisations at $\phi_i = 90°$ and $\phi_i = 0°$. For a plane wave with $\theta_i = 60°$.

3.8 Frequency domain investigation of grating lobes

Simulations and measurements so far have shown that energy can be redirected into the direction of grating lobes, defined by Bragg's Law; relating the period of the structure and frequency of the signal to the angle at which this backscatter will occur. Simulations were conducted in the time domain, resulting in scattering plots of the structure. Due to the large simulation time of each permutation of a parameter, each model in the time domain was finitely thin with E or H-boundaries to remove edge effects in this axis. This means that subsequent analysis of grating lobes is limited to this plane only - i.e. $\phi_i = 0°$ only (see Fig. 3.18).

Frequency domain simulations in CST offer an opportunity to evaluate the propagating waves and their direction by simulating the structure using a Floquet port. This assigns a unit cell boundary condition to a small part of the structure making the surface infinitely large. S-parameter results can be obtained for a number of modes, although only propagating ones are of importance. Depending on the periodicity and frequency of a signal, there could be any number of grating lobes.

The grating lobe diagram can visually show when different modes will be propagating. Where they exist inside the circles (as seen in Fig. 3.20), these modes will

propagate. If they fall outside they will be evanescent and die off [47]. As the propagation of higher order modes in the r_x and r_z axis are dependant on the periodicity in those directions, the co-ordinates of the respective modes can be defined by:

$$\hat{r}(k,n) = (s_x + k\frac{\lambda}{D_x}, s_z + n\frac{\lambda}{D_z}) \tag{3.2}$$

If the principal mode is given by the co-ordinates (s_x, s_z), the modes are propagating when:

$$s_y = \sqrt{1 - s_x^2 - s_z^2} \tag{3.3}$$

is real and s_x and s_z lie inside the circle of the grating lobe diagram. For the case where $D_x > \frac{\lambda}{2}$, the circles can overlap as shown in Fig. 3.20 where the points $\hat{r}(0,0)$ and $\hat{r}(-1,0)$ represent the principle mode and grating lobe mode respectively. In this case, both these modes will be propagating.

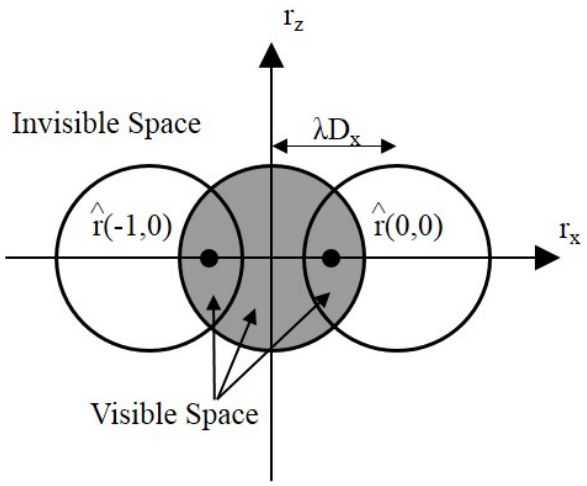

Figure 3.20: Grating lobe diagram for $D_x > \frac{\lambda}{2}$.

A series of floquet mode simulations have been performed for all of the structures, focussing on important sweeps of certain parameters.

3.8.1 CR-FSS floquet mode plots

The effect of changing the height of the combs on both $\hat{r}(0,0)$ and $\hat{r}(-1,0)$ modes is shown in Fig. 3.21 for both TE and TM polarisation. It is clear that the nulls in the $\hat{r}(0,0)$ mode coincide with the peaks in the $\hat{r}(-1,0)$ mode as energy is directed

into these. General trends show that as the fin height increases, the frequency at which there is a null in $\hat{r}(0,0)$ increases. For much higher fin heights above 20 mm additional grating lobes appear in $\hat{r}(-1,0)$ for both TE and TM polarisation.

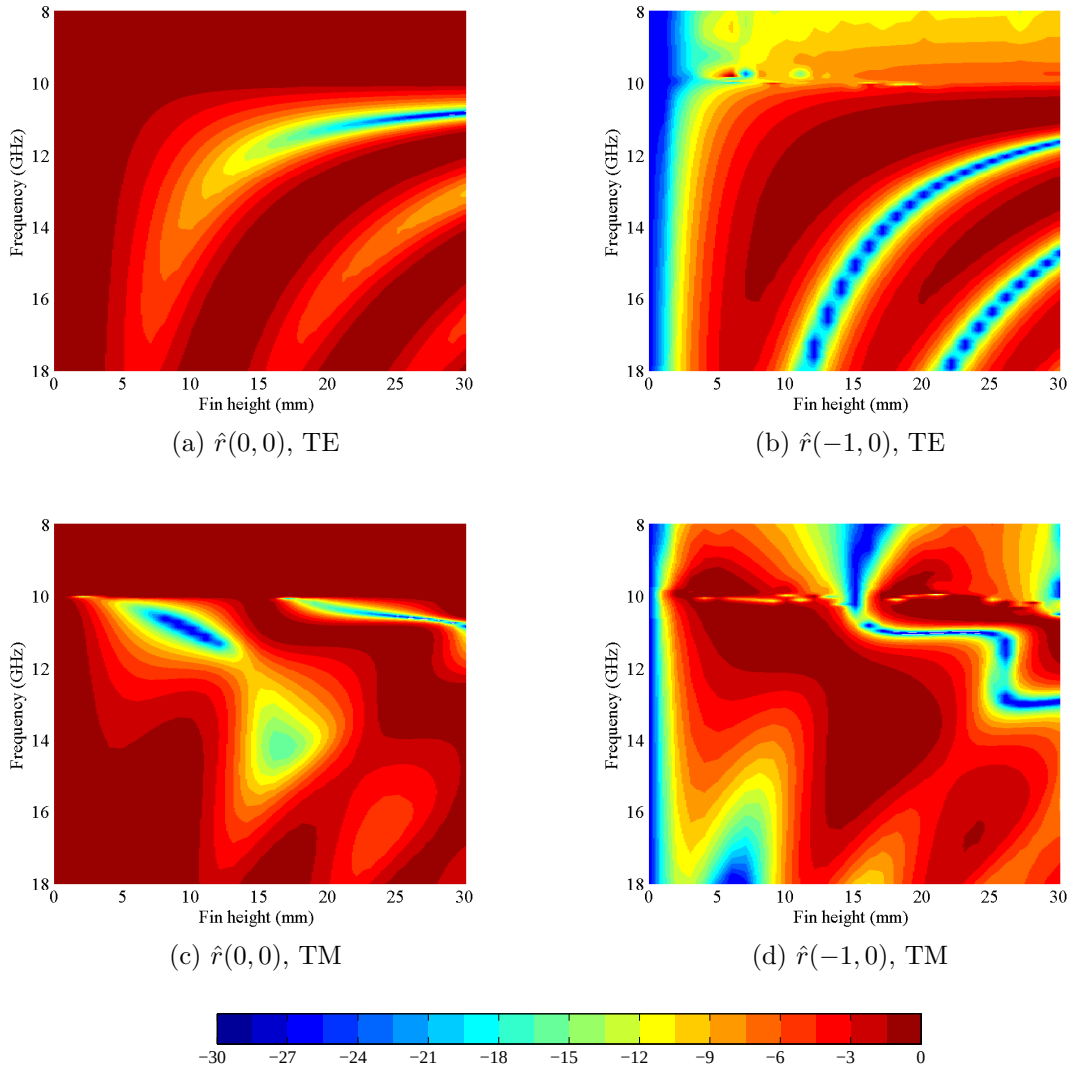

(a) $\hat{r}(0,0)$, TE

(b) $\hat{r}(-1,0)$, TE

(c) $\hat{r}(0,0)$, TM

(d) $\hat{r}(-1,0)$, TM

Figure 3.21: S-parameter (dB) results for a range of fin heights for the principle direction $\hat{r}(0,0)$ and higher-order propagating mode $\hat{r}(-1,0)$ for $\theta_i = 50°$, fin period of 16 mm, and thickness of 1.6 mm.

As previously shown in the time domain simulations, fin period is an important factor in the frequency range at which these structures will reduce specular scatter. Fig. 3.22 summarises the effect on both the $\hat{r}(0,0)$ and $\hat{r}(-1,0)$ modes.

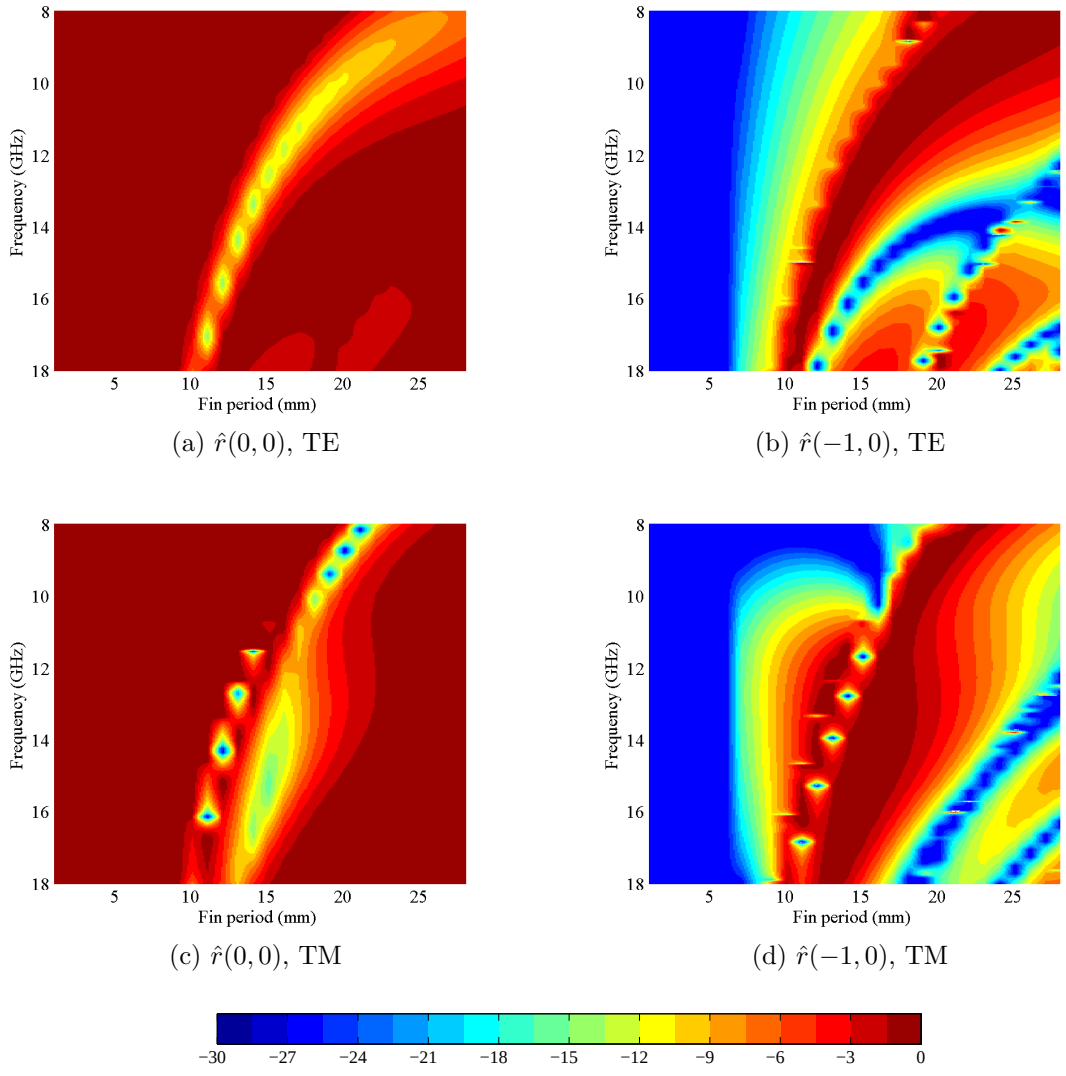

(a) $\hat{r}(0,0)$, TE

(b) $\hat{r}(-1,0)$, TE

(c) $\hat{r}(0,0)$, TM

(d) $\hat{r}(-1,0)$, TM

Figure 3.22: S-parameter (dB) results for a range of fin periods for the principle direction $\hat{r}(0,0)$ and higher-order propagating mode $\hat{r}(-1,0)$. for $\theta_i = 50°$, a fin thickness of 1.6 mm and a fin height of 15 mm.

3.9 Conclusions

This chapter has introduced the main concepts of specular reflection reduction using periodic comb structures. Specific analysis of specular scatter reduction frequency ranges compared to flat PEC plates is given using CST simulations, NRL measurements, and more complex results in the bi-static measurement chamber. TE polarised responses are often more narrowband than their TM equivalent, irrespective of angle of incidence or frequency. Various simulations highlight the effects of fin height, periodicity and thickness on the frequency response. Three dimensional scattering plots show the change in angle of backscatter as the frequency is increased. For signals which are incident with the surface by $\phi_i = 90°$, the CR-FSS has been shown to be ineffectual and thus an alternate surface design is considered in the following chapter.

Chapter 4

Pin Reflection FSS

A pin surface is investigated in order to understand its performance compared to a comb structure. The main motivations behind this design are to reduce material use and to prevent the reduction in performance associated with the CR-FSS when the plane wave is not perpendicular to the comb direction.

4.1 Introduction

The previous chapter addressed the use of a periodic comb surface to reduce specular reflections and re-direct these at a chosen angle in the backscatter region. However, the ability to reduce specular reflections decreases as the angle in the azimuth plane, ϕ tends to 90°. In both interior and exterior scenarios, this could cause a reduction in performance. A simple yet effect solution is required due to the potential increase in building material costs.

It is proposed that a surface which is radially symmetrical every 90° could be used to solve this issue. This would mean that the surface would look the same whether ϕ was 0° or 90°. Initial designs suggested an array of pins could satisfy the construction specification, whilst saving considerably on material and possible manufacturing costs due to the ease of production. The pin reflection frequency selective surface (PR-FSS) was optimised and analysed using conventional measurement and simulation techniques described previously in the last two chapters.

This chapter can be summarised as follows:

- Simulations on how the pin separation, d effects the reduction in specular scatter, and the optimum choice of d.
- The PR-FSS construction for experimentation, and accurate modelling in CST.
- Effects of the pin height, and angle of incidence on the reduction in specular scatter magnitude.
- Comprehensive comparison between the PR-FSS and CR-FSS.
- Review of the surface scattering for angles of incidence of 50° and 60° using simulations and measurements.

4.2 Pin separation

The fin structure of the CR-FSS can be periodically separated to create an array of pins, the distance of which is to be defined as pin separation, d. This pin separation distance is perpendicular to the periodic distance of the comb previously described. Simulation results in this section are used to investigate the effect increasing the pin separation has on the reduction in specular scatter. The optimum pin separation would have the largest dimension that still offers comparable performance to the previously examined CR-FSS. This is because some loss in performance can be acceptable if there is a large decrease in material use. Table 4.1 gives examples of the amount of material reduction that can be achieved with various pin separation distances. This material reduction does not include the ground plane. This can help reduce both weight and cost, potentially becoming viable in scenarios where low weight solutions are required.

Once again, simulations were performed in CST MWS, for a CR-FSS ($d = 0$ mm) and PR-FSS with d ranging from 1 to 41 mm, in steps of 2 mm. As the number of pins was kept constant for each simulation (a single pin in the y-axis), the width of the ground plate, W changes and is equal to d, as defined in Fig. 4.1. This is important, as for accurate comparison, the width of the flat PEC plate must be the same dimensions as the ground plate of the PR-FSS. The PR-FSS structure is

rotationally symmetrical in $\phi_i = 0°/90°$ directions, meeting the design requirements previously mentioned.

Pin separation, d (mm)	Reduction in fin (%)	Notes
0	0	CR-FSS
5	64	
10	84	
16	90	
25	93.6	

Table 4.1: The reduction in fin material when using a pin structure of thickness $t = 1.6$ mm

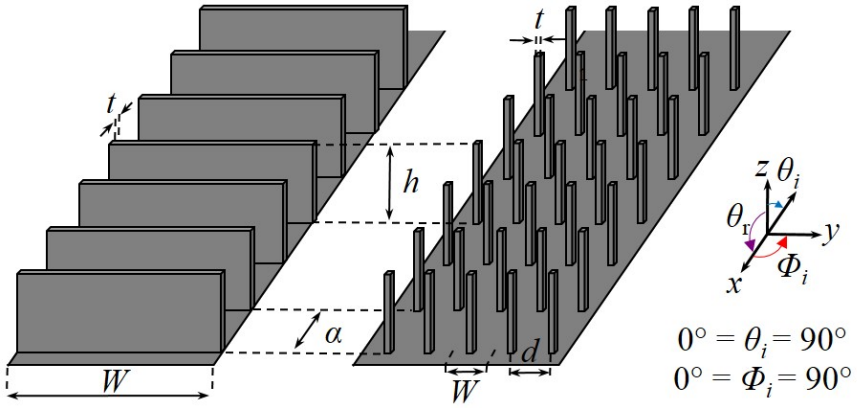

Figure 4.1: A cross-sectional view of (a) the CR-FSS first simulated in chapter 3, and (b) the PR-FSS. The dimensions of the CR-FSS and PR-FSS are period α, pin separation d, thickness t, simulated surface width W, and height h. The angle of incidence, θ_i and angle of reflection, θ_r are measured with respect to z in the xz plane, and the angle of rotation, ϕ_i in the xy plane is measured with respect to x.

A rectangular pin was used in simulations, with a pin thickness of 1.6 mm, (in both the x-axis and y-axis), as shown in Fig. 4.1. A rectangular pin is used due to the difficulty of simulating a threaded screw, both with the design of the threading and the meshing on the structure for accurate simulation results. As d is increased in length, the separation between pins becomes larger. Logically, it is assumed that

surface performance would degrade as this distance increases, however simulation results reveal important features about the surface.

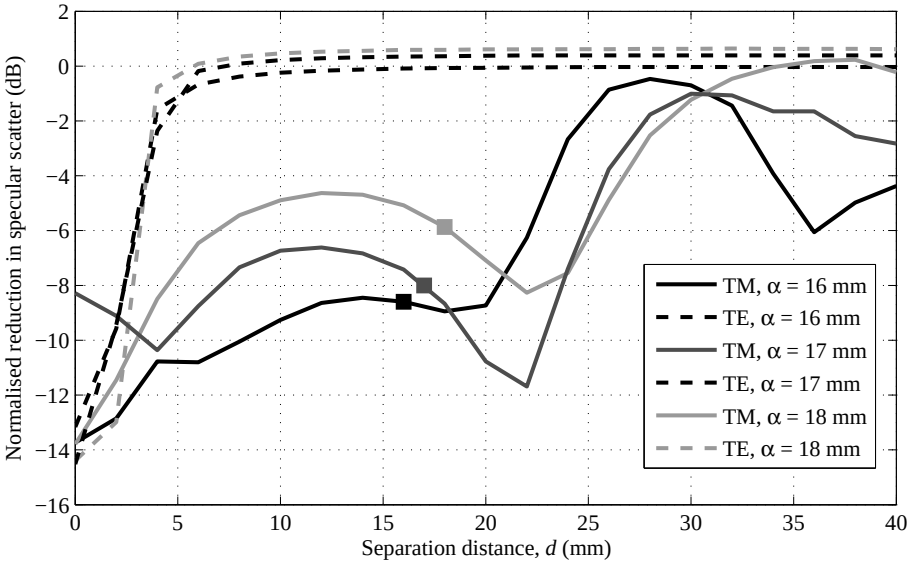

Figure 4.2: Simulated results showing the relationship between pin separation and reduction in received forward scatter for TM and TE polarisations at $f = 12$ GHz.

Simulation results are presented in Fig. 4.2 for TM and TE polarised plane waves. For both polarisations, a PR-FSS with periods of 16 mm, +17 mm, and 18 mm are investigated. The graph was produced by plotting the difference in specular scatter magnitude for each value of d, at $\theta_i = 60°$ and $f = 12$ GHz for the range of separation distances specified previously. The reduction in specular scatter is the difference between the result of a flat PEC plate of the same width as the respective PR-FSS at 12 GHz.

Distinct differences can be seen between TM and TE polarisations. For TM polarisation, the point at which the pin period equals the pin separation ($\alpha = d$) is noted by a square marker for clarity. This is an important marker, as it means that the period in both the $x-$ and $y-$axis is equal, making the surface rotationally symmetrical.

As expected, the CR-FSS (i.e. $d = 0$ mm) has the greatest reduction in specular scatter, at approximately 13 dB for both TM and TE polarizations for $\alpha = 16$ mm

and 18 mm. At $\alpha = 17$ mm, the reduction in specular scatter offered by the CR-FSS is similar to that of the symmetrical PR-FSS. As the pin separation is increased, the PR-FSS becomes less effective at reducing specular scatter. For TM polarization, surfaces with $d \leq 20$ mm have an effective reduction of at least 8 dB when $\alpha = 16$ mm. For TE polarization, the PR-FSS is ineffectual at reducing specular scatter, unless pin separation is very low (< 4 mm). This is because the pin elements are perpendicular to the electric field and thus the propagating signal is not coupled onto the respective elements. Therefore none of the propagating signal is reflected. This is contrary to the TM case whereby the elements are parallel to the electric field and thus can be coupled and reflected. Further analysis using the current distributions is conducted later in the chapter.

It can thus be concluded that the PR-FSS will not work TE polarisation for a rotationally symmetrical surface, and closer investigation for TM polarisation is required.

4.3 Simulations and NRL measurements

Analysis of the PR-FSS is conducted using CST simulations and comparative measurements. With consideration of the initial pin separation simulations in section 4.2, a pin separation, d of 16 mm is used, as this also matches the surface period of the PR-FSS, and the CR-FSS tested in chapter. 3. Comparison of the CR-FSS and PR-FSS using simulations at various angles of incidence is also reported on. The experimental set-up for the NRL reflectivity arch is described in detail in Section A.2.2. Simplifications for fast but accurate modelling of the pin structure are described here.

4.3.1 PR-FSS construction

Experimental surface manufacture: the PR-FSS had an array of 16 mm long screws inserted into the ground plane to form a 39×39 grid, totalling 1521 pins. Each hole was tapped to provide a thread to tightly secure the screws, ensuring a good electrical contact between the screws and the plate, thus reducing the possible effects of unnecessary resistance.

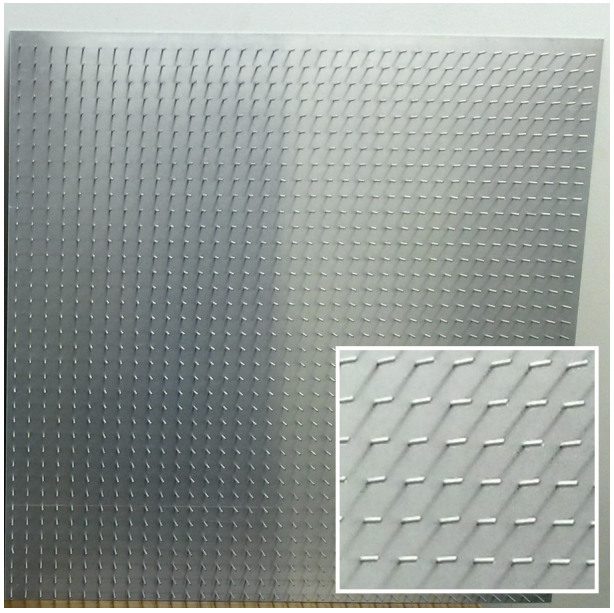

Figure 4.3: The aluminium prototypes of the 39×39 PR-FSS with magnification of the pin structure in the inset image.

As the ground plate was 1 mm thick, the resulting pin height was 15 mm. Future simulations show that 15 mm is an adequate height for the pins, although not the optimum at 12 GHz. The final surface is shown in Fig. 4.3. The total size of the ground plate is 600 mm^2.

CST simplifications: various simplifications have been made in the simulation of this surface, compared to the experimental surface. The screws were modelled in CST as rectangular pins instead of threaded screws, as accurate simulation would require very high mesh density and simulations would be too lengthy. Slight inaccuracies between measurement and simulation results may be due to this modification. With the rectangular pins the mesh that was required was similar to that used previously, as confirmed by the convergence of the simulation results. The accuracy of the simulation results when compared to measurement results also reiterates that the simulation model and meshing were suitable.

4.3.2 Pin height

As seen previously with the CR-FSS, the height of the pin affects the reduction in specular scatter at a given frequency. As the PR-FSS only works for TM polarisation, only this is considered in Fig. 4.4. For $f = 12$ GHz and $\theta_i = 60°$, the peak reduction in specular scatter occurs at 17 mm (0.68λ), compared to 14 mm for the CR-FSS in Fig. 3.4. A 6 dB reduction in specular scatter is visible between 13 mm and 20 mm. Evidently, the choice of pin height will affect performance in the following simulations and experiments. For accurate comparison between the CR-FSS and PR-FSS structures, a pin height of 15 mm was chosen. Although not at the optimum as illustrated in Fig. 4.4, there is still acceptable reduction in specular scatter.

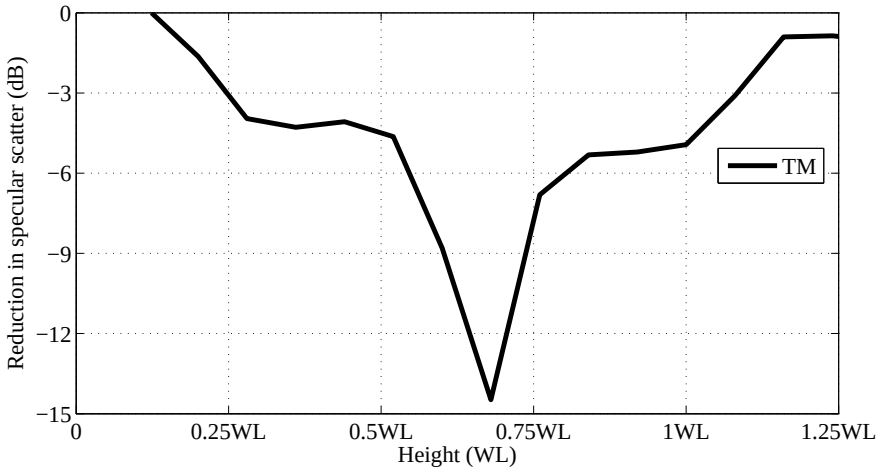

Figure 4.4: Pin height simulation results for the PR-FSS as a function of wavelength ($\alpha = 16$ mm and $d = 16$ mm) for TM polarised signals with $\theta_i = 60°$ at $f = 12$ GHz. ($\lambda = 25$ mm). Only TM polarisation is considered as the surface is completely ineffective for TE polarised excitation.

A full frequency domain analysis has been conducted in Fig. 4.13, where there is a correlation between pin height and resonant frequency where the greatest reduction in specular scatter occurs has been plotted. This optimum pin height generally occurs for pin heights of 0.5λ to 0.7λ, depending on frequency.

4.3.3 Oblique incidence angle performance

The performance of the PR-FSS for varying incidence angle is investigated at 12 GHz. Simulation results were obtained by changing the angle of incidence of the plane wave and exporting the far-field monitor data at the frequency of interest. For comparison with the CR-FSS, a PR-FSS was excited by a TM polarised plane wave in CST, and the far-field data extracted at 12 GHz. As before, a range of incidence angles from 0° to 90° were considered with 5° steps, with a 1° resolution between 45° and 55° used to obtain more accurate results at the peak values. Measurement data from the NRL reflectivity arch are used to validate the simulated results, with a 2° resolution up to 60° due to limitations of the system.

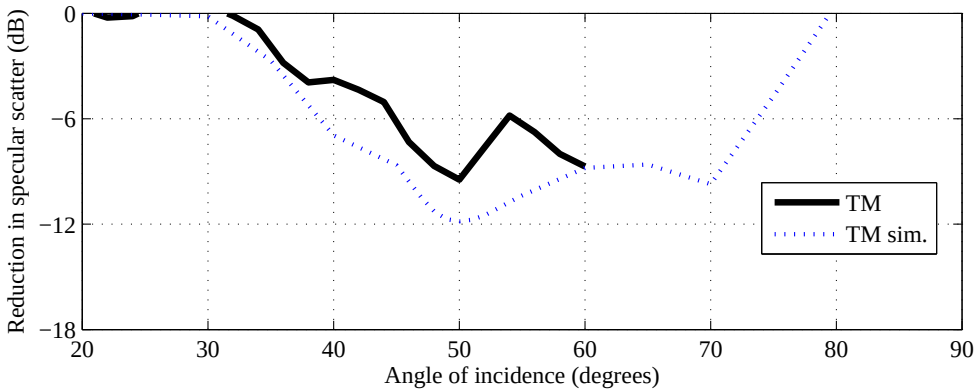

Figure 4.5: Relationship between the reduction in specular scatter and angle of incidence for TM and TE polarisation at $f = 12$ GHz.

Compared to the TM performance of the CR-FSS in Fig. 3.8, the CST simulation shows a similar level of reduction over a similar range: at least 6 dB between 38° and 74°, with a peak at 50°. The NRL measurement shows a close trend to the simulation, peaking at 50°, although at 54°, the measurement seems to be lower than the simulation predicted.

4.4 PR-FSS and CR-FSS comparisons

Extensive comparisons of the frequency response of the CR-FSS and PR-FSS were completed, with 3 dB and 6 dB bandwidths listed in Table 4.2. Also listed are the frequencies at which the 3 dB band starts and ends. Four angles of incidence are considered here: 40°, 50°, 60°, and 70°, as the reduction is greater at these angles of incidence, as seen in the previous section.

For TM polarisation, the CR-FSS has a larger 6 dB bandwidth than the PR-FSS for all respective angles of incidence. This is the same for the 3 dB bandwidths. This suggests that the PR-FSS has a reduced operational bandwidth for TM polarisation. The start and stop frequencies also reduce for the PR-FSS in all of the cases in Table. 4.2.

Comparison between the CR-FSS and PR-FSS for TE polarisation is not possible as the PR-FSS is ineffectual for TE polarisation. For the CR-FSS, the 3 dB and 6 dB bandwidths for TE polarisation are smaller than the retrospective TM polarisations.

The PR-FSS also exhibits frequency responses which are harmonic, hence there is multiple 3 dB frequency ranges for $\theta_i = 40°$ and $\theta_i = 70°$. This is discussed further in section 4.7.

Table 4.2: Simulated 3 dB and 6 dB bandwidths for the CR-FSS for TE and TM polarized signals and the PR-FSS for the TM polarization; for a range of angles of incidence. The 3 dB start and stop frequencies are also listed. The numbers listed in brackets refer to a second 3 dB frequency range, beginning and ending at the described frequencies.

CR-FSS								
	TE				**TM**			
θ_i (°)	3 dB start frequency (GHz)	3 dB stop frequency (GHz)	3 dB b'width (%)	6 dB b'width (%)	3 dB start frequency (GHz)	3 dB stop frequency (GHz)	3 dB b'width (%)	6 dB b'width (%)
40	11.50	13.93	66.21	31.88	11.76	18.17	79.43	64.19
50	10.78	13.38	63.34	46.39	11.26	17.25	82.63	69.53
60	10.28	13.22	46.23	30.63	11.17	16.45	71.26	57.58
70	10.69	13.52	59.08	25.68	10.81	17.13	77.99	60.67
PR-FSS								
40	-	-	-	-	11.58 (13.33)	13.27 (17.51)	75.06	55.24
50	-	-	-	-	10.66	16.00	54.54	42.11
60	-	-	-	-	10.02	14.37	39.92	27.32
70	-	-	-	-	9.69 (16.12)	15.05 (17.10)	73.36	49.90

4.5 Specular scatter reduction

This section presents and discusses the results of NRL reflectivity measurements and simulated models of the PR-FSS at various angles of incidence. Both TE and TM polarisations are shown, despite the PR-FSS not working for TE polarisation, as previously shown.

4.5.1 Reduction at 50°

The reduction of specular scatter at $\theta_i = 50°$ is shown in Fig. 4.6. As expected, both the simulated results and experimental measurements show that there is no reduction for TE polarisation. For TM polarisation, there is a 3 dB reduction between a range of 10.8 GHz and 16.8 GHz, with a harmonic visible at 13.2 GHz (13.5 GHz for the measured result). Section 4.7 discusses the possible causes of this harmonic when using a pin structure. At least 6 dB reduction is visible between 11.3 GHz and 15.8 GHz for the measured result and 11 GHz and 15.6 GHz for the simulated. The harmonic of the simulated result causes the 6 dB frequency range to be split between 13.1 and 13.4 GHz.

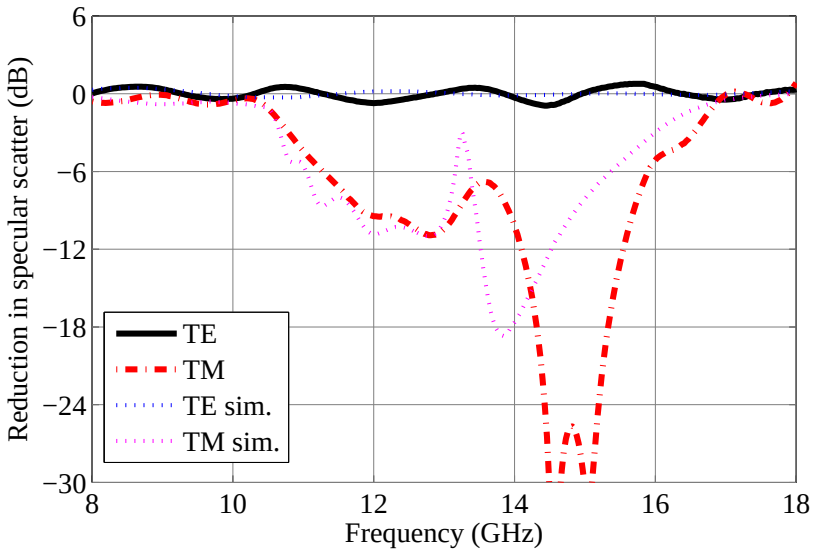

Figure 4.6: A comparison of the measured and simulated results for TE and TM polarisation for $\theta_i = 50°$.

4.5.2 Reduction at 60°

The reduction in specular scatter magnitude at 60° is shown in Fig. 4.7. Once again, both simulations and measurements show that the surface does not work for TE polarisation. For TM polarisation, the NRL measurement and CST simulation show good agreement. There is a 6 dB start and stop frequency between 10.1 GHz and 13.7 GHz, and 9.9 GHz and 13.5 GHz for the simulation and measurement result respectively. There is a peak reduction of 14 dB and 16 dB at 10.65 GHz and 10.75 GHz respectively, for simulations and measurements.

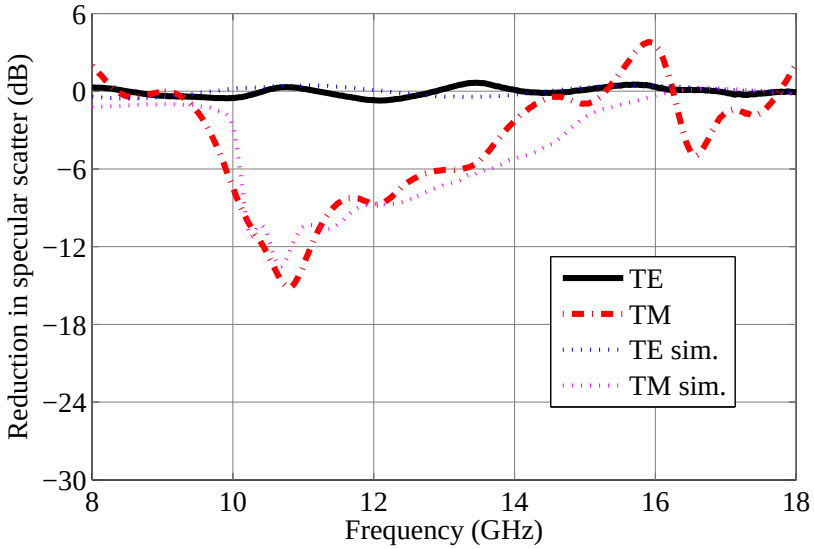

Figure 4.7: A comparison of the measured and simulated results for TE and TM polarisation for $\theta_i = 60°$.

4.6 Angular stability across the frequency range

Following analysis of the oblique incidence angle sweep in section 4.3.3 and the reduction across the whole frequency ranges for $\theta_i = 50°$ and 60°, it seems that the angular stability is not as good for the PR-FSS as it is for the CR-FSS. Although at 12 GHz there is 12 dB and 8 dB reductions at 50° and 60° repetitively the peak reductions are changeable. At 50°, the peak in reduction is at 14 to 15 GHz (measurement to simulation), with a second lower peak in the 10 to 13 GHz region. This peak remains at 60°, however the large peak at 14 GHz does not exist.

These changeable frequency ranges mean that the PR-FSS does not have very good angular stability, something which could be essential in indoor propagation control down corridors.

4.7 Pin surface currents

4.7.1 TM and TE polarisation differences

The calculation of pin surface currents using CST was conducted to understand further why the PR-FSS was ineffectual for TE polarisation. A comparison between two identical PR-FSS was used, with surface current monitors at $f = 11$ and 15 GHz. The respective E/H-field probes were used to obtain the initial frequency responses for the TE and TM polarised plane wave at $\theta_i = 60°$.

The direction of the electric field effects the interaction of the pins with, as seen in Fig. 4.8. Normalised reduction in specular scatter is shown for both TM and TE polarisations - with TM offering 6 dB reduction between 10 and 13 GHz, and TE being totally ineffectual. Beginning with TM polarisation, the current distribution at 11 GHz shows that the majority of the current occurs at the base of the pins and on the front side of the pin, suggesting much of the field is reflected back towards the transmitter. Each pin also offers very similar magnitudes and patterns of reflection. At 15 GHz, where the surface is no longer in operating range, the uniformity of reflection is lost. On the pin where the highest surface current, the current is evenly distributed around the pin, and not lop-sided like for the 11 GHz currents.

For TE polarisation, the electric field lies parallel to the y-axis and perpendicular to the direction of propagation.This results in the pins having no effect on the propagating wave, with pins with current distributions equal on both sides. For example, for TE polarisation at 15 GHz the pin with highest surface current, has equal distribution on the non-visible side. There is also no surface current at the base of the pin, resulting in no backscatter or reduction in specular scatter.

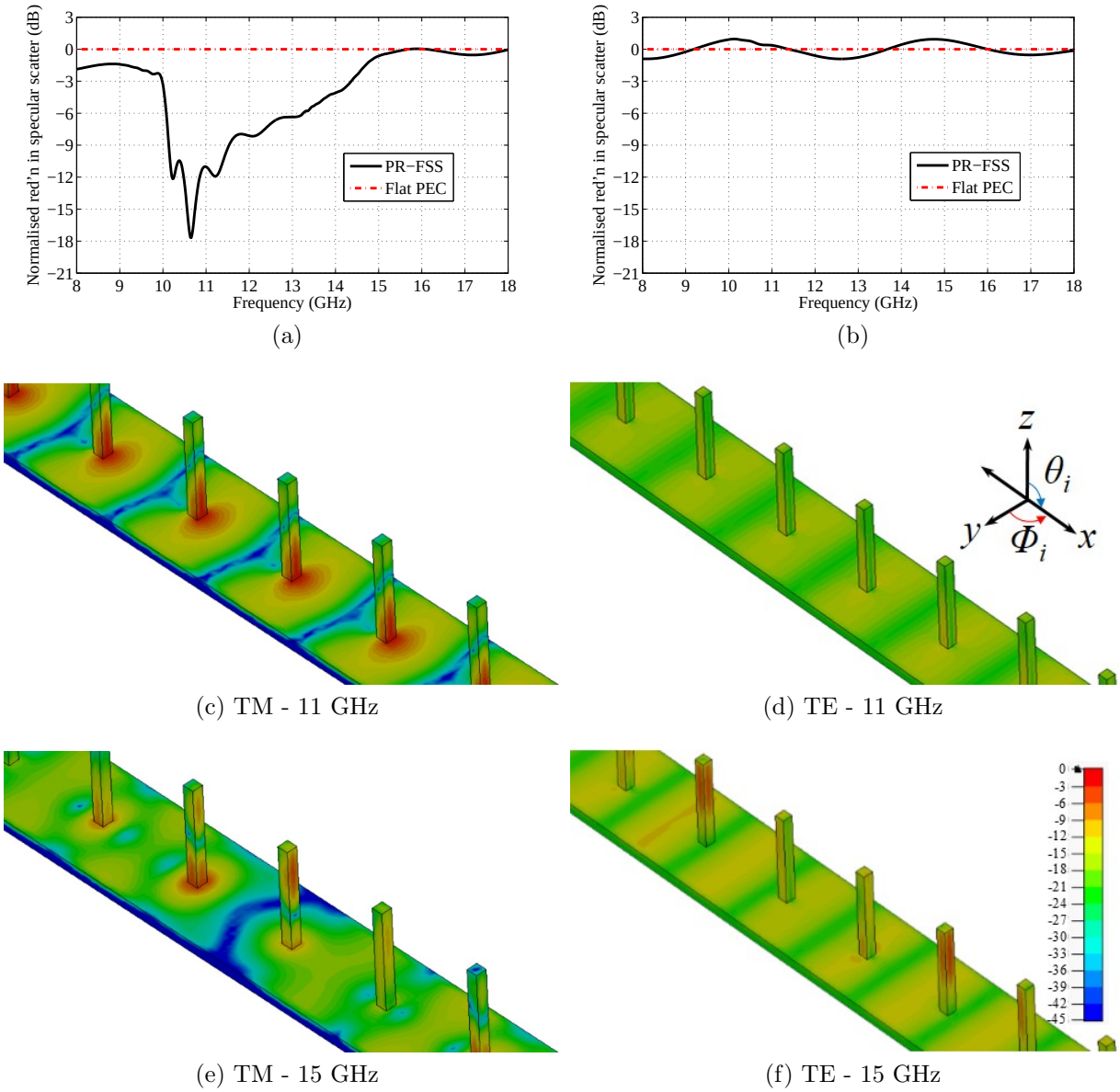

Figure 4.8: The normalised frequency response for a PR-FSS with plane wave excitation for (a) TM and (b) TE polarised at $\theta_i = 60°$, and the respective surface current distributions for (c) TM and (d) TE polarisation at 11 GHz, and (e) TM and (f) TE polarisation at 15 GHz.

4.7.2 Null in frequency response

At certain angles of incidence, nulls are introduced into the frequency response. Inspection of the surface currents is used to explain why these occur. Multiple periods are used in the y-axis to clearly illustrate the surface currents on the ground plate diagonally between the pins.

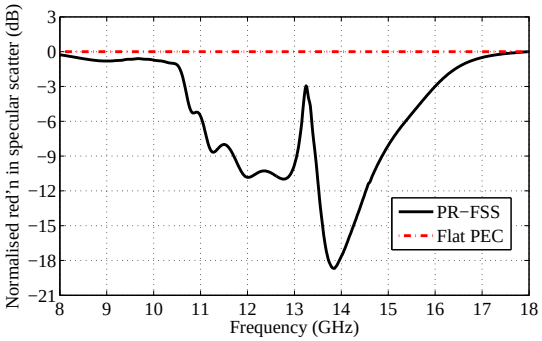

(a)

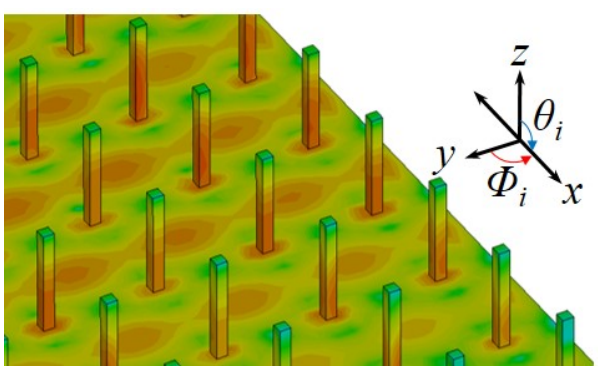

(b)

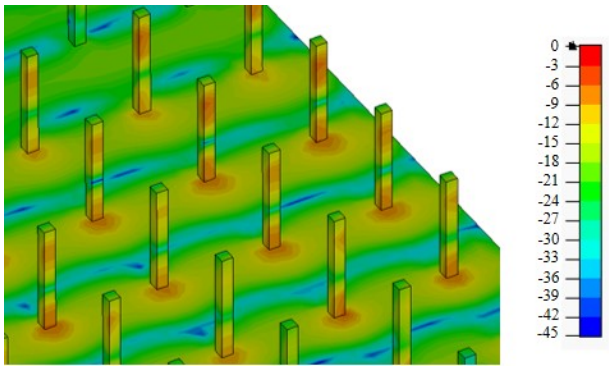

(c)

Figure 4.9: (a) The nomalised frequency response for a a TM polarised plane wave with $\theta_i = 50°$, and surface currents at (b) 13.2 GHz where the harmonic occurs, and (c) 14 GHz, where the surface is effective at reducing specular scatter.

Fig. 4.9(a) shows the simulated frequency response for a a TM polarised plane wave with $\theta_i = 50°$, initially shown in Fig. 4.6. Also shown are two surface current plots to aid in understanding why this harmonic occurs. The null in the response at 13.2 GHz where there is no reduction in specular scatter, shows a current distribution around the bottom of the pin which is equally distributed instead of being focussed in the direction of the incoming plane wave like at 14 GHz. At $f = 13.2$ in Fig.4.9(b), the current is evenly distributed, around the base of the pin itself and over the whole

ground plane. This is similar to a PEC surface where there would be an even current distribution over the whole surface. The current density at the base of the pins is also similar to that diagonally in between the pins on the ground plate. However, for the peak in reduction at $f = 14$ GHz, the current distribution is maximum at one side of the base of a pin and is much greater than anywhere else on the ground plate, resulting in a reduction in specular scatter and redirection as backscatter.

4.8 Simulated scattering plots

The simulated scattering plots of the PR-FSS are shown in Fig. 4.10 and Fig. 4.11 for TM and TE polarisation respectively. A plane wave with an angle of incidence of 60° is used to excite the structure, thus specular scatter occurs at this scattering angle. The flat plate scattering shows the peak energy is scattered in this angle. The PR-FSS reduces this specular scatter evidently between 10 and 14 GHz for TM polarisation in Fig. 4.10b, where the energy is scattered back towards to the source.

For TE polarisation, the PR-FSS is expectedly in-effectual at reducing the specular scatter, as shown in Fig. 4.11b. There is a visible backscatter lobe, however this is of much lower power than for TM polarisation.

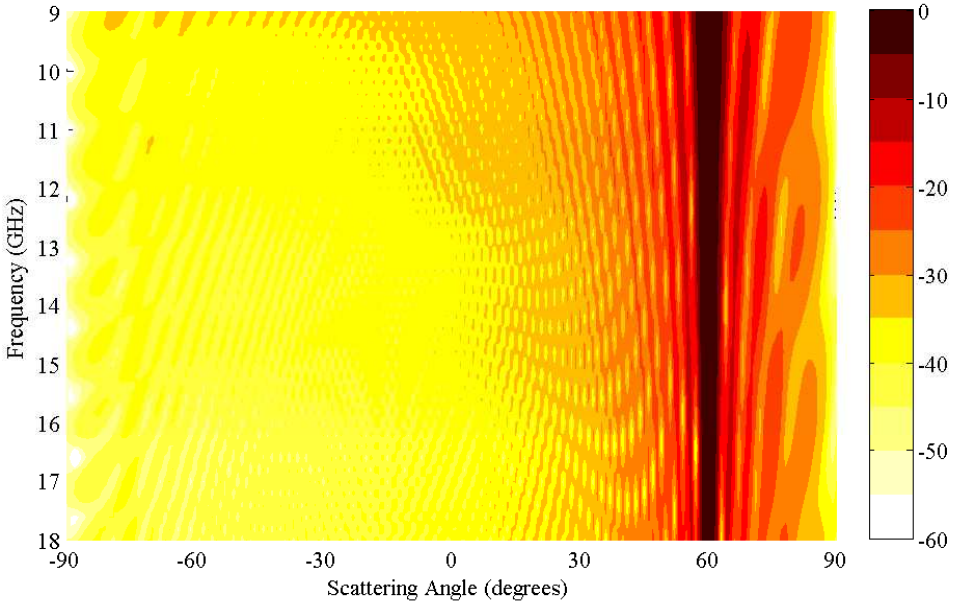

(a) Flat plate, TM polarisation

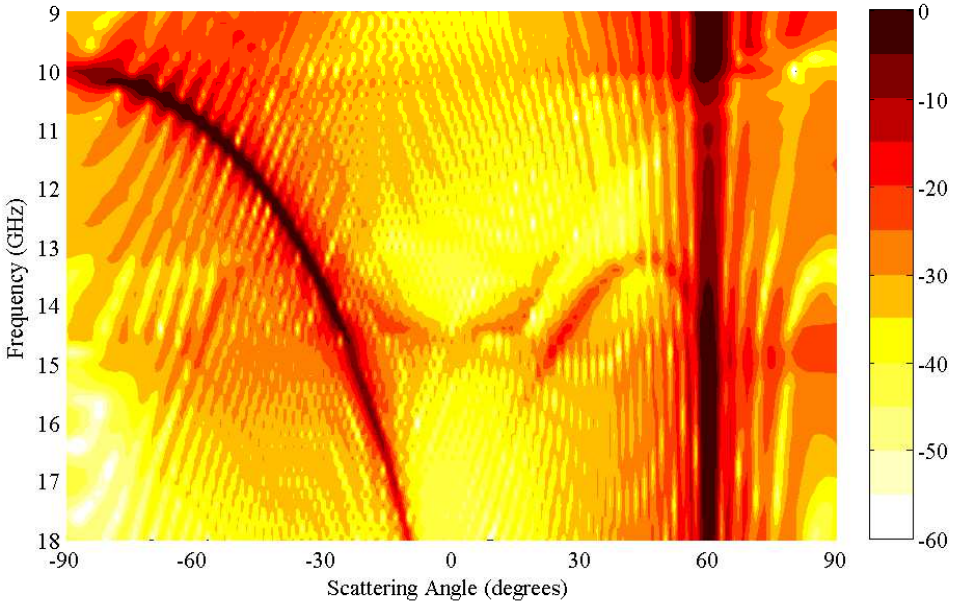

(b) PR-FSS, TM polarisation

Figure 4.10: Simulated full scattering results between 9 and 18 GHz for TM polarisation. Illustrated are the (a) flat plate and (b) PR-FSS for $\theta_i = 60°$.

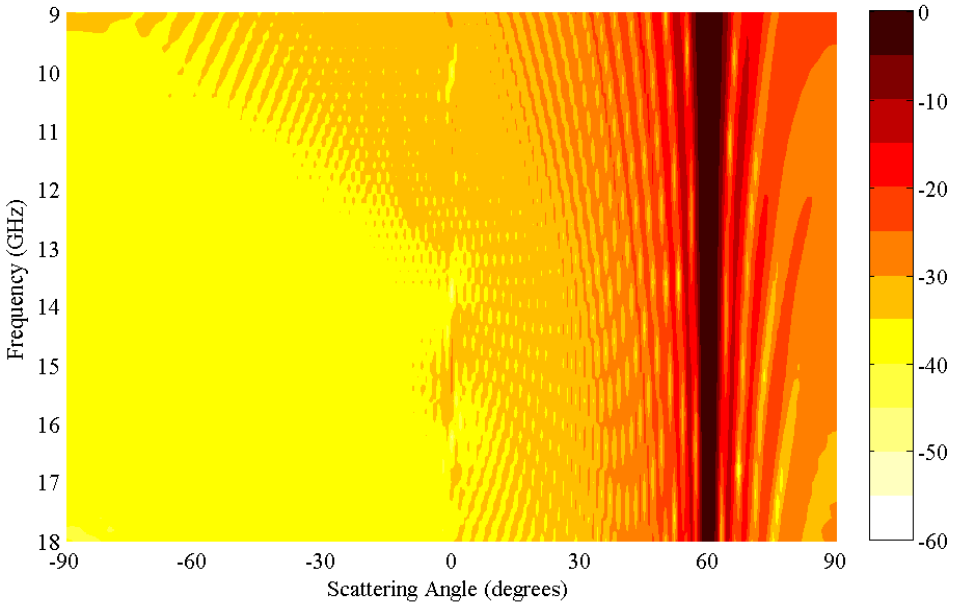

(a) Flat plate, TE polarisation

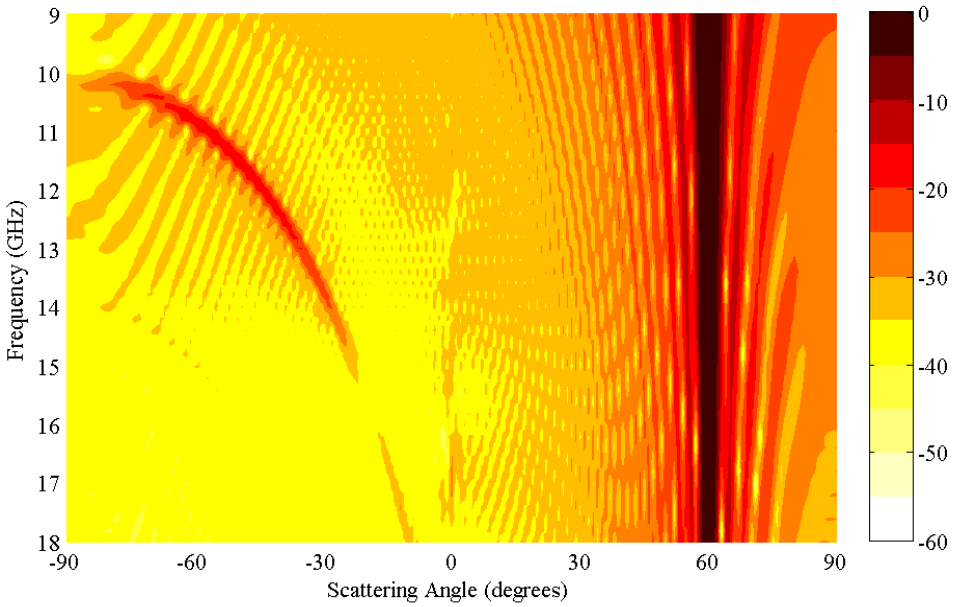

(b) PR-FSS, TE polarisation

Figure 4.11: Simulated full scattering results between 9 and 18 GHz for TE polarisation. Illustrated are the (a) flat plate and (b) PR-FSS for $\theta_i = 60°$.

4.9 Scattering plot of the PR-FSS

Scattering measurements were conducted to validate whether the scattering angles were measurable on an aluminium prototype. As highlighted earlier in the chapter, the pins of the prototype differed from those simulated due to ease of manufacture and simulation respectively. For comparison with simulations and previous scattering measurements, a frequency range of 8 to 18 GHz was measured for the full scattering range between -90° and 90°. The PR-FSS is shown for TM polarisation in Fig. 4.12. Reduction in specular scatter and the backscatter lobe are both evident in the time gated measurement.

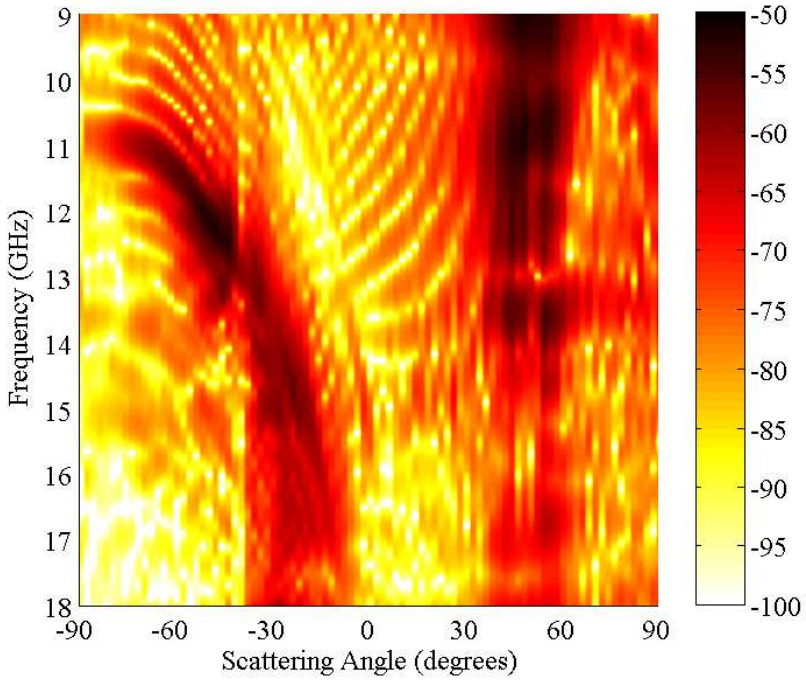

(a)

Figure 4.12: Scattering measurement for a PR-FSS for a TM polarised wave for θ_i = 50°.

4.10 PR-FSS floquet mode plots

Floquet simulation results are shown for TM polarisation only due to the fact that the structure does not reduce the specular scatter much in TE polarisation as shown previously in the chapter. Fig. 4.14 shows simulation results of changing pin height. The PR-FSS $\hat{r}(0,0)$ mode shows a similar response to increasing pin height as the CR-FSS; that is an increase in fin height leads to the null position increasing in frequency.

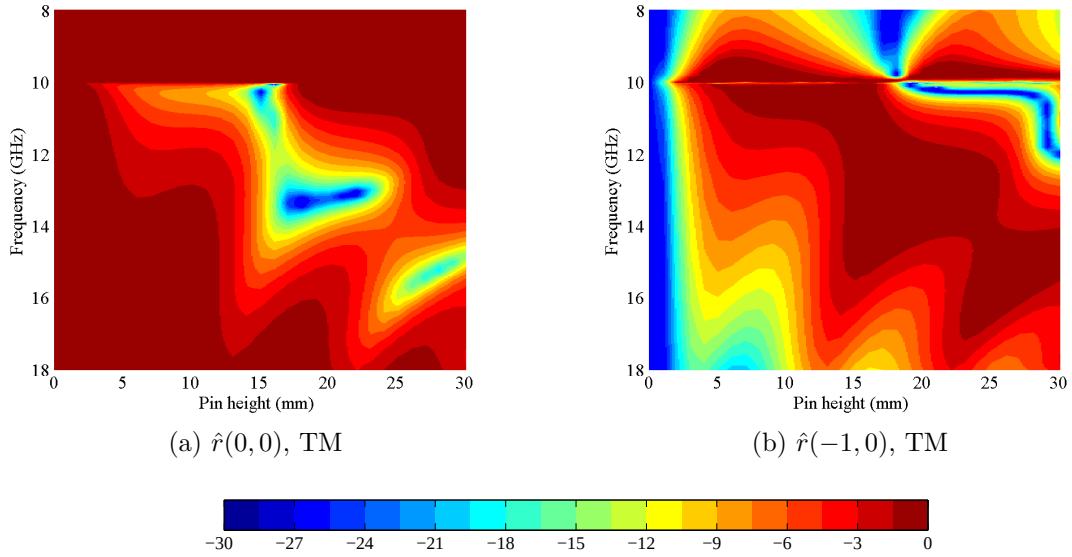

(a) $\hat{r}(0,0)$, TM

(b) $\hat{r}(-1,0)$, TM

Figure 4.13: S-parameter (dB) results for a range of pin heights for the principle direction $\hat{r}(0,0)$ and higher-order propagating mode $\hat{r}(-1,0)$ for $\theta_i = 50°$, pin thickness of 1.6 mm and period 16 mm. Results for TE show that there is little effect on either scattering mode.

Additionally, the effect of increasing pin period can be seen in Fig. 4.14. There is a fairly narrow operating band at the presented frequency range where periods of 12 to 16 mm offer the greatest reduction in specular scatter, shown by the null in $\hat{r}(0,0)$, with energy redirected into the grating lobe in $\hat{r}(-1,0)$.

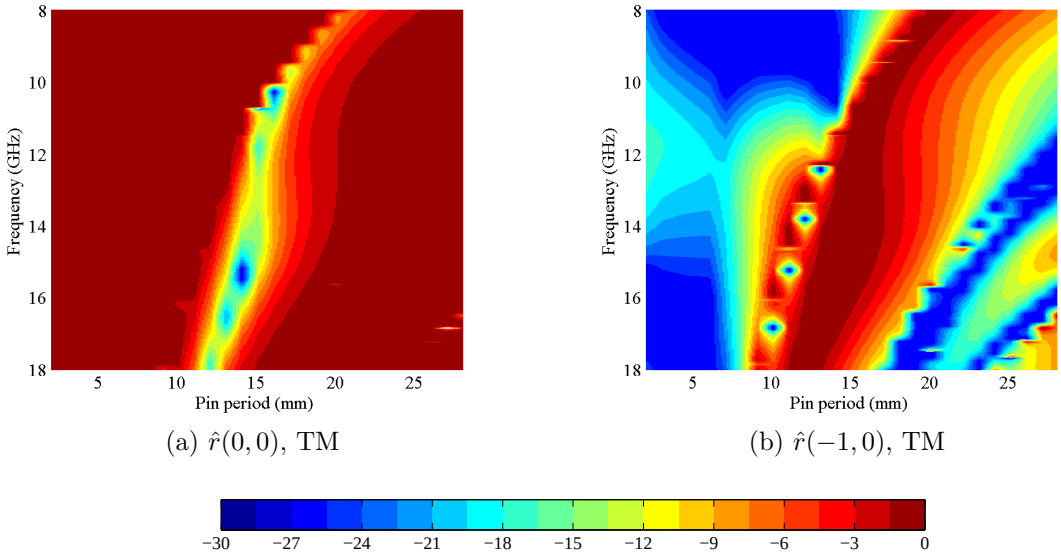

(a) $\hat{r}(0,0)$, TM

(b) $\hat{r}(-1,0)$, TM

Figure 4.14: S-parameter (dB) results for a range of pin periods for the principle direction $\hat{r}(0,0)$ and higher-order propagating mode $\hat{r}(-1,0)$ for $\theta_i = 50°$, pin height 15 mm, and thickness 1.6 mm. Results for TE show that there is little effect on either scattering mode.

4.11 Conclusions

This section has proposed the use of a PR-FSS for the purpose of reducing specular reflections. The initial development of the surface stemmed from the poor performance of the CR-FSS at $\phi_i = 90°$ and the necessity for a surface that was rotationally symmetrical. Initial analysis showed that a pin separation equal to the period was possible, with the reduction in performance not as large as anticipated.

An aluminium surface was constructed for testing, with a 39×39 array of screws secured into a 600 mm^2 ground plane. Simplifications for CST modelling were made using rectangular pegs instead of the screw shape used in the aluminium surface. Measurements and simulations show good agreement, for a range of angles of incidence, however the angular stability of the PR-FSS is questionable due to large peaks at unwanted frequencies. The fact that the surface is not very stable across a wide range of angles of incidence means that it could well be unsuitable for indoor propagation reduction where only one frequency range is to be prevented from propagating.

Even though the rotational symmetry solves the issue proposed in the previous chapter, the pin surface is ineffectual for TE polarisation, making it less useful in multipath environments, such as the corridor application suggested in this Thesis.

Furthermore, simulations show that to work at its optimum performance, the height of the PR-FSS is similar to the period, as with the CR-FSS. This means that at lower frequencies the height is still an issue in indoor applications, where it must fit inside small corridor cavities comfortably.

Chapter 5

Slanted-Comb FSS

At frequencies more commonly used for in-building communications (such as 2.4 GHz), surface parameters are scaled, making them much larger and potentially large element heights could cause issue with installation in narrow wall cavities. To understand potential issues that this could cause, slanting of the comb surface is investigated in order to reduce the effective structure height. Once again, simulation results and measurement of a brass prototype show the surface could be effective at reducing specular scatter, even when slanted at different angles.

5.1 Introduction

This chapter investigates the use of a slanted comb frequency selective surface (SC-FSS) to reduce specular scatter and are variations of the comb surfaces reported in chapter 3 . Various parameters of the CR-FSS such as height and period become much larger when scaled to be optimised to 2.4 GHz (which has a half wavelength of 62.5 mm). In real-life application this could require an insulation with a large height profile, possibly causing issue with installation in some corridors. Reducing the fin height negatively effects the reduction in specular scatter at the required frequency thus, the effect of slanting the combs is investigated. To examine the performance of the SC-FSS, a variety of simulations and experimental measurements are conducted.

A variety of simulation results are used to characterise the surface performance. The frequency response for both TE and TM polarisation is simulated for a range of angles of incidence. For each angle of incidence, a range of slant angles is to be simulated. The scattering patterns for the whole range of slant angles is presented

at various frequencies, and the effect of alternately slanting the periodic surface is presented. Measurements of a brass surface are used to understand potential problems with production, and validate simulation results. Full scattering measurements are conducted on the bi-static measurement system.

5.2 Simulation set-up

Simulations in CST Microwave Studio (MWS) have previously shown that periodic structures can be accurately modelled and compared to measurements. Slanting structures offer a greater deal of complexity when simulated in the time domain due to the use of hexahedral mesh. This means that slanted structures dissect the mesh cells often forming staircase cells if too coarse. This thus requires the simulation environment to have many more mesh cells than simpler models of the CR-FSS and PR-FSS structures, increasing simulation time.

The SC-FSS could be modelled using perfectly electrical conducting (PEC) material, and was constructed using a ground plane and slanted fins, as shown in Fig. 5.1. There are various pre-defined parameters, including fin thickness, t = 1.6 mm, the period of the comb elements, α = 16 mm, and the slanted height of the surface, h_s = $h + \tan\theta_s$, where h = 15 mm and is the height before slanting. The retrospective slant angle is θ_s. A plane wave illumination was once again used, with the use of the time domain solver, electric and magnetic field probes, and far-field monitors at a range of frequencies.

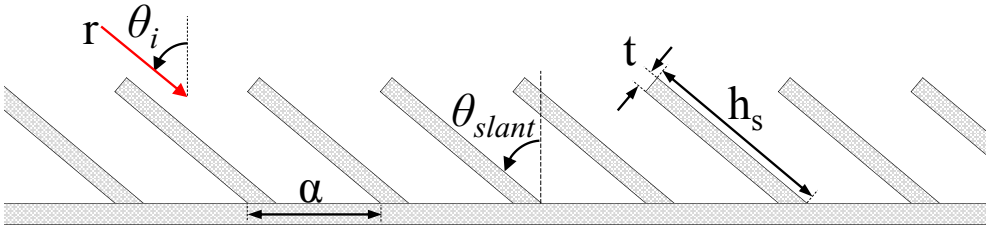

Figure 5.1: A slanted comb frequency selective surface (SC-FSS), with slant angle, θ_{slant} measured from the normal. The fin period, α, height, h_s and thickness, t are labelled. Also shown is the propagating wave, with angle of incidence, θ_i and propagation direction, r.

5.3 Simulation of comb slant angle

This section will present how the frequency response for both TE and TM polarisation changes when the surface fins are gradually slanted. An initial angle of incidence of 50° is used, with a further set of simulations for TM polarisation at 60°. The slant angle ranges from 0° to 90° in 5° steps.

5.3.1 Frequency response at θ_i of 50° - TM polarisation

Due to the quantity of simulated results obtained, the remainder of this section is split into further sub-sections, denoting the frequency response at 50° for TM and TE polarisation between 9 and 18 GHz.

The reduction in specular scatter for a variety of different slant angles is presented in Figs. 5.2 to 5.5. Incremental steps in slant angle were simulated, with an electric field probe positioned at the specular scatter angle. In this case, the plane wave was TM polarised and had an angle of incidence, θ_i of 50°. Compared to the CR-FSS (when $\theta_{slant} = 0°$), the SC-FSS has much more harmonic response, regardless of θ_{slant}. For example, in Fig. 5.2 at 13.5 GHz, a SC-FSS with $\theta_{slant} = 20°$ has worse performance compared to $\theta_{slant} = 0°$. That is, there is a difference in reduction in specular scatter of 21 dB (from -26 dB to -5 dB.)

As the slant angle is increased initially ($0° < \theta_{slant} < 20°$), large harmonics are introduced and the performance over the majority of the original working frequency range deteriorates. By $\theta_{slant} = 25°$, performance is particularly poor and a the -6 dB bandwidth lies between 10.8 GHz and 12 GHz. The peak reduction is only -12 dB at this slant angle, compared to -25 dB for $\theta_{slant} = 0°$. Interestingly for $\theta_{slant} > 45°$, the -6 dB bandwidth increases beyond the simulated frequency range. Further investigation showed that the stop frequency for those slant angles extending past the plotted values was between 19 and 20 GHz, so the response was not extended greatly. Obvious peaks in harmonics for $\theta_{slant} = 55°$, 60°, 65°, and 75° occur at 13.5, 15, 15.9, and 16.6 GHz respectively.

The additional harmonics introduced by slanting the comb structure have the effect of increasing the bandwidth of the response.

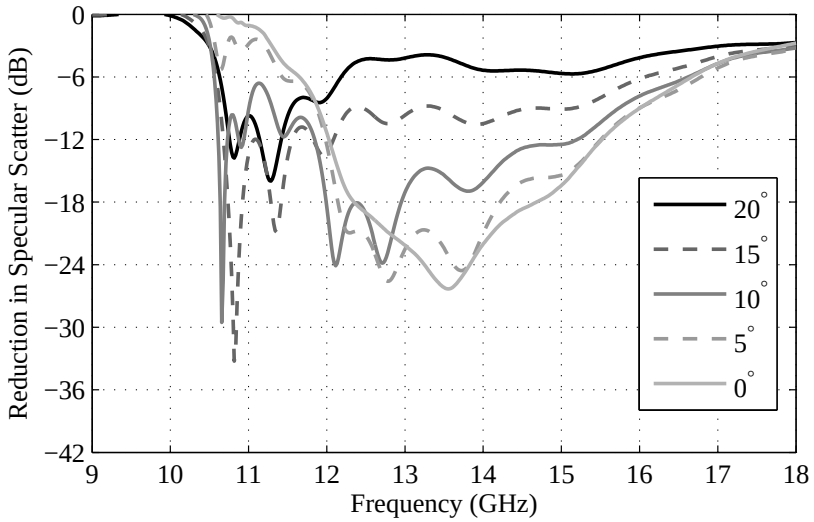

Figure 5.2: Normalised reduction in specular scatter for a slanted FSS with $\theta_{slant} = 20°$ to $0°$ for $\theta_i = 50°$ and TM polarisation.

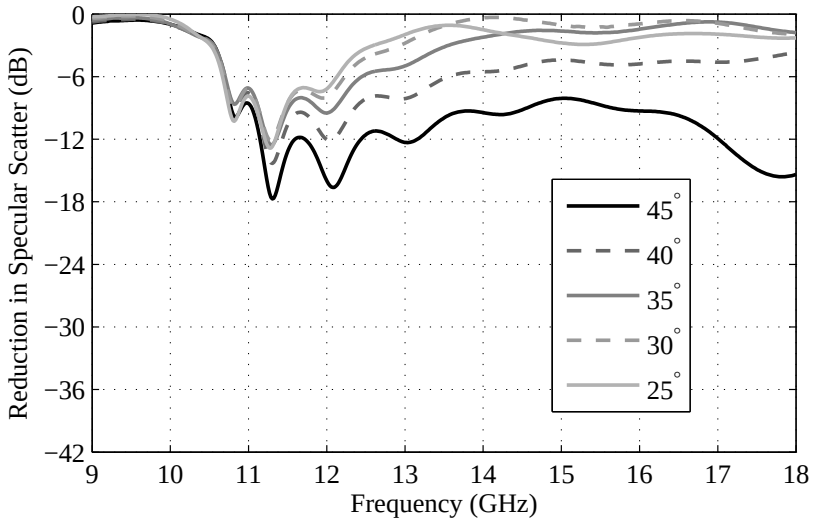

Figure 5.3: Normalised reduction in specular scatter for a slanted FSS with $\theta_{slant} = 45°$ to $25°$ for $\theta_i = 50°$ and TM polarisation.

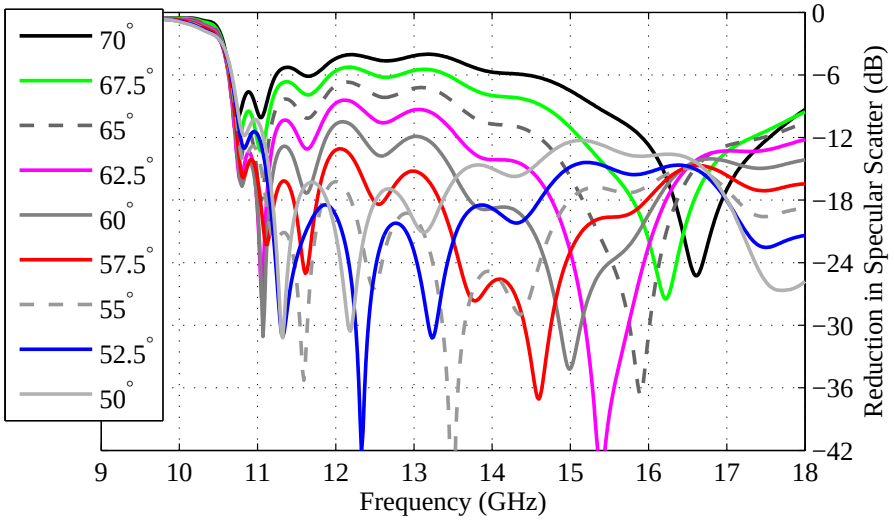

Figure 5.4: Normalised reduction in specular scatter for a slanted FSS with $\theta_{slant} = 70°$ to $50°$ for $\theta_i = 50°$ and TM polarisation.

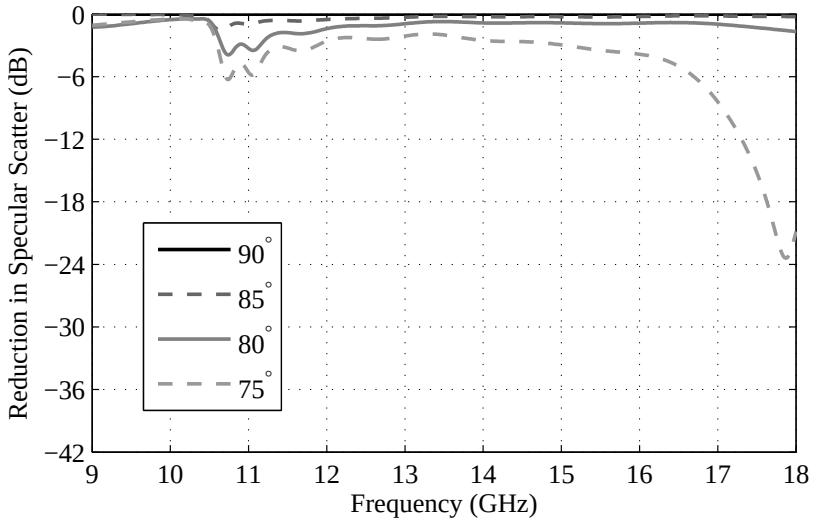

Figure 5.5: Normalised reduction in specular scatter for a slanted FSS with $\theta_{slant} = 90°$ to $75°$ for $\theta_i = 50°$ and TM polarisation.

5.3.2 Frequency response at θ_i of 50° - TE polarisation

For a 50° TE polarization plane wave, the change in frequency response is more clear. As the slant angle is increased, the harmonic frequency increases and the performance of the surface decreased. The response also becomes more broadband when compared to the CR-FSS ($\theta_{slant} = 0°$). The full range of responses can be seen in Fig. 5.6 to 5.9

Although the peak reduction does decrease as slant angle increases, the performance for θ_{slant} =50° is still reasonable in that the reduction in specular scatter is still nearly 12 dB. However, the peak frequency at which this occurs is at 16 GHz - a considerable shift in frequency.

As the electric field is perpendicular to the direction of propagation, an increase in slant angle is similar to a reduction in fin height. Both cases result in a similar increase in resonant peak, and this is highlighted in Chapter 7 in Fig. 7.3.

Finally, for extreme slant angles, such as those shown in Fig. 5.9, there is no reduction in specular scatter up to 18 GHz.

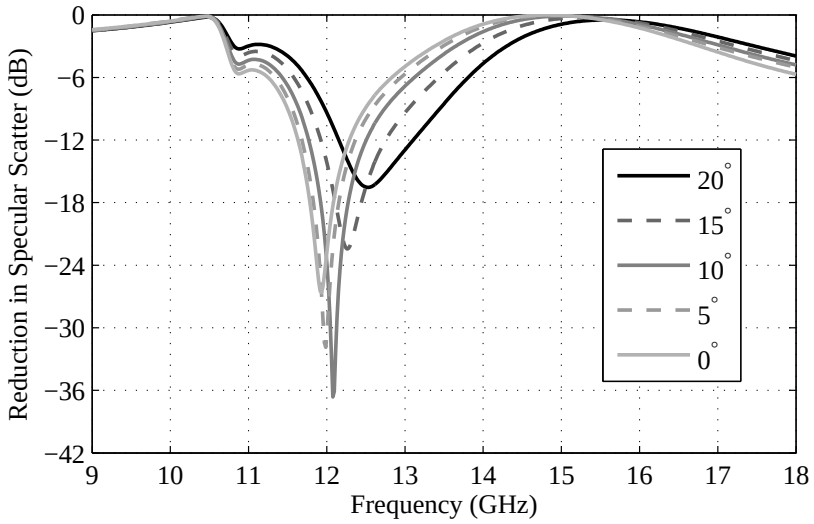

Figure 5.6: Normalised reduction in specular scatter for a slanted FSS with $\theta_{slant} = 20°$ to $0°$ for $\theta_i = 50°$ and TE polarisation.

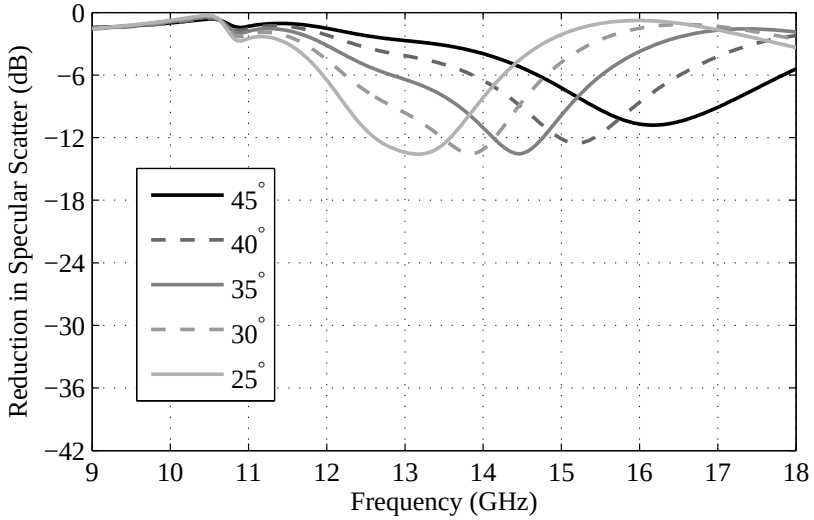

Figure 5.7: Normalised reduction in specular scatter for a slanted FSS with $\theta_{slant} = 45°$ to $25°$ for $\theta_i = 50°$ and TE polarisation.

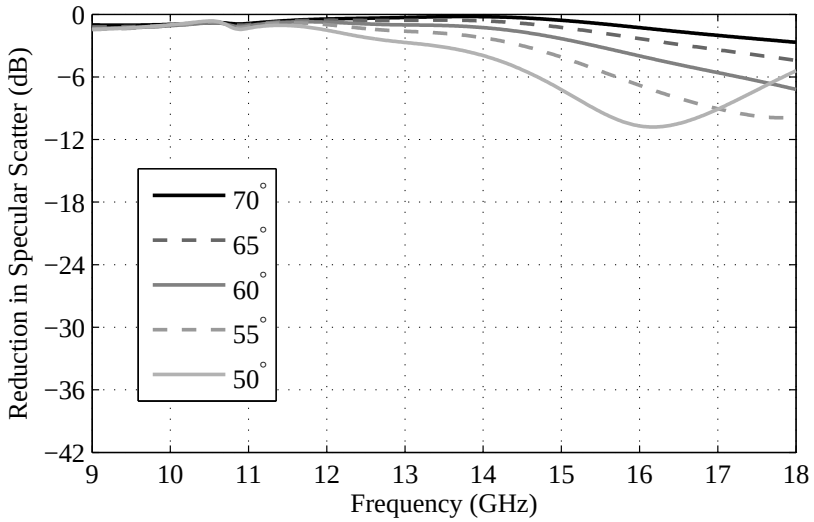

Figure 5.8: Normalised reduction in specular scatter for a slanted FSS with $\theta_{slant} = 70°$ to $50°$ for $\theta_i = 50°$ and TE polarisation.

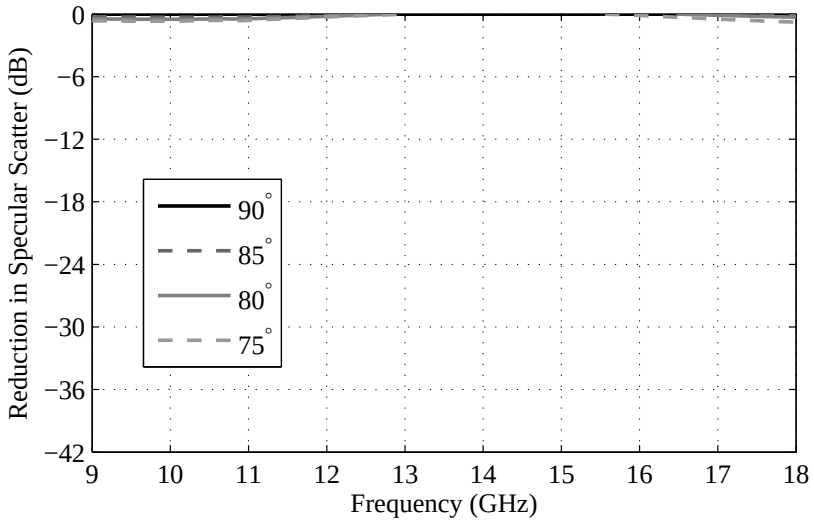

Figure 5.9: Normalised reduction in specular scatter for a slanted FSS with $\theta_{slant} = 90°$ to $75°$ for $\theta_i = 50°$ and TE polarisation.

5.3.3 Frequency response at θ_i of 60° - TM polarisation

Furthermore, a sweep of slant angles for an angle of incidence of 60° for TM polarisation was completed. The reduction in specular scatter for a variety of different slant angles is presented in Fig. 5.10 to 5.13.

The results at this angle of incidence are similar to those at 50°, where the intiail slanting seen in Fig. 5.10 decreases the performance between 12 and 17 GHz, whilst increasing between 10 and 12 GHz. Performance continues to decrease in Fig. 5.11 until the second harmonic appears in Fig. 5.12, at approximately $\theta_{slant} = 60°$.

When the combs are nearly parallel with the ground plane in Fig. 5.13, i.e. $\theta_{slant} \approx 80°$, the specular scatter reduction is zero once again.

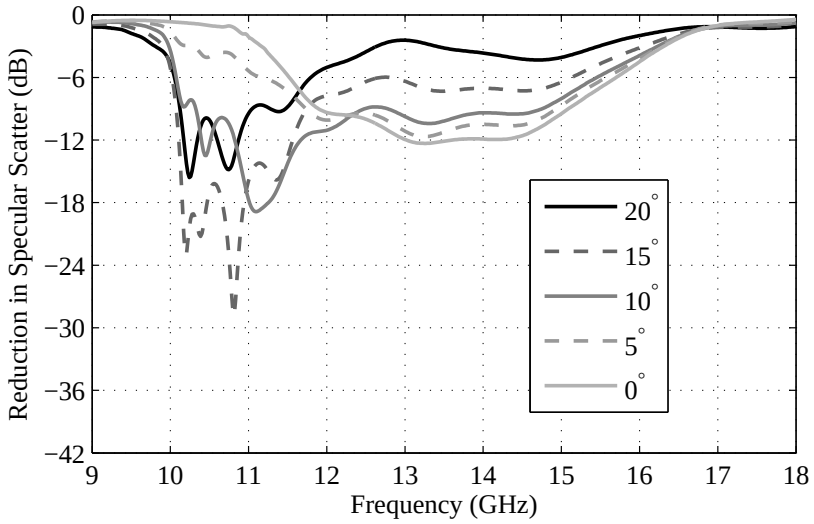

Figure 5.10: Normalised reduction in specular scatter for a slanted FSS with $\theta_{slant} = 20°$ to $0°$ for $\theta_i = 60°$ and TM polarisation.

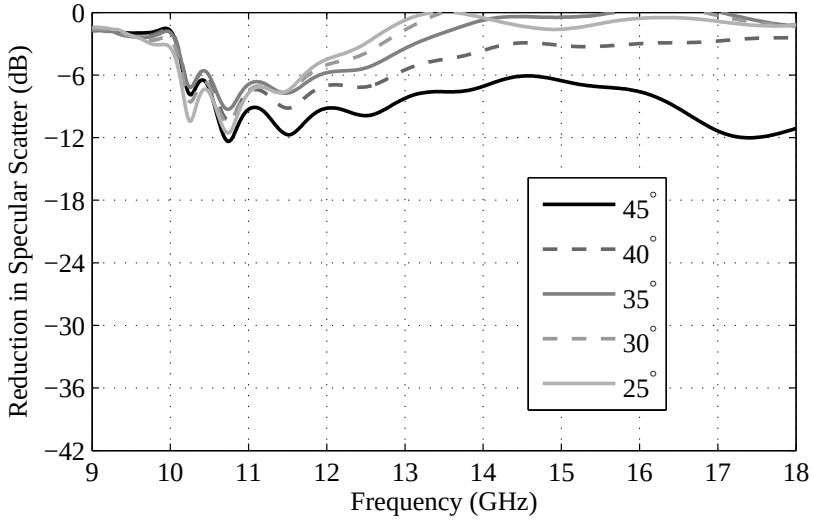

Figure 5.11: Normalised reduction in specular scatter for a slanted FSS with $\theta_{slant} = 45°$ to $25°$ for $\theta_i = 60°$ and TM polarisation.

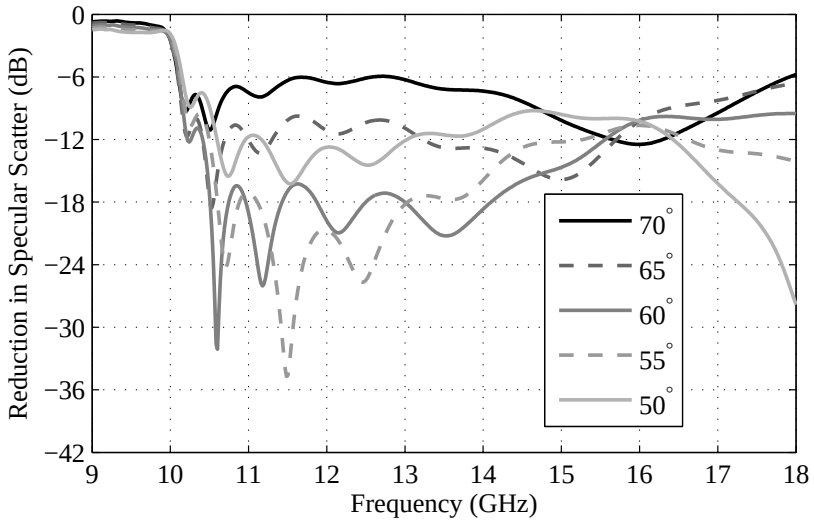

Figure 5.12: Normalised reduction in specular scatter for a slanted FSS with $\theta_{slant} = 70°$ to $50°$ for $\theta_i = 60°$ and TM polarisation.

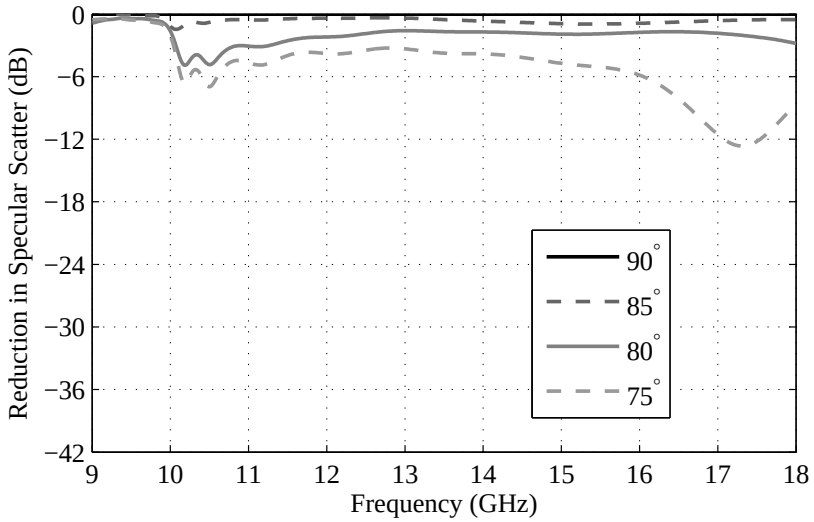

Figure 5.13: Normalised reduction in specular scatter for a slanted FSS with $\theta_{slant} = 90°$ to $75°$ for $\theta_i = 60°$ and TM polarisation.

5.3.4 Variation of slant angle on scattering

The performance of the SC-FSS at 15 GHz and 16 GHz is further investigated and simulation results are illustrated in Fig. 5.14 for a TM polarized wave at $\theta_i = 50°$. Far-field scattering results show the level of backscatter (negative scattering angles) and specular scatter (positive scattering angles). The slant angle, and scattering angle axes have a resolution of 5° and 1° respectively. In Fig. 5.14 , the scattering characteristics of a flat plate are the same as a SC-FSS with $\theta_s = \pm 90°$. This is because the fins are parallel to the ground plane.

The scattering graph at a frequency of 15 GHz is shown in Fig. 5.14a for an angle of incidence of 50°. The direct specular scatter is clearly seen at $\theta_s = 50°$, and the backscatter at 28°. For a SC-FSS with $\theta_{slant} = \pm 60°$ similar performance can be achieved compared to a CR-FSS ($\theta_{slant} = 0°$). That is, similar levels of reduction in specular scatter and increase in backscatter can be maintained, despite the SC-FSS being slanted by 60°. For 16 GHz, $\theta_{slant} = \pm 65°$ offers the largest reduction in specular scatter, as previously noted in Figs. 5.4. At this frequency, the peak in backscatter has also shifted to $\theta_s = -24°$.

This analysis shows the problems associated with choosing slant angle of the comb depending on frequency of interest, for optimum performance of the structure compared to a CR-FSS. Even slight inaccuracies in choosing slant angle can have detrimental effects on the reduction in specular scatter magnitude.

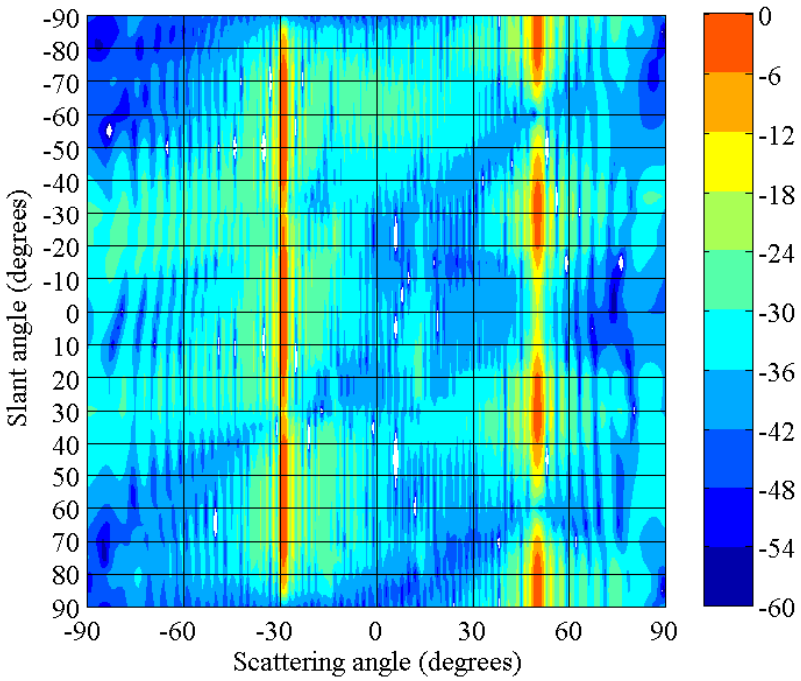

(a) 15 GHz

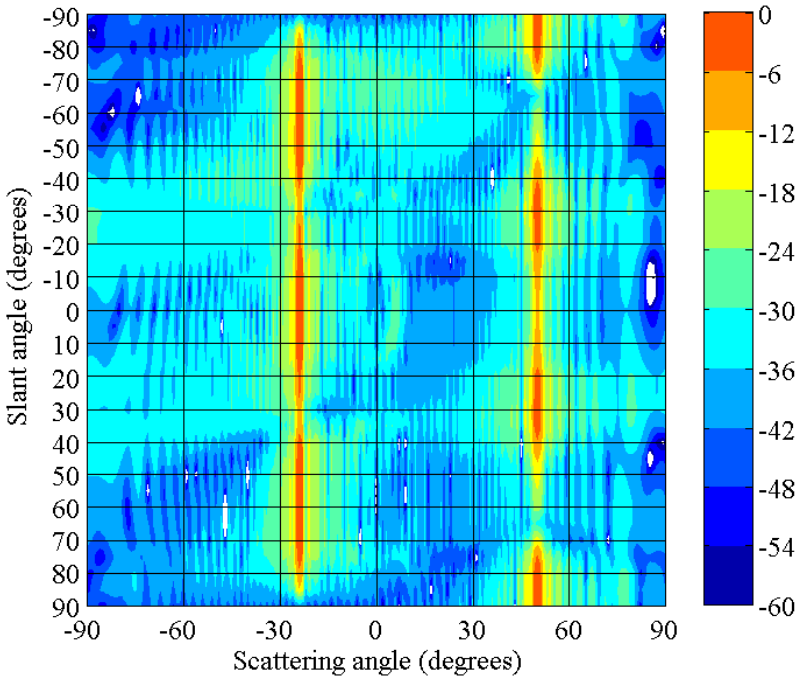

(b) 16 GHz

Figure 5.14: The effects of slant angle on scattering performance, finding the optimum slant angle for frequencies of (a) 15 GHz and (b) 16 GHz.

5.3.5 Far-field scattering patterns

In this section, a brief analysis of the scattering patterns for a slanted comb frequency selective surface (SC-FSS) is given. The far-field response at various frequencies is analysed. Figs. 5.16a, 5.16b and 5.16c show the far-field response of the SC-FSS with $\theta_{slant} = 55°$, compared to a flat PEC surface for frequencies of 10 GHz, 13.5 GHz and 17 GHz respectively.

The reduction in specular scatter magnitude is shown in Fig. 5.15 (reproduced from Fig. 5.4), where there is a wide -6 dB frequency range starting from 10.8 GHz to more than 18 GHz. Thus, at a frequency of 10 GHz, there is no reduction in specular scatter and no signal is re-directed as backscatter, as shown in Fig. 5.16a.

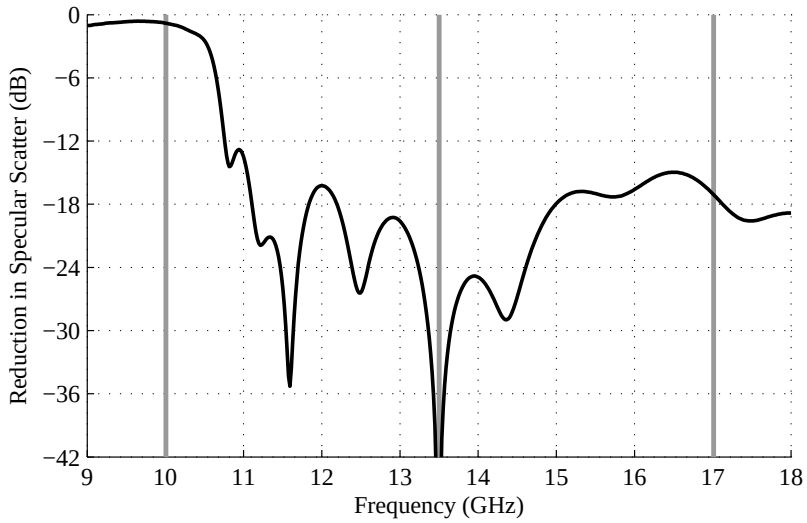

Figure 5.15: Simulated frequency plot for a 55° slanted FSS, for $\theta_i = 50°$.

The far-field scattering pattern at 13.5 GHz in Fig. 5.16b shows complete suppression of the specular scatter. This is re-directed to the backscatter region at -40°. Similarly, there is a -18 dB reduction at 17 GHz, seen in Fig. 5.16c. As the frequency is increased, the backscatter angle changes to approximately -20°.

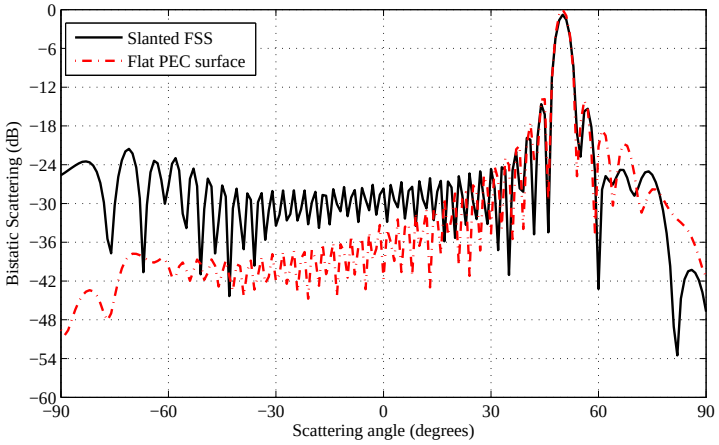

(a) $f = 10$ GHz.

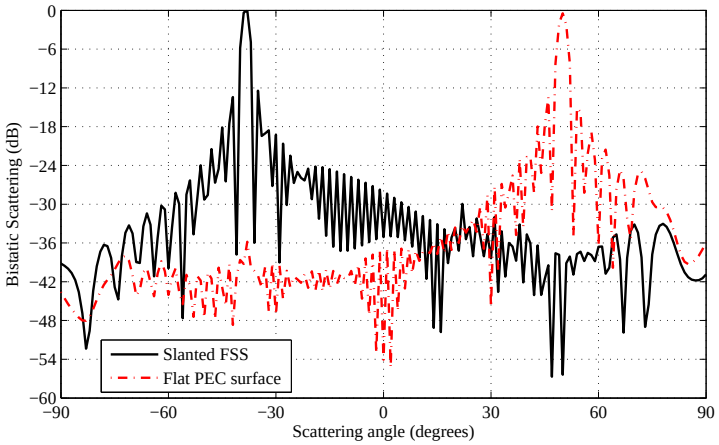

(b) $f = 13.5$ GHz.

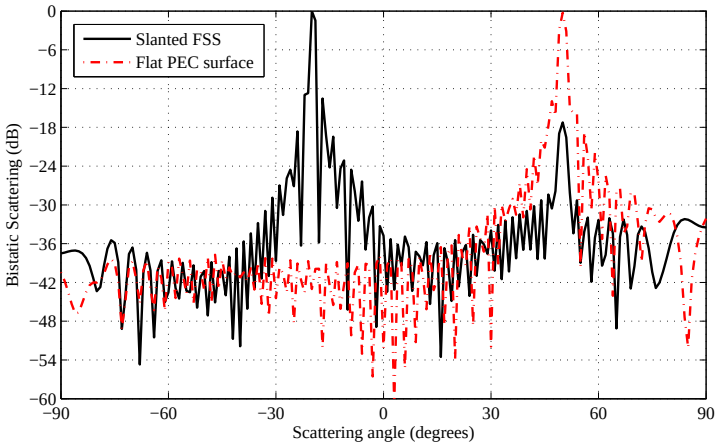

(c) $f = 17$ GHz.

Figure 5.16: Simulated far-field scattering patterns for a 55° slanted FSS, for $\theta_i = 50°$ and TM polarisation at various frequencies.

5.4 Alternate periodic surface

It can be concluded from the initial simulations that the SC-FSS can offer acceptable levels of reduction in specular scatter depending on frequency and slant angle, particularly for TM polarization. Further investigation on alternately slanted fins reveal some interesting scattering features. The alternate slanting of fins is shown in Fig. 5.17, where the angle of slanting varies between θ_{slant} and $\theta_{slant(2)}$. The purpose of this section is to understand how providing variably slanted elements can affect both the specular scatter and backscatter properties of an incident plane wave. Initially, CST simulations are used to provide scattering characteristics for TM polarization. This is because TE polarized signals exhibit a poor performance between the frequency range of interest for slant angles greater than 50°.

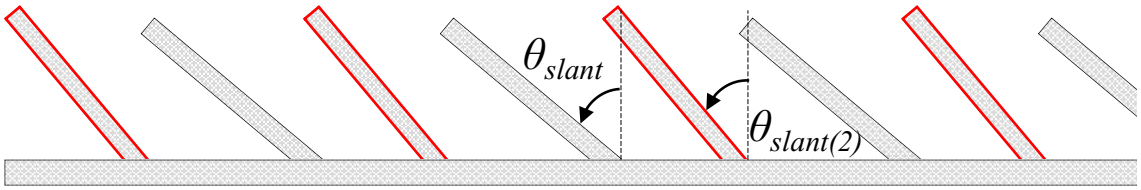

Figure 5.17: Asymmetrical combs can introduce significant changes into scattering patterns and frequency responses. The fins highlighted with a bold outline have been moved at a separate slant angle to the others.

The initial simulation result for $\theta_{slant} = 50°$ is shown in Fig. 5.18a, where there is one grating lobe between 5 and 18 GHz for scattering angles, $\theta_s = -70°$ and $-20°$. For the angle of direct backscatter ($-50°$), the grating lobe occurs at 12.2 GHz, as suggested by both results in Fig. 5.18a and 5.18b. There is also a large region of reduction in specular scatter, with at least 10 dB between 10.6 GHz to more than 18 GHz.

Alternately slanting the comb structure can have effects on the number of backscatter lobes and the specular scatter reduction range. In this case, two variations are investigated: (1) $\theta_{slant} = 50°$ and $\theta_{slant(2)} = 40°$ and (2) $\theta_{slant} = 50°$ and $\theta_{slant(2)} = 0°$. These represent both small and large differences in θ_{slant} and $\theta_{slant(2)}$. The slight change in slant angle for case (1) reveals emerging secondary and tertiary backscat-

ter lobes at 6.1 GHz and slightly greater than 18 GHz respectively, as shown in Fig. 5.18d. These are both visible in Fig. 5.18c. The specular scatter reduction is affected, particularly between 10.8 and 13 GHz, where the level of reduction is less than for the uniformly slanted surface between this range.

Further reduction of $\theta_{slant(2)}$ to 0° results in backscatter harmonics with comparable magnitude to the original backscatter lobe at 6.1 GHz. The elements slanted at $\theta_{slant(2)} = 0°$ become completely vertical. Results are shown in Fig. 5.18e and Fig. 5.18f. Despite the change in slant angles, the position of the grating lobes does not change, however there is an increase in backscatter level for case (2). The secondary grating lobe at 6.1 GHz is only 6 dB lower in magnitude than the initial one. The level of the tertiary lobe cannot be quantified, however the side lobes at between 17 and 18 GHz are of similar magnitude to the primary grating lobe. For case (2) there is also a reduction in specular scatter between 5 and 10 GHz, peaking at 30 dB reduction at 8.2 GHz.

By switching between continuous and alternating slant angles, simulations have shown that a secondary frequency region in which specular scatter is reduced can be exploited. Secondary and tertiary grating lobes can be introduced by using alternating slant angles, increasing the amount of signal in the backscatter region between 5 and 18 GHz.

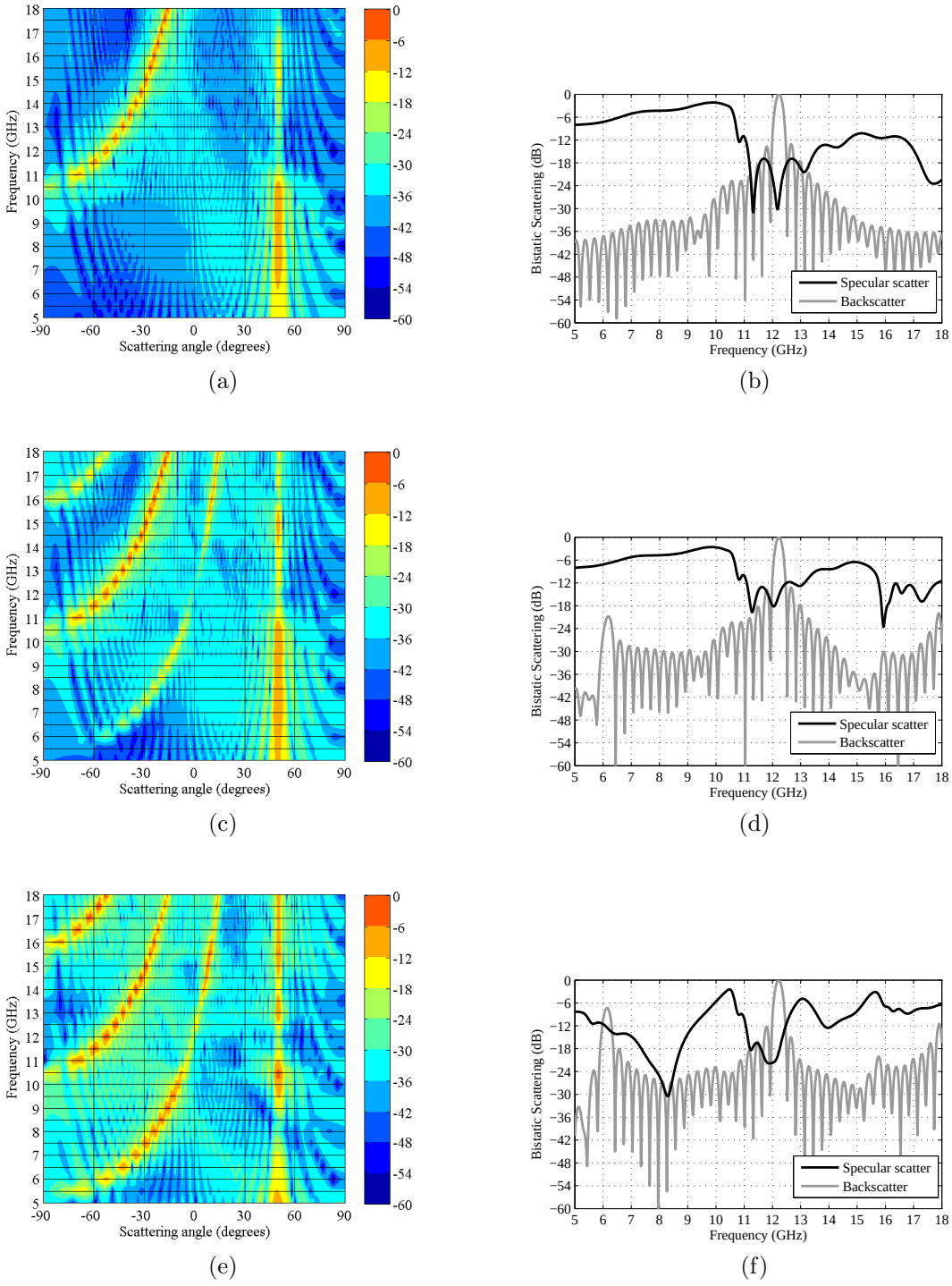

Figure 5.18: Frequency versus scattering angle plots and graphs showing specular and backscatter frequency ranges for and SC-FSS with (a and b) $\theta_{slant} = 50°$, and asymmetrical SC-FSS with (c and d) 50° and 40° and (e and f) 50° and 0°.

5.5 Experimental measurement

Compared to the previous two surfaces (the CR-FSS and PR-FSS) the SC-FSS proved more difficult to manufacture and the comb elements were troublesome to align. Due to the potential expense of the material cost and manufacture, there were limited options for production. The cheapest method was to produce a number of small brass fins which were to be connected to a large ground plane. As with previous surfaces, the ground plane measured 600×600 mm^2. Both the fins and ground plane were made from brass.

Figure 5.19: Experimental brass surface used for testing and validation of simulations.

Each fin measured 16 mm in height, 1 mm in thickness, and 600 mm in width. The period of the surface (16 mm) was manually marked out and each fin retrospectively secured using conductive tape. The final surface is shown in Fig. 5.19. By using a flexible connection, the slant angle of each fin could be altered and set using templates, as shown in Fig. 5.20.

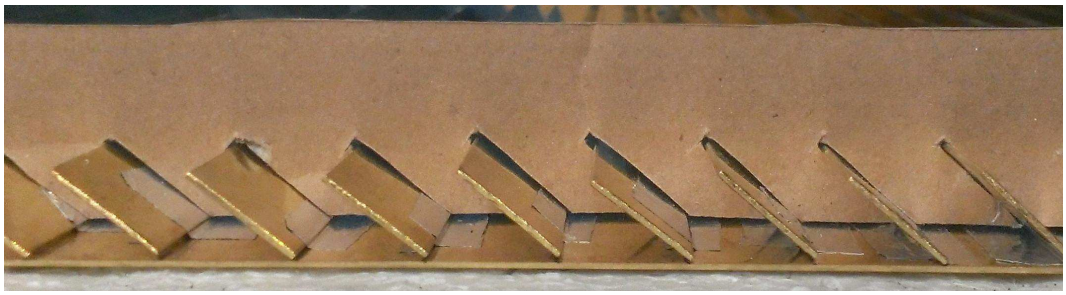

Figure 5.20: Experimental brass surface used for testing and validation of simulations.

5.5.1 Angular measurements

The specular scatter from the SC-FSS was measured compared to a flat plate, with the differences in magnitudes for TE and TM polarisation plotted in Fig. 5.21. The measurement results are compared to simulations, where it is shown that the correlation is much less than for the previous ones completed in chapters 3 and 4 for the CR-FSS and PR-FSS respectively. Three angles of incidence were measured: 40°, 50°, and 60°.

For TE polarisation, there is a definitive peak reduction between approximately 12 and 14.5 GHz for the three angles of incidence measured. These results show similarities with the simulations in Fig. 5.7, where the slant angle is between 25° to 45°. This response is as expected for TE polarisation, although the harmonic frequency has shifted. This could have been caused by the template being inaccurate, where the fins are able to rotate more than 50°, possibly to 40°-45°. Furthermore, some of the elements were not straight which caused the periodicity in some areas of the surface to not be as expected.

For TM polarisation, the response is a little more difficult to analyse. What is evidents is that depending on angle of incidence, the greatest reduction seems to be in different frequency bands. As the response at 40° seems most like simulations, it is likely that inaccuracies in the NRL arch at the highest angles of incidence are effecting results.

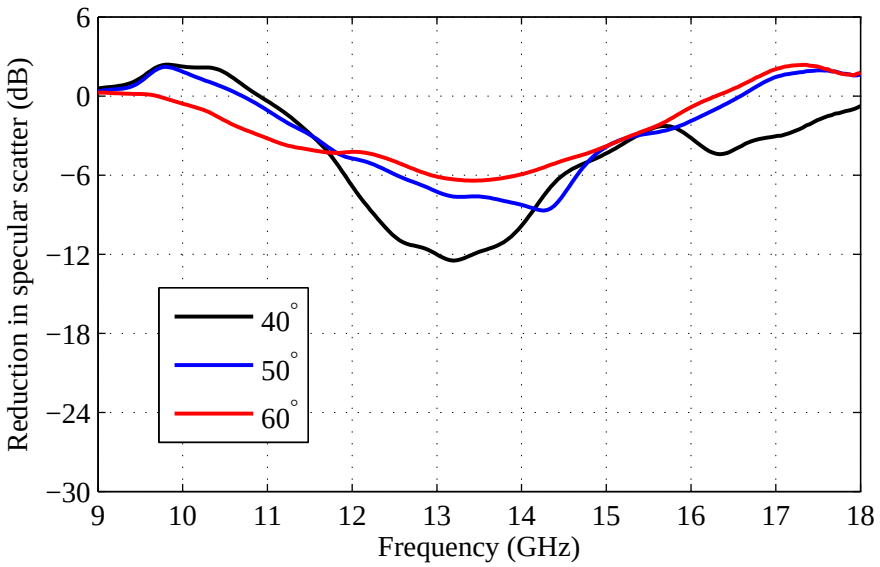

(a) TE polarisation

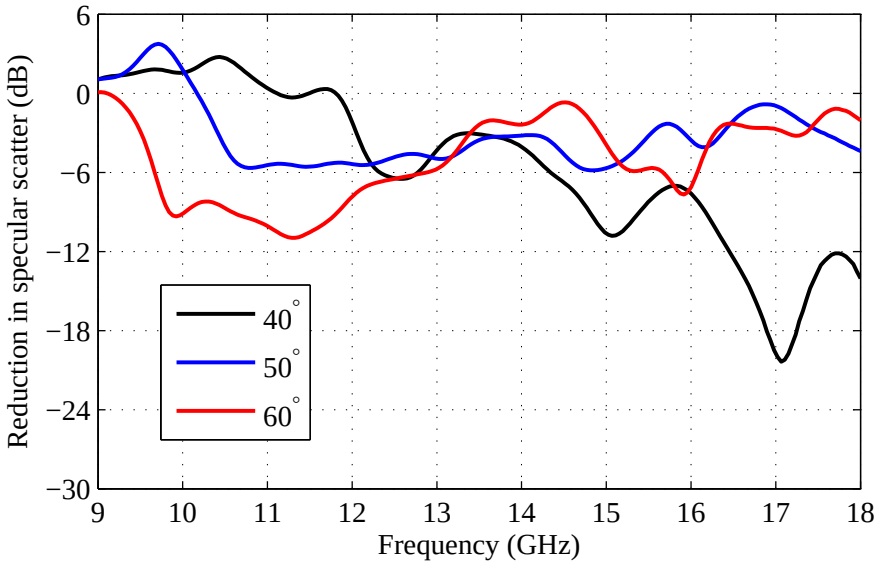

(b) TM polarisation

Figure 5.21: Measured frequency response of the SC-FSS with $\theta_{slant} = 50°$ for a range of angles of incidence for (a) TE and (b) TM polarisation.

5.5.2 Measured scattering plots

As simulated scattering plots have already been analysed for both symmetrical and asymmetrical slanted surfaces, measurements of the surfaces are conducted for comparison. Scattering measurements were completed using the bi-static measurement, and results for both TE and TM polarisation are presented in Figs. 5.22 and 5.23 respectively. For comparison, both flat plate and SC-FSS measurements were conducted.

The angle of incidence was 50°. As expected from Bragg's Law, the frequency of direct backscatter occurs at 12.2 GHz. That is, for a surface period of 16 mm, and angle of incidence of 50°, $f_B = 3 \times 10^8/(2 \times 0.016 \times \sin(50)) = 12.2$ GHz. As expected, there is a large reduction in specular scatter, although this is particularly visible for TM polarisation.

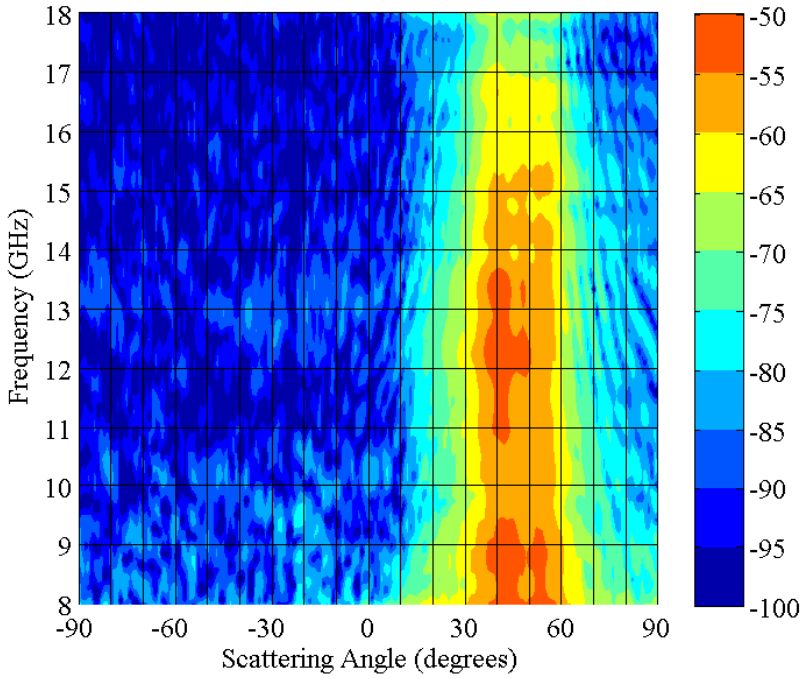

(a) Flat surface

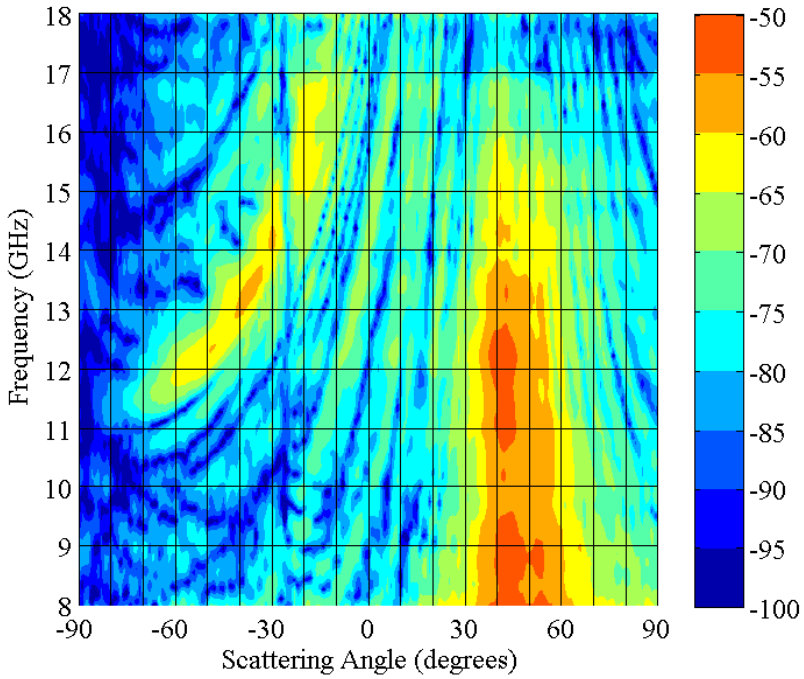

(b) Slanted-comb FSS

Figure 5.22: Measured scattering plots for TE polarisation.

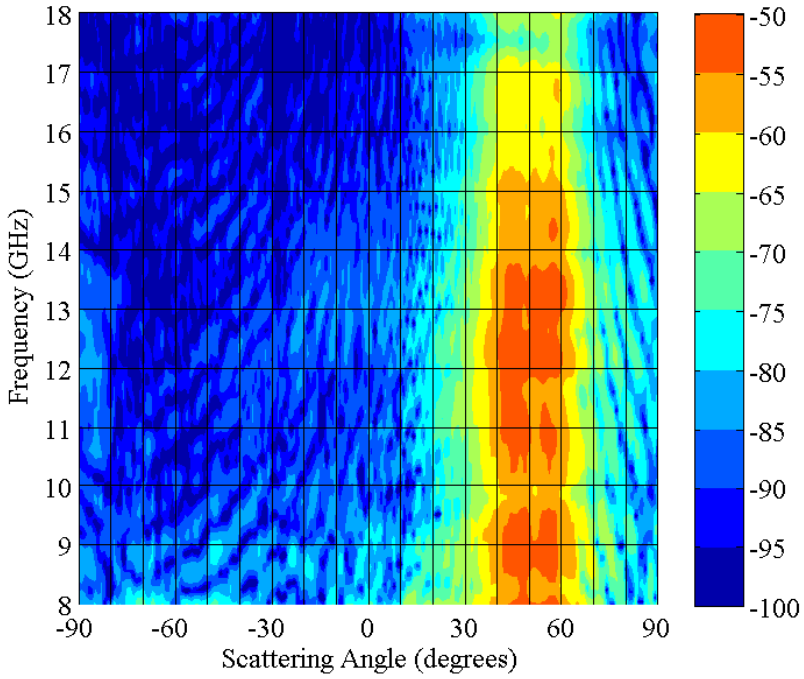

(a) Flat surface

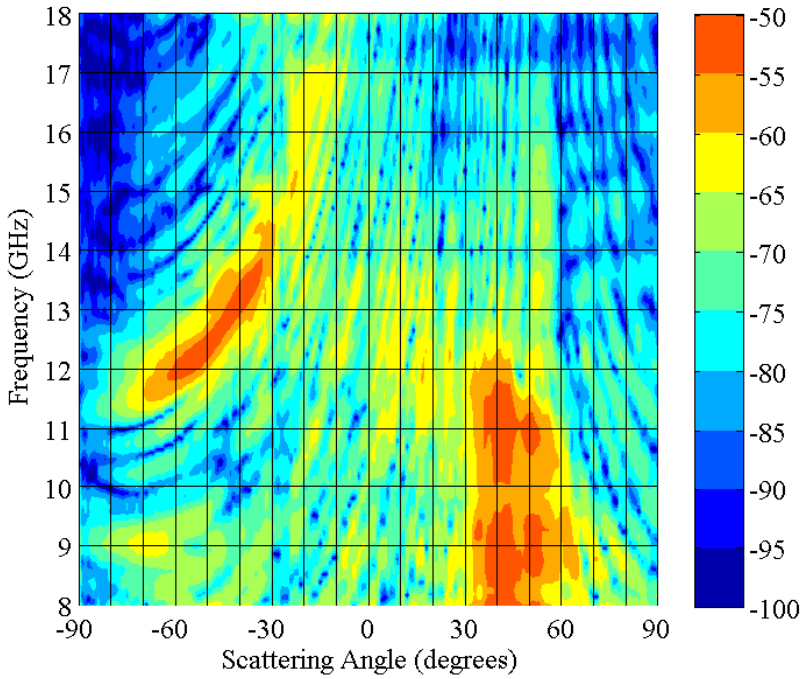

(b) Slanted-comb FSS

Figure 5.23: Measured scattering plots for TM polarisation.

5.6 SC-FSS floquet mode plots

The frequency domain analysis of the SC-FSS structures repeat the trends shown in the time domain simulations. A full sweep of slant angle was completed between 0° and 90°.

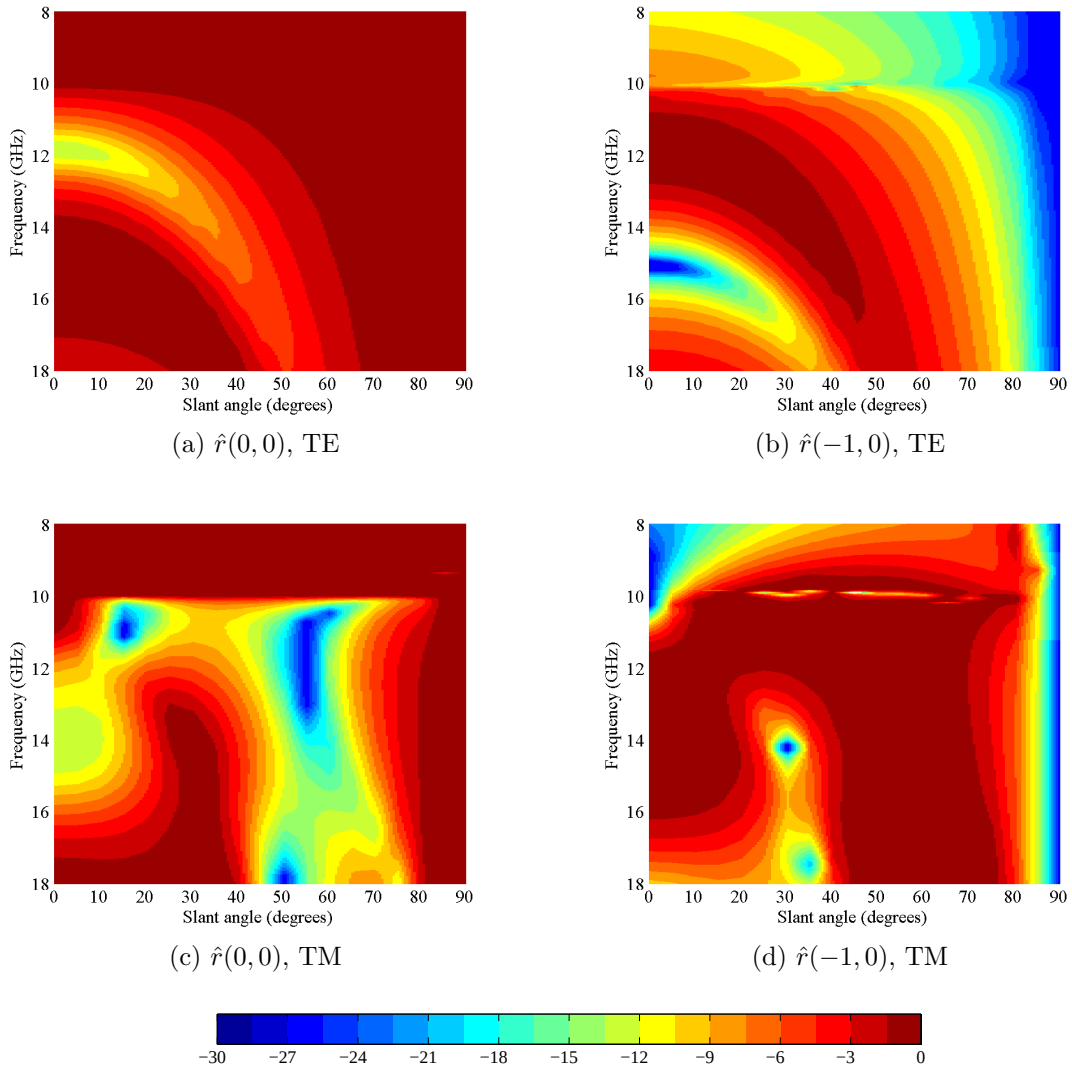

(a) $\hat{r}(0,0)$, TE

(b) $\hat{r}(-1,0)$, TE

(c) $\hat{r}(0,0)$, TM

(d) $\hat{r}(-1,0)$, TM

Figure 5.24: S-parameter (dB) results for a range of slant angles for the principle direction $\hat{r}(0,0)$ and higher-order propagating mode $\hat{r}(-1,0)$ for $\theta_i = 50°$.

Fig. 5.24 shows that the main specular scatter reduction increases in frequency as

the slant angle increases for TE polarisation. It also gets increasingly narrowband and the null depth is not as pronounced. Indeed, for large portions of the frequency band and for much of the slant angles, the structure reduces the specular scatter poorly compared to a flat plate.

For TM polarisation, the structure gets much broadband as the slant angle increases towards 55°. All of this energy is directed into the respective $\hat{r}(-1, 0)$ mode. The structure is particularly resonant for TM polarisation, where the E-field can be coupled into the slanted combs, offering a more resonant $\hat{r}(0, 0)$ mode response. For slant angles greater than 75° the structure becomes more like a flat ground plane and does not change the specular scatter.

5.7 Conclusions

In order to reduce the required surface height, but still offer adequate performance at the required frequency ranges, it was proposed that the comb elements be slanted. The effects of the specular and scattering patterns are simulated using the conventional techniques previously shown in the thesis. It has been shown that a SC-FSS can be used to offer sufficient specular reduction over a wide bandwidth, although the response often has unwanted harmonics.

A brass prototype is manufactured, with changeable slant angles for measurement for validation of simulations. Further simulations using frequency domain floquet analysis show that the structure is extremely resonant for TM polarisation and offers substitutional scattering reduction. In TE polarisation, the performance is much worse.

Chapter 6

Crenelated CR-FSS

This chapter prototypes the CR-FSS as a foam substrate lined with foil, similar in composition to metallic insulation building materials. Furthermore, the effect of the crenelation angle of the comb on the specular scatter is investigated. Both simulations and measurements are used to verify the frequency and scattering from the surfaces.

6.1 Introduction

This chapter investigates the use of crenelated CR-FSS for reducing specular reflections, but aims to solve a number of unanswered questions yet to have been considered in the previous chapters. Firstly, the prototype material of this surface differ from previous sections as materials that could be used for installation in a building structure are used to prototype the structures. Previously, the construction of prototype surfaces has been from metals such as aluminium and brass. These are expensive and do not reflect the proposed construction method in suggested applications such as those used as thermal insulation materials like Celotex [79]. It is therefore proposed that a foam-based substrate with a foil topping be used to create the crenelated structure.

As the strength of the foam substrate may be affected by using the existing vertical periodic elements, additional structure strength could be achieved using a crenelated design, as seen in Fig. 6.1. Sloping the comb elements could also help in the application of foils to the foam substrate, as discussed later in this chapter. Several foam substrates of various slope angles are accurately milled, with an example surface

shown in Fig. 6.2.

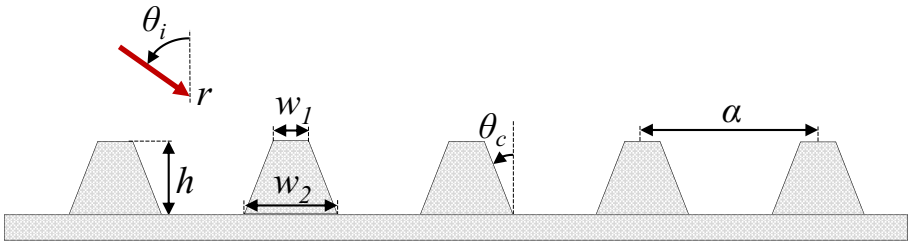

Figure 6.1: The crenelations in the foam are strengthened using sloped edges, with angle θ_c. The periodic elements have top width, w_1, bottom width, w_2 and height, h. The surfaces are illuminated with a plane wave with direction of propagation, r and angle of incidence of θ_i. The foam substrate is then lined with the metallic foil to produce the frequency selective surface.

6.2 Surface design considerations

6.2.1 Foam substrate manufacture

To compare with results presented in chapter 3, the foam elements were periodically spaced 16 mm apart. The top width of the foam substrate, w_1 is constant regardless of the slope angle, θ_c. As θ_c is increased the bottom width, w_2 increases. The height, h of each element is kept constant at 15 mm.

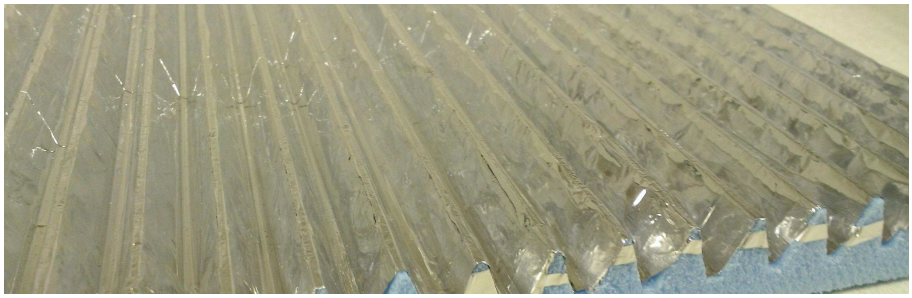

Figure 6.2: One of the foam prototypes, milled from foam with a foil reflective surface. In this case $\theta_c = 20°$ is shown. The foil is secured to the foam substrate using conductive tape.

Although the foam is accurately milled, the application of foil to the substrate

proved difficult and seemed to alter the frequency response of the measured surfaces compared to expected measurements. This was particularly the case for surfaces with $\theta_c = 0°$ and $10°$ as it was difficult to form the foil around $90°$ and $80°$ corners. This meant that once the manufactured surfaced had been foiled, the surface had thicker fins than expected, making w_1 variable, depending on the value of θ_c. Thus, the consequences of producing a surface with thicker elements are considered. Also, the accuracy of simulation models for crenelated surfaces is considered.

Finally, the use of smaller 300 mm^2 surfaces for measurement was investigated. The use of 600 mm^2 surfaces had previously been used in this Thesis. In measurement systems such as the NRL arch, there can be issues with edge diffractions if the surfaces under test are not comparably large to multiple numbers of wavelengths at the lowest frequency of interest. Although the use of 300 mm^2 surfaces have previously been reported on in literature [76], this chapter considers whether surface size adversely effects the measurement process by comparing the measured results with simulations.

6.2.2 Accuracy of simulation models

Simulation of such models has shown to produce an accurate prediction of previous surfaces, such as those in chapter 3–5. Initial simulations of the prototypes proved difficult to match to measured results due to the inaccuracies in expected parameters following the foiling process. As suggested previously, the unforeseen increase in the element thickness to surface period ratio during the foiling of the foam substrate effected the frequency response. Following accurate measurement of the prototypes, simulation models were updated and provide a more accurate comparison to respective prototypes. Simulation results reporting the initial expected response are shown in section 6.5.

The meshing used in CST required a PEC refinement of 9 to adequately model the crenelated structure. This meant there was an increase in mesh cells around the crenelated edges of the surface, compared to those in the free space around the structure. This simulation model had 5 million mesh cells, much more than previous simulations and thus increased total simulation time.

6.3 Experimental prototype and measurement

The prototyping of these surfaces differs from those reported in previous chapters, as they are precisely milled into a foam substrate with a metallic foil layer on top to form the periodic surface, as shown in Fig. 6.2. The periodic comb elements were milled into a square foam substrate measuring 300 mm on each side.

The specular scatter from each surface was measured using a Naval Research Laboratories (NRL) reflectivity arch. Two American Electronic Laboratories (AEL) H1498 wideband horn antennas were used to measure the reflected signal at an angle of incidence of 50°. An Agilent E8720 vector network analyser (VNA) was used to measure between a frequency of 8 and 18 GHz, with 401 discrete frequency points. A sweep time of 2 seconds was and time gating techniques were used to remove unwanted scattering and coupling from the final measurement.

The measured results for TE and TM polarisation are shown in Figs. 6.3a and 6.3b respectively. For TE polarisation the harmonic response diminishes as θ_c is increased. There seems to be no major shift in resonant frequency. For TM polarisation, the change in harmonic frequency is large, ranging from 12 GHz, to 14 GHz and finally to 16.5 GHz as θ_c is increased from 0° to 20°.

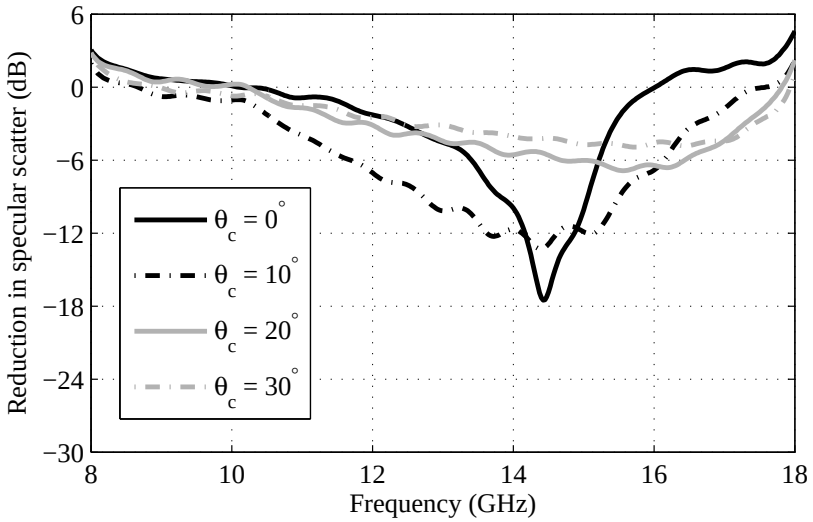

(a) TE polarisation

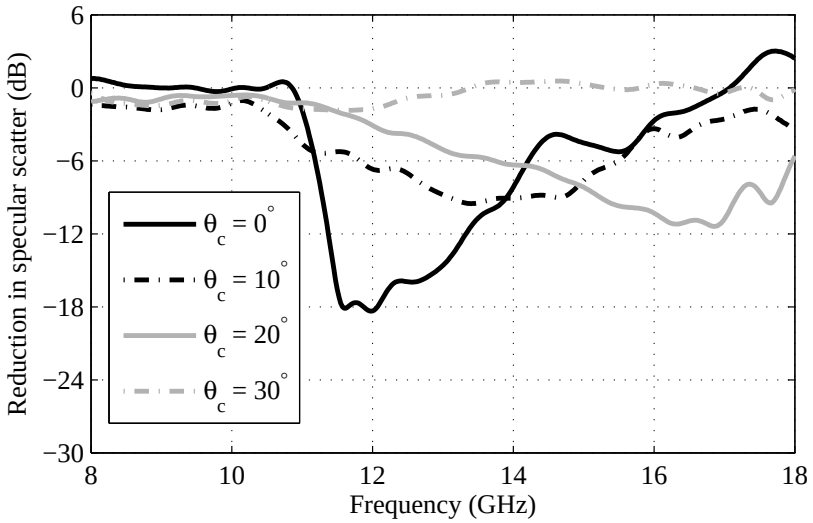

(b) TM polarisation

Figure 6.3: Measurements for corrugated surface with $\theta_c = 0°$, 10°, 20° and 30° for TE and TM polarisation, with $\theta_i = 50°$.

6.4 Simulations

As changing the physical structure of the comb surface is expected to alter the frequency response, this was initially investigated. Simulations of four slope angles were investigated using CST Microwave Studio, using the time domain solver. These were $\theta_c = 0°$, 10°, 20° and 30°, where $\theta_c = 0°$ represents a CR-FSS surface. Plane wave excitation with an angle of incidence, $\theta_i = 50°$ was used to illuminate a PEC periodic surface, using the time domain solver. Fine meshing was used to ensure a suitable representation of the sloped elements in the simulation model, as previously discussed. In each case the period, $\alpha = 16$ mm, and height, $h = 16$ mm were kept constant.

The results for TE and TM polarisation at $\theta_i = 50°$ are shown in Figs. 6.4a and 6.4b respectively. The w_1 width was 4.5 mm, 2.8 mm, 3 mm and 1.6 mm for $\theta_c = 0°$, 10°, 20° and 30° respectively. This was to compensate for the increase in thickness during coating of the foam substrate in reflective foil, and to provide accurate comparison to measurements. For TE polarisation similarity between the simulated and measured results in Figs. 6.4a and 6.3a is good, with the $\theta_c = 0°$ offering the best peak performance at 14.4 GHz, with reduction in specular scatter decreasing as the slant angle is increased. At $\theta_c = 10°$, the measured 6 dB bandwidth is actually larger as there is less of a harmonic response. There is little observable difference between the $\theta_c = 0°$ and 10° simulated results where the harmonic peak is still visible. Simulations and measurements for $\theta_c = 20°$ and 30° match well.

For TM polarisation, a comparison between simulated and measured results in Figs. 6.4b and 6.3b. A less than accurate match in reduction in the magnitude of specular scatter can be particularly seen for $\theta_c = 0°$ where the where the simulated peak harmonic at 12 GHz in Fig. 6.4a is nearly 12 dB lower than measured in Fig. 6.3a. The other simulated results show good correlation, although the harmonic at 15.5 GHz for $\theta_c = 10°$ is not as pronounced in measurements. Once again, simulations and measurements for $\theta_c = 20°$ and 30° correlate well.

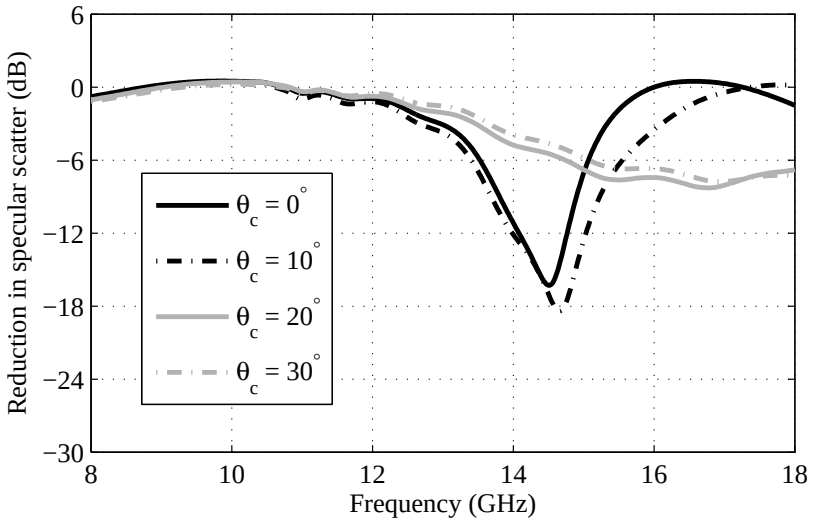

(a) TE polarisation

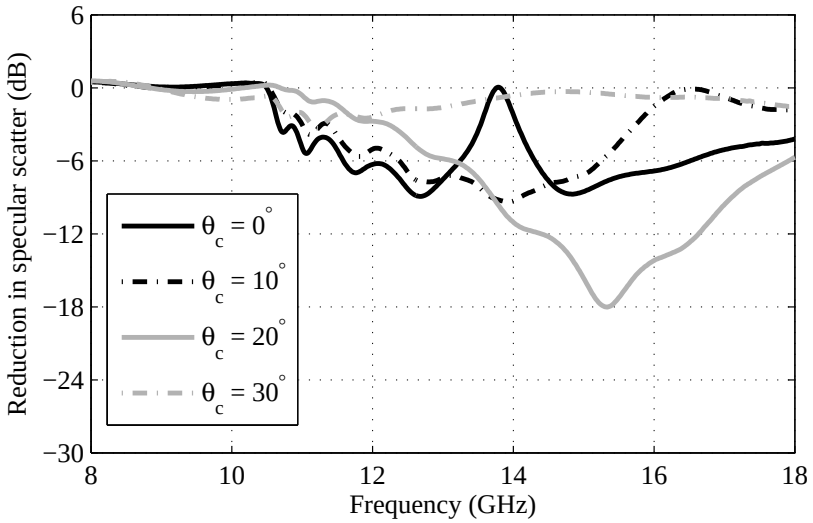

(b) TM polarisation

Figure 6.4: Simulations for corrugated surface with $\theta_c = 0°$, $10°$, $20°$ and $30°$ for TE and TM polarisation, with $\theta_i = 50°$.

6.5 Equal thickness simulations

Thus far, simulations have reflected the dimensions of the prototype surfaces to accurately show that the measurement results can be verified. However, it is also important to understand the trends of keeping the top thickness w_1 equal, whilst increasing the slope angle, θ_c, as these were the original design criteria.

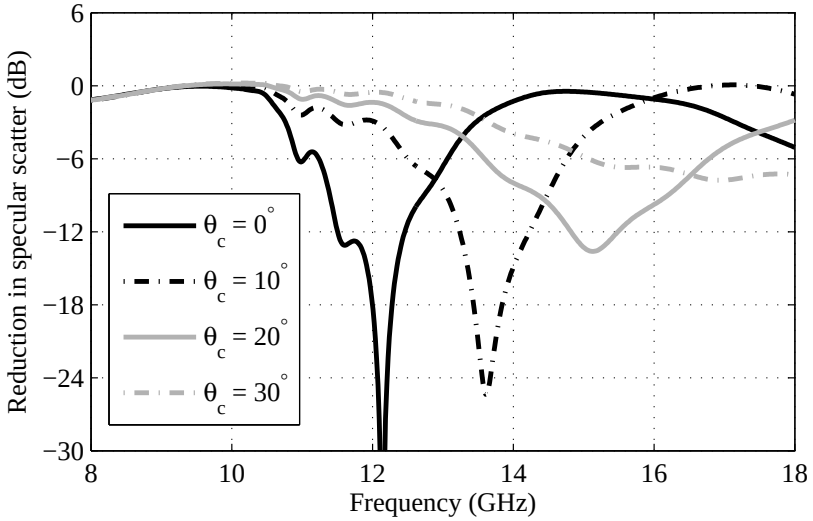

(a) TE polarisation

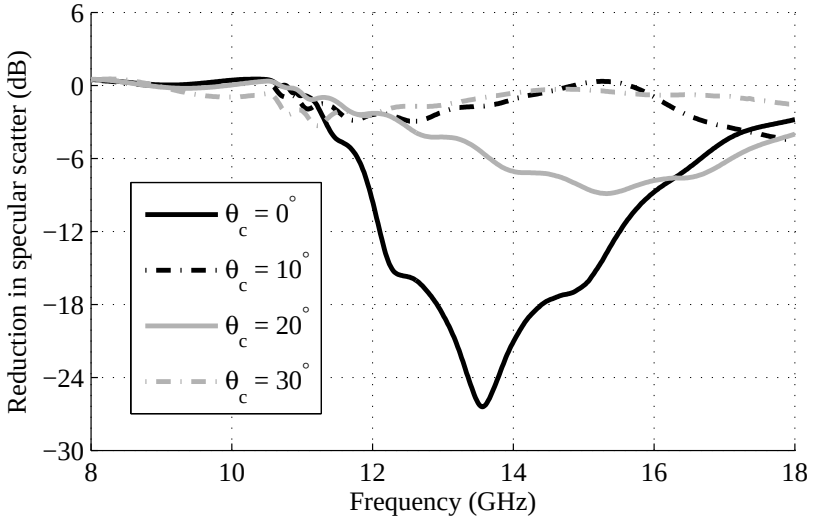

(b) TM polarisation

Figure 6.5: The frequency response of the crenelated surface structures for a fixed thickness for TE and TM polarisation.

For TE polarisation, increasing the slant angle clearly increases the harmonic frequency, but reduces the potential peak reduction in specular scatter. The change in response is much more erratic for TM polarisation, with performance reducing as θ_c is increased.

6.6 Oblique incidence performance

The reduction in magnitudes over a full range of angles of incidence is important, as if the frequency range in which the surface performs varies by a large amount, overall system performance will be reduced. As previously mentioned, this is because when the surface is installed in a building structure, there will be a range of oblique angles of incidence. The operational range is investigated between 40° and 60° for two surface angles, $\theta_c = 10°$ and $\theta_c = 20°$.

For $\theta_c = 10°$ both the TE and TM response seem quite stable. Although the magnitude of reduction is reduced in Fig. 6.6a at $\theta_i = 50°$, the peak harmonic does not shift considerably between $\theta_i = 40°$ and 60°. The angular stability is much better for $\theta_c = 20°$, where the level of reduction does not considerably alter. However, the 6 dB bandwidths do shift down in frequency as the angle of incidence increases. This should not cause issue due to the large bandwidth covering a large range of frequencies.

Increasing the crenelation angle to 20° alters the performance for both TE and TM polarisations. For TE polarisation (Fig. 6.7a) the peak harmonic is shifted to the right, resulting in a -18 dB reduction at 17.2 GHz at $\theta_i = 40°$, as the incidence angle is increased, the performance at this frequency is reduced. Furthermore, for TM polarisation (Fig. 6.7b) the response is also shifted the right, with the performance slightly reducing as the angle of incidence increases.

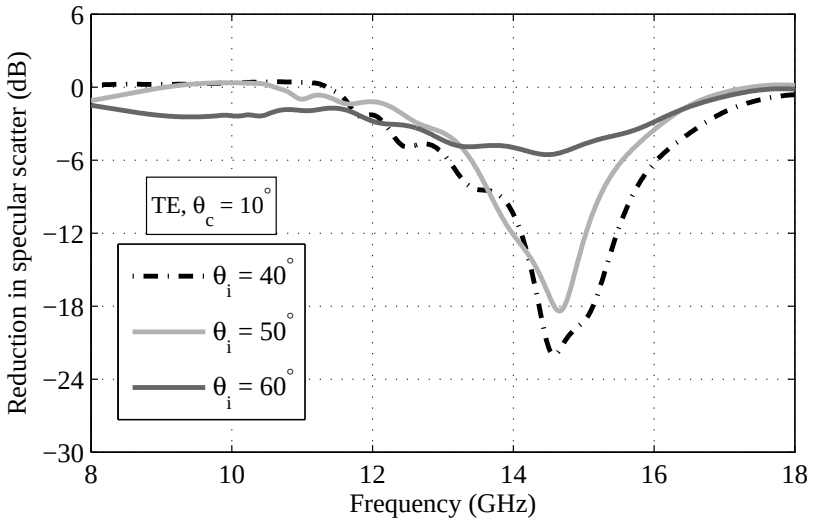

(a) TE polarisation

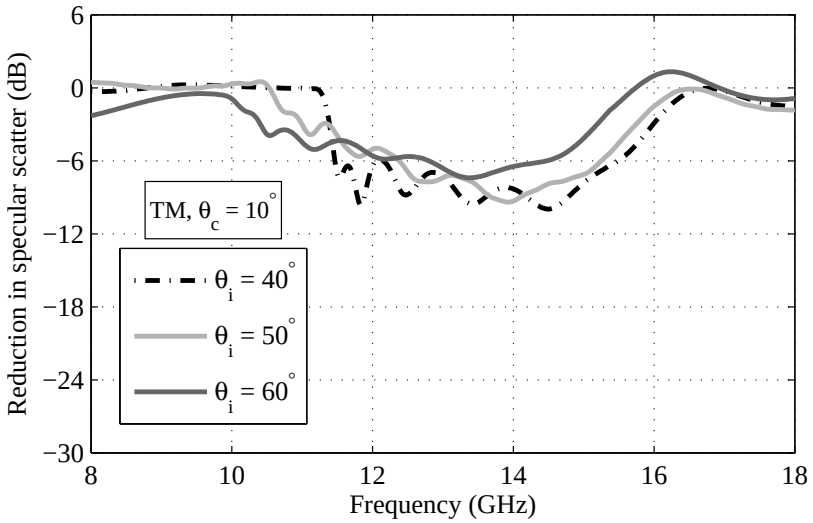

(b) TM polarisation

Figure 6.6: The frequency response of the crenelated surface structures with $\theta_c = 10°$ for varying angles of incidence, and (a) TE and (b) TM polarisation.

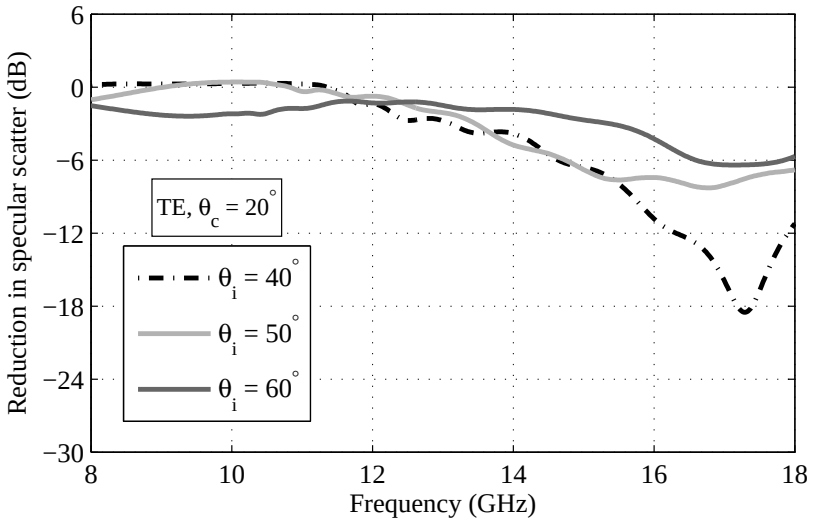

(a) TE polarisation

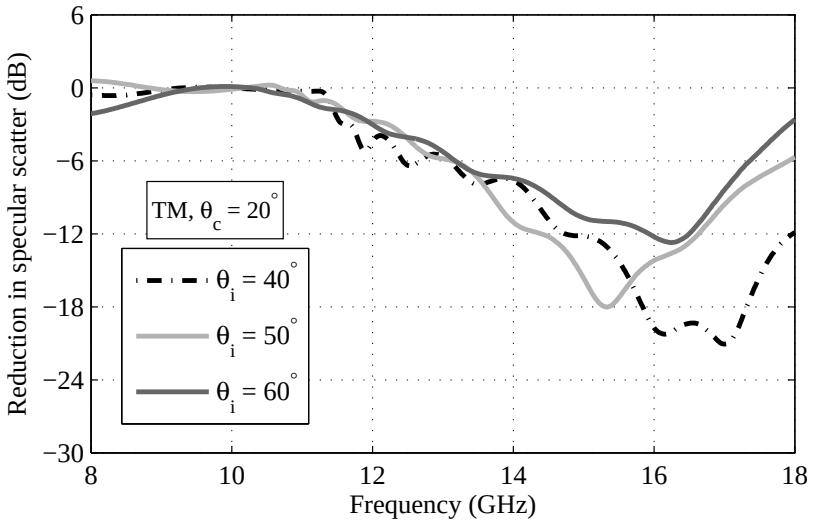

(b) TM polarisation

Figure 6.7: The frequency response of the crenelated surface structures with $\theta_c = 20°$ for varying angles of incidence, and (a) TE and (b) TM polarisation.

6.7 Crenelated CR-FSS floquet mode plots

A full range of crenelation angles were simulated in the frequency domain and plotted against the usual frequency range in Fig. 6.8. The TE $\hat{r}(0,0)$ mode shows that the structure does not offer good reduction in specular scatter as the crenelation angle increases.

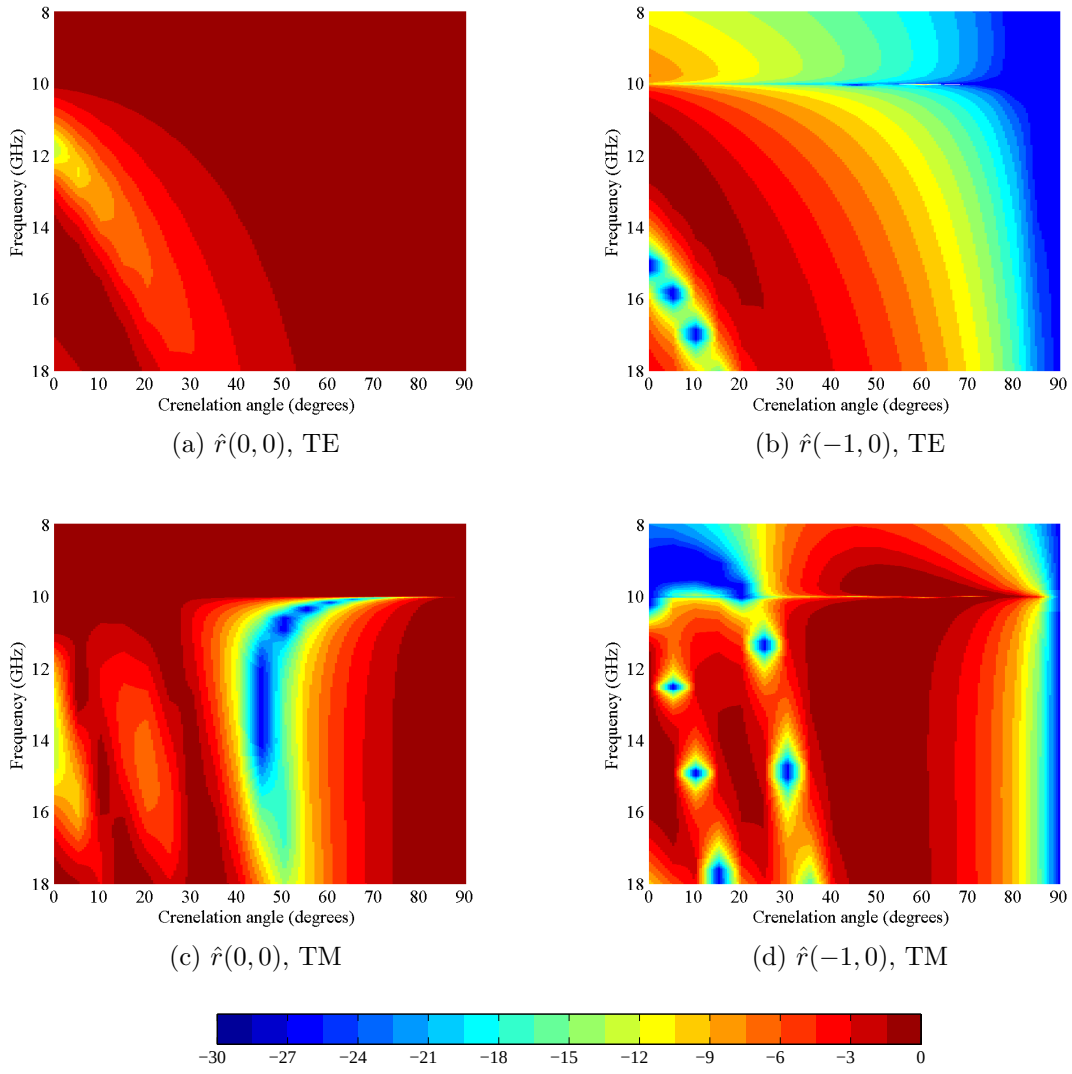

(a) $\hat{r}(0,0)$, TE

(b) $\hat{r}(-1,0)$, TE

(c) $\hat{r}(0,0)$, TM

(d) $\hat{r}(-1,0)$, TM

Figure 6.8: S-parameter (dB) results for a range of crenelation angles for the principle direction $\hat{r}(0,0)$ and higher-order propagating mode $\hat{r}(-1,0)$ for $\theta_i = 50°$.

Interestingly for TM polarisation, most energy is redirected into the $\hat{r}(-1,0)$ mode

over a large frequency range for a crenelation angle between 45° and 50°.

6.8 Conclusion

This chapter has explored the possibility of using a corrugated comb frequency selective surface with sloped periodic elements in order to reduce the specular scatter of an incoming wave. Simulation and measurement results are given for both TM and TE polarised plane waves, with $\theta_i = 50°$. Slope angles of $\theta_c = 0°$, $10°$, $20°$ and $30°$ are all investigated using CST simulations and foam prototype coated in reflective foil. For accurate representation in the simulation model, their respective top widths, w_1 are 4.5 mm, 2.8 mm, 3 mm, and 1.6 mm. Finally, the effect of changing fin width is demonstrated using further simulations. Small changes in w_1 can alter the frequency response drastically, suggesting that care should be taken in mass manufacture of such surfaces.

Chapter 7

Validation at 2.4 GHz

Additional optimisation at 2.4 GHz is done using simulations in order to understand the required parameters for a basic CR-FSS structure which could be applied at a useful frequency in-building. By overlapping the TM and TE reduction peaks, performance should be optimised for the multipath environments that it will be installed in, although the multipath propagation down corridors can alter expected results. In-building simulations are used to validate the application of such surfaces in indoor environments.

7.1 Introduction

This thesis concludes by providing a simulation analysis of the comb reflection frequency selective surface (CR-FSS) optimised at 2.4 GHz. Although the ability to simply scale the various dimensions of the structure with frequency have been previously discussed, important issues such as higher frequency harmonics are vague. This is because they occur at higher frequencies than measurable or realistically modelled using simulation software (25-30 GHz).

An initial parameter study is performed to align the performance for both TE and TM polarisation in the 2.4 GHz Wi-Fi band. At this frequency, the reduction in specular scatter should be at a maximum compared to a flat metal plate. Further analysis of the structure provides a detailed understanding of performance for various angles of incidence, and other surface parameters. Finally, the surface is applied to a corridor in a small in-building scenario to understand the possible performance

at a range of frequencies for the purpose of reducing co-channel interference.

7.2 Frequency band design

As previously seen in the X and K_u bands, a stable broadband frequency reduction can be designed for a wide range of angles of incidence. Several frequency bands should be considered to be allowed to pass:

- TETRA emergency service bands: 380 - 393 MHz, 410 - 430 MHz (some higher frequency ones overlap with GSM 900).
- GSM 900: 880 - 960 MHz.
- GSM 1800: 1710 - 1880 MHz.
- 3G: 1920 - 2170 MHz.

The following should be prevented from propagating:

- Wi-FI 2.4 GHz bands: 2412 - 2484 MHz.
- Wi-Fi 5 GHz bands: 5150 - 5350 MHz, 5470 - 5725 MHz, 5725 - 5850 MHz.

In summary, specular scatter in the 2.4 to 2.5 GHz range should be prevented. The potential use in the 5 GHz frequency band is to be investigated, as the harmonics for both TE and TM polarisation are expected in this region.

7.3 Initial surface design and periodicity results

The previously investigated surface was designed to work in the 10 to 15 GHz range, depending on angle of incidence and polarisation. A simple scaling factor of 5 to 6 would be required to reduce the working frequency to approximately 2.4 GHz. In this case, a periodicity sweep of 70 to 95 mm for both TE and TM polarisation was conducted. It should also be noted, that the maximum direct backscatter at 2.45 GHz will occur at an angle according to Bragg's Law.

$$\alpha = \frac{c}{2f_B \sin\theta_i} = \frac{3{\times}10^8}{2 \times 2.45{\times}10^9 \times \sin(50)} = 79.9 \text{ mm} \tag{7.1}$$

7.3.1 Simulation set-up

Simulations using CST have been shown to provide accurate representations of the surfaces, and their associated performance based of several different factors. A frequency range of 0 to 8 GHz was simulated, with plane wave excitation and electric- and magnetic-field probes used to measure results for both TM and TE polarisation. The combs were modelled as PEC materials once again, and the simulation model was set-up exactly the same as in chapter 3. The initial height and thickness of the comb elements was 80 mm and 4 mm respectively. The surface was 20 mm wide and used periodic boundaries to remove scattering from the edge effects.

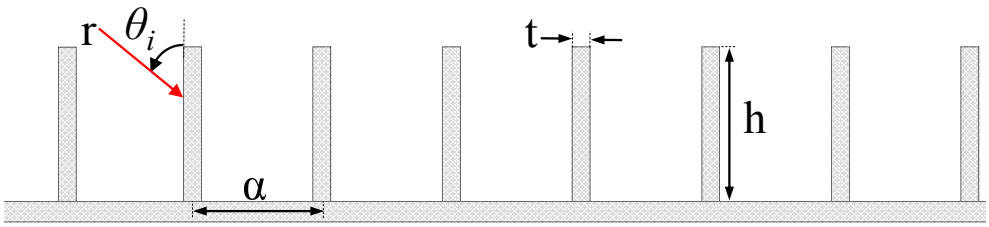

Figure 7.1: The surface constructed in CST had a height, h of 80 mm, a thickness of 4 mm, and varying surface periodicities, α.

7.3.2 Periodicity results

The frequency response for both TE and TM polarisations are shown in Fig. 7.2. As expected, when the period of the surface increases, the resonant frequency decreases. Furthermore, there are multiple resonant frequencies, which should be avoided in the main frequency bands, such as 5.1 to 5.8 GHz for the design. If a dual band surface was required, careful tuning to ensure that the surface lies in both the 2.4 GHz and 5 GHz frequency bands would be possible.

The resonant frequencies and bandwidths of both the TM and TE polarised plane waves would also ideally be very similar. For simulated results in Fig. 7.2, the resonant frequencies are summarised in Table 7.1. This seems to occur for periods of 90 to 95 mm. Below this, the TE polarised signals have lower resonant frequencies than TM polarised ones.

Table 7.1: Resonant frequency for both TE and TM polarisation of the CR-FSS at varying periods, with height = 80 mm, and thickness = 4 mm.

	Resonant Frequency (GHz)	
Period (mm)	**TE polarisation**	**TM polarisation**
70	2.55	3.14
75	2.39	2.84
80	2.27	2.62
85	2.17	2.34
90	2.08	2.10
95	2.00	2.00

The next stage of the simulations will be to understand the effects of changing height, thickness, and period of the surface to tune the surface so that, for both polarisations the resonant frequency will lie at 2.45 GHz and potentially in the 5 GHz region. Furthermore, scaling of the 95 mm period which works at 2 GHz will be done to allow the peak reduction for both polarisations in the 2.4 GHz band.

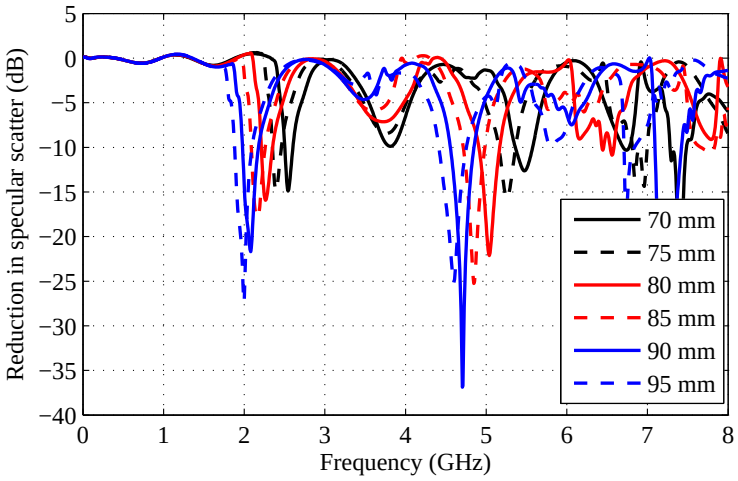

(a) TE polarisation

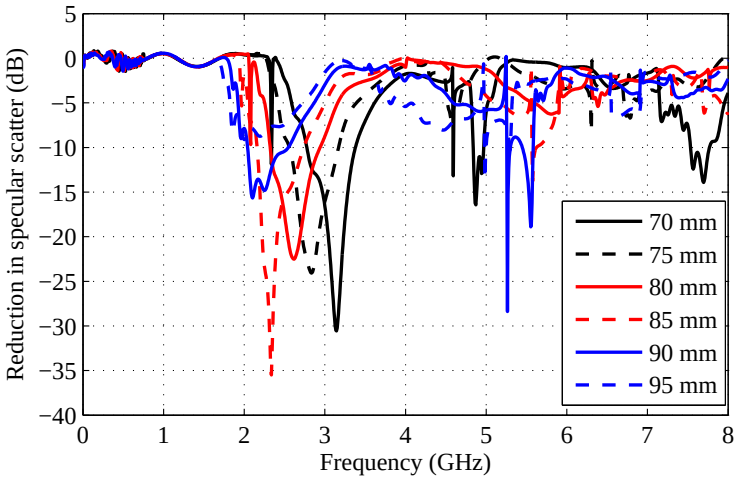

(b) TM polarisation

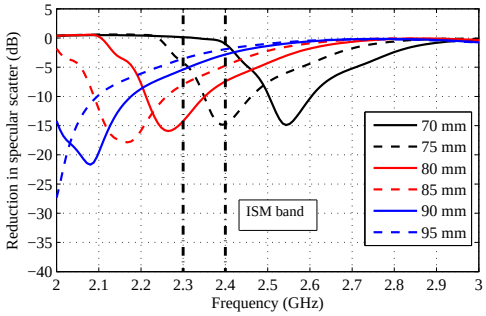

(c) TE polarisation

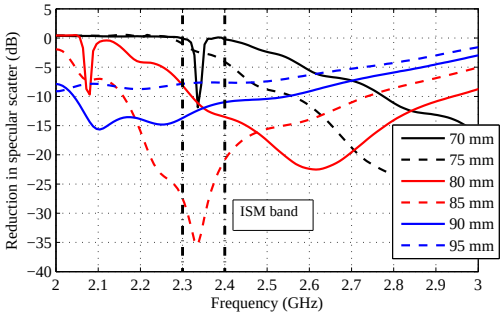

(d) TM polarisation

Figure 7.2: Simulation results of a 2.4 GHz surface for varying surface periodicities at $\theta_i = 50°$ for (a) TE and (b) TM polarisation. The ISM band is highlighted in (c) and (d) for TE and TM polarisation respectively.

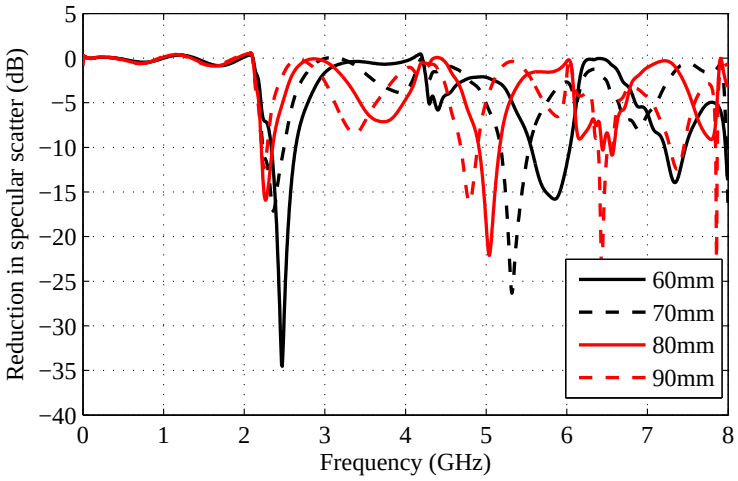

(a) TE polarisation

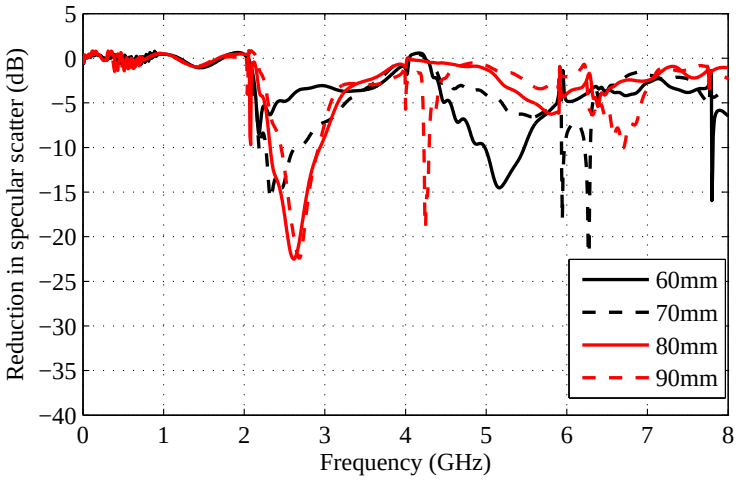

(b) TM polarisation

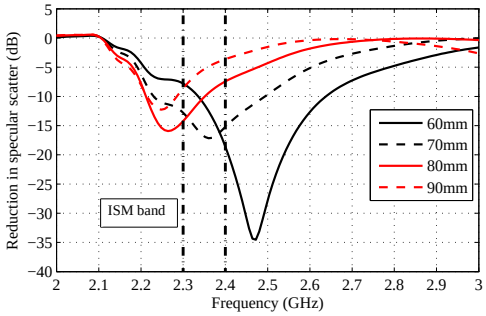

(c) TE polarisation

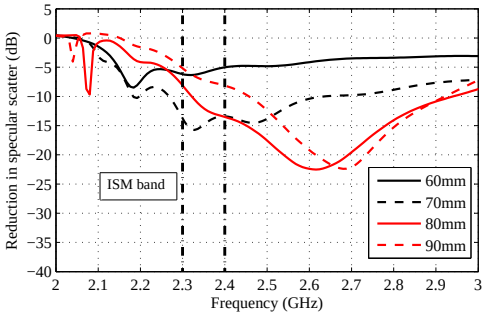

(d) TM polarisation

Figure 7.3: Simulation results of a 2.4 GHz surface for varying surface heights at $\theta_i = 50°$ for (a) TE and (b) TM polarisation. The period is constant at 80 mm. The ISM band is highlighted in (c) and (d) for TE and TM polarisation respectively.

7.4 2.4 GHz surface for TE and TM polarisations

As suggested previously, a surface which has a peak in reduction at the same frequency for both TE and TM polarisations would be beneficial. Initial simulations have shown that at 95 mm, the resonant frequency lies at 2 GHz, with fin height of 80 mm and thickness of 4 mm.

A suitably scaled surface designed for a frequency of 2.4 GHz is designed. In this case, the height of the surface is 70 mm, the period is 80 mm, and the thickness is 4 mm. Simulations are run in CST over a wide frequency band to understand where possible harmonics of the surface would occur.

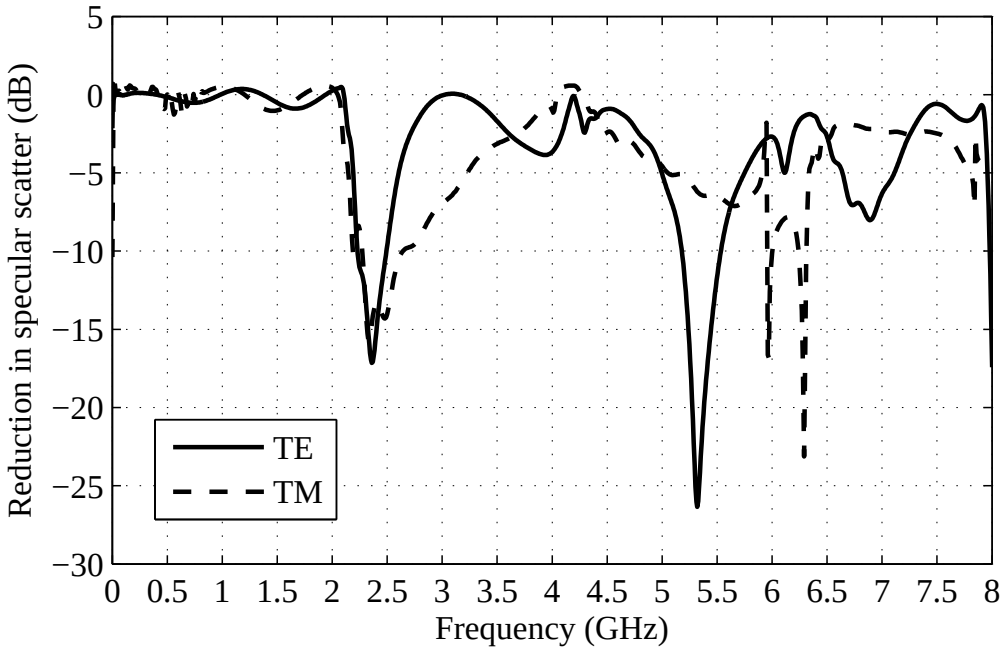

Figure 7.4: The frequency response of a CR-FSS when compared to a flat plate, optimised for working at 2.4 GHz.

The resonant frequency for both TE and TM polarisation is at 2.4 GHz, with a start 3 dB frequency of approximately 2.1 GHz. The TE response is more narrow band than the TM due to the extended 3 dB stop frequency, as shown in Fig. 7.4.

Further harmonics occur in the 5 to 7 GHz region, which would also cause reductions at these frequencies. At frequencies lower than 2 GHz there is no reduction at all,

meaning that signals at these frequencies should propagate normal down the corridor if the surface was installed. This is further analysed in section 7.6, where full building simulations at 1.5 and 2.4 GHz are conducted to understand the frequency selectiveness of the surface.

7.4.1 Oblique incidence performance

The surface is to be positioned in a corridor of a full building, and the parameters summarised in this section are to be used to obtain results. However, the performance of the surface over a range of angles of incidence is unknown. Simulations at 40° , 50° and 60° are done and the simulated results of the specular scatter reduction are shown for TE and TM polarisation in Figs. 7.5a and 7.5b respectively.

For TE polarisation, the surface is stable for angles of incidence between 40° and 60°. The peak in harmonic shifts from between 2.45 and 2.25 GHz respectively, and is wide enough to offer at least 5 dB reduction for a bandwidth of 400 MHz between 2.2 and 2.6 GHz.

For TM polarisation, the results show that at least 5 dB reduction occurs over a much wider bandwidth. Additionally, from 40° to 60°, the peak in reduction shifts from 2.6 to 2.15 GHz. For 40°, there is at least 5 dB reduction between 2.45 and 3.4 GHz. At 50° this lies between 2.2 and 3.25 GHz, and for 60° it is between 2 and 3.25 GHz.

Overall system-level performance will only be fully understood in the multipath environment of a full building simulation. In this case, a range of signals of varying angle and polarisation will be incident on the CR-FSS structure.

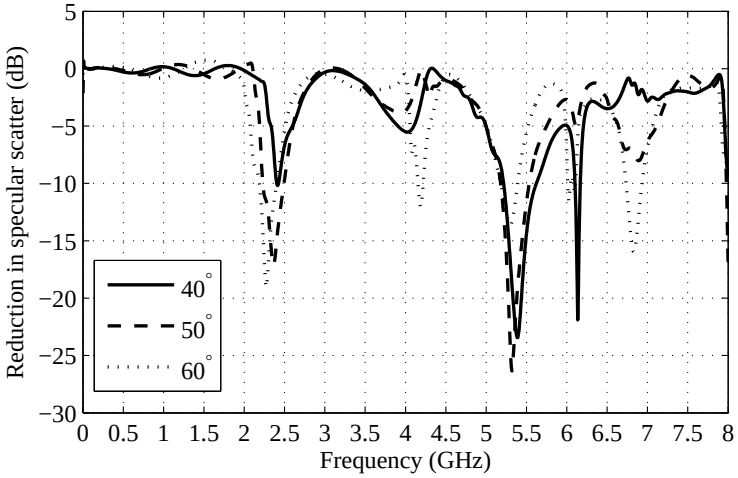

(a) TE polarisation

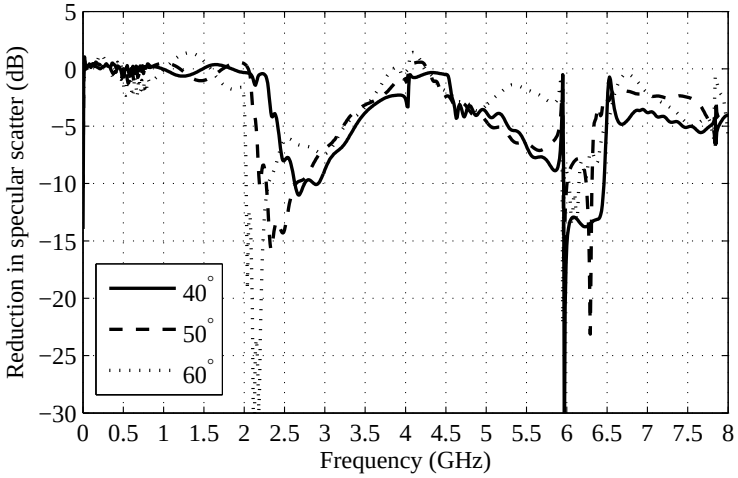

(b) TM polarisation

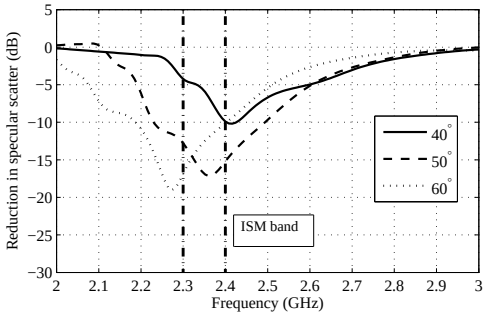

(c) TE polarisation

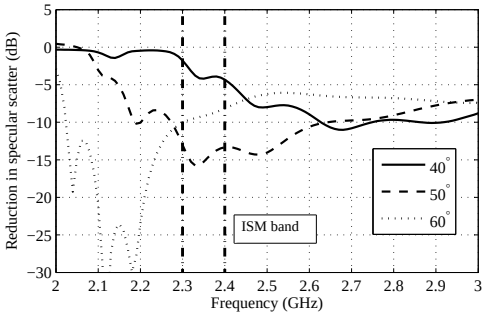

(d) TM polarisation

Figure 7.5: Simulation results of a 2.4 GHz surface for varying angles of incidence. The ISM band is highlighted in (c) and (d) for TE and TM polarisation respectively.

7.5 Scattering

Simulated scattering plots for TE and TM polarisation are shown in Fig. 7.6. As expected, at the specular scatter angle, there are reductions in scattering level at 2.4 GHz and 5.5 GHz for both TE and TM polarisation. There are primary and secondary backscatter lobes for frequencies above 2 and 4 GHz respectively.

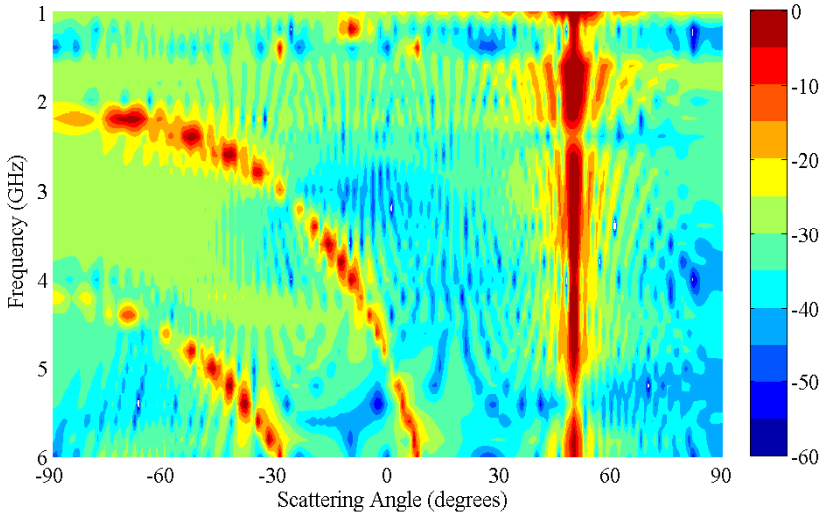

(a) TE polarisation

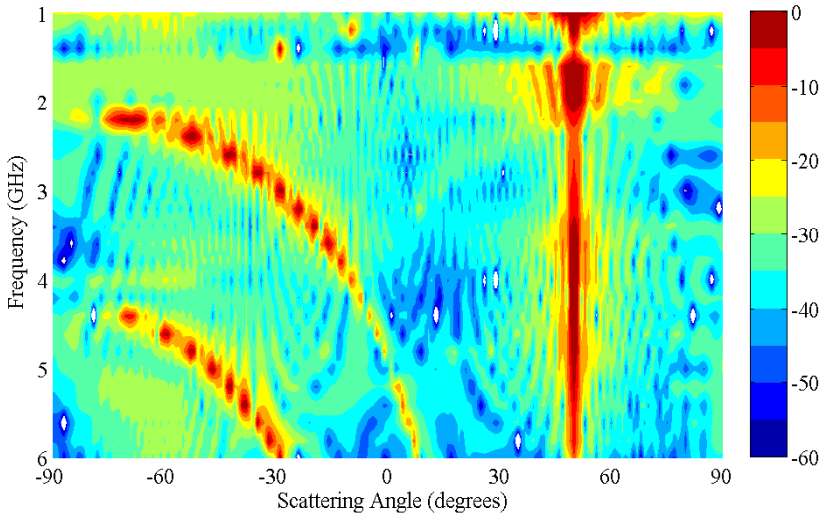

(b) TM polarisation

Figure 7.6: Scattering simulation results of a 2.4 GHz surface at 50° for (a) TE and (b) TM polarisation.

7.6 Full building simulation

Full building simulations have been previously used to analyse the performance of frequency selective surfaces (FSS) [82], with use of measurements often also used [83, 84]. A similar analysis using CST MWS is completed in this section to compare the use of a CR-FSS with a simple metallic wall. The following will describe the building construction, port excitation, results extraction, and finally visualisation and analysis of the results.

Previous analysis of in-building propagation has involved the use of cumulative distribution function (CDF) plots for the analysis of E-field [85, 86], signal-to-noise ratio (SIR) and capacity [87]. A 20 dB increase for the case of SIR and capacity can be considered normal when using frequency selective surfaces, and thus further increase in SIR, or the decrease in E-field levels following the installation of the CR-FSS would be beneficial.

Due to the variety of different propagation routes and node positions, basic scenarios are used to gauge the best installation procedures. For each scenario, an uncoated corridor, and one with a CR-FSS will be done in order to statistically analyse the difference between both. Each scenario consists of a building with only metallic walls. This is because:

- In many existing FSS installations, the building has to be retrofitted with metallic insulation to ensure an isolated environment for the FSS to work correctly.
- Energy efficient buildings are more commonly using metallic insulation as a method of improving the thermal efficiency of the structure.
- The performance of the CR-FSS relies on the channelled propagation down corridors.
- It greatly reduces the model complexity, reducing simulation execution time and potential for error.

Excitation at the required frequency was ensured by using a dipole length port. The resonant frequency was adjustable, depending on the length of this port. Signals at the required frequencies of 2.4 GHz and 1.5 GHz required dipole lengths of 49 mm

and 84 mm respectively. The fields at the frequency of interest were extracted using a two-dimensional cut-plane E-field monitor. The E-field levels are presented in this two-dimensional plane for a variety of scenarios, useful for both visual comparison and statistical analysis.

As the CR-FSS structure is designed to be frequency selective, the propagation should reduce propagations at 2.4 GHz and not alter the scattering at 1.5 GHz.

7.7 Initial simulation model and results

The initial simulation provides a small scenario, with dimensions shown in Fig. 7.7. Although the dimensions are smaller than a usual building might be, it should offer a sensible idea as to whether the CR-FSS is effective at reducing specular scatter in a multipath environment. This is because initial simulations on the surface itself show that a reduction of up to 10 dB can be achieved from one bounce from the CR-FSS.

To provide an exact comparison of the flat and comb scenarios, the walls were all assigned PEC properties. To prevent the whole structure from becoming resonant, no roof or floor materials were assigned (open boundary), although the height of the building was chosen so that the majority of the scattering energy remained in the building simulation and did not escape vertically.

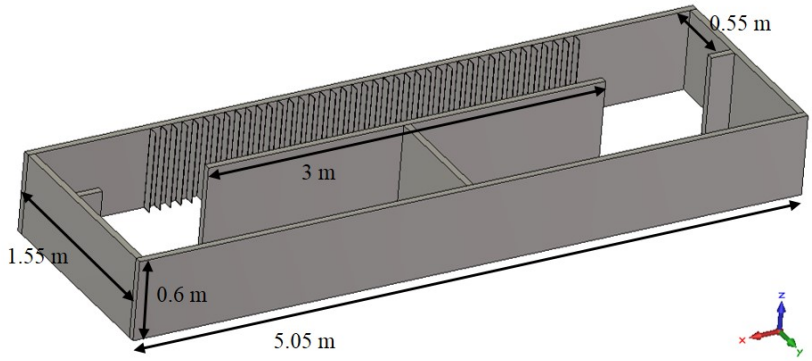

Figure 7.7: Scenario 1: the CR-FSS was installed on only one corridor wall. The transmitter is located arbitrarily in the right hand room.

Simulations were run for 2.4 GHz and 1.5 GHz, with results respectively shown in Figs. 7.8 and 7.9. Visual comparison of the room at 2.4 GHz for the normal building (Fig. 7.8a) and the building with the CR-FSS installed (Fig. 7.8b) show that most of the electromagnetic energy at this frequency is prevented from reaching the bottom left hand room. This seems to be a result of reducing the direction propagation paths down the corridor itself. Further statistical analysis in Fig. 7.8c shows that there is approximately a 3 dB reduction in mean signal level in this region. The levels of E-field in the transmitting room are near equal, as shown in Fig. 7.8d. It is also possible to see that in Fig. 7.8b, specular propagation is redirected back towards the transmitting room as predicted. This inevitably prevents signals reaching the

bottom empty room.

The simulations at 1.5 GHz show this reduction to be frequency selective, as no reduction is encountered at this frequency, and the E-field levels remain the same in the receiving room, as shown in the CDF plot in Fig. 7.9c. For a more realistic simulation, it is proposed that the corridor be made longer to offer a more representative model of a building.

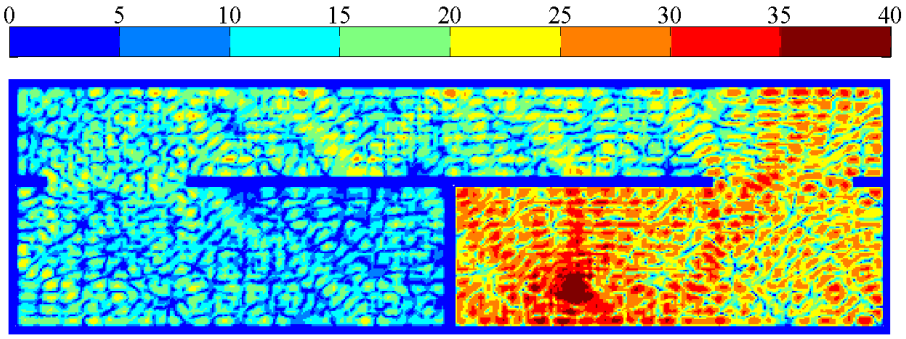

(a) Unlined building

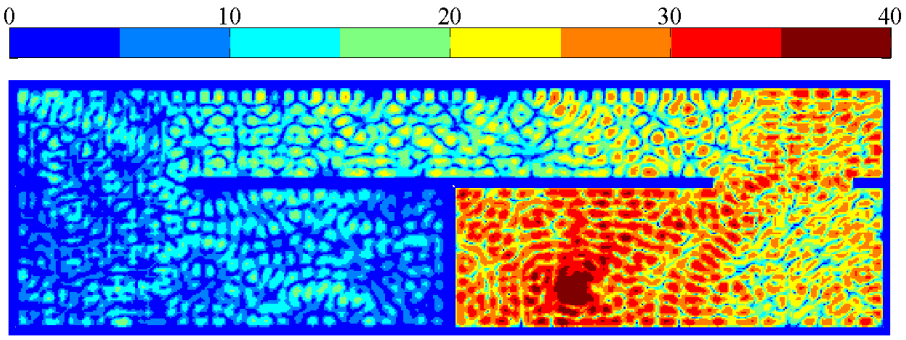

(b) Building with CR-FSS installed

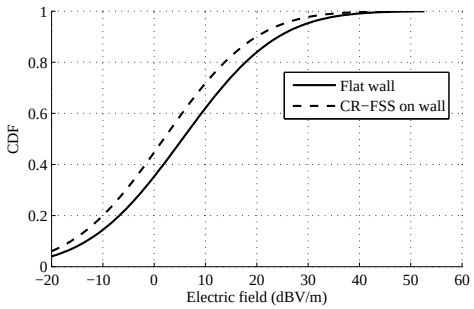

(c) Empty room

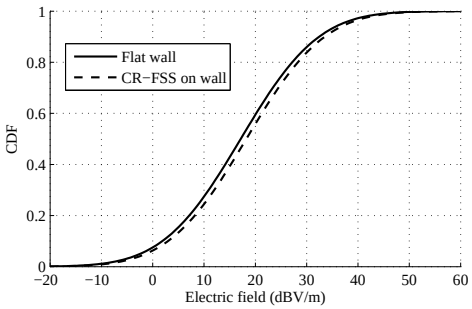

(d) Room with Tx

Figure 7.8: Full building simulations at 2.4 GHz, with (a) flat metallic walls and (b) walls with CR-FSS installed. There are CDF plots of the propagation comparing the E-fields in (c) the receiver room and (d) the transmitter room.

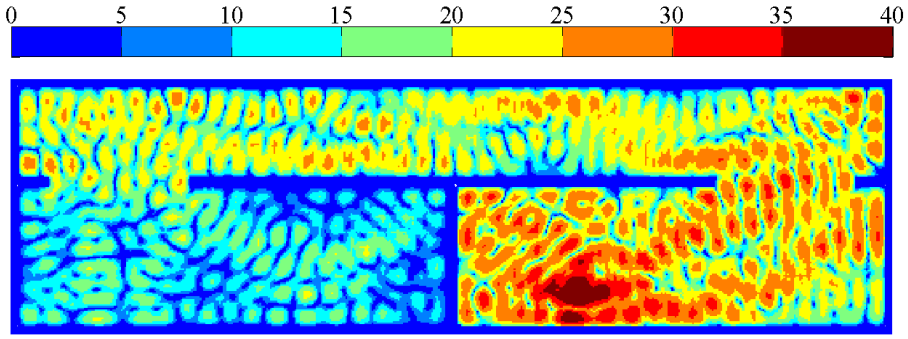

(a) Unlined building

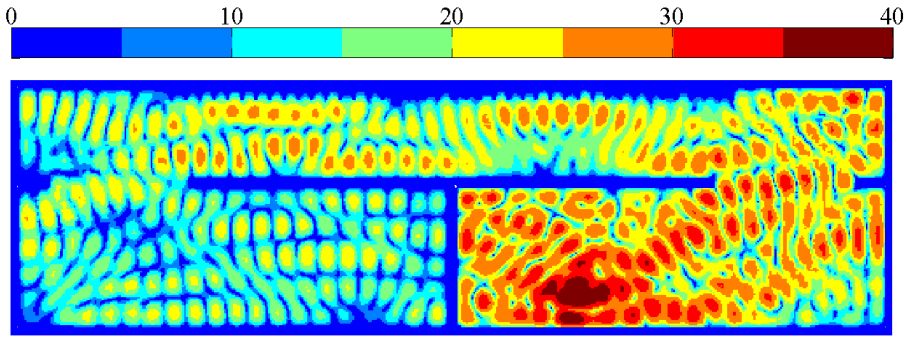

(b) Building with CR-FSS installed

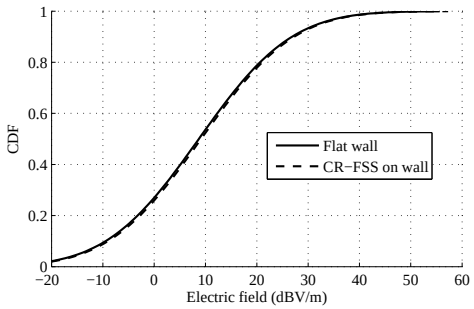

(c) Empty room

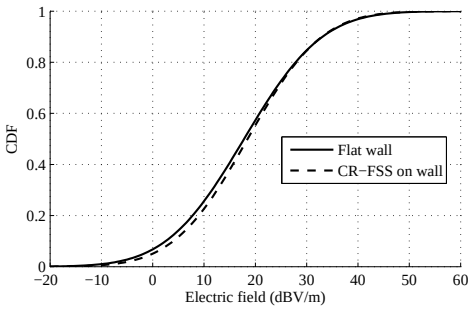

(d) Room with Tx

Figure 7.9: Full building simulations at 1.5 GHz, with (a) flat metallic walls and (b) walls with CR-FSS installed. There are CDF plots of the propagation comparing the E-fields in (c) the receiver room and (d) the transmitter room.

7.8 Increasing corridor length

In this section, a larger simulation with a longer corridor of 5.5 m is conducted. Once again, comparison of the E-field levels in various areas of the building are done to statistically analyse the performance of the CR-FSS. Results at 2.4 GHz and 1.5 GHz are shown in Figs. 7.11 and 7.12 respectively. Additional repetitions of the CR-FSS are placed along a single side of the corridor.

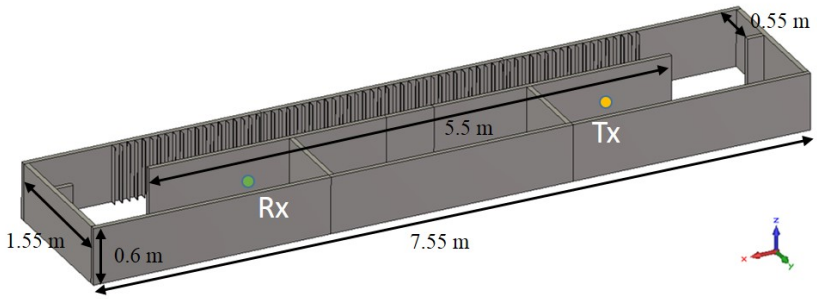

Figure 7.10: Scenario 2: the use of a larger corridor to analyse the potential increase in performance when using the CR-FSS.

The results at 2.4 GHz show that the reduction is much larger than for the smaller simulation model. This is confirmed by the CDF plot in the bottom left hand room, where there is a reduction of approximately 14 dB (Fig. 7.11c).

Despite the increased length of the corridor and the effectiveness at 2.4 GHz, the performance is shown to be frequency selective as there is no reduction at 1.5 GHz. This is highlighted both in the E-field plot comparison (Figs. 7.12a and 7.12b) and the empty room CDF plot (Fig. 7.12d).

It is possible to see that a large portion of the transmitted power actually enters the corridor and begins propagating, like in Fig. 7.11a. By extending the CR-FSS around this corner, it may be possible to reduce the propagation further by re-directing this propagation back into the transmitting room.

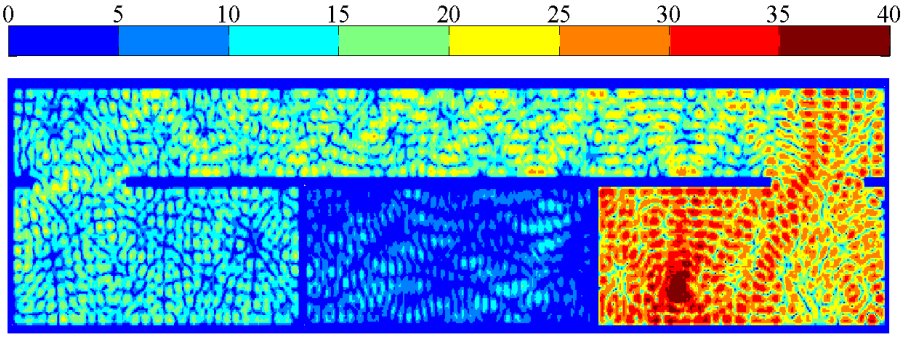

(a) Unlined building

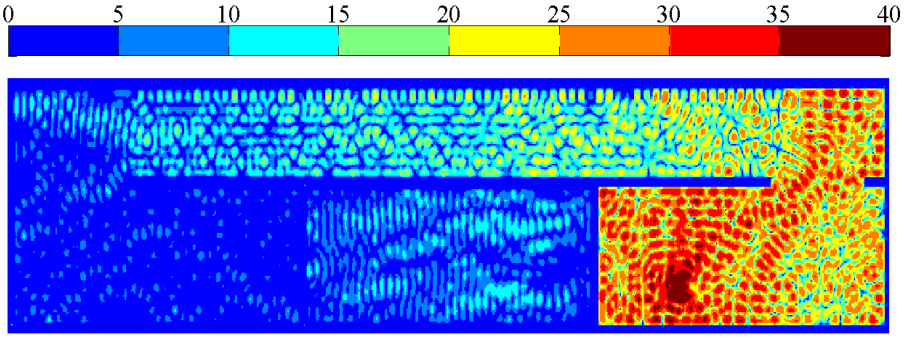

(b) Building with CR-FSS installed

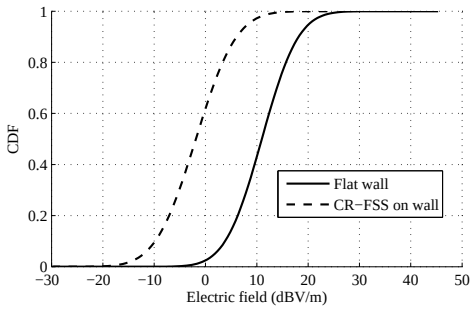

(c) Empty room

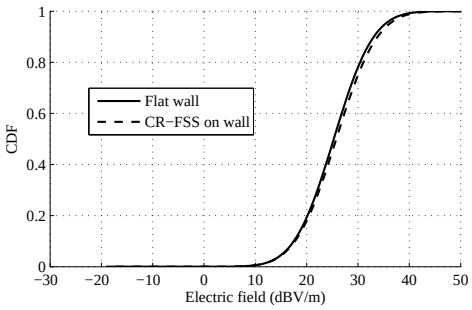

(d) Room with Tx

Figure 7.11: Full building simulations at 2.4 GHz, with a corridor length of 5.5 meters, with (a) flat metallic walls and (b) walls with CR-FSS installed. There are CDF plots of the propagation comparing the E-fields in (c) the receiver room and (d) the transmitter room.

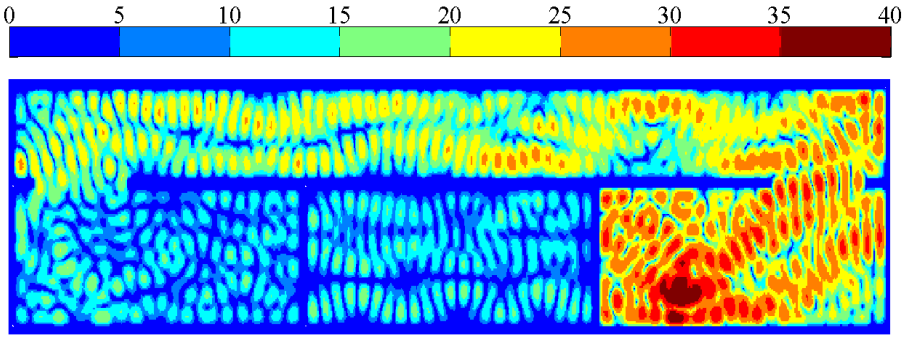

(a) Unlined building

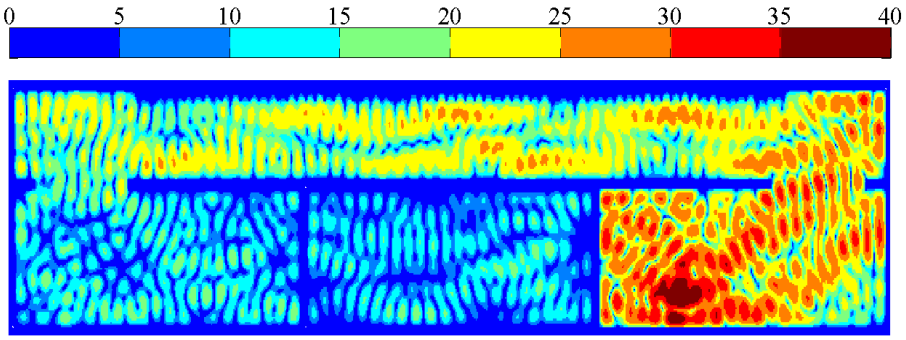

(b) Building with CR-FSS installed

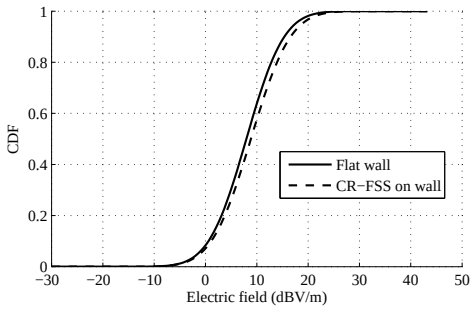

(c) Empty room

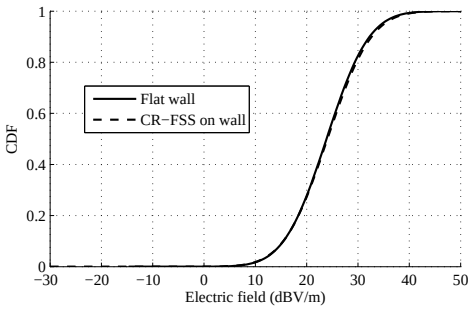

(d) Room with Tx

Figure 7.12: Full building simulations at 1.5 GHz, with a corridor length of 5.5 meters, with (a) flat metallic walls and (b) walls with CR-FSS installed. There are CDF plots of the propagation comparing the E-fields in (c) the receiver room and (d) the transmitter room.

7.9 Double lining of walls with CR-FSS

It was also proposed that a double installation of a CR-FSS could be used to further improve the magnitude of reduction. The CR-FSS is applied to both sides of the corridor. The CDF shows that there is a mean reduction of 19 dB at 2.4 GHz, as shown in Fig. 7.14d. This is a 5 dB improvement when only one CR-FSS surface is used. The CDF at 1.5 GHz (Fig. Fig. 7.15c) for the same room shows that there is no reduction in E-field, which is expected. Thus it can be summarised that the double lining offers the best reduction.

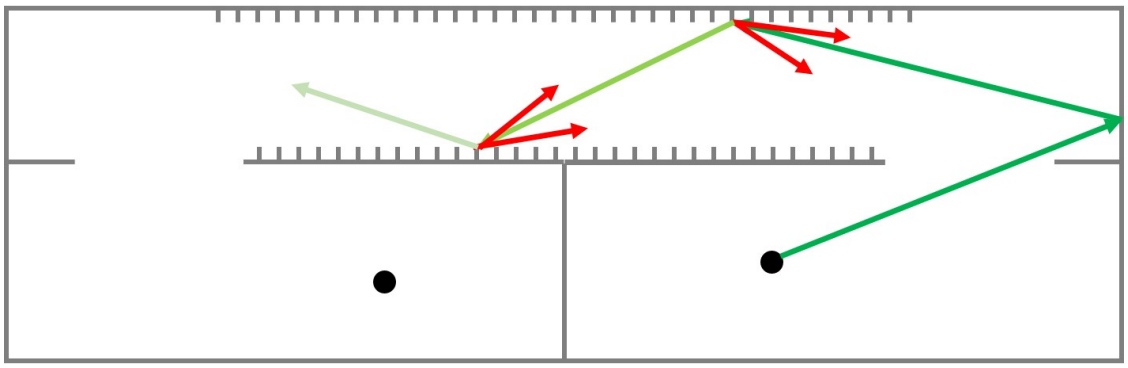

Figure 7.13: An additional comb surface on the other corridor wall could potentially increase the reduction in scattering down the corridor, further increasing the SIR.

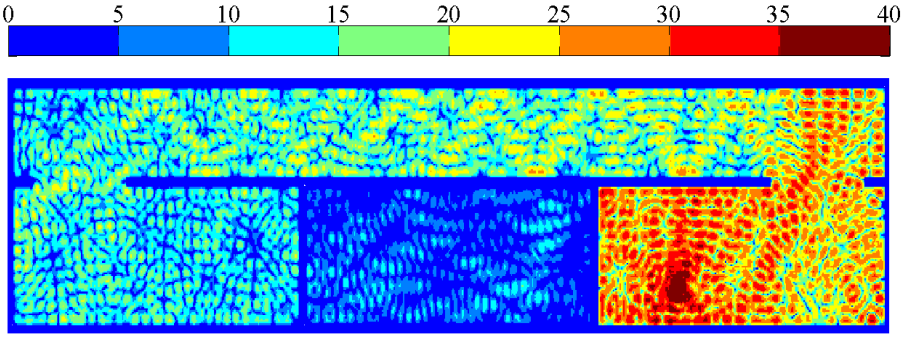

(a) Unlined building

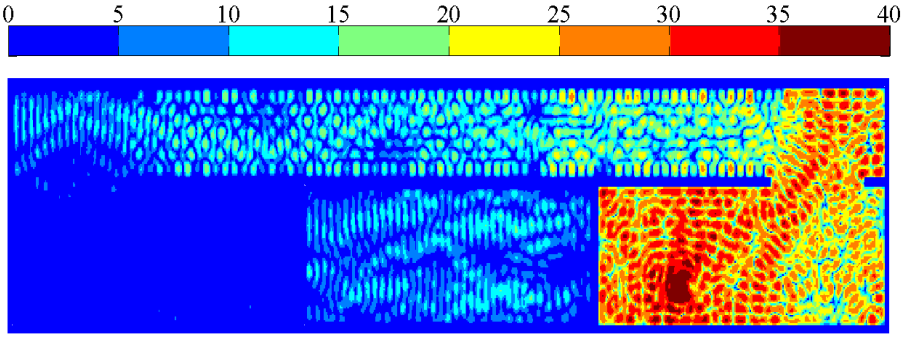

(b) Building with two CR-FSS installed

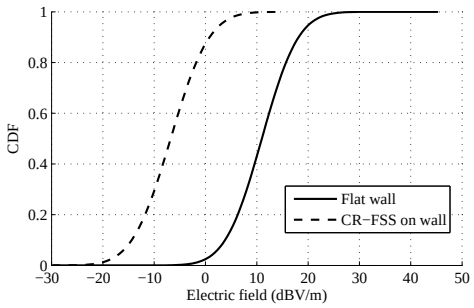

(c) Empty room

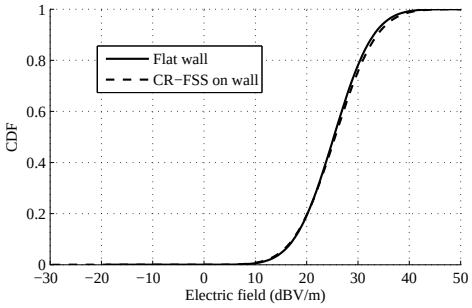

(d) Room with Tx

Figure 7.14: Full building simulations at 2.4 GHz, with a corridor length of 5.5 meters, with (a) flat metallic walls and (b) walls with two CR-FSS installed. There are CDF plots of the propagation comparing the E-fields in (c) the receiver room and (d) the transmitter room.

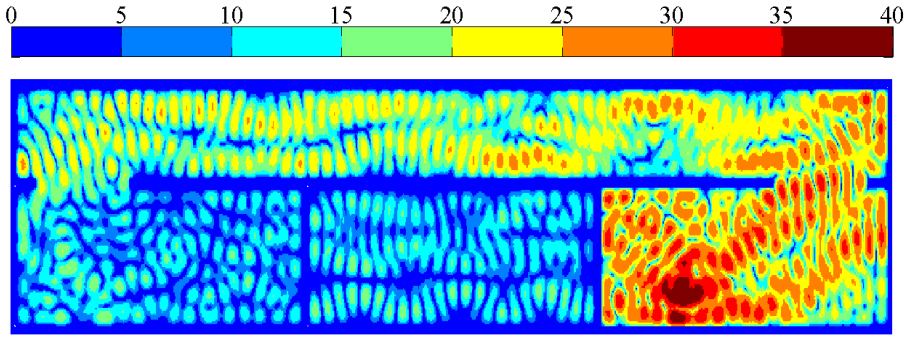

(a) Unlined building

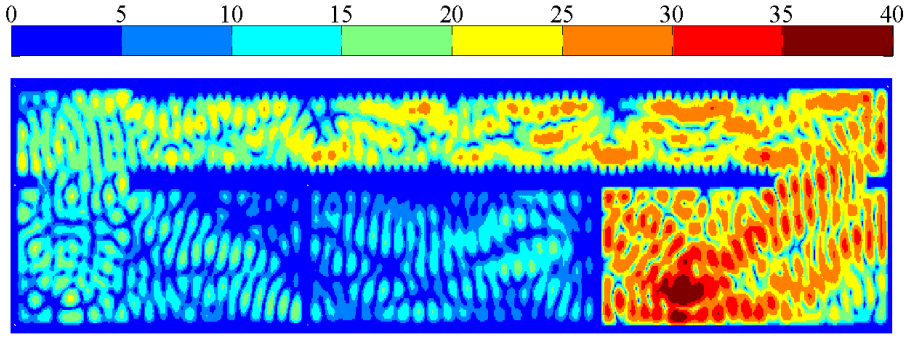

(b) Building with two CR-FSS installed

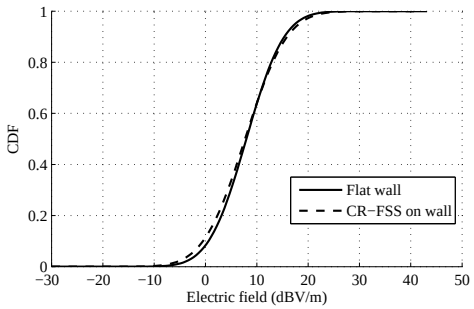

(c) Empty room

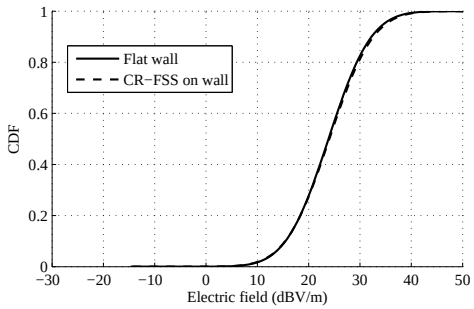

(d) Room with Tx

Figure 7.15: Full building simulations at 1.5 GHz, with a corridor length of 5.5 meters, with (a) flat metallic walls and (b) walls with two CR-FSS installed. There are CDF plots of the propagation comparing the E-fields in (c) the receiver room and (d) the transmitter room.

7.10 Signal-to-interference ratio plots

In order to further quantify the effect that the CR-FSS corridor installation has on the transmitting ranges of each transmitter, the signal-to-interference ratio (SIR) can be calculated. It is predicted that by decreasing the propagating fields down the corridor, the SIR will be improved for both rooms due to the increased electromagnetic separation at the required frequency ranges.

7.10.1 Averaged E-field plots

In order to calculate and present the SIR clearly, the E-field field plots must first be averaged over several wavelengths in order to remove the small scale fading [88]. For this scenario, four cases will be considered for comparison:

1. Unlined building at 1.5 GHz.
2. Building with two CR-FSS installed at 1.5 GHz.
3. Unlined building at 2.4 GHz.
4. Building with two CR-FSS installed at 2.4 GHz.

The resulting averaged E-field plots are shown in Figs. 7.16 and 7.17. Following the averaging of the E-field values, the propagation paths are much more clear, particularly for the case of the building with no CR-FSS installed in Fig. 7.17a. Specifically, the output of the Matlab matrix formed by calculating the averaged value of a determined number of surrounding values. In this case, a 10 by 10 square centimetre averaging produces a clear picture of the electromagnetic scatter whilst reducing the amount of fading and unwanted peaks and nulls in the propagating signal.

Prior to this process, all values which either equal zero or are less than - 25 dB are assigned to not-a-number (NaN). This is because when calculating the average numbers, NaN is discarded in calculation. In the previous plots CST assigns the PEC wall structures as 0 dB and the E-fields immediately next to the walls are assigned low E-field values in the range of -25 to -100 dB. In order to remove both of these from any averaging calculations, their values are assigned as NaN and are

plotted as white in the following averaged E-field plots.

The averaged plots in Fig. 7.16 are for a transmission at 1.5 GHz, with just metallic walls in Fig. 7.16a and a doubly CR-FSS lined corridor in Fig. 7.16b. Although no statistical analysis will be conducted on these averaged plots, it is interesting to note that the two plots are much more similar in E-field level than the 2.4 GHz averaged plots in Fig. 7.17.

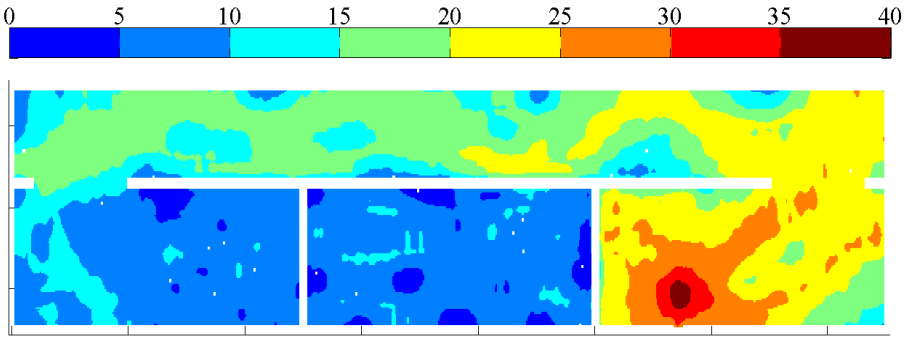

(a) Unlined building

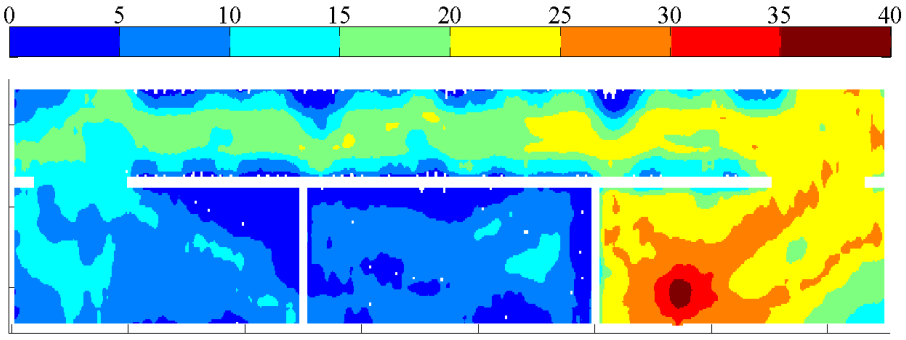

(b) Building with two CR-FSS installed

Figure 7.16: E-field plots for a dipole transmitting at 1.5 GHz, with each cell averaged using 100 values over 100 square cm.

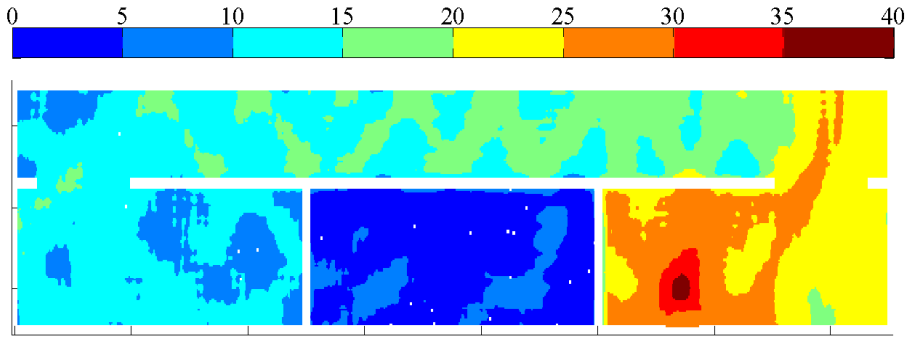

(a) Unlined building

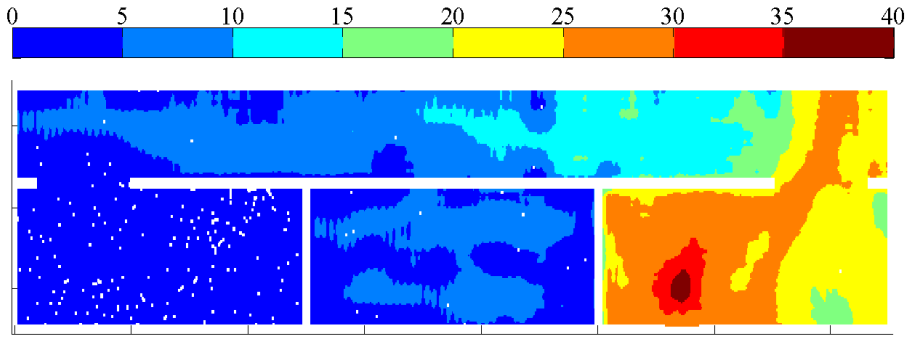

(b) Building with two CR-FSS installed

Figure 7.17: E-field plots for a dipole transmitting at 2.4 GHz, with each cell averaged using 100 values over 100 square cm.

7.10.2 SIR plots

Now that the E-field plots have been averaged, it is possible to calculate the signal to interference ratio (SIR) at each given point in the matrix, representing the SIR at any specific point in the building itself. As the SIR requires at least two transmitting nodes, a secondary node and E-field pattern is acquired by simply mirroring the E-field matrix result so that the transmitter is in the original 'Empty room' and that the empty room is the 'Room with Tx', as shown in Fig. 7.18. The secondary transmitter results in an interfering signal, the propagation of which can also be altered by the CR-FSS structure. This will give a realistic scenario of a single channel, two transmitter network. Similar scenarios have been constructed in [90] where the signal-to-interference-and-noise ratio (SINR) is calculated and the effect of absorber on walls of a building are characterised.

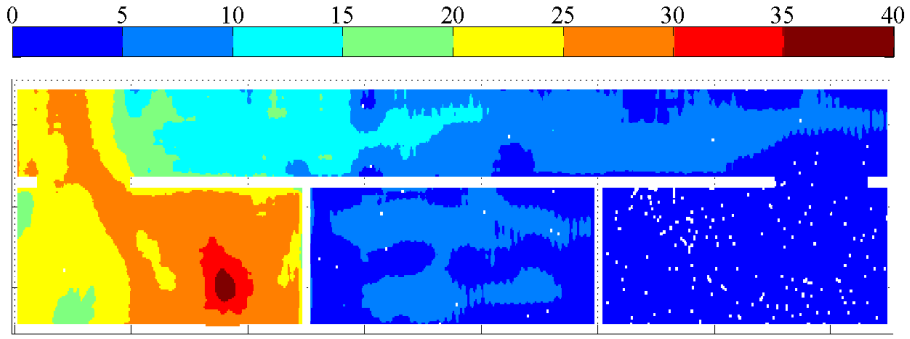

(a)

Figure 7.18: Creating a secondary plot for the calculation of SIR. This plot is the mirrored version of Fig. 7.17b.

For this case, we operate under the premise that it is favourable to be connected to the network with the highest signal/E-field strength. Under this assumption, the signal part of the SIR will be the maximum E-field at a specific point in the results matrix when comparing Fig. 7.17b and 7.18. The resulting information is plotted in Fig. 7.19 and form the basis of the SIR. Similarly, the minimum E-field at each matrix element when comparing the two cases is the interference. The SIR can be calculated by dividing the signal level by the interference, as shown in equation 7.2.

$$\mathrm{SIR} = 20\log\left(\frac{\max(E_z(x,y)_\mathrm{A}, E_z(x,y)_\mathrm{B})}{\min(E_z(x,y)_\mathrm{A}, E_z(x,y)_\mathrm{B})}\right) \tag{7.2}$$

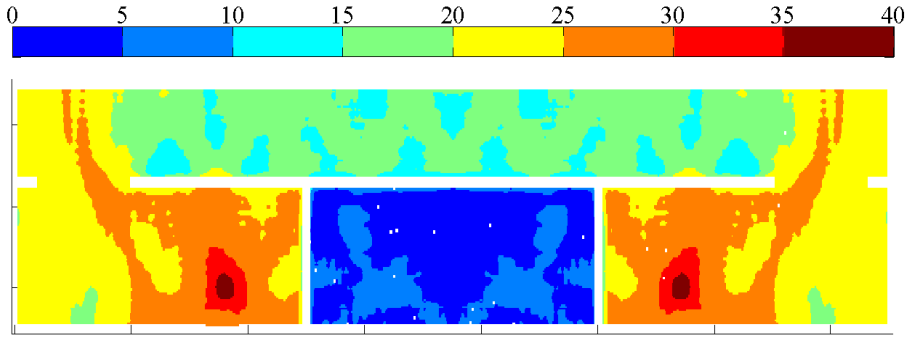

(a) Unlined building

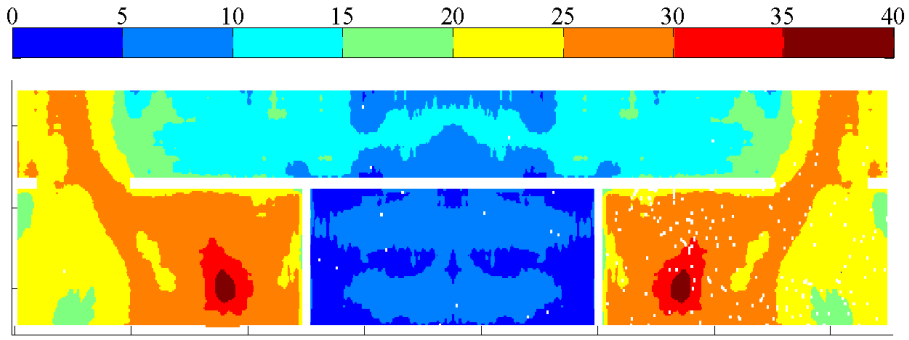

(b) Building with two CR-FSS installed

Figure 7.19: Plots showing the highest E-field level available from either transmitter at 2.4 GHz.

where $E_z(x,y)_{\mathrm{A}}$ and $E_z(x,y)_{\mathrm{B}}$ are the linear E-fields in the z-plane at each x and y element for the two matrices formed. Conducted for both the unlined and CR-FSS lined corridors, SIR plots are shown in Fig. 7.20.

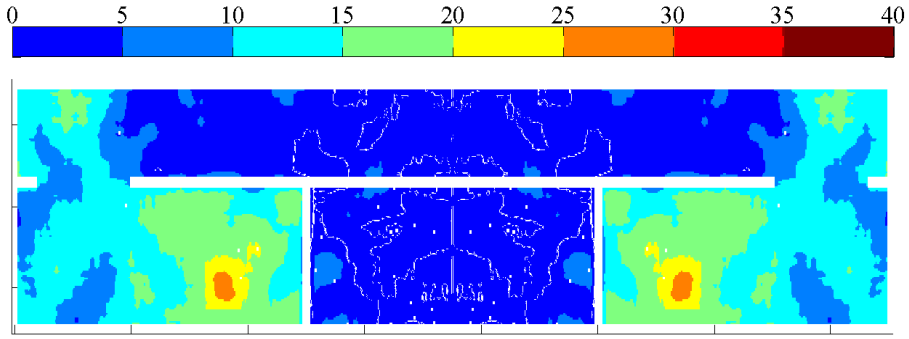

(a) Unlined building

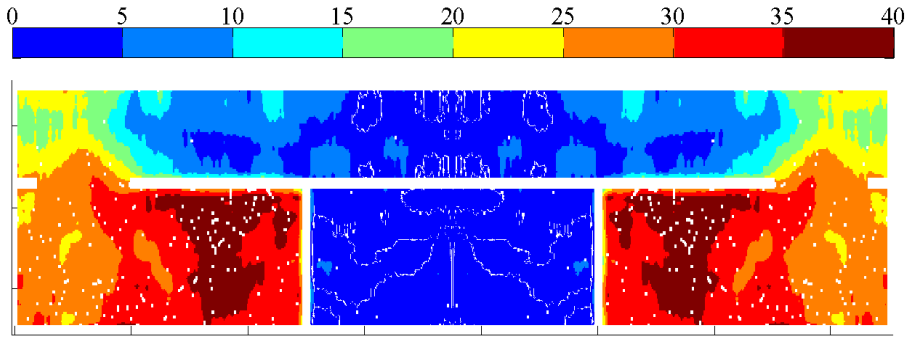

(b) Building with two CR-FSS installed

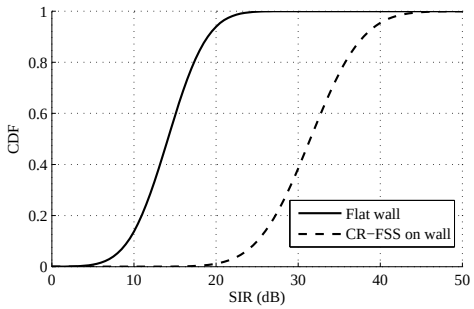

(c) CDF of transmitting room

Figure 7.20: Signal-to-interference plots for the respective in-building simulations at 2.4 GHz.

The plots in Fig. 7.20 show that much higher SIR is possible in the rooms, and indeed in the corridor regions when the CR-FSS is installed in the building. The results of these simulations are to be used as a proof of concept rather than for specific numerical analysis, particularly due to the inaccuracies of the building fabric.

For completion, the SIR plots are shown for 1.5 GHz in Fig. 7.21 for an unlined corridor, and one with a CR-FSS installed. Little difference in SIR can be seen in the individual rooms, confirming that the CR-FSS does not effect the propagation at this frequency.

It is difficult to quantify whether the amount of attenuation shown in these scenarios is good enough to disrupt multipath propagation in an indoor environment. We can consider that a range of variables will alter the propagation and ability to isolate rooms sufficiently. Firstly, the antennas themselves can transmit at a range of frequencies, distances, and have different gains, transmission powers, and receiver sensitivities. The propagation environment will also vary a great deal with the building structure being composed of different materials and furniture. It has however been acknowledged in [89] that various other solutions only offer up to 20 dB attenuation in shielded rooms, and only when doors are closed. Furthermore, results in [90] for an absorber lined corridor show improvements in SNR ranging from 10 to 30 dB, depending on reflectivity of the absorber used.

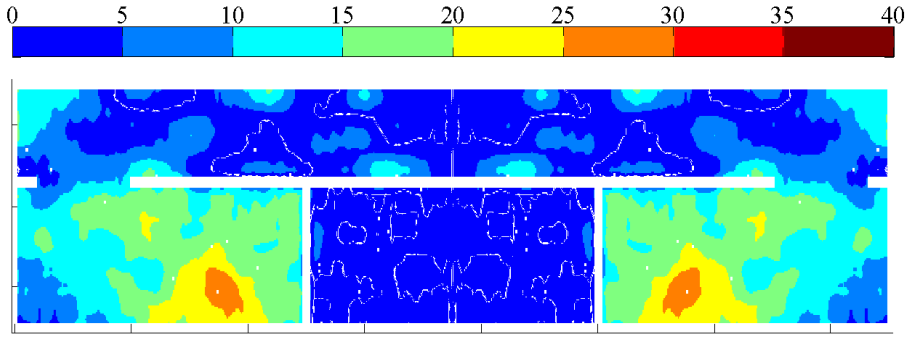

(a) Unlined building

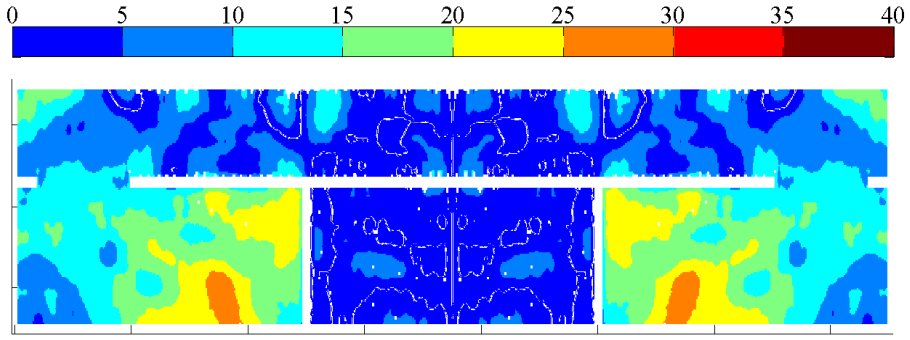

(b) Building with two CR-FSS installed

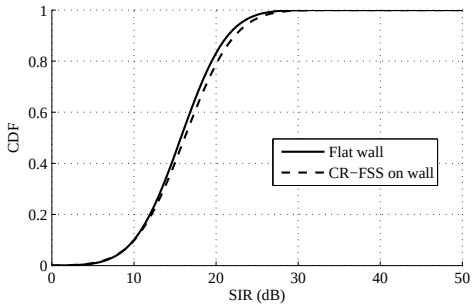

(c) CDF of transmitting room

Figure 7.21: Signal-to-interference plots for the respective in-building simulations at 1.5 GHz.

7.11 Conclusions

This chapter is used as a validation of the comb reflection frequency selective surface (CR-FSS) and the application in a corridor. The initial sections of the chapter considered the optimisation of a structure for 2.4 GHz for both TE and TM polarisation for a range of angles of incidence so that it would be suitable for use in a multipath environment. Although initially designed to operate solely in the 2.4 GHz band, the second harmonics lie in the 5 to 6 GHz region, meaning that the higher frequency Wi-Fi bands may be affected.

Following this, in-building propagation simulations were run on CST MWS. The model was constructed using PEC walls for accurate comparison of the the unlined and CR-FSS lined corridors, whilst also serving to increase simulation time. Each model was finely meshed to accurately simulate the effect of multiple repetitions of the comb structure. In order to increase simulation time whilst maintaining E-field accuracy the building was modelled with no roof or floor.

Cumulative distribution function (CDF) plots for two frequencies (1.5 GHz and 2.4 GHz) show both the out-of-band and in-band performance respectively. At 1.5 GHz, there is no reduction of E-field in the 'Empty room' despite the use of the CR-FSS lined corridors; whereas at 2.4 GHz there is significant reduction of E-fields. The performance of a wireless system can thus be summarised using signal-to-interference ratio (SIR) plots, where once again at 2.4 GHz the performance of Wi-Fi transmitters is shown to be increased in individual rooms due to the electromagnetic separation down the corridor.

Chapter 8

Conclusions

Concluding remarks on the work conducted in this Thesis. Includes a summary of the research, the contribution to current and state-of-the-art literature in the field of electromagnetics, and the potential for use in future work.

8.1 Thesis summary

This thesis has investigated the use of a range of passive frequency selective structures that can be used to reduce specular reflections from propagating signals. Furthermore, these reflections can be redirected at a pre-defined backscatter angle. The main application of such a structure is in a corridor environment, where multipath and oblique propagations are common. In particular, wireless friendly and energy efficient buildings have become increasingly popular for research, whereby frequency selective surfaces (FSS) are utilised to isolate wireless networks from each other for the purpose of security, reduced interference, and increased network capacity. Despite the installation of FSS in metallic walls, propagation down corridors has the potential to reduce the performance of these solutions.

This work offers several contributions to the design and analysis of passive FSS and to the study of electromagnetic propagation as a whole. The design and measurement of several passive structures have been conducted to understand their performance in multipath environments. A bi-static three dimensional measurement system was developed and optimised for the purpose of measuring such structures and measurement result coincide well with CST MWS simulation work. Finally, CST MWS was used for in-building propagation studies and provides a method of

validation of the comb reflection FSS (CR-FSS) at 2.4 GHz.

Several criteria were initially used to define the design stages of the passive FSS structures. These were:

- The surface should be cheap to manufacture and should add limited additional cost to the normal design of a building.
- As it is proposed to be installed in a corridor environment, the structure height should be assumed to be an important design consideration.
- The surface should reduce specular propagations at a variety of angles of incidence down the corridor environment. This is in both the azimuth and elevation planes of incidence.
- Performance should be adequate for both transverse electric (TE) and transverse magnetic (TM) polarisations.

A variety of measurement and simulation results are presented, some requiring more complex measurement systems such as the automated bi-static measurement rig described in chapter A.2 for analysis of full scattering patterns of a variety of reflective FSS. Initial surface design work began with investigation of existing comb structures and their scattering performance and particularly how well they reduce specular reflections. The use of a comb reflection frequency selective surface (CR-FSS) to achieve good reductions in specular scatter, re-directing this in a pre-defined direction based on frequency and angle of incidence is described in chapter 3.

A pin reflection FSS (PR-FSS) is designed to overcome some of the shortcomings of the CR-FSS in chapter 4 by producing a rotationally symmetrical surface, however the performance at TE polarisation is significantly reduced. Thus, it can be expected that there will be a trade-off when comparing both surfaces when applied to a multi-path environment. This is likely to be scenario specific and decisions will likely to have to be made during the design stage of any building modifications.

Further surface designs include a slanted comb FSS (SC-FSS) detailed in chapter 5. The idea for this structure stems from trying to reduce the effective height of the comb structure, thus making it more plausible for a variety of applications where

space is a decisive factor. The design, simulation, and manufacture of such surfaces have shown to be more difficult than basic comb or pin structures, making mass-production more expensive and time consuming. Furthermore, simulation and measurement results show that the angular stability of such surfaces is not as good as previous surface designs, making its multipath performance less understandable.

Chapter 6 details the final structure investigated. The initial idea of the crenelated CR-FSS stems from the production of the CR-FSS from foam materials, which were found to be susceptible to damage and difficult to line with foil. Increasing the crenelation angle of the surface structure is found to add structural support, however its scattering characteristics subsequently change. It can be broadly said that the reduction in specular scatter is reduced when the crenelation angle is increased.

A final validation and optimisation of the CR-FSS at 2.4 GHz is conducted in CST MWS. This includes choice of parameters which make the specular scatter reductions overlap at 2.4 GHz for both TE and TM polarisation, whilst maintaining adequate angular stability over a wide range of angles of incidence. Full in-building simulations show that by installing the pre-designed structure in a corridor environment, a frequency selective performance can be achieved. Scenario examples show that at 1.5 GHz the structure does not effect the propagation of signals at all; however, at 2.4 GHz there is a large reduction in signal level. Cumulative distribution function (CDF) plots are used to statistically prove the effectiveness of the CR-FSS structure.

8.2 Contribution to existing literature

The work described in this Thesis offers an additional method of increasing the electromagnetic separation of co-channel transmitting nodes in a building by reducing the propagation down a corridor. This is most likely to be in a scenario either where there are multiple 2.4 GHz transmitters or in a building which has been designed to be wireless friendly with the use of metallic walls (used for isolation of rooms). The work detailed in this Thesis has contributed to several areas of propagation in the following ways:

- **Consideration of the propagation down corridors** - before this research,

wireless friendly building design did not consider the issue of preventing propagation down corridors. The main aim was to isolate individual rooms using metallic walls, and have control over which frequencies can pass to other parts of the building using FSS. Ideally this is fine, however users of buildings often leave doors open and the doors themselves can leak electromagnetic energy due to air gaps if they are poorly fitted in the building. Propagation down corridors offer several design issues such as the requirement for oblique incidence performance and sufficient bandwidth over a range of angles.

- **Design, measurement, and simulation of a variety of surface structures** - Four different passive surface structures are investigated for their suitability to reduce specular reflections. The majority of this work covers the design of such structures and their advantages/disadvantages in reducing specular scatter for both TM and TE polarisation. Some structures are effective for both (CR-FSS), whilst others are useful for only one polarisation, but offer reduction for a range of azimuth and elevation angles (PR-FSS). Furthermore, implementation in narrow corridors using slanted-comb FSS (SC-FSS) and surfaces with ease of production considered (crenelated CR-FSS).

- **Use of the rotational scattering measurement system in other PhD projects** - the bi-static rotating measurement system described in Chapter A.2 is being used in current PhD projects, utilising the time domain gating features implemented in this project to improve measurement accuracy.

- **Published papers on the subject area** - to date, the work from this Thesis has been disseminated in several journals and at a variety of conferences including two IEEE Transactions.

8.3 Further work

During the course of the PhD work many further ideas have been considered. This section details those thoughts based on reading literature in the area, discussion with colleagues, and work that could be completed to reinforce research described

in this Thesis.

8.3.1 In-situ measurements

Following the simulation of building propagation in chapter 7, it is proposed that an in-situ experimental measurement be conducted to evaluate the performance of a CR-FSS structure installed in a corridor. Potential cost and installation difficulties will make this a difficult task and the potential outputs at this stage of research were deemed non-essential considering both surface characterisation and in-building simulations have been performed. This would also give an understanding the optimisation of such surfaces in a real life scenario.

8.3.2 Further indoor simulations

Work conducted in chapter 7 can be further expanded to understand the effect of multiple transmitters (not limited to 2) on the signal-to-interference ratio (SIR). This will also offer an insight into the performance of the CR-FSS in much larger buildings rather than just one corridor.

Furthermore, following the measurement of building materials in section **??**, their effect on propagation can not be under valued. The in-building simulations in this Thesis consider only PEC walls for the purpose of speed of simulation and exact comparison of unlined and CR-FSS lined corridor walls. The placement of plasterboard materials on top of the CR-FSS structures is likely to have an effect on reduction frequency ranges and possibly performance despite their low relative permittivity.

8.3.3 Active Structures

Active structures are becoming increasingly popular in in-building propagation control, particularly for their ability to change transmission characteristics, as previously described in the literature review in this thesis. The analysis and design of the pin reflection FSS (PR-FSS) in chapter 4 for example, was conducted in the hope of transforming this surface into a switchable active surface. The pins in this case would be able to be disconnected and reconnected to the ground plane in order to

change its scattering characteristics.

A three dimensional microstrip surface was modelled using CST and simulated, initially using ideal open and short circuits between the pin and ground plane. Results of the specular scatter showed that there was a significant difference between both cases. Further implementation of the surface using controllable pin diodes to switch between each case showed that although the specular scatter region could be altered, it did not match the performance of the perfect open and short cases. Nonetheless, this is a possible area for future research in electromagnetic scattering of three dimensional periodic structures.

References

[1] G.H.-H. Sung, K.W. Sowerby, M.J. Neve and A.G. Williamson, "A Frequency-Selective Wall for Interference Reduction in Wireless Indoor Environments," *IEEE Antennas Propag. Mag.*, vol. 48, no. 5, pp. 29–37, 2006.

[2] Channel Deployment Issues for 2.4-GHz 802.11 WLANs, Cisco Systems, CA, USA, 2004.

[3] Office of Communications, *UK Interface Requirement 2005 - UK Radio Interface Requirement for Wideband Transmission System operating in the 2.4 GHz ISM Band and Using Wide Band Modulation Techniques*. London, UK, 2006.

[4] Linksys, Differentiating the 5 GHz and 2.4 GHz frequency bands, white paper, 2014.

[5] Office of Communications, *UK Interface Requirement 2006 - Wireless Access Systems (WAS) including RLANs operations in the 5150-5725 MHz band*. London, UK, 2006.

[6] Netgear, *Why choose Simultaneous Dual Band?*, San Jose, CA, 2011.

[7] Cisco, *The Zettabyte Era: Trends and Analysis*, White Paper, 2014.

[8] Office of Communications, *Communications Market Report 2013*. London, 2013.

[9] Department of Energy and Climate Change, *Energy Efficiency Strategy - 2013 Update*. London, UK, 2013.

[10] Communities and Local Government, Consultation on policy options, *Zero carbon for new non-domestic buildings*, 2009.

[11] UK Green Building Council. (2011, Sept 07). Zero Carbon Homes. Available: http://www.ukgbc.org/site/info-centre/display-category?id=22

[12] A.K. Brown, "The Wireless Friendly Building," *Loughborough Antennas and Propagation Conference (LAPC)*, pp. 62–66, 2010.

[13] The University of Sheffield, WiFEEB Project, Available: http://eeepro.shef.ac.uk/wifeeb/objectives.html

[14] W. Rotman, "A Study of Single-Surface Corrugated Guides," *Proceedings of the IRE*, vol. 39, no. 8, pp.952–959, 1951.

[15] J. Heath, and E. Jull "Total backscatter from conducting rectangular corrugations," *IEEE Trans. Antennas Propag.*, vol. 27, no. 1, pp. 95–97, 1979.

[16] A.K. Bhattacharyya and S. Tandon, "A corrugated surface with low backscatter," *IEEE Trans. Antennas Propag.*, vol. 32, no. 8, pp. 870–872, 1984.

[17] G. Ebbeson, "The use of fin-corrugated periodic surfaces for the reduction of interference from large reflecting surfaces", Thesis, University of British Columbia, USA, 1974.

[18] R. Geise, A. Enders, H. Vahle and H. Spieker, "Scaled Measurements of Instrument-Landing-System Disturbances Due to Large Taxiing Aircraft," *IEEE Trans. Electromagnetic Compatibility*, vol.50, no.3, pp.485–490, 2008.

[19] E.V. Jull, and J.W. Heath, "The Reduction of Interference from Large Reflecting Surfaces," in *IEEE Trans. Antennas Propag.*, vol. 25, no. 4, pp. 565–570, 1977.

[20] E.V. Jull, and J.W. Heath, "Conducting surface corrugations for multipath interference suppression," in *Proceedings of the Institution of Electrical Engineers*, 1978, pp. 1321–1326.

[21] Airbus Group (2014). "EADS Innovation Works teams with Airbus to create "Stealthy" airport buildings", [Online]. Available: http://www.airbus-group.com/airbusgroup/int/en/our-innovation/latest-news/EADS-Innovation-Works-teams-with-Airbus-to-create–stealthy–airport-buildings.html

[22] A. Thain, J.-P. Estienne, J. Robert, G. Peres, G. Cambon, L. Evain and B. Spitz, "Controlling propagation environments using Intelligent Walls," in *Proceedings of 6th European Conference on Antennas and Propagation (EUCAP)*, Prague, 2012, pp.2392–2395.

[23] W.H. Bragg and W.L. Bragg, "The structure of the Diamond," *Proc. of the Royal Society of London. Series A*, vol. 89, no. 610, pp. 277–291, 1913.

[24] K.A. Jose, and K.G. Nair, "Reflector-backed perfectly blazed strip gratings simulate corrugated reflector effects," *Electron. Lett.*, vol. 23, no. 2, pp. 86–87, 1987.

[25] A.R. Chandran, T. Mathew, C.K. Anandan, P. Mohanan, and K. Vasudevan, "Frequency tunable metallo-dielectric structure for backscattering reduction," *Electron. Lett.*, vol. 40, no. 20, pp. 1245–1246, 2004.

[26] G. Whitman and F. Schwering, "Scattering by periodic metal surfaces with sinusoidal height profiles–A theoretical approach," *IEEE Trans. Antennas Propag.*, vol. 25, no. 6, pp. 869–876, 1977.

[27] C. Molero, R. Rodriguez-Berral, F. Mesa and F. Medina, "Analytical Circuit Model for 1-D Periodic T-Shaped Corrugated Surfaces," *IEEE Trans. Antennas Propag.*, vol. 62, no. 2, pp. 794–803, 2014.

[28] R. Rodriguez-Berral, C. Molero, F. Medina and F. Mesa, "Analytical Wideband Model for Strip/Slit Gratings Loaded With Dielectric Slabs," *IEEE Trans. Microwave Theory & Techniques*, vol. 60, no. 12, pp. 3908–3918, 2012.

[29] H. Kapasi, J. Blackburn and C. Mias, "The use of corrugated surfaces to improve wireless signal strength in the shadow region of buildings," *Microw. and Opt. Techn. Let.*, vol. 46, no. 5, pp. 467–469, 2005.

[30] P. Kyritsi and D.C. Cox, " Propagation characteristics of horizontally and vertically polarized electric fields in an indoor environment: simple model and results", *IEEE Vehicular Technology Conference*, 2001.

[31] D.C. Cox, R.R. Murray, H.W. Arnold, A. Norris and M. Wazowicz,"Cross-polarization coupling measured for 800 MHz radio transmission in and around houses and large buildings", *IEEE Trans. Antennas Propag.*, vol. 34, no. 1, pp. 83–87, 1986.

[32] J.-B. Yan and J.T. Barnhard, "Investigation of the Influence of Reflective Insulation on Indoor Reception in Rural Houses" in *IEEE Antennas Wireless Propag. Lett.*, vol. 10, pp. 423–426, 2011.

[33] L. Subrt, P. Pechac, A. Vallecchi, L. Ford, R. Langley and J. Rigelsford, "Advanced modelling of intelligent walls for indoor smart environments", *8th European Conference on Antennas and Propagation (EuCAP)*, 2014, pp. 620–622.

[34] L. Subrt, P. Pechac, L. Ford, R. Langley, R and J. Rigelsford, "Controlling coverage for indoor wireless networks using Metalized Active FSS Walls," *Asia-Pacific Conference on Communications (APCC)*, 2013, pp. 496–500.

[35] M. Gustafsson, A. Karlsson, A.P.P. Rebelo, and B. Widenberg, "Design of Frequency Selective Windows for Improved Indoor Outdoor Communication" *IEEE Trans. Antennas Propag.*, vol. 54, no. 6, pp. 1897–1900, 2006.

[36] BRE, Passivhaus primer: Designer's guide: A guide for the design team and local authorities, UK.

[37] F.A. Chaudhry, M. Raspopoulos and S. Stavrou, "Effect of Frequency Selective Surfaces on radio wave propagation in indoor environments," in *Proceedings of 11th European Wireless Conference on Next Generation Wireless and Mobile Comms. and Services*, Nicosia, Cyprus, 2005, pp.1–6.

[38] G.H.-H. Sung, K.W. Sowerby and A.G. Williamson, "Modeling a Low-Cost Frequency Selective Wall for Wireless-Friendly Indoor Environments," *IEEE Antennas and Wireless Propag. Lett.*, vol. 5, pp. 311–314, 2006.

[39] J.C. Batchelor, E.A. Parker, B. Sanz-Izquierdo, J.-B. Robertson, I.T. Ekpo and A.G. Williamson, "Designing FSS for wireless propagation control within buildings," in *Proceedings of Loughborough Antennas and Propagation Conference*, Loughborough, 2009, pp. 14–17.

[40] M. Raspopoulos and S. Stavrou, "Frequency Selective Buildings Through Frequency Selective Surfaces", in *Proceedings of Loughborough Antennas and Propagation Conference*, Loughborough, 2011, pp. 2998–3005.

[41] S.N. Azemi, K. Ghorbani, W.S.T. Rowe, "Angularly Stable Frequency Selective Surface With Miniaturized Unit Cell," *IEEE Microwave and Wireless Components Letters*, vol. 25, no. 7, pp. 454–456, 2015.

[42] Remcom, Wirless Insite EM software, http://www.remcom.com/wireless-insite, Accessed: 2015.

[43] B. Sanz-Izquierdo, I.T. Ekpo, B. Robertson, E.A Parker and J.C. Batchelor, "Wideband EM architecture of buildings: six-to-one dual-passband filter for indoor wireless environments" *Electron. Lett.*, vol. 44, no. 21, pp. 1268–1269, 2008.

[44] L. Subrt, D. Grace and P. Pechac, "Controlling the Short-Range Propagation Environment Using Active Frequency Selective Surfaces" *Radioengineering*, vol.19, no.4, pp.610–617, 2010.

[45] L. Subrt and P. Pechac, "Influence of Modelling Diffraction on Electromagnetic Wave Propagation Predictions in Subterranean Galleries," in *Proceedings of 5th European Conference on Antennas and Propagation (EUCAP)*, Rome, 2011, pp.1651–1654.

[46] L. Subrt and P. Pechac, "Intelligent walls as autonomous parts of smart indoor environments," *IET Comms.*, vol.6, no.8, pp.1004–1010, 2012.

[47] B. Munk, "Frequency Selective Surfaces: Theory and Design", 2000.

[48] S. Genovesi, F. Costa and A. Monorchio, "Low-Profile Array With Reduced Radar Cross Section by Using Hybrid Frequency Selective Surfaces," *IEEE Trans. Antennas Propag.*, vol. 60, no. 5, pp. 2327–2335, 2012.

[49] S. Simms, and V. Fusco, "Chessboard reflector for RCS reduction," *Electron. Lett.*, vol. 44, no. 4, pp. 316–317, 2008.

[50] M. Paquay, J.-C. Iriarte, I. Ederra, R. Gonzalo and P. de Maagt, "Thin AMC Structure for Radar Cross-Section Reduction," *IEEE Trans. Antennas Propag.*, vol. 55, no. 12, pp. 3630–3638, 2007.

[51] E. Doumanis, G. Goussetis, G. Papageorgiou, V. Fusco, R. Cahill and D. Linton, "Design of Engineered Reflectors for Radar Cross Section Modification," *IEEE Trans. Antennas Propag.*, vol. 61, no. 1, pp. 232–239, 2013.

[52] D. Lynch, *Introduction to RF Stealth*, Hertfordshire, UK: SciTech, 2004.

[53] J. Pinto, J.C.G. Matthews and G.C. Sarno, "Stealth technology for wind turbines," *IET Radar, Sonar, & Nav.*, vol.4, no.1, pp. 126–133, 2010.

[54] R. Natarajan, M. Kanagasabai, S. Baisakhiya, R. Sivasamy, S. Palaniswamy and J.K. Pakkathillam, "A Compact Frequency Selective Surface With Stable Response for WLAN Applications,"*IEEE Trans. Antennas Propag.*, vol. 12, pp. 718–720, 2013.

[55] L. Subrt and P. Pechac, "Controlling propagation environments using Intelligent Walls," in *Proceedings of 6th European Conference on Antennas and Propagation (EUCAP)*, Prague, 2012, pp.26–30.

[56] D. Stolhofer, H. Doelecke, Y. Liu and P. O'Leary, "Rf Propagation Through Transparent Conductors In Energy Efficient Windows," in *Proceedings of IEEE European Wireless Conference*, Lucca, Italy, 2010, pp. 177–181.

[57] S.I. Sohail, G.I. Kiani and K.P. Esselle, "Enhancing RF/microwave efficient transmission through energy saving glass windows using Frequency Selective surface," in *Proceedings of 2011 IEEE International Symposium on Antennas and Propagation (APSURSI)*, Washington, USA, 2011, pp. 2262-2263.

[58] A. Munir, V. Fusco and O. Malyuskin, "Tunable Frequency Selective Surfaces Characterisation," in *38th European Microwave Conference*, Amsterdam, The Netherlands, 2008, pp. 813–816

[59] B. Sanz-Izquierdo, E.A. Parker, J.-B. Robertson, and J.C. Batchelor, "Tuning patch-form FSS," *Electron. Lett.*, vol. 46, no. 5, pp. 329–330, 2010.

[60] B. Sanz-Izquierdo, E.A. Parker, J.-B. Robertson, and J.C. Batchelor, "Tuning technique for active FSS arrays," *Electron. Lett.*, vol. 45, no. 22, pp. 1107–1109, 2009.

[61] C. Mias, "Varactor-tunable and dipole-grid-based frequency-selective surface," *Microwave and Optical Tech. Lett.*, vol. 43, no. 6, pp. 508–511, 2004.

[62] G.I. Kiani, K.L. Ford, L.G. Olsson, K.P. Esselle and C.J. Panagamuwa, "Switchable Frequency Selective Surface for Reconfigurable Electromagnetic

Architecture of Buildings," *IEEE Trans. Antennas Propag.*, vol. 58, no. 2, pp. 581–584, 2010.

[63] G.I. Kiani, K.P. Esselle, A.R. Weily and K.L. Ford, "Active frequency selective surface using PIN diodes," in *Proceedings of IEEE Antennas and Propagation Society International Symposium*, Hawaii, USA, 2007, pp. 4525–4528.

[64] D. Sievenpiper, Z. Lijun, R. F. J. Broas, N. G. Alexopolous and E. Yablonovitch, "High-impedance electromagnetic surfaces with a forbidden frequency band," *IEEE Trans. Microw. Theory Techn.*, vol. 47, no.11, pp.2059–2074, 1999.

[65] Ford, K.L.; Rigelsford, J.M., "Street Furniture Antenna Radiation Pattern Control Using AMC Surfaces," *IEEE Trans. Antennas Propag.* , vol.56, no.9, pp.3049–3052, 2008.

[66] W.W. Salisbury "Absorbent body for electromagnetic wave," U.S. Patent 2 599 944, June 10, 1952.

[67] R.L. Fante, "Reflection Properties of the Salisbury Screen," *IEEE Trans. Antennas Propag.*, vol. 36, no. 10, pp. 1443–1454, 1988.

[68] B. Chambers and A. Tennant, "Characteristics of a salisbury screen radar absorber covered by a dielectric skin," *Electron. Lett.*, vol. 30, no. 21, pp. 1797–1799, 1994.

[69] A. Tennant and B. Chambers, " Single-Layer Tuneable Microwave Absorber Using an Active FSS," *IEEE Microwave and Wireless Components Lett.*, vol. 15, no. 1, pp. 46–47, 2004.

[70] K.J. Vinoy and R.M. Jha, Radar Absorbing Materials: From Theory to Design and Characterization, 1996.

[71] P. Saville, "Review of Radar Absorbing Materials", Technical Memorandum, Defence Research and Development Canada, Canada, 2005.

[72] K.L. Ford and B. Chambers, "Application of Impedance Loading to Geometric Transition Radar Absorbent Material," *IEEE Trans. Electromagnetic Comp.*, vol. 49, no. 2, pp. 339–345, 2007.

[73] K.L. Ford, D.G. Holtby and B. Chambers, "Oblique Incidence Optimisation of a Pyramidal Absorber using a Frequency Selective Surface," in *Proceedings of 4th European Conference on Antennas and Propagation (EUCAP)*, Barcelona, 2010, pp.1–4.

[74] B. Chambers and K.L. Ford, "Topology for tunable radar absorbers," *Electron. Lett.*, vol. 36, no. 1, pp. 50–52, 2000.

[75] D.G. Holtby, K.L. Ford and B. Chambers, "Optimisation of a Stepped Permittivity Impedance Loaded (SPIL) Absorber," *Electronics Letters*, vol. 45, no. 7, p. 339, 2009.

[76] F.C. Smith, B. Chambers, J.C. Bennett, "Calibration techniques for free space reflection coefficient measurements," *Science, Measurement and Technology, IEE Proceedings A* , vol. 139, no. 5, pp.247–253, 1992.

[77] CST Microwave Studio, Performance (2013). [Online]. Available: https://www.cst.com/Products/CSTmws/Performance

[78] CST Microwave Studio, (2013). [Online]. Available: http://www.cst.com

[79] Celotex, celotex wall insulaton, Available: http://www.celotex.co.uk/applications/wall-insulation

[80] K. Pahlavan and P. Krishnamurthy, "Network Planning," in Principles of Wireless Networks: A Unified Approach, London, UK, Prentice Hall, 2002, ch. 5, sec. 5, pp. 237.

[81] G. Whitman and F. Schwering, "Reciprocity identity for periodic surface scattering," *IEEE Trans. Antennas Propag.*, vol. 27, no. 2, pp. 252–254, 1979.

[82] M.J. Neve, M. Leung and J. Cater, "Inter-Building Propagation Modelling for Indoor Wireless Communications System Deployment", in *Proceedings of 8th European Conference on Antennas and Propagation (EUCAP)*, Prague, 2014, pp.791–793.

[83] N. Albano, M. Canaletti, A. D'Orazio, M. De Sario, G. Gaudino, V. Petruzzelli and F. Prudenzano, "Measurements and Modeling of Propagation Losses in Buildings at 1.8 GHz and 2.1 GHz", *IEEE Antennas and Propagation Society International Symposium*, pp. 3089–3092, 2006.

[84] D.J.Y. Lee, W.C.Y. Lee, "Propagation Prediction in and Through Buildings", *IEEETrans. on Vehicular Tech.*, Vol. 49, No.5, 1529–1533, 2000.

[85] S.E. Alexander, "Radio propagation within buildings at 900 MHz," *Electron. Lett.*, vol. 18, no. 21, pp. 913–914, 1982.

[86] Y.H. Alharbi, J.M. Rigelsford, R.J. Langley and A.O. Al Amoudi, "Analysis of wireless propagation within a Victorian house for smart meter applications," *Loughborough Antennas and Propagation Conference (LAPC)*, pp. 519–522, 2014.

[87] J.-V. Rodriguez, M. Gustafsson, F. Tufvesson, A. Karlsson and L. Juan-Llacer, "Frequency-selective wallpaper for reducing interference while increasing MIMO capacity in indoor environments," in *Proceedings of 2nd European Conference on Antennas and Propagation (EUCAP)*, 2007.

[88] A.C.M. Austin, M.J. Neve and G.B. Rowe, "Modelling interference for indoor wireless systems using the FDTD method, in *IEEE Antennas and Propagation Society International Symposium*, pp.1–4, 2009.

[89] D.C.K. Lee, M.J. Neve, K.W. Sowerby, "The Impact of Structural Shielding on the Performance of Wireless Systems in a Single-Floor Office Building," *IEEE Trans. Wireless Comms* , vol. 6, no. 5, pp.1787–1695, 2007.

[90] K.L. Ford, "Investigation of the Use of Absorbing Materials for Indoor Co-Channel Applications" in *Proceedings of 9th European Conference on Antennas and Propagation (EUCAP)*, Lisbon, 2015.

[91] Agielnt Technologies, "Agilent Time Domain Analysis Using a Network Analyzer", *Application Note 1287-12*, 2012.

[92] R.B. Dybdal, "Radar cross section measurements," *Proceedings of the IEEE*, vol. 75, no. 4, pp. 498–516, 1987.

[93] M.C. Rezende, I.M. Martin, M.A.S. Miacci and E.L. Nohara, "Radar cross section measurements (8-12 GHz) of flat plates painted with microwave absorbing materials," in *Proceedings of the 2001 International Microwave and Optoelectronics Conference*, Belem, Brazil, 2001, pp. 263–267.

[94] McCool TD, "Analysis and testing of a bistatic radar cross section measurement capability for the AFIT anechoic chamber", M.Sc. thesis, Departmnet of the Air Force Air University, Air Force Institute of Technology, OH., USA, 1990.

[95] Hauck B, Ulaby F, DeRoo R. "Polarimetric Bistatic-Measurement Facility for Point and Distributed Targets," *IEEE Antennas and Propagation Magazine*, Vol. 40, No.1, 31–41, 1998.

[96] Bellez S, Roussel H, Dahon D, Geffrin J-M. "A rigorous forest scattering model validation through comparison with indoor bistatic scattering measurements," *Progress In Electromagnetics Research B*, Vol. 33, 1-19, 2011.

[97] Escot-Bocanegra D, Poyatos-Martınez D, Montiel-Sanchez I, Saez de Adana FM, Gonzalez-Diego I. "Spherical indoor facility applied to bistatic radar cross section measurements," *Progress In Electromagnetics Research Letters*, Vol. 26, 181-187, 2011.

[98] Escot D, Poyetos D, Aguilar JA, Montiel I, Gonzalez I, de Adana FS, "Indoor 3D Full Polarimetric Bistatic Spherical Facility for Electromagnetic Tests," *IEEE Antennas and Propagation Magazine*, Vol. 52, No. 4, 112–118, 2010.

[99] Chung BK, Chuah HT, Bredow JW. "A microwave anechoic chamber for radar-cross section measurement," *IEEE Antennas and Propagation Magazine*, Vol. 39, No.3, 21–26, 1997.

[100] Keysight Technologies, "A Comparison of Agilent 20 GHz Microwave Network Analyzers 8720D and 8720ES versus PNA-L N5230C", *Technical Overview*, 2008.

[101] ABB - Motion control and software tools, (2014). [Online]. Available: http://www.baldormotion.com/products/mint/overview.asp

[102] Holtby DG. Impedance loaded geometric transition absorbers [dissertation]. Sheffield (UK): The University of Sheffield; 2010.

[103] Keysight Technologies, "Time Domain Analysis Using a Network Analyzer", *Application Note*, 2014.

[104] Agilent Technologies, "Agilent 8719D, 8720D, and 8722D Network Analyzers", *Data Sheet*, 2000.

[105] Knott EF, Shaeffer J, and Tuley N, "Chapter 1: Introuduction", *Radar Cross Section*, pp. 12, 2004.

Appendix A

Appendices

A.1 A note on mode-matching

Although the work covered in this Thesis does not directly mention mode-matching techniques, an analytical based paper was published by the author, with results that could be directly applicable to the research conducted as part of this PhD work. As well as the development of mathematical principles for the analysis of periodic comb surfaces, experimental and CST simulation results were conducted to characterise and validate the structures and mathematical approach.

The paper, '*A mode matching technique for analysis of scattering by periodic comb surfaces*' is overleaf.

A Mode Matching Technique for Analysis of Scattering by Periodic Comb Surfaces

Pavel Valtr, Christopher J. Davenport, Pavel Pechac, *Senior Member, IEEE,* and Jonathan M. Rigelsford, *Senior Member, IEEE*

***Abstract*—Numerical techniques for calculating electromagnetic fields within three dimensional surfaces are computationally intensive. Therefore, this paper presents the application of a mode-matching technique developed for analyzing electromagnetic scattering from periodic comb surfaces illuminated by a plane wave. A set of linear equations have been developed to calculate mode coefficients of the field distribution for both E-polarized and H-polarized incident waves. Analysis is performed for two cases where the comb thickness is either infinitely thin or of a finite thickness. The technique is shown to accurately predict both field intensities within the near-field of the periodic surface and far-field scattering patterns. Results are compared to those obtained using the finite integration techniques (FIT) implemented in CST Microwave Studio. Furthermore, numerical results are compared to measurements of an aluminum prototype. Additional far-field scattering measurements using a bi-static system provide additional confidence in CST simulations and the mode-matching methods presented here.**

***Index Terms*—Mode matching, electromagnetic scattering, periodic structures, CST Microwave Studio.**

I. Introduction

The use of periodic structures and surfaces to control scattering of electromagnetic waves has been comprehensively investigated. Their use in both indoor and outdoor environments have been explored. Typical examples include using periodic comb surfaces for reducing the interference caused by an Instrument Landing System (ILS) at airports [1]. Alternatively, corrugated surfaces can be used to improve signal coverage close to a building due to surface wave propagation [2]. The control of propagation in indoor environments was described in [3], where various periodic structures can reduce the specular scatter down corridors. By suppressing interference between adjacent co-channel Wi-Fi access points, signal coverage can be improved [4].

Manuscript received 18th November, 2014. This work was supported by FP7 Marie Curie IAPP project No. 286333 WiFEEB - Wireless Friendly Energy Efficient Buildings.

P. Valtr and P. Pechac are with the Department of Electromagnetic Field, Faculty of Electrical Engineering, Czech Technical University in Prague, Technicka 2, 166 27 Prague 6, Czech Republic (e-mail: Pavel.Valtr@fel.cvut.cz, pechac@fel.cvut.cz).

C.J. Davenport and J.M. Rigelsford are with the Department of Electronic & Electrical Engineering at The University of Sheffield, Sir Frederick Mappin Building, Mappin Street, Sheffield, S1 3JD, UK (e-mail: christopher.davenport@sheffield.ac.uk, j.m.rigelsford@sheffield.ac.uk)

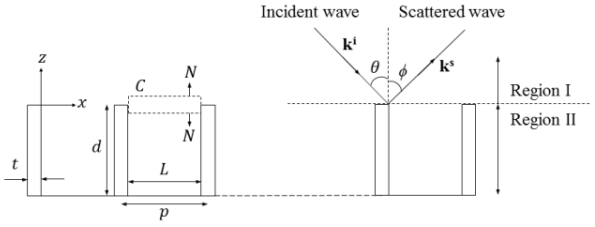

Fig. 1. Geometry of the corrugated surface problem.

Mathematically, the scattering properties of periodic comb surfaces were studied by several authors [5, 6]. In [7], a mode matching technique was applied to scattering by an inclined strip grating and in [8] this method was used to arrive at simple approximate closed-form formulas for mode coefficients of a parallel-plate waveguide. In this work we apply mode-matching technique to solve the problem of scattering by a comb grating structure. Analytical solutions have been applied to many different periodic structures, such as sinusoidal [9], saw-shaped [10], and comb [11] gratings. A comparison of different methods is described in [12], with the scattering from a sinusoid considered with use of the Masel, Merrill, and Miller (MMM) method [13], the Modified Physical Optics (MPO) method [14], and Waterman's Plane Harmonics (WPH) [15] method all discussed. Mode matching methods have been investigated in [16], where the analysis is based on Green's second theorem, describing the integration around a closed contour. Various periodic structures such as high impedance surfaces (HIS) are analyzed using the mode matching analysis in [17].

In this paper, we present a mode-matching solution to the scattering and fields within a periodic comb surfaces, reinforced by CST simulations and experimental measurement of an aluminum surface. Building on the work referenced above, we present analytical solutions for calculating the electric field within or above a comb surface. Equations are developed for both TE and TM polarizations and can be applied to combs having any finite thickness. This enables computationally fast analysis of periodic scattering surfaces.

Section II introduces the use of Floquet scattering modes in combination with waveguide cavity theory to calculate field distribution of a periodic comb structure. Section III provides a generic field matching solution, whereby the thickness of the fins does not affect the analytical solution, to calculate the

respective field at a certain position on the structure. Section IV uses the electric field calculation for infinitely thin fins (t=0) to calculate the far-field scattering pattern of the structure. These analytical results are verified using CST simulations. Section V expands on the field calculation to consider when there is a finite thickness to the fins (t>0). Once again, CST simulations are produced to compare to our analytical results. Section VI uses experimental measurements and further CST simulations to further verify the analytical work presented in this paper. The paper is concluded in Section VII.

II. Analytical Formulation

In this section we present the analytical formulation of the equations required to calculate the electromagnetic fields within a periodic comb surface. A two-dimensional geometry of the periodic surface and incident wave is shown in Fig. 1. The structure consists of perfectly conducting periodic fins of thickness t on a ground plane. In contrast to previous research [17], this work considers surfaces which are electrically large in terms of the wavelength of the illuminating source. The period and height of the fins are denoted by p and d, respectively. The inner distance between the fins is L, where $L = p - t$. Mathematically, the problem is split into two different regions, where the field is calculated by different equations. Region I is positioned above the structure at z>0. Region II occurs in the structure itself, at distance -d<z<0. These regions are labelled as I and II (see Fig. 1).

The electromagnetic plane wave illuminating the periodic surface, is represented by the vector $\mathbf{k}^i$ and is incident in Region I at an angle, θ and is reflected (as specular scatter) at an angle, ϕ. The angles θ and ϕ are positive when the x-component of $\mathbf{k}^i$ and $\mathbf{k}^s$ are respectively in the positive direction of x-axis. The scattering scenario is treated as a two-dimensional problem within the x-z plane.

Using the time harmonic phasor form ($e^{j\omega t}$) of an incident plane wave illuminating the surface expressed as:

$$e^{-j(\alpha_0 x - \beta_0 z)} \tag{1}$$

the resulting wave is scattered from the periodic surface and can be expressed as the summation of spatial harmonics based on Floquet theory [18], namely:

$$\sum_{m=-\infty}^{\infty} A_m e^{-j(\alpha_m x + \beta_m z)} \tag{2}$$

Then the total field in Region I, representing the y-component of electric or magnetic field intensity in the case of a TE or TM polarized incident wave, can therefore be expressed as:

$$\psi^I = e^{-j(\alpha_0 x - \beta_0 z)} + \sum_{m=-\infty}^{\infty} A_m e^{-j(\alpha_m x + \beta_m z)} \tag{3}$$

Where unitary amplitude of incident wave is assumed, k_0 is the wave number, and where α and β are x and z components of k_0, respectively.

$$\alpha_m = \alpha_0 + \frac{2\pi m}{p} \tag{4a}$$

$$\beta_m = \sqrt{{k_0}^2 - {\alpha_m}^2} \tag{4b}$$

and

$$\alpha_0 = k_0 sin\theta \tag{4c}$$

Due to the electrically large size of the features of the periodic surface, the total field in Region II can therefore be written as a summation of forward-travelling and reflected wave within a waveguide cavity as:

$$\psi_{TE}^{II} = \sum_{m=1}^{\infty} B_m sin\frac{m\pi x}{L}\left[e^{jk_m z} - e^{-jk_m(2d+z)}\right] \tag{5a}$$

in the case of TE-polarized incident wave and as

$$\psi_{TM}^{II} = \sum_{m=0}^{\infty} B_m cos\frac{m\pi x}{L}\left[e^{jk_m z} + e^{-jk_m(2d+z)}\right] \tag{5b}$$

in the case of TM-polarized incident wave. Where the imaginary part of k_m must be negative to ensure wave attenuation along the z-axis:

$$k_m = \sqrt{{k_0}^2 - \left(\frac{m\pi}{L}\right)^2} \tag{6}$$

Equation 2a and 2b enable us to develop a series of analytical formula described in the following sections of this paper.

III. Generic Field Matching Solution For Fins of Arbitrary Thickness

In this section we develop a generic field matching solution for the periodic surface illustrated in Fig. 1 comprising of fins of arbitrary thickness. Such a solution enables us to predict the field distribution within or near to an infinite periodic structure. The validity of the theory is assumed for structures with a finite number of fins as well.

Firstly this has been achieved by developing the work published in [7, 8] to utilize Green's second theorem [19] in order to match fields ψ^I and ψ^{II}. By selecting the integration path intersecting regions I and II, thus relating both fields in one equation. Therefore Green's second theorem can be expressed in the form

$$\oint_C \left(\phi \frac{\partial \psi}{\partial N} - \psi \frac{\partial \phi}{\partial N}\right) dl = \iint_S (\phi \nabla^2 \psi - \psi \nabla^2 \phi)\, ds \tag{7}$$

where the integration is made along an arbitrary closed curve, C and forms a boundary of surface, S. The curve C is represented by its outer normal, N. The function ϕ is an auxiliary function; in the case where ϕ satisfies Helmholtz equation, the right side of (7) is equal to zero. In our case the curve C is chosen as indicated in Fig. 1, where the integration is completed over one period of the grating. The contribution to the integral is in both directions of the x-axis only; the contribution in the direction of z-axis is negligible. Assuming ϕ satisfies Helmholtz equation, (7) yields

$$\int_0^L \left(\phi \frac{\partial \psi^I}{\partial z} - \psi^I \frac{\partial \phi}{\partial z}\right) dx + \int_L^0 \left(\phi \frac{\partial \psi^{II}}{\partial z} - \psi^{II} \frac{\partial \phi}{\partial z}\right) dx = 0 \tag{8}$$

In general, ψ^I and ψ^{II} are expressed using an infinite number of coefficients: A_m and B_m, for ψ^I and ψ^{II} respectively. Practically, the number of coefficients is limited as m = -M,…, -1, 0, 1, …, M in the case of A_m coefficients and m = 1, 2, …, 2M + 1 in the case of B_m coefficients, resulting in overall number of unknowns in (8) equal to 4M + 2. Therefore 2M + 1 of pairs of linearly independent equations are needed to solve for A_m and B_m coefficients. This is achieved by selecting 2M + 1 linearly independent pairs of ϕ as

$$\phi_n^{+TE} = sin\left(\frac{n\pi x}{L}\right) e^{-jk_n z} \tag{9a}$$

$$\phi_n^{-TE} = sin\left(\frac{n\pi x}{L}\right) e^{jk_n z} \tag{9b}$$

for TE polarization where n = 1, 2, …, 2M+1. Similarly, they can be represented as

$$\phi_n^{+TM} = cos\left(\frac{n\pi x}{L}\right) e^{-jk_n z} \tag{9c}$$

$$\phi_n^{-TM} = cos\left(\frac{n\pi x}{L}\right) e^{jk_n z} \tag{9d}$$

for TM polarizations where n = 0, 1, …, 2M. Inserting (3), (5) and (9) in (8) gives following set of linear equations that are used to calculate A_m and B_m.

$$\sum_{m=-\infty}^{\infty} (\beta_m - k_n) \cdot F_{n,m} A_m + G_n B_n = (\beta_0 + k_n) \cdot F_{n,0} \tag{10a}$$

$$\sum_{m=-\infty}^{\infty} (\beta_m + k_n) \cdot F_{n,m} A_m + G_n{}' B_n = (\beta_0 - k_n) \cdot F_{n,0} \tag{10b}$$

Where

$$F_{n,m} = \frac{n\pi/L}{(n\pi/L)^2 - \alpha_m{}^2}[1 - e^{-j\alpha_m L} cos(n\pi)] \quad \text{for TE pol.} \tag{11a}$$

$$F_{n,m} = \frac{j\alpha_m}{(n\pi/L)^2 - \alpha_m{}^2}[1 - e^{-j\alpha_m L} cos(n\pi)] \quad \text{for TM pol.} \tag{11b}$$

and where

$$\begin{aligned} G_n &= k_n L \\ G_n{}' &= k_n L e^{-2jk_n d} \end{aligned} \quad \text{for TE pol.}$$

$$\begin{aligned} G_n &= 2k_n L \\ G_n{}' &= -2k_n L e^{-2jk_n d} \end{aligned} \quad \text{for TM pol.}, n = 0$$

$$\begin{aligned} G_n &= k_n L \\ G_n{}' &= -k_n L e^{-2jk_n d} \end{aligned} \quad \text{for TM pol.}, n \neq 0$$

The field distribution within or near to the structure is now readily available using (3, 5) with use of A_m and B_m coefficients, that are in turn obtained by solving the set of equations (10). As Region I and Region II have to be identical at the boundary (z=0), the number of harmonics in each region must be the same i.e. 2M+1. This is also necessary for the numerical stability of solving Eq. 10a and 10b. In general, for a given geometry the number of modes considered M, must increase as the frequency of interest increases. For the examples presented in this work M=19, although M=7 would provide comparable results for frequencies up to 20 GHz.

A. Comparison of analytical simulation with CST for infinitely thin combs

The analytical solution generated in the previous section is compared to the finite integral technique (FIT)-based software CST Microwave Studio [20], in order to verify the theoretical prediction of field distribution by (3, 5) using coefficients obtained by the procedure described earlier in this section. For both the analytical solution and the CST simulation, the tested periodic surface consists of 12 fins separated by a fin period, p of 20 mm. The height d of each fin, d is 50 mm. The width of the structure along the y-axis direction is 400 mm. CST simulations were performed for both the full 3D structure and the representative 2D structure using periodic boundaries as described in [4] which is more computationally efficient.

The magnitude of the y-component of the electric field intensity, E_y for TE, and magnetic field intensity, H_y for TM polarized incident waves are shown in Fig. 2, where $E_y = \psi^I$ and $H_y = \psi^I / Z_0$. The field is calculated with respect to unitary amplitude of incident electric field intensity. The observation point is in the center of the structure at height z = 20 mm and -20 mm. The field intensity is shown as a function of frequency for incidence angle θ = 50˚. The predicted field outside (z = 20 mm) and inside (z = -20 mm) the structure are shown in Fig. 2 and Fig. 3 respectively. The results show that there is excellent agreement between the mode-matching approach described previously, and the fully numerical solution obtained by CST.

It can be observed that the CST simulation result for 2D and 3D cases are almost identical.

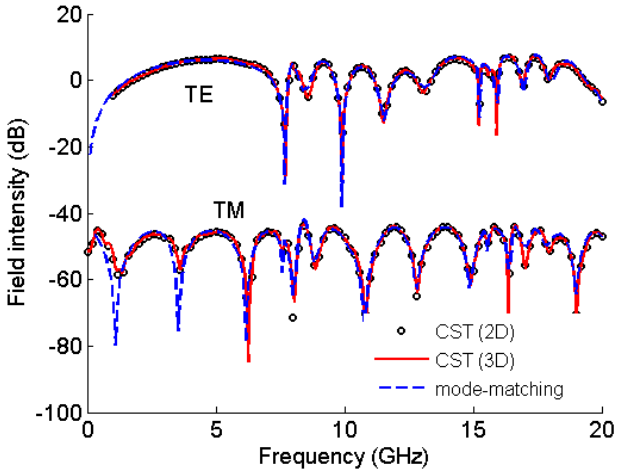

Fig. 2. Comparison of modelling results; considering the field outside the structure at [x; y; z] = [11 cm; 0 cm; 2 cm].

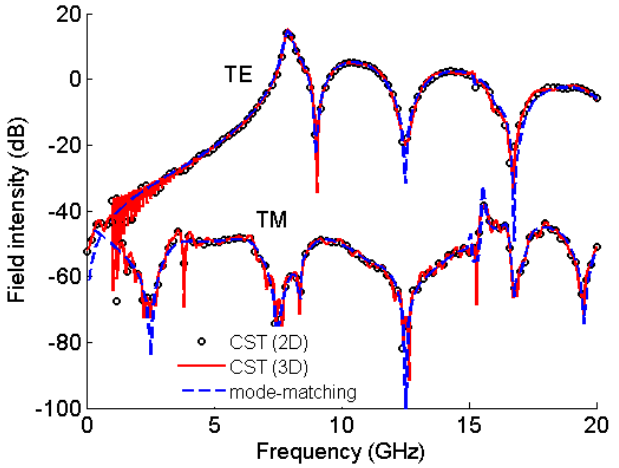

Fig. 3. Comparison of modelling results; now considering the field inside the structure at [x; y; z] = [11 cm; 0 cm; -2 cm].

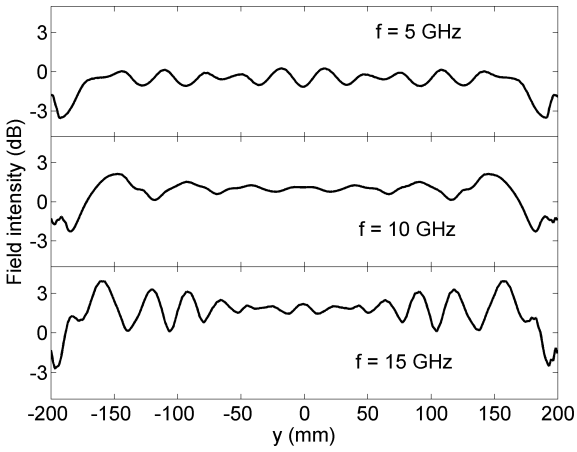

Fig. 4. Field amplitude as a function of *y* (x = 11 cm, z = 0 cm) for TE-polarized wave and for three distinct frequencies 5 GHz, 10 GHz and 15 GHz.

The CST simulated *E*-field intensity on the boundary of the two regions as a function of y-dimension (x = 11cm, z= 0 cm) is shown in Fig. 4 documenting that the field along the y-axis can be considered roughly invariant.

As well as obtaining accurate results for the examples given in this paper, the analytical mode-matching method several orders of magnitude faster than CST. For example, for a computer with a 2.83 GHz processor and 8 GB RAM, the mode matching technique takes 200 ms to analyze the structure for one polarization and 200 frequency points as shown in Figs 2 and 3. The calculation of the same result using CST takes approximately 10 minutes for the 3D case and approximately 60 seconds for the 2D case.

B. Comparison of analytical results with CST for combs with a thickness greater than zero

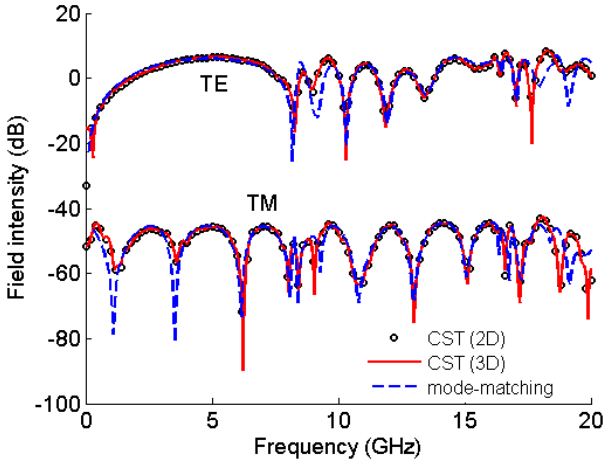

Fig. 5. Comparison of modelling results; considering the field on the boundary of the Region I and Region II, [x; y; z] = [11 cm 0 cm 2 cm]. For a thickness, t = 1.6 mm

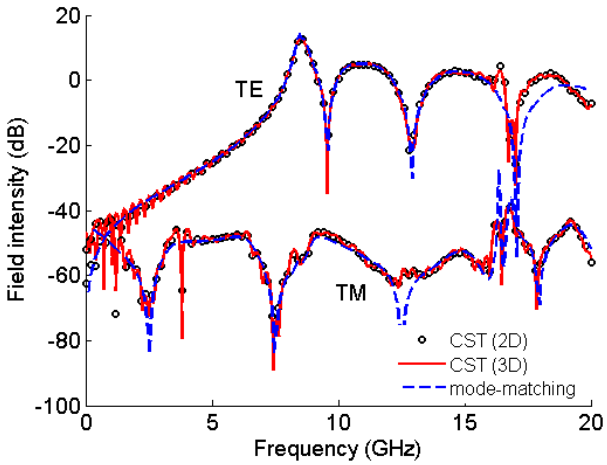

Fig. 6. Comparison of modelling results; field on the boundary of the Region I and Region II, [x; y; z] = [11 cm 0 cm -2 cm]. For a thickness, t = 1.6 mm

Numerical simulations and the proposed analytical technique are compared for fins of non-zero thickness is shown in Figs. 5 and 6 for surfaces with a thickness of 1.6 mm. The results show there is still a good agreement between the proposed approach

based on mode matching and the fully numerical solution by CST for non-zero thickness. Increased fin thickness lowers the separation of the plates of the waveguide formed by the fins and shifts the frequency pattern in Figs. 5 and 6 towards higher frequencies compared to the case of infinitely thin fins. This applies only to TE polarization, however. For TM polarization the fin thickness is not significant.

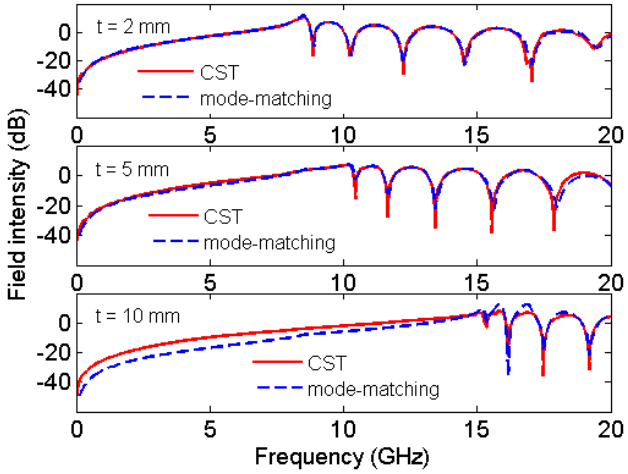

Fig. 7a. Comparison of modelling results for TE polarization; field on the boundary of the Region I and Region II, [x; y; z] = [11 cm 0 cm 0 cm]. Thickness *t* varies from 2.0 mm to 10 mm as indicated.

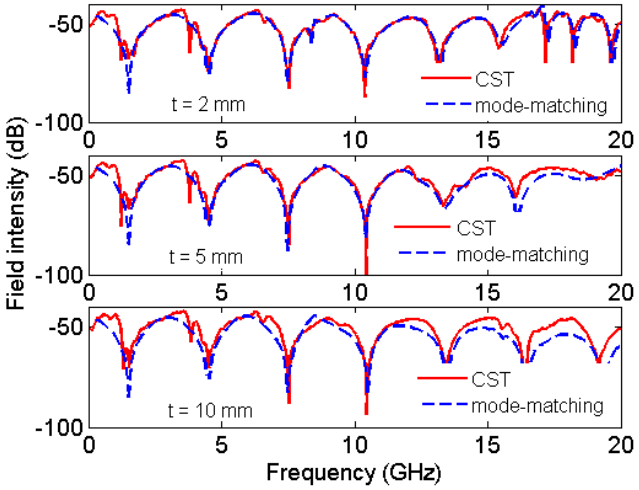

Fig. 7b. Comparison of modelling results for TM polarization; field on the boundary of the Region I and Region II, [x; y; z] = [11 cm 0 cm 0 cm]. Thickness *t* varies from 2.0 mm to 10 mm as indicated.

To investigate the influence of the fin thickness t on the mode-matching simulation accuracy, comparisons have been made for three cases (t = 2 mm, t = 5 mm and t = 10 mm) while keeping the fins' period constant (p = 20 mm). The resulting comparisons can be seen in Fig. 7a and 7b for TE and TM polarization, respectively. It can be observed that the two results correspond quite well for smaller fin thickness (where t/p <= 0.25) while diverging for increased fin thickness (where t/p = 0.5).

IV. Far-Field Scattering for Infinitely Thin Combs

In order to calculate the far-field scattering by the periodic surface with infinitely thin combs, the scattered component of the field $\psi^I(x, y)$ has to be calculated at points where z=0 and integrated over the surface of the structure using Kirchhoff-Huygens principle as [21]

$$E_s = \frac{jk_0}{4\pi r}\int_{-t}^{X}\int_{-W/2}^{W/2}\psi_s{}^I(x,0)e^{jk_0 x\sin\phi}(\cos\theta+\cos\phi)\,dydx \tag{12}$$

where

$$\psi_s{}^I(x,z) = \sum_{m=-\infty}^{\infty} A_m e^{-j(\alpha_m x+\beta_m z)} \tag{13}$$

and where the exponential term in (12) represents the phase shift relative to an element at x=0. The phase term $e^{-jk_0 r}$ is neglected in (12). W is the width of the structure measured along the y-axis and X is the dimension of the structure along the x-axis which can be expressed as $X = (N_f - 1)\cdot p$ where N_f is the number of fins and p is the fin period. The distance, r is the distance between the surface and the receiving point, and is the same for all points on the structure due to the far-field scattering assumption. Evaluating (12) gives the far-field scattering at a distance r in the x-z plane as a function of incidence, θ and scattering angle, ϕ.

$$E_s = \frac{k_0 W(\cos\theta+\cos\phi)}{4\pi r}\sum_{m=-\infty}^{\infty} A_m \frac{e^{-j(\alpha_m - k_0\sin\phi)X}-1}{k_0\sin\phi-\alpha_m} \tag{14}$$

Fig. 8 shows the far-field scattering pattern of the structure as a function of scattering angle, ϕ at a frequency of 12 GHz. In this case, the fins of the structure are infinitely thin. The angle of incidence, θ is 50°. In this case, the reference distance for the pattern calculation was 1 m. relatively good agreement can be observed between the CST prediction and mode matching simulation using (14). Our mode matching equations offer a good prediction of the expected CST result in a much faster

$$E_s{}^{TE} = \frac{k_0 W}{4\pi r}(\cos\theta+\cos\phi)\sum_{n=0}^{N_f-2}\sum_{m=-\infty}^{\infty}\frac{A_m e^{j(k_0\sin\phi-\alpha_m)np}}{k_0\sin\phi-\alpha_m}\left[e^{j(k_0\sin\phi-\alpha_m)L}-1\right] \tag{15}$$

$$E_s{}^{TM} = \frac{k_0 W}{4\pi r}(\cos\theta+\cos\phi)\left(\sum_{n=0}^{N_f-2}\sum_{m=-\infty}^{\infty}\frac{A_m e^{j(k_0\sin\phi-\alpha_m)np}}{k_0\sin\phi-\alpha_m}\left[e^{j(k_0\sin\phi-\alpha_m)L}-1\right]-\sum_{n=0}^{N_f-1}\frac{e^{jk_0(\sin\phi-\sin\theta)np}}{k_0(\sin\phi-\sin\theta)}\left[1-e^{-jk_0(\sin\phi-\sin\theta)t}\right]\right) \tag{16}$$

solver time, with small discretion for $\phi > 75°$ and $\phi < -55°$ for TE and TM polarization.

V. Far-field Scattering for Combs with a Thickness Greater than Zero

A similar approach as in Section IV was used to derive formulas analogical to (14) for a structure with fins of a thickness greater than zero. Note that the amplitude of ${\psi_s}^I(x,0)$ is equal to zero and one for $n(L+t)-t<x<n(L+t)$ in the case of TE and TM polarization, respectively, due to boundary conditions; $n = 0, 1, \ldots, N_f - 1$. Evaluating (12) and taking into account boundary conditions gives equations (15, 16). Fig. 9 shows the far-field scattering pattern of the structure as a function of scattering angle, ϕ. The periodic structure is the same as in the previous case with exception of thickness of the fins set equal to t = 1.6 mm.

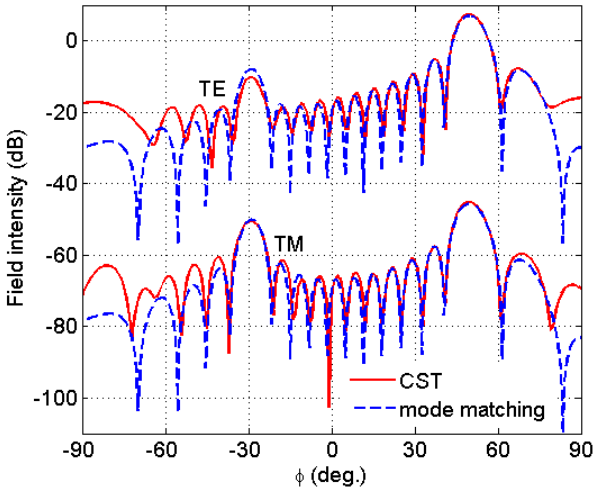

Fig. 8. Comparison of CST modelling results and mode matching formula using equation (10). The far-field scattering pattern for an angle of incidence, θ = 50˚ for t = 0 mm at a frequency of 12 GHz.

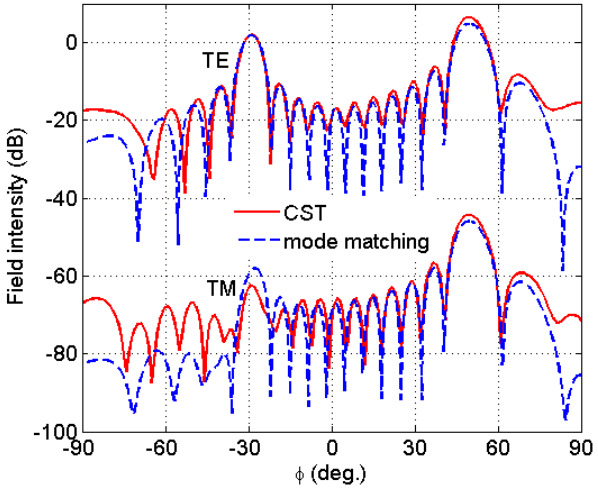

Fig. 9. Comparison of CST modelling results and mode matching formula using equation (10). The far-field scattering pattern for an angle of incidence, θ = 50˚ for t = 1.6 mm at a frequency of 12 GHz.

The frequency of interest is 12 GHz. As can be seen from comparison of Figs. 8 and 9, the fin thickness has an impact on the scattering pattern.

VI. Experimental Measurement of Far-field Characteristics

Further investigation of the far-field characteristics was conducted using CST simulations, the mode-matching method, and retrospective far-field scattering measurements. To perform accurate measurements for comparison and validation of the other two techniques, a prototype aluminum surface was manufactured using bent aluminum strips secured using rivets to an aluminum ground plane, creating a surface with overall dimensions of 621 × 600 mm. The constructed surface had a fin period of 23 mm, height of 50 mm, and thickness of 1.6 mm. The final prototype is shown in Fig. 10.

Measurements of the aluminum surface were conducted to characterize the far-field scattering of the surface, relative to angle of scatter. These were conducted in a bi-static measurement chamber, developed in [22]. A frequency range of 8 to 18 GHz was measured, using a sweep time of 2 seconds, and intermediate frequency bandwidth (IFBW) of 1 KHz on an Agilent E8720 vector network analyzer (VNA). Relevant time gates were used to remove noise.

Fig. 10. The constructed aluminum surface, with a fin period of 23 mm, height of 50 mm, and thickness of 1.6 mm. The surface has 27 reputations of fins secured on a ground plane of 621 × 600 mm.

A. Far-field measurements at 12 GHz

The scattering from the periodic aluminum prototype and a flat metal plate were measured for both TM and TE polarization, and plots at 12 GHz are shown in Figs. 11 and 12 respecitvely. For TM polarization, there is a clear reduction in specular scatter at 50°, redirected as backscatter at approximately -20°. Due to the large beamwidth of the horn antenna, the peak in specular scatter covers a large angle of scatter than in CST simulations and mode-matching solutions. A similar response is shown for TE polarization in Fig. 12, although the surface does not have such a large reduction in specular scatter at this frequency for TE polarization. Once again, there is a peak increase in backscatter at -20°.

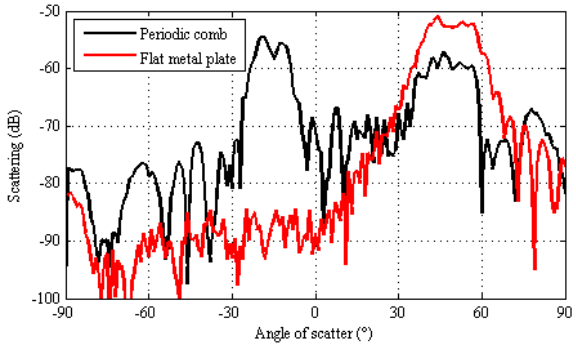

Fig. 11. The far-field scattering pattern for TM polarization at a frequency of 12 GHz, comparing results from the periodic comb and flat plate.

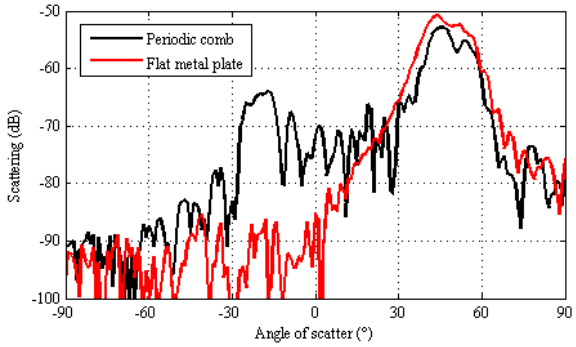

Fig. 12. The far-field scattering pattern for TE polarization at a frequency of 12 GHz, comparing results from the periodic comb and flat plate.

B. Full scattering analysis

Measurement results were extended to produce a scattering measurement across a whole range of frequencies for comparison with both CST simulations and mode-matching results. This was done for TM polarisation and an angle of incidence of 50°.

A full frequency sweep of the scattering characteristics using the bi-static measurement system is shown in Fig. 13. The main scattering lobes can be compared to Figs. 14, where a similar response is obtained using the mode matching technique, whilst illuminated with a unitary amplitude plane wave and receiver reference distance equal to 1 meter. For both cases it is possible to see the sweeping backscatter angle as the frequency increases. As previously described in literature this is linked to Bragg's Law [4, 22]. The beamwidth in Fig. 13 is much larger due to the types of antenna horn used in measurement.

Simulation results of the CST model in Fig. 15 reveal an identical response to that Fig. 14, showing that the mode-matching technique can be used to accurately obtain results much more quickly than measurements and numerical techniques.

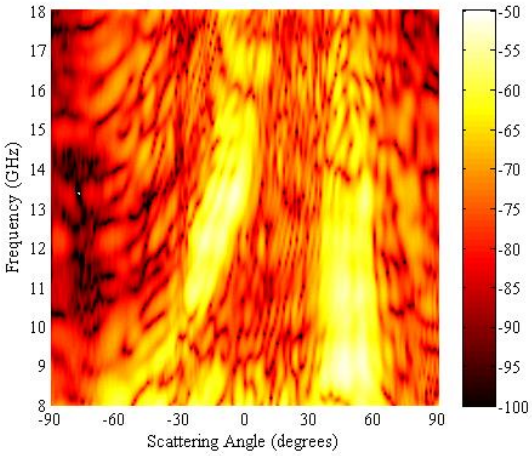

Fig. 13. The measured scattering magnitude for a frequency of 8 GHz and 18 GHz between scattering angles of -90° and 90° for TM polarization.

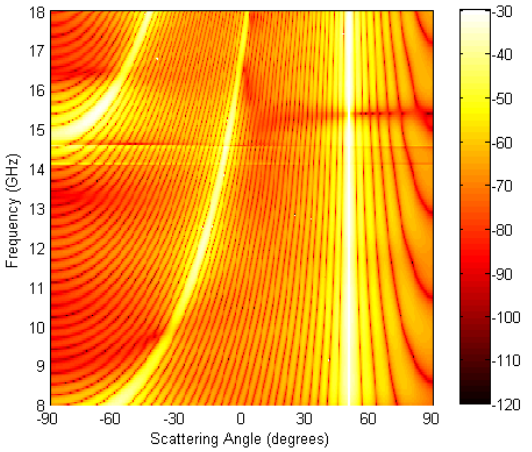

Fig. 14. The mode matching scattering magnitude for a frequency of 8 GHz and 18 GHz between scattering angles of -90° and 90° for TM polarization.

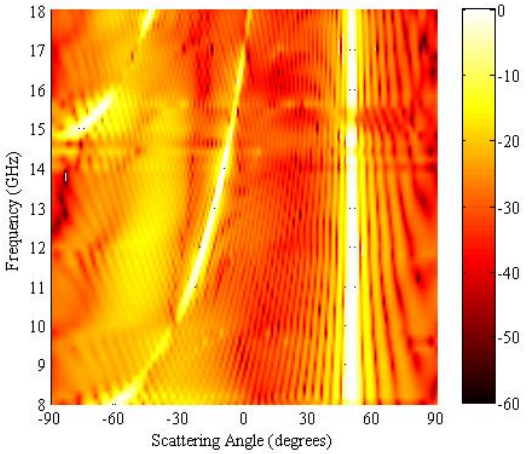

Fig. 15. CST simulation plot of the scattering magnitude for a frequency of 8 GHz and 18 GHz between scattering angles of -90° and 90° for TM polarization.

VII. Conclusions

In this work we have presented a novel mode-matching technique that is suitable for calculating the electric and magnetic fields within the near-field region of a periodic comb surface and the resultant far-field scattering pattern. The fields can be expressed as an infinite sum of modes and the coefficients of individual modes are obtained by solving the proposed set of linear equations. The proposed technique is suitable for analysis of such surfaces illuminated by both E-polarized and H-polarized incident waves. Analysis has been performed for two cases where the comb thickness is either infinitely thin or of a finite thickness. Calculated results are in good agreement to those obtained using the finite integration techniques (FIT) implemented in CST Microwave Studio (CST MSW). Our mode matching technique is computational faster by several orders of magnitude when compared to FIT. Furthermore, numerical results are compared to measurements of an aluminum prototype. Far-field scattering measurements are obtained using a bi-static system. These results provide additional confidence in the validity of CST simulations and the mode matching methods presented within this paper.

References

[1] A. Thain, J. P. Estienne, J. Robert, G. Peres, G. Cambon, L. Evain and B. Spitz, "A solution for ILS disturbance due to a building," in *European Conf. on Antennas and Propagation (EuCAP)*, Prague, Czech Rep., 2012, pp. 2392–2395.

[2] H. Kapasi, J. Blackburn and C. Mias, "The use of corrugated surfaces to improve wireless signal strength in the shadow region of buildings," *Microw. and Opt. Techn. Let.*, vol. 46, no. 5, pp. 467-469, Sept., 2005.

[3] C. J. Davenport, J. M. Rigelsford, J. Zhang and H. Altan, "Periodic comb reflection frequency selective surface for interference reduction," in *Antennas and Propag. Conf. (LAPC)*, Loughborough, UK, 2013, pp. 615–618.

[4] C. J. Davenport and J. M. Rigelsford, "Specular Reflection Reduction using Periodic Frequency Selective Surfaces," *IEEE Trans. Antennas Propagat.*, vol. 62, no. 9, pp. 4518–4527, 2014.

[5] T. J. Park and H. J. Eom, "TE-scattering and reception by a parallel-plate waveguide array," *IEEE Trans. Antennas Propagat.*, vol. 42, no. 6, pp. 862–865, June 1994.

[6] G. A. Kriegsmann and B. J. McCartin, "Scattering by a rectangular corrugated surface: an approximate theory," *IEEE Trans. Antennas Propagat.*, vol. 44, no. 8, pp. 1193–1194, Aug. 1996.

[7] E. E. Kriezis and D. P. Chrissoulidis, "EM-wave scattering by an inclined strip grating," *IEEE Trans. Antennas Propagat.*, vol. 41, no. 11, pp. 1473–1480, Nov. 1993.

[8] P. Valtr and P. Pechac, "Closed-form approximation for parallel-plate waveguide coefficients," *Radioengineering*, vol. 22, no. 4, pp. 1296–1300, Dec. 2013.

[9] J. L. Uretsky, "The scattering of plane waves from periodic surfaces," *Ann. Phys.*, vol. 33, pp. 400–427, 1965.

[10] P. M. van den Berg, "Diffraction theory of a reflection grating," *Appl. Sci. Res.*, vol. 24, pp. 261–293, July 1971.

[11] E. V. Jull and G. Ebbeson, "The reduction of interference from large reflecting surfaces," *IEEE Trans. Antennas Propagat.*, vol.25, no.4, pp. 565–570, July 1977.

[12] S.-L. Chuang and J. A. Kong, "Scattering of Waves from Periodic Surfaces," *Proceedings of the IEEE*, vol. 69, no. 9, pp. 1132–1144, Sept. 1981.

[13] R. I. Masel, R. P. Merrill and W. H. Miller, "Quantum scattering from a sinusoidal hard wall: Atomic diffraction from solid surfaces", *Phys. Rev. B*, vol. 12, pp. 5545–5551, 1975.

[14] J. A. DeSanto, "Scattering from a sinusoid: Derivation of linear equations for the field amplitudes," *J. Acoust. Soc. Amer.*, vol. 57, pp. 1195–1197, 1975.

[15] P. C. Waterman, "Scattering by periodic surface", *J. Acoust. Soc. Amer.*, vol. 57, pp. 791–802, 1975.

[16] A. I. Papadopoulos and D. P. Chrissoulidis, "EM wave scattering by a dihedral strip grating," *Antennas and Propagation Society International Symposium*, vol. 1, pp.102–106, June 1993.

[17] R.-B. Hwang, "Scattering Characteristics of Plane Wave by a 1D Periodic Structure Consisting of a Cavities Array," in *Periodic Structures: Mode-Matching Approach and Applications in Electromagnetic Engineering*, 1st ed. Singapore, Singapore: John Wiley & Sons, 2013, ch. 6, sec. 1, pp. 246–255.

[18] S. Tretyakov, "Periodical structures, arrays, and meshes," in *Analytical Modeling in Applied Electromagnetics*, Norwood: Artech House, 2003, ch. 4, pp. 69-118.

[19] G. James, "Green's theorm in a plane", in *Advanced Modern Engineering Mathematics*, 3rd ed. Edinburgh, Scotland, Pearson, 2004, ch. 7, sec. 4, pp. 570.

[20] Computer Simulation Technology (CST), [Online]. Available: http://www.cst.com/Content/Products/MWS/Overview.aspx.

[21] H. L. Bertoni, "Diffraction by edges and corners," in *Radio Propagation for Modern Wireless Systems*, New Jersey: Prentice Hall, 2000, ch. 5, pp. 107-139.

[22] C.J. Davenport and J. M. Rigelsford, "Novel indoor bi-static measurement facility for full scattering characterisation of surfaces at oblique incidence," *Journal of Electromagnetic Waves and Applications*, vol. 28. no. 14, pp. 1798–1806, 2014.

Pavel Valtr received his Ing. (M.Sc.) and Ph.D. degrees both in Radio Electronics from the Czech Technical University in Prague, Czech Republic, in 2004 and 2007, respectively.

From 2007 to 2009 he was a Research Fellow at the University of Vigo, Vigo, Spain working on various topics in electromagnetic wave propagation including rough surface and vegetation scattering and land mobile satellite channel modeling. In 2009 he joined the European Space Agency (ESA/ESTEC), Noordwijk, The Netherlands as a Post-Doctoral Research Fellow. Since 2012 he has been with the Czech Technical University in Prague as a Researcher. His research interests include wireless and satellite communications and computational methods in electromagnetics.

Dr. Valtr received the Young Scientist Award of XXVIII General Assembly of the International Union of Radio Science (URSI) in 2005.

Christopher J. Davenport received the M.Eng. degree in Electrical Engineering from the University of Sheffield, Sheffield, UK in 2010.

He has been studying for the PhD degree at the Department of Electronic and Electrical Engineering at the University of Sheffield, since 2011. His current research interests include periodic frequency selective surfaces (FSS), implantable RFID, and active FSS.

Mr Davenport was co-recipient of the 2nd place award at Loughborough Antennas and Propagation Conference (LAPC) for Best Non-Student Paper in 2013.

Pavel Pechac received the M.Sc. degree and the Ph.D. degree in Radio Electronics from the Czech Technical University in Prague, Czech Republic, in 1993 and 1999 respectively. He is currently a Professor at the Department of Electromagnetic Field, Czech Technical University in Prague. His research interests are in the field of radiowave propagation and wireless systems.

Jonathan M. Rigelsford (SM'13) received the MEng and PhD degrees in Electronic Engineering from the University of Hull, Hull, UK in 1997 and 2001 respectively.

From 2000 to 2002, he worked as Senior Design Engineer at Jaybeam Limited, designing antennas for cellular base stations. From late 2002, until 2014 he was a Senior Experimental Officer for the Communications Group within the Department of Electronic and Electrical Engineering, University of Sheffield, Sheffield, UK. He is now a Senior Research Fellow at the same institution.

Dr Rigelsford has been an active member of the Antenna Interface Standards Group (AISG) from 2002 to 2010 being elected to the board of directors during that time. More recently, he has become Secretary to the Wireless Friendly Building Forum, an industrial/academic initiative to promote understanding of radio propagation within the built environments.

His current research interests include RF propagation, adaptive antennas, RFID and cyber security.

A.2 Measurement techniques

This chapter introduces the main measurement techniques used in validating the surfaces built in this thesis. This includes the development of a bi-static measurement system specifically designed for the measurement of reflective frequency selective surfaces. Methods used in removing noise and coupling from measurements are described.

A.2.1 Introduction

The measurement of the frequency selective surfaces investigated in this project is essential for validation of simulations and theoretical predictions. This chapter describes a variety of different issues with measurement, including:

- Naval Research Laboratories (NRL) arch measurement set-up.
- Bi-static scattering measurement design and set-up.
- Time gating techniques for improving measurement accuracy in both experimental systems.
- Target size constraints.
- Calibration and validation of the experimental systems.

To summarise, two main measurement systems and their calibration are discussed. Work on the design and development of the bi-static measurement system is published in a journal paper entitled *"Novel indoor bi-static measurement facility for full scattering characterisation of surfaces at oblique incidence"*.

A.2.2 NRL reflectivity arch

Initial measurements on the prototype surfaces were conducted on the Naval Research Laboratories (NRL) reflectivity arch at the University of Sheffield. The arch illustrated in Fig. A.1a is used to perform specular scatter measurements in the characterisation of the FSS in this thesis.

The experimental set-up consists of a bi-static measurement arrangement, suitable for measuring the specular scatter of any surface positioned on the target area. The transmit and receive antennas are focused on the target, and are positioned manually using an external positioning system. An angular range of 5° to 60° is available for both transmitter and receiver. The angles are measured from the normal to the surface, as shown in Fig. A.1b.

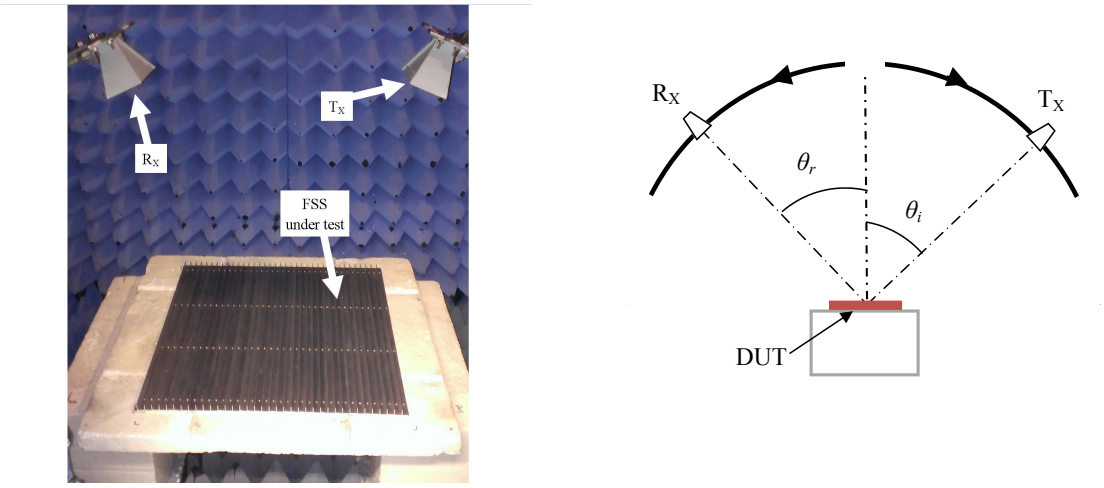

(a) (b)

Figure A.1: (a)The bi-static NRL reflectivity arch used to measure the frequency range of both the CR-FSS and PR-FSS prototypes, (b) a schematic view of the measurement system. The sample is 600 mm^2.

A.2.2.1 Network analyser settings

The 2 port Agilent 8720D vector network analyser (VNA) showin in Fig. A.2 was used to perform S21 measurements in the NRL arch, with the VNA settings displayed in Table A.1. In most measurements, a frequency range of 2 to 18 GHz

was used with 401 discrete points. A sweep time of 2 seconds and an intermediate frequency of 1 kHz was adequate for accurate measurement.

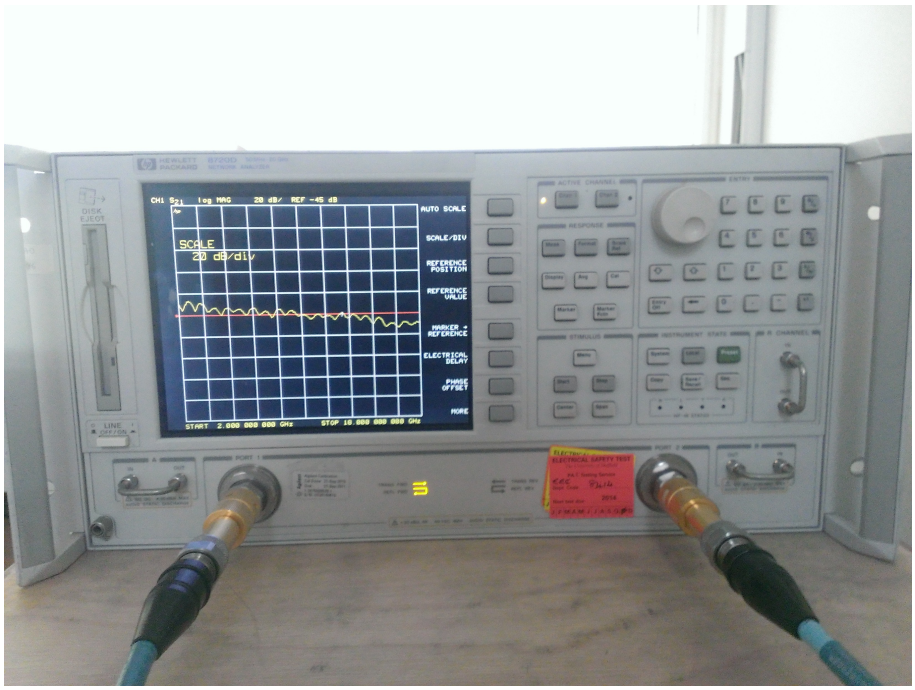

Figure A.2: The Agilent 8720D vector network analyser (VNA) used in both the NRL reflectivity arch and the bi-static measurement chamber.

Although not essential for measurements of this nature, the NRL arch is positioned in an anechoic chamber. Various calibration techniques are used in characterisation of FSS surfaces, and are described here. The measurement steps are shown below:

1. The transmitter angle, θ_i and receiver angle, θ_r are manually positioned.
2. Time gating is applied to remove coupling and reflections from inside the chamber.
3. The flat metal plate is positioned in the target area and the S21 result is saved.
4. The FSS are positioned in the same position as the flat plate, and the S21 result is saved.
5. Steps 4 and 5 are repeated for each θ_i and θ_r angle, and each polarisation. This data is then used to compare the difference between measured magnitudes.

Table A.1: VNA parameters and relevant measurement distances for the NRL reflectivity arch.

Parameter	Value
Start frequency	2 GHz
Stop frequency	18 GHz
Sweep time	2 s
Number of points	401
IF bandwidth	1 kHz
Transmit Power	0 dB
Time gate start	16.1 ns
Time gate stop	17.9 ns
Angular range	5° to 65°
Angular step	1°
Receiver to SUT distance	0.72 m
Transmitter to SUT distance	0.72 m

A.2.2.2 Polarisation of the horn antennas

In this thesis, the polarisation of the horns is described as either transverse magnetic (TM) or transverse electric (TE). For TE modes the magnetic field is perpendicular to the propagation direction, while for TM modes the electric field is perpendicular to propagation.

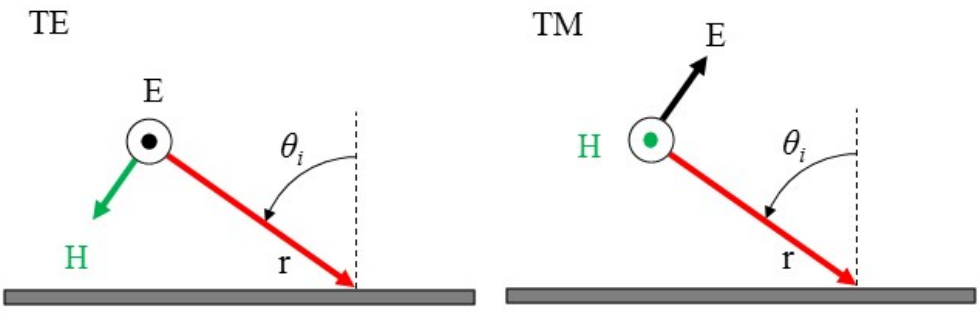

Figure A.3: TE and TM polarisations with respect to direction of propagation, r

A.2.2.3 Calibration of the NRL arch

The process of calibration in the NRL arch is described in more detail in this section. The purpose of calibration is to remove any unwanted received signals that can result in erroneous measurements. A step-by-step guide in the time gating technique used in the measurement of the surfaces in this report is given. The first step is to set up all frequency domain settings such as start and stop frequencies, number of points, IF bandwidth and sweep time as these all alter the time domain response, subsequently changing any time gate which has been implemented.

A time domain measurement of an empty room is then compared to that of a flat plate and compared on screen in the time domain. The main reflection from the plate is easily seen, as shown in Fig. A.4, revealing where respective time gates should be positioned. Unwanted reflections from side walls and metal elements in the room, and the direct line of sight coupling are subsequently time gated out of the measurement.

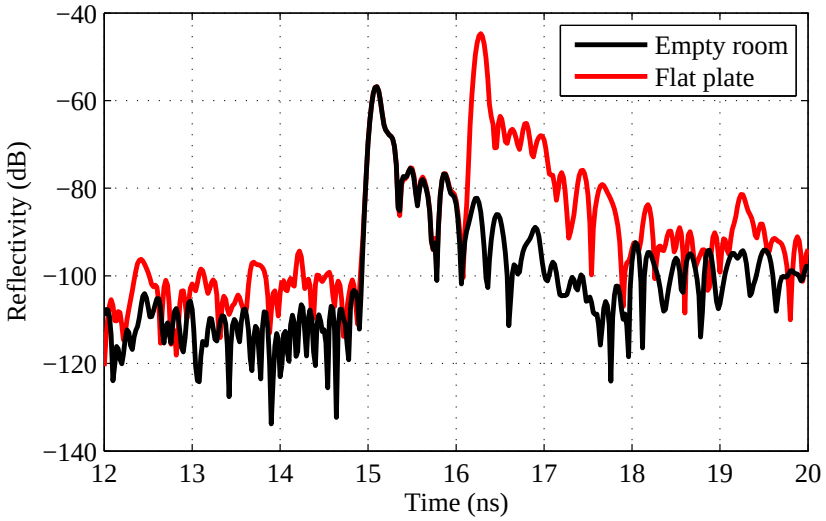

Figure A.4: The time domain response of the empty room and flat plate shows where respective time gates should be positioned.

A time gate is thus applied between 16.1 ns and 17.9 ns and the resultant time domain response is shown in Fig. A.5a. Displaying the frequency domain response reveals a much clearer measurement, as shown in Fig. A.5b. There is a distinguish-

able decrease in measured reflectivity as the frequency increases due to the free space path loss increasing. As long as the gate position encompasses the main peak in the time domain, there should be no substantial change in the frequency domain. [91] . The gate should be wide enough to include important features of the device under test, but discount any reflections from unimportant features or coupling between antennas.

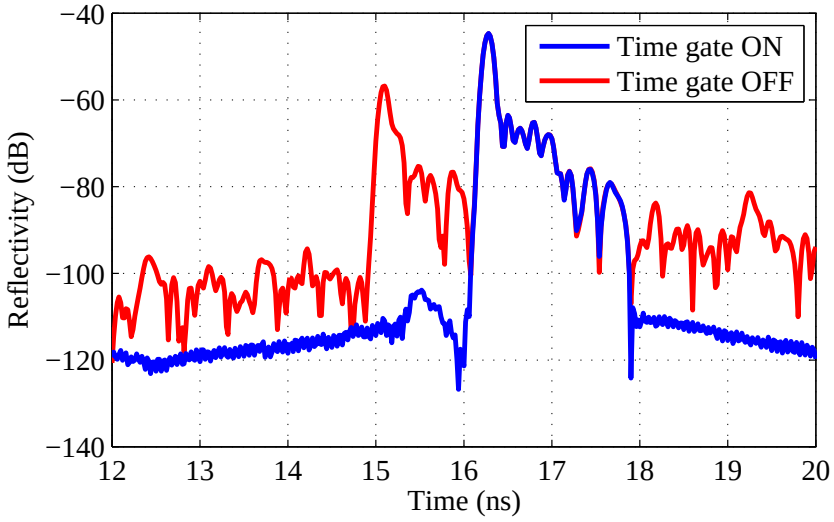

(a)

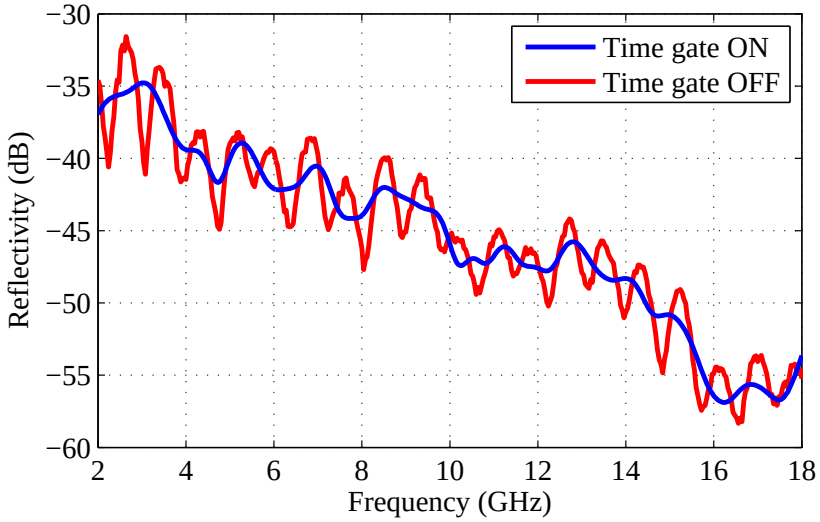

(b)

Figure A.5: The (a) time domain and (b) frequency domain response for a flat PEC plate.

A.2.3 Bi-static measurement chamber

A.2.3.1 Introduction

Although the NRL reflectivity arch can produce very accurate and precise measurement results, it is limited to specular scatter measurements. Results of the backscatter region are not possible due to the design of the system. It was proposed that a bi-static system be developed to perform 360° measurement of any frequency selective surface (FSS) designed in this thesis.

Research of existing bi-static systems are reported in [92–95]; however, many of the current measurement systems have limitations in providing full circular scattering results. The bi-static system described in [96] has limited angular measurement range, as the receiver does not move near to, or in front of the transmitter, which means that backscatter measurements will not be performed.

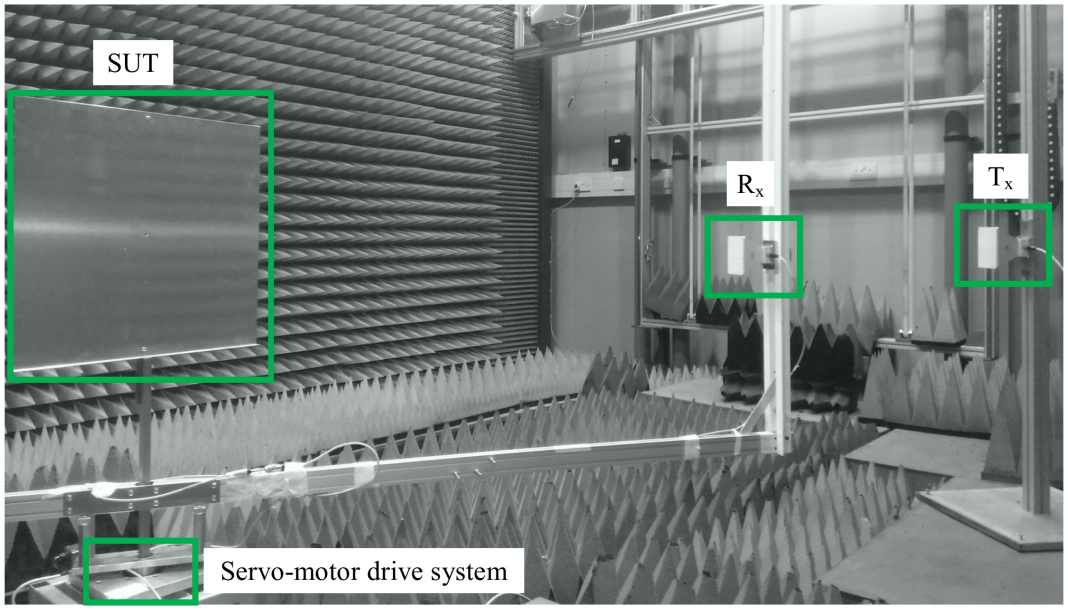

Figure A.6: The bi-static measurement system includes a receiver mounted on a rotating arm capable of rotating accurately over a 360° range. The angle of rotation is controlled by a pre-programmed servo motor.

For many surfaces, the scatter towards the transmitter is of interest, and this is considered in the design of our system. Alternative facilities are capable of more complex hemispherical measurements, requiring expensive control systems and long

measurement times [97, 98] and the potential high cost of development was considered in our system.

Angular resolution of results is often an issue. The use of a fixed rail measurement system with 30° resolution is described in [99], although it requires multiple fixed receive antennas at each of the angles of interest. This system requires not only extensive control systems to switch between antenna of interest, but also multiple antennas; increasing the cost of the system. There is therefore motivation for the design of a bi-static system capable of 360° measurements at high resolution and low cost.

A.2.3.2 Hardware construction and configuration

The bi-static measurement system was constructed in a partially anechoic chamber measuring 6 m × 4 m × 3.5 m. The final experimental rig is pictured in Fig. A.6. The system allows for an accurate and fast scattering measurement of a centralised target – see Fig. A.7 for the top-down view of the system.

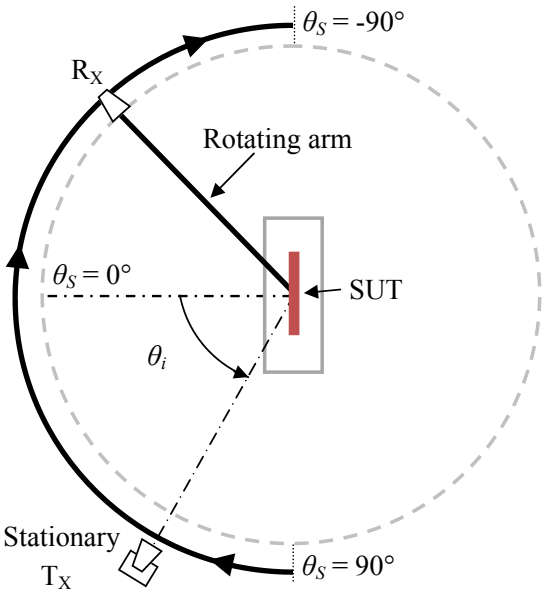

Figure A.7: Top-down view of the bi-static RCS measurement system described in this paper. For many applications, only the reflection from the front of the surface-under-test (SUT) is of interest.

Targets of varying size can be mounted on the flat plate in the centre of the system.

The transmit horn was connected to a stationary beam, 2.3 m from the target. This was manually positioned, using a laser level to confirm the angle of incidence to the target. The receive antenna was secured to a rotating arm, 1.65 m from the target. The rotating arm was connected to a servo motor located in the middle of the system. Surfaces under test can be loaded onto the turntable which is also positioned in the centre of the system. Two QPAR wideband horn antennas (P/N 6878/24) were used for the receiver and transmitter. Measurements are limited to frequencies between 1.5 and 18 GHz when using these horns. Only TE and TM polarisation measurements are available when using these horns.

The dynamic range of the system is best quantified in the empty chamber measurements in Fig. A.10, where the maximum signal comes from the direct path coupling between receiver and transmitter antennas between 210 ° and 230° and the minimum signal is from when the receiver and transmitter are at right angles to each other, between 90° and 150°. Measurements show the dynamic range spans from -50 dB to -115 dB. The dynamic range of the Agilent 8720D VNA itself is 100 dB [100].

The transmit and receive horns are electrically connected to ports 1 and 2 respectively of an Agilent E8720 Vector Network Analyser (VNA) via RF coaxial cables. The VNA was then connected to a PC for data transfer via a GPIB-to-USB link. The VNA data is written continuously to a text file for the duration of the measurement. When run under full angular resolution, a 360° measurement with 0.5° steps can be done, although in many cases, a 1° step will suffice.

Inevitably, the movement of the receive horn arm also moves the RF cables. Phase instabilities could be introduced, although in this case phase was not measured. In a scenario where the phase is of importance and is required to be measured, it is likely another method of attaching the cables to the horns to reduce cable movement will be required, considering the cost of phase stable cables.

A.2.3.3 Software design

Microsoft Visual Basic (VB) and MINT [101] software is used to programme the VNA and servomotor, with the user able to select a range of parameters on a graphical user interface (GUI), such as start and stop frequency, number of discrete measurement points and angular step. Table A.2 summarises the selectable parameters

Table A.2: Summary of the parameters used to programme the VNA and servomotor controls, and relevant measurement distances for the bi-static measurement system.

Parameter	**Value**
Start frequency	8 GHz
Stop frequency	18 GHz
Sweep time	2 s
Number of points	401
IF bandwidth	1 kHz
Transmit Power	0 dB
Time gate start	27 ns
Time gate stop	29 ns
Angular range	360°
Angular step	1°
Receiver to SUT distance	1.65 m
Transmitter to SUT distance	2.3 m

available in the GUI, an example of which can be seen in Fig. A.8.

Credit for the basic motor control and GUI can be given to Daniel Holtby, Lee Ford and Jonathan Rigelsford. Further additions described here were added by the author to improve the measurement accuracy and also remove consistent bugs which caused the system to crash resulting in a necessary restart of the system. The most important of these additions was the use of a time gating technique and is considered in the next sections. The user is also able to select between measurements in the time and frequency domains, where the start and stop values in the GUI will change the time start and stop points.

A.2.3.4 Applications of the system

The high accuracy and resolution of the bi-static system lends itself to many applications. Full characterisation of FSS backed with large metallic ground plates are possible with just a 180° receiver sweep angle. For FSS where through measurements are needed, the 360° sweep enables both specular and forward scattering

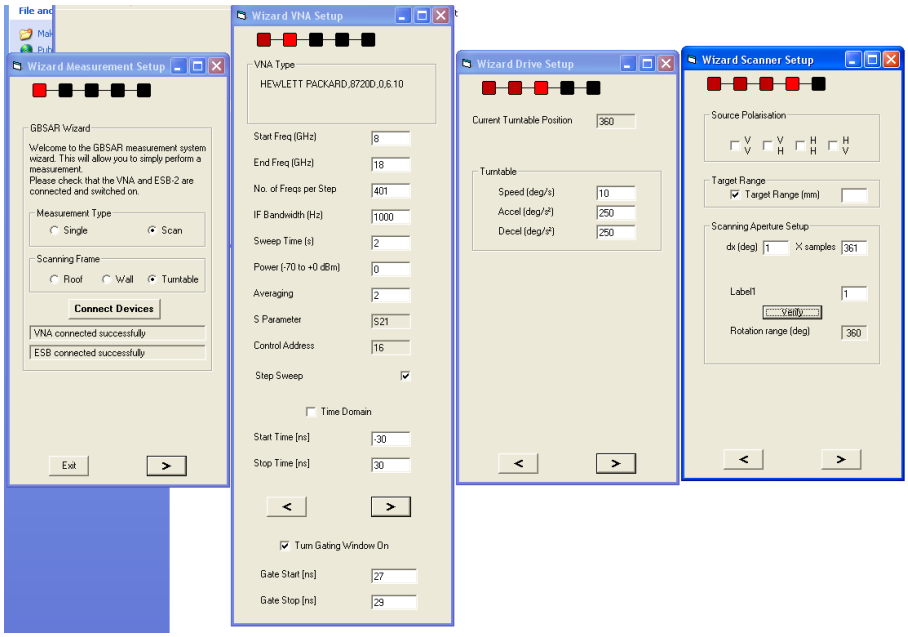

Figure A.8: The graphical user interface (GUI) for the rotating bi-static measurement system.

to be measured. Radar absorbing materials (RAM) can also be tested, with a 1° resolution possible. Antenna measurements are possible using this bi-static system, although their characterisation are best suited to traditional measurement systems, such as near-field characterisation chambers.

A.2.3.5 Measurements with no time gating

To reveal areas of unexpected reflections or coupling which could affect scattering measurements, an empty chamber measurement was initially done. Although both TE and TM polarisations were examined, only TM polarisation is discussed here for brevity. The SUT and turntable with supporting pole were removed from the centre of the system.

For this measurement, the transmitter was positioned at $\theta_{R_x} = 42°$. The measurement technique illustrated in Fig. A.9 was used to obtain a full 360° receiver angle resolution, for a frequency range of 8 to 18 GHz, and scattering results are shown in Fig. A.10a and Fig. A.10b for TM and TE polarisation respectively.

The scattering measurements in Fig. A.10 reveal two regions of coupling which may

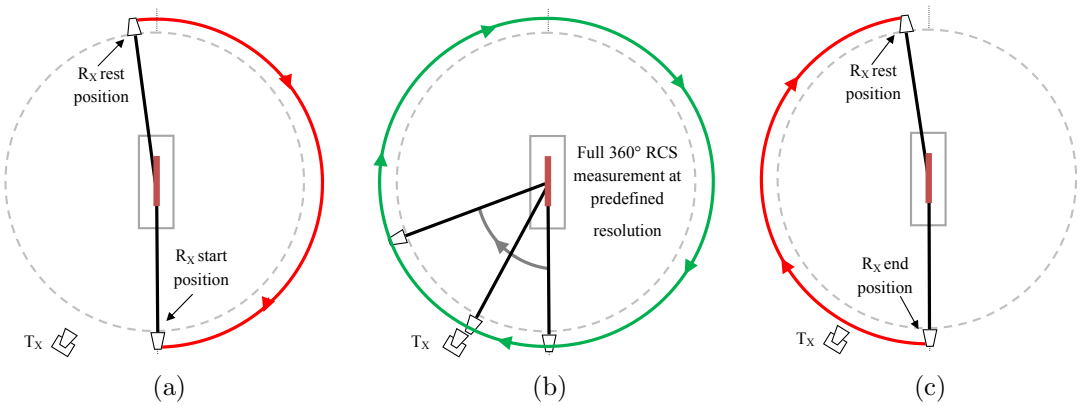

Figure A.9: The bi-static measurement system is programmed to start at a receiver angle of 0°. (a) The start position can be changed to suit the position of the transmitter, and the SUT. (b) A full circular measurement is completed at the users predefined resolution, and (c) the receiver returns to the rest position,ready for the next measurement.

be an issue when completing further scattering measurements. The first region of concern is evident between 0° and 80°. This is due to the receiver moving in front of the transmitter, as illustrated in Fig. A.9. This interference may cause issues in measuring backscatter reflections.

As the receiver moves away from the transmitter in the angle range 80° to 150°, the level of coupling is reduced; however, not to a suitable level. This means that coupling between the antenna and receiver is still an issue, even when separated by such a large distance. The final region lies between 150° and 300°, and reveals a very high level of line-of-sight (LOS) coupling. This occurs when the receiver is directly opposite the transmitter. For oblique incidence measurements, the specular scatter is likely to occur in the receiver angle ranges 120° to 160°, depending on angle of incidence, and so the LOS may affect accuracy of results.

Indeed, in initial measurements of both a flat plate and CR-FSS structure, the measurement results have been affected by the noisy conditions substantially. The measurement in Fig. A.11 shows that there is noise in parts of the measurement, such as between scattering angles of -60° and -30°, and 60° and 90°, caused by coupling of the receiver and transmitter horns and line-of-sight (LOS) respectively.

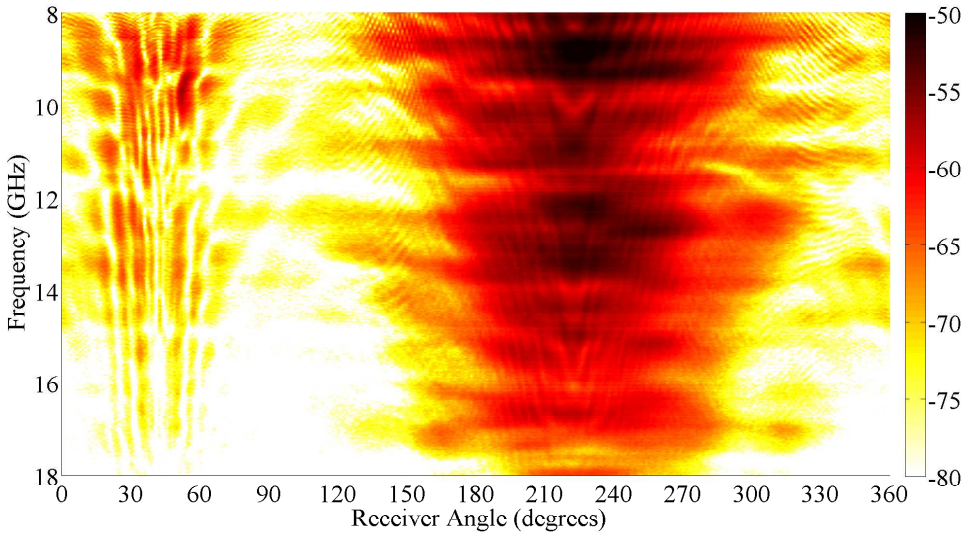

(a) TM polarisation.

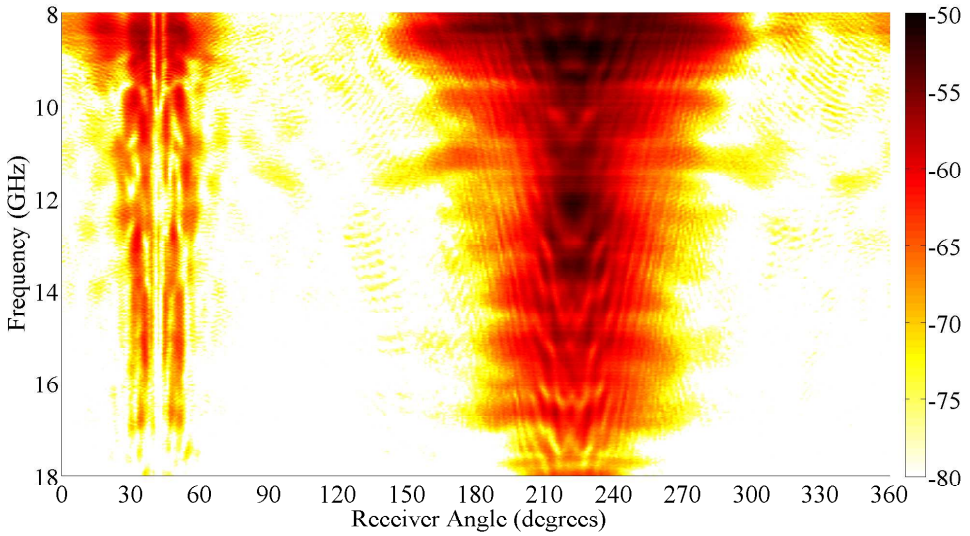

(b) TE polarisation.

Figure A.10: Scattering plots of an empty chamber for (a) TM and (b) TE polarisation, for a receiver range of 0° to 360°.

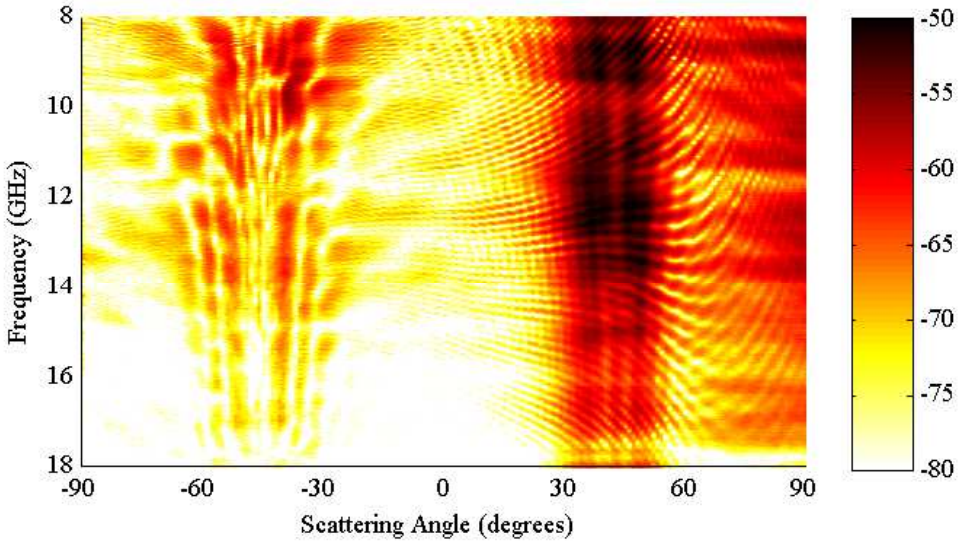

(a) Flat plate

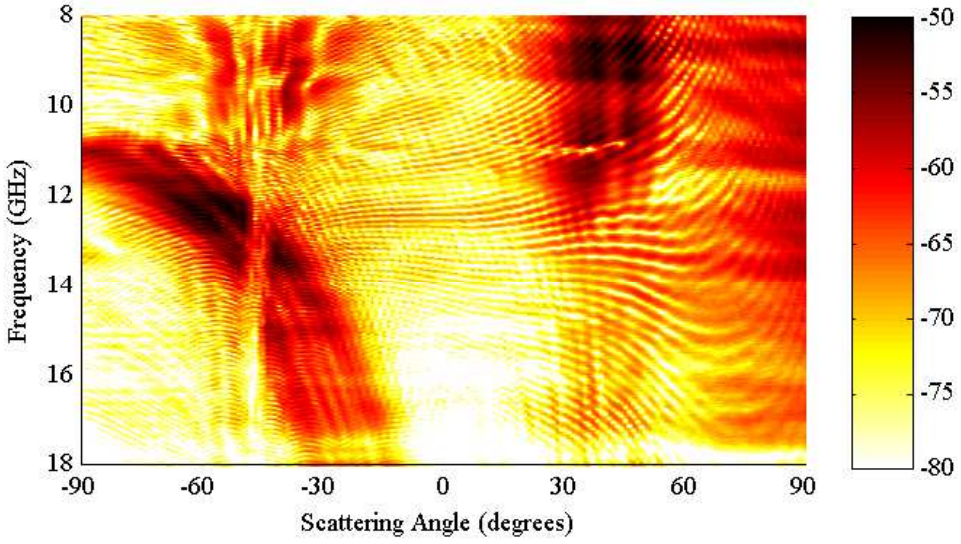

(b) CR-FSS.

Figure A.11: Measurement of (a) a flat plate and (b) a CR-FSS structure prior to time gating.

A.2.3.6 Time gated measurements

Unwanted reflections and coupling are often removed using time gating techniques to improve the accuracy of results. The application of such a technique is more difficult in an actively moving bi-static measurement system compared to traditional stationary ones. Firstly, a full time domain measurement of the flat metal plate is conducted to understand where a suitable time gate should be placed. The system was programmed to perform a time domain measurement between 0 and 35 ns. The resulting scattering from a flat plate is illustrated in Fig. A.12.

In the time domain, the specular scatter from the flat plate occurs between 120° and 170°, due to the wide beamwidth of the horn antennas. This is evident at approximately 27.8 ns. Also visible over the full receiver angle range is a sweeping signal caused by the coupling between the moving receiver and transmitter. This receiver-transmitter coupling is the main cause of the non-time gated results in Fig. A.11. At 42°, the transmit and receive horns are aligned completely, resulting in the shortest coupling distance, and thus the shortest coupling time, at 16 ns. Conversely, the maximum transmit time occurs at approximately 28 ns at 222°, when the receiver is opposite the transmitter.

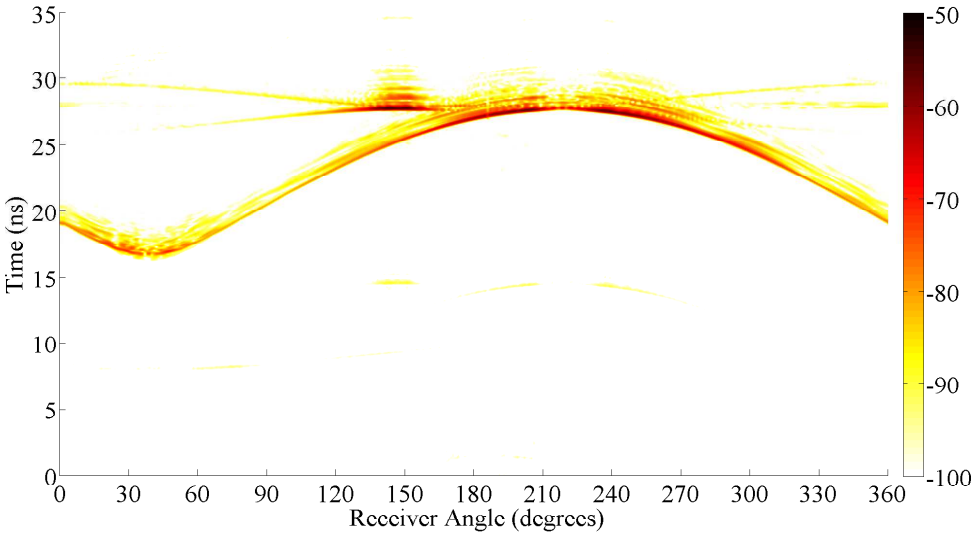

Figure A.12: The measured response of a flat plate in the time domain, showing regions of receiver-transmitter coupling, and specular scatter between 120° and 170°.

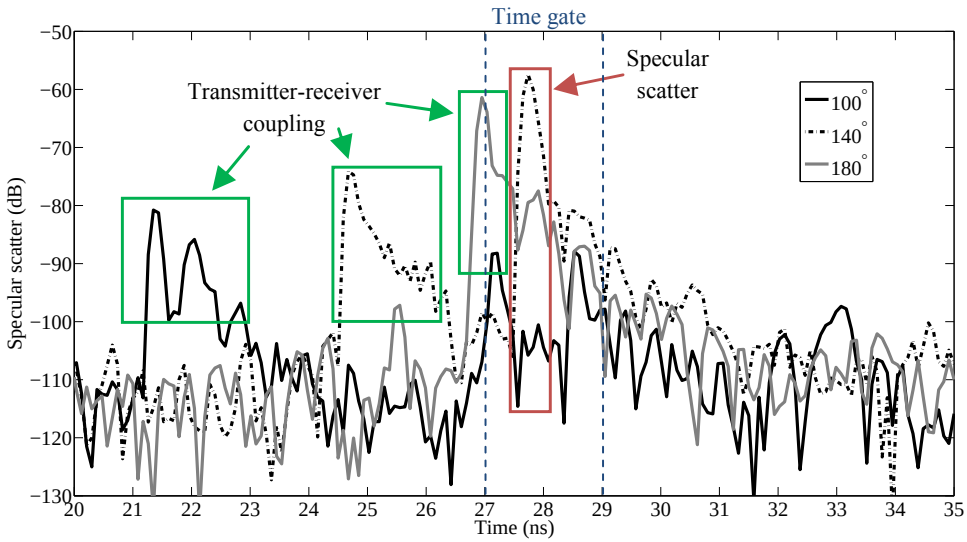

Figure A.13: Time domain response for $\theta_{R_x} = 100°$, 140°, and 180°. The main specular scatter peak occurs at 27.8 ns. The other visible peaks are due to coupling between the antenna and receiver.

The use of a time gate is introduced, with the user able to input gate start and stop parameters on the GUI. For measurements completed in this bi-static system, a time gate between 27 and 29 ns will remove the majority of the coupling. Fig. A.13 highlights that the time gate can remove transmitter-receiver coupling for a range of angles of receiver. The improved scattering plots are presented in the results sections of the surface design chapters.

The windowing function used on the Agilent 8720D VNAs in both the NRL measurements and bi-static measurements was the 'normal' gate as defined in [104]. Step rise time, impulse width, and span can be altered by changing the gate type as described in [103].

A.2.3.7 Far-field requirements

Far-field requirements were considered according to equations 3.1 and 3.2, where the distance from the transmitter to the SUT, and the distance between the SUT and the receiver should be separated by at least R_1 m and R_2 m respectively [102].

$$R_1 = \frac{2D_1^2}{\lambda} \tag{A.1}$$

where D_1 is the largest dimension of the SUT, and λ is the wavelength at the highest frequency. The dimensions of the SUT were 0.6 m $\times$ 0.6 m, thus $D_1 = 0.6$ m. For a measurement of $f = 18$ GHz, $\lambda = 0.0167$ m, and accordingly $R_1 = 43$ m. Considering now the far-field criteria for the receiver with respect to the SUT, the required separation, R_2 is

$$R_2 = \frac{2D_2^2}{\lambda} \tag{A.2}$$

where D_2 is the largest dimension of the SUT, and λ is the wavelength at the highest frequency. For a 600 mm^2 flat metal plate, $D_2 = 0.6$ m. Therefore, at 8 GHz, $R_2 = 19$ m, and at 18 GHz, $R_2 = 43$ m. Ideally, the target would be very small to reduce R_2; however, this introduces issues with diffraction from the target edges. The target must be relatively large (usually target length = 10λ), as diffraction from the edges can occur if the edges are visible to the main beam of the antenna.

These edge effects are mitigated by having a large target size, compared to the lowest frequency of interest. At 8 GHz, $\lambda = 37$ mm, which is 1/20th the target length. However, leading and trailing edge effects are evident in Fig. A.12. The angle of incidence is also an issue, as for oblique angles, the surface will appear much smaller than if the transmission is normal to the surface. Once again, the large size of the target helps keep any issues to a minimum.

The fact that measurements for both the NRL reflectivity arch and the bi-static rotating measurement system may take place in the near-field limits the potential to measure the relative phase of a signal. Coincidently, both techniques are only used for measurement of the amplitude of the signal. For measurements that do take place in the near-field, reflectivity readings are likely to be lower than when measured in the far-field. [105].

A.2.4 Potential improvements to the bi-static measurement system

Despite the measurement system being able to perform accurate and precise measurements, there are a few improvements that could be made to increase the usability and functionality of the rig.

Firstly, the positioning of the transmitting horn is difficult to do due to the fact it is free standing as shown in Fig. A.14. Although a laser level and protractor are used to set the angle of incidence, finer alterations must be made after viewing the results. This makes the whole measurement system much more cumbersome than it potentially could be.

Figure A.14: The transmitting horn in the bi-static measurement system.

As it is free standing, the distance between the target and the transmitting horn is also changeable, making repeatable results difficult especially if the system has been reconfigured. To improve this part of the measurement system, there should

be a method of mechanically setting and fixing the angle of incidence and distance from the centre of the target. This would also ensure that the horn is directed at the centre of the target. Automatation of the transmitter horn in a similar way to the receiever horn would allow for multiple measurements to accuratly be completed with minimal input from the user of the system.

The connection to the receiving antenna requires a fixed cable which is twisted around the centre of the rig after each measurement, requiring uncoupling and reattaching. This reduces the number of measurements that can be done per day and has several risk factors. During the measurement process, the cable often got caught around the centre of the target, requiring manual untangling of the coaxial whilst the system was running. This did no effect measurements as the receiver was behind the target at this stage. Also, continual bending and twisting of the cable is likely to effect its performance over a long period of time, requiring replacement more often than required if an alternative solution was used.

It is proposed that a rotary joint could be used to connect the rotating receive antenna to the VNA. This would mean that none of the cables actually twist around the target, and that multiple measurements could be done without untangling and reattaching the coaxial cable.

A.3 Other potential calibration techniques

Further to the calibration techniques discussed so far in this chapter, additional techniques are available. For example, subtracting the background noise of the measurement system can be done to obtain just the scattering characteristics of the target under test. However, in order to implement this calibration, phase information is also required for each measurement angle and at each frequency point. As it was unclear as to whether this could be achieved using the respective VNA, and initial calibration techniques gave clear results this was not investigated further.

Implementation of this technique would also require very accurate positioning of both the transmit and receive antennas, as well as the target itself. This is so that each angle of measurement could be coherently subtracted to remove the coupling

detailed previously. Small errors in this measurement could result in inaccurate final results after the subtraction of the measured s-parameters.

A.3.1 Conclusions

Measurements will be used to validate a variety of surface designs and respective CST simulations. A bi-static measurement system has been developed to provide a large quantity of data over various angles of scattering and broadband frequency range. By performing initial measurements in the time domain, a suitable time gate can be used to improve the clarity of scattering measurements of a variety of reflective FSS. Despite this, a range of improvements have been suggested for improving both the accuracy and speed of future measurements, as well as the repeatability.